ADVANCED PHOTOTHERMAL OPTICAL COHERENCE TOMOGRAPHY (PT-OCT) FOR QUANTIFICATION OF TISSUE COMPOSITION

Mohammad-Hossein Salimi

A DISSERTATION SUBMITTED TO

THE FACULTY OF GRADUATE STUDIES

IN PARTIAL FULFILLMENT OF THE REQUIREMENTS

FOR THE DEGREE OF

DOCTOR OF PHILOSOPHY

Graduate Program in Mechanical Engineering,

York University

Toronto, Ontario

July 2022

Abstract

Optical coherence tomography (OCT) is an imaging technique that forms 2D or 3D images of tissue structures with micron-level resolution. Today, OCT systems are widely used in medicine, especially in the fields of ophthalmology, interventional cardiology, oncology, and dermatology. Although OCT images provide insightful structural information of tissues, these images are not specific to the chemical composition of the tissue. Yet, chemical tissue composition is frequently relevant to the stage of a disease (e.g., atherosclerosis), leading to poor diagnostic performance of structural OCT images.

Photo-thermal optical coherence tomography (PT-OCT) is a functional extension of OCT with the potential to overcome this shortcoming by overlaying the 3D structural images of OCT with depth-resolved light absorption information. Potentially, signal analysis of the light absorption maps can be used to obtain refined insight into the chemical composition of tissue. Such analysis, however, is complex because the underlying physics of PT-OCT is multifactorial. Aside from tissue chemical composition, the optical, thermal, and mechanical properties of tissue affect PT-OCT signals; system/instrumentation parameters also influence PT-OCT signals. As such, obtaining refined insight into tissue chemical composition requires in-depth research aimed at answering several key unknowns and questions about this technique.

The goal of this dissertation is to generate in-depth knowledge on sample and system parameters affecting PT-OCT signals, to develop strategies for optimal detection of a molecule of interest (MOI) and potentially for its quantification, and to improve the imaging rate of the system. The following items are major outcomes of this dissertation:

1- Generated comprehensive theory that discovers relations between sample/tissue properties and experimental conditions and their multifactorial effects on PT-OCT signals.

2- Developed system and experimentation strategies for detection of multiple molecules of interest with high specificity.

3- Generated optimized machine learning-powered model, in light of the above two outcomes, for automated depth-resolved interpretation of tissue composition from PT-OCT images.

4- Increased the imaging rate of PT-OCT by orders of magnitude by introducing a new variant of PT-OCT based on pulsed photothermal excitation.

5- Developed algorithms for signal denoising and improving the quality of received signals and the contrast in images which in return enables faster PT-OCT imaging.

Dedication

I would like to dedicate this dissertation to my beloved country, "**Iran**", its beautiful "***Persian Gulf***", its kind and nice people, and its great scientists of all times:

- *Khayyam* (the great mathematician who first presented the solution of cubic equations and the inventor of the precise "Jalali" calendar)
- *Al-Haytham* (the father of modern optics)
- *Avicenna* (the pioneer in medicine)
- *Al-Khwarizmi* (the inventor of algorithm and the creator of algebra)
- *Al-Biruni* (was the first scientist to formally propose that the speed of light is finite)
- *Al-Farisi* (had a major contribution in Optics, and studied prism and refraction of light)
- *Ibn-Sahl* (the great physician and the discoverer of the law of refraction)
- *Al-Kashi* (the great mathematician and astronomer, pioneer in trigonometry, who invented the cosine rule)
- *Al-Razi* (the pioneer in medicine and pharmacy, and the father of psychology and psychotherapy)

To name a few.

Acknowledgments

I would like to express my sincere gratitude toward my supervisors, Prof. Nima Tabatabaei (Lassonde School of Engineering, York University), and Prof. Martin Villiger (The Wellman Center for Photomedicine, Harvard Medical School) for their endless support and leadership.

I would like to express my thanks to the committee members, Prof. Paul O'Brien, and Prof. Simone Pisana for their constructive feedbacks during this study. I would also like to express my great appreciation to Prof. Alex Vitkin for accepting to be the external referee and Prof. Ali Sadeghi-Naini for accepting to be the internal referee of this dissertation. I am also grateful to Prof. Thomas Cooper for holding my PhD examination as the chair of the session.

I would like to extend my deepest gratitude to my dad, Prof. Qobad Salimi (MD/PhD), and my mom, Farzaneh, for continuous encouragement throughout my years of study.

Last but not least, I would like to express my deepest appreciation to my life teacher, Prof. Seyyed-Adil Naderali, who familiarized me with the meaning of life, and the philosophy behind the universe.

Table of Contents

List of Figures

List of Tables

List of Acronyms

2D	two dimensional
3D	three dimensional
ADAM	Adaptive moment estimation
AFM	Atomic force microscopy
AI	Artificial intelligence
ANN	Artificial neural network
CW	Continuous wave
DL	Deep learning
D-OCT	Doppler optical coherence tomography
EDTA	Ethylenediaminetetracetic acid
ETOH	Ethanol alcohol
FDA	Food and drug administration
FDM	Finite difference method
FD-OCT	Fourier domain optical coherence tomography
FFT	Fast Fourier transformation
FWHM	Full width at half maximum
GT	Ground truth
H&E	Haematoxylin and eosin
HAZ	Heat affected zone
ICG	Indocyanine green
IV-OCT	Intravascular optical coherence tomography
IVUS	Intravascular ultrasound
Mayo	Mayonnaise
ML	Machine learning
MOI	Molecule of interest

MSE	Mean squared error
NC	Necrotic core
ND Filter	Neutral density filter
NIR	Near infrared
NIRAF-OCT	Near infrared autofluorescence optical coherence tomography
NIRF-OCT	Near infrared fluorescence optical coherence tomography
NIRS-OCT	Near infrared spectroscopy optical coherence tomography
O.C.T	Optimal cutting temperature
OCE	optical coherence elastography
OCM	optical coherence microscopy
OCT	Optical coherence tomography
OCT-A	Optical coherence tomography angiography
OD	Optical density
OPL	Optical path length
PBS	Phosphate-buffered saline
PDMS	Polydimethylsiloxane
Pseudo-MOI	Pseudo molecule of interest
PT	Photothermal
PT-OCT	Photothermal optical coherence tomography
RBF	Radial basis function
ReLU	Rectified linear response unit
RMSE	Root mean squared error
SD-OCT	Spectral domain optical coherence tomography
SNR	Signal to noise ratio
SS-OCT	Swept source optical coherence tomography
SSIM	Structural similarity

STFFT	Short time fast Fourier transformation
SVM	Support vector machine
TCFA	Thin cap fibroatheroma
TD-OCT	Time domain optical coherence tomography
TE-OCT	Thermo-elastic optical coherence tomography
TMAZ	Thermo-mechanically affected zone
TM-PT-OCT	Transient mode photothermal optical coherence tomography
TW	Thermal wave

List of Symbols

S(k)	Spectral power of the light source
I_R	Intensify of the refence arm
I_S	Intensify of the sample arm
κ	wavenumber
ΔL	*O*ptical path length difference
δ	Delta Dirac function
γ	Inverse Fourier of the spectral power
Δz	Axial resolution of OCT
Δx	Lateral resolution of OCT
Δλ	Bandwidth
λ_0	Center wavelength
l_c	Coherence length
f	Focal length
W	Waist beam radius
T	Temperature
t	Time
μ_a	Absorption coefficient
t_L	Laser exposure time
ζ	concentration-dependent material parameter
I_{PT}	PT power fluence rate
P	Medium density
c	Specific heat of the medium
α	Thermal diffusivity of the medium
n	Refractive index
dn/dT	Thermo-optic coefficient
β	Thermal expansion coefficient

P	Laser power
Ψ	Relative concentration
e	Thermal effusivity
f	Frequency of PT laser amplitude modulation
L_{ray}	Rayleigh range
z	Depth of the sample
ξ	Radial to the center of the beam at a specific depth
Φ	Vectorial distance to the center of the beam
Q	Heat source
$\tilde{Q}$	Heat source distribution in the frequency domain
$\tilde{\theta}$	Temperature in the temporal frequency domain
$\tilde{\sigma}$	Complex wave number
μ	Thermal diffusion length
q	Heat flux
u	Radial displacement
w	Axial displacement
σ_r, σ_θ, σ_z	Mechanical stress in radial, azimuthal and axial directions
ε_r, ε_θ, ε_z	Mechanical strain in radial, azimuthal and axial directions
$\Delta\phi$	Phase variation
D_{fp}	distance from the selected pixel to the focal plane
D_{top}	distance from the selected pixel to the top surface of the sample
Gr_{pixl}	Gray level of the selected pixel in the OCT image
Gr_{line}	Average of gray level of the pixels above the selected pixel
PT_{Amp}	Amplitude of pixel's PT-OCT signal
t_D	Delay time
t_P	pulse duration
φ_{time}	Time-lapse of OCT phase
S_{pulse}	Signal amplitude with the pulse method

σ_{noise}	Standard deviation of the averaged noise
T_{filt}	Percentage of light transmittance

1: Introduction

1.1. Background

Optical coherence tomography (OCT) is a non-invasive and high-resolution optical imaging method which can capture two- or three-dimensional images from optical scattering media. OCT is widely used in tomographic imaging of biological tissues as the imaging resolution (1-10μm) and the high speed of OCT allow for rapid and 3D visualization of tissue internal structures. OCT works based on interferometric measurement of the pathlength differences and intensities of back-scattered light from tissue microstructures [1]. Generally, near-infrared (NIR) coherent light sources are used in OCT in order to achieve millimeter-range penetration depth while maintaining ~10μm image resolution in biological tissues [1]. In 1990, Fercher presented the first images from a fundus human eye *in vivo* using white light interferometry [2]. This pioneering work of Fercher laid the basis for development of OCT system. The concept and fundamental principles of OCT was published in 1990 by Naohiro Tanno [3], and in 1991 by Huang *et al.*, in Fujimoto lab at the Massachusetts Institute of Technology (MIT) [4]. Since 1990, the technology has undergone significant transformations becoming a popular imaging method for interrogating biological tissues. Today, OCT systems are widely used in medicine, especially in the fields of ophthalmology, cardiology, oncology and dermatology[1]. Some of the key appealing attributes of OCT technology for medical diagnosis and screening include [5, 6]:

- Ability to perform real-time and fast sub-surface imaging of tissue *in vivo*
- Image resolution and penetration depth suitable for interrogation of disease-induced abnormalities without use of exogenous contrast agents
- Ability to miniaturize the imaging head of OCT in form of catheters and small probes and integration in standard-of-care medical devices such as catheters, endoscopes, laparoscopes, or needles
- Ability to interrogate excised tissue with minimal sample preparation
- Use of non-ionizing electromagnetic radiation

Accordingly, OCT systems have been used for interrogation of tissue located in areas where acquisition of excisional biopsy is not feasible (e.g., the eye, arteries, or nervous tissues) [1]. Moreover, the high imaging speed of OCT has enabled practitioners to comprehensively image large areas at various

anatomical sites of the human body in order to screen for diseases with patchy and discontinuous nature; thus, significantly eliminating the intrinsic sampling error of random excisional biopsies. Rapidness, resolution/imaging depth, and ability to miniaturize into endoscopes/catheters combined have enabled medical practitioners to make instant diagnosis based on OCT images (aka. Optical biopsy) [7].

In comparison to other medical imaging technologies, OCT offers ranges of penetration depth and resolution that cannot be provided by other medical imaging technologies. Figure 1 provides a comparison of depth of penetration and resolution of mainstream morphological tissue imaging methods (i.e., ultrasonography, confocal microscopy, and OCT). Ultrasonography can image in depth up to 10 cm but with low resolution of ~300 micrometers which is frequently insufficient to resolve disease-induced morphological abnormalities. OCT, on the other hand, resolves morphological signatures of biological tissue with resolution of 1-15 micrometer. In terms of penetration depth, OCT's imaging depth is significantly lower than that of Ultrasonography, but significantly larger than that of confocal microscopy. As such, OCT imaging performance fills the gap between ultrasonography and confocal microscopy by generating fine resolution images from structures close to the interrogated surface of tissue.

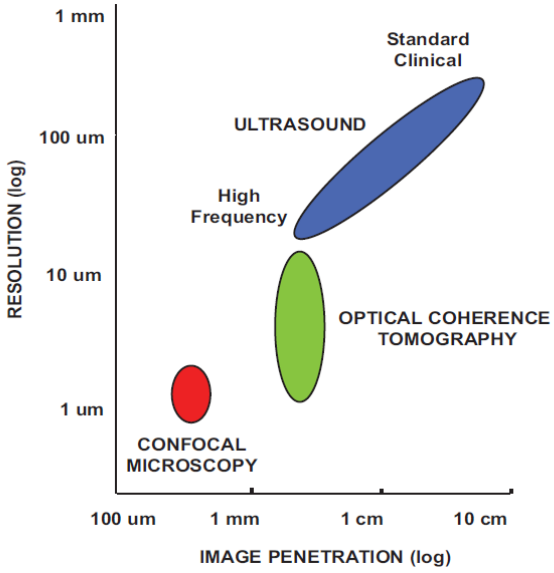

Figure 1. Comparison of image resolution and penetration depth for conventional structural imaging methods used in medicine and biology. OCT fills the gap between ultrasound and confocal microscopy. Figure adapted from[7]. Copyright 2015, Springer Nature Publishing Group.

1.2. Applications of OCT in Medicine

In medicine, OCT systems are widely used for research and clinical purposes, specifically in the fields of ophthalmology, cardiology, dermatology, oncology, urology, dentistry and gastroenterology[7]. In the field of ophthalmology, OCT has achieved greatest success, making OCT a gold standard method for

diagnosis of retinal diseases[8, 9]. OCT is ubiquitous in eye clinics and routinely used for diagnosis and screening of macular hole, macular pucker, macular edema, glaucoma, diabetic retinopathy, vitreous traction[10-13]. Success of OCT in ophthalmology is mostly due to the fact that human eye structure consists of multiple layers of semi-transparent media that allow the NIR light of OCT to penetrate down to the posterior parts (fundus oculi) to form tomography of the organ (Fig.2).

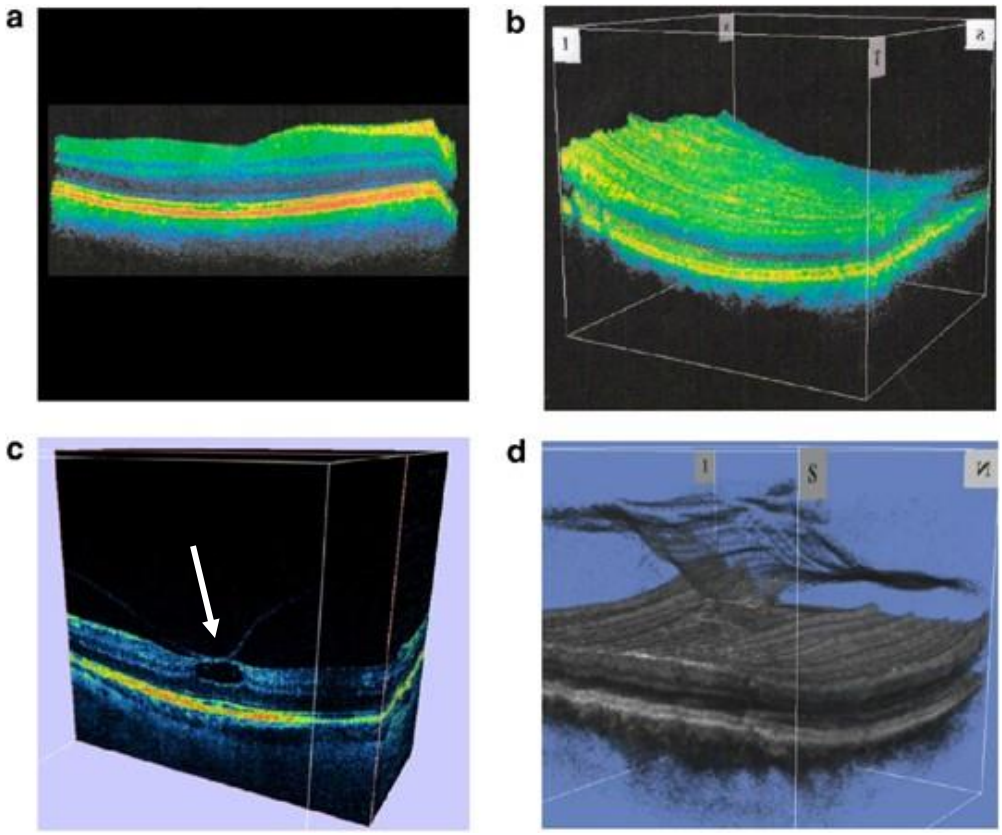

Figure 2. Images from human eye captured by different OCT system configurations and brands. Fourier-domain OCT images: (a) , (b) 3D volume with two different views of retinal layers (Topcon 3D 1000 system). (c) Posterior vitreous detachment (PVD) that appears as detached layers in OCT images from the posterior eye; cyst (S OCT Copernicus system). The PVD abnormality is pointed out by the white arrow. (d) PVD shown in 3D inserting into macular hole (Topcon 3D 1000). To have a better contrast, retinal layers are usually labeled with different colors. By forming such high quality and fine resolution 3D images from human eye, OCT has become a gold standard in the field of ophthalmology; No scale bar was provided in the original figure. Figure adapted from[14]. Copyright 2008, Springer Nature.

In dermatology, OCT can resolve skin layers (epidermis, dermal-epidermal junction and dermis) to show vascular network, layer thickness, and the hypo-structure for dermatological pathology purposes (Fig.3)[15, 16]. For example, OCT has been employed in diagnosis of skin cancer, inflammatory skin diseases, vascular disease of skin, and also employed in physiological studies to monitor and control various treatments such

as follicular unit extraction, laser-assisted drug delivery through nails and skin, and for semiautomated localization of the dermo-epidermal junction (DEJ)[17].

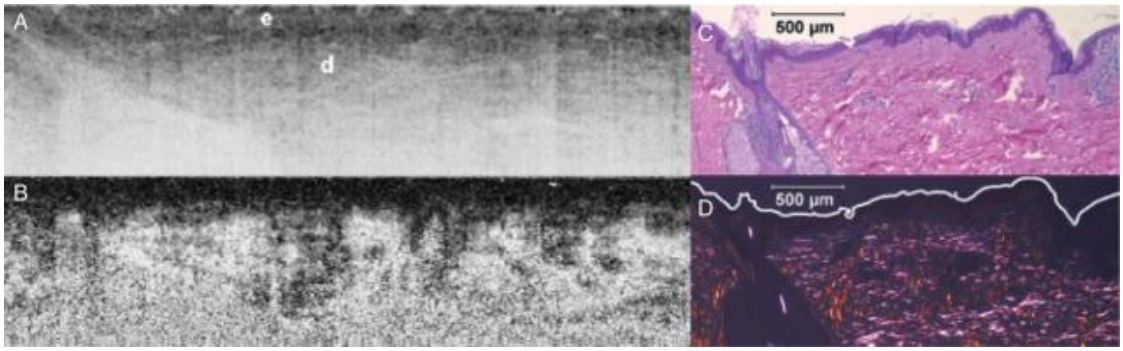

Figure 3. Examples of OCT images of normal human skin, *in vivo*. (a) Conventional and (b) polarization-sensitive images from the upper arm, 5 mm wide by 1.2 mm deep. Corresponding histology from the same location (H&E stain), viewed with (c) brightfield and (d) polarized microscopy. The OCT results clearly show the different layers of the human skin sample, consistent with the histological images; also, more information regarding collagen morphology can be obtained from the polarization-sensitive images; see the reference for more information. Figure adapted from[18]. Copyright 2004, Elsevier, The Society for Investigative Dermatology, Inc.

In oncology, OCT systems have been used in imaging structural changes at early stages of cancer, including those arising in the breast, brain, bladder, the gastrointestinal tract (Fig.4), respiratory organs, and the skin[19]. In these areas, OCT has been making key contributions on several fronts, such as: screening for cancer, guiding excision of biopsies, providing real-time feedback in the operation room as intraoperative imaging of cancer, and monitoring tumor responses to treatments such as photodynamic therapy, radiotherapy, and chemotherapy[19].

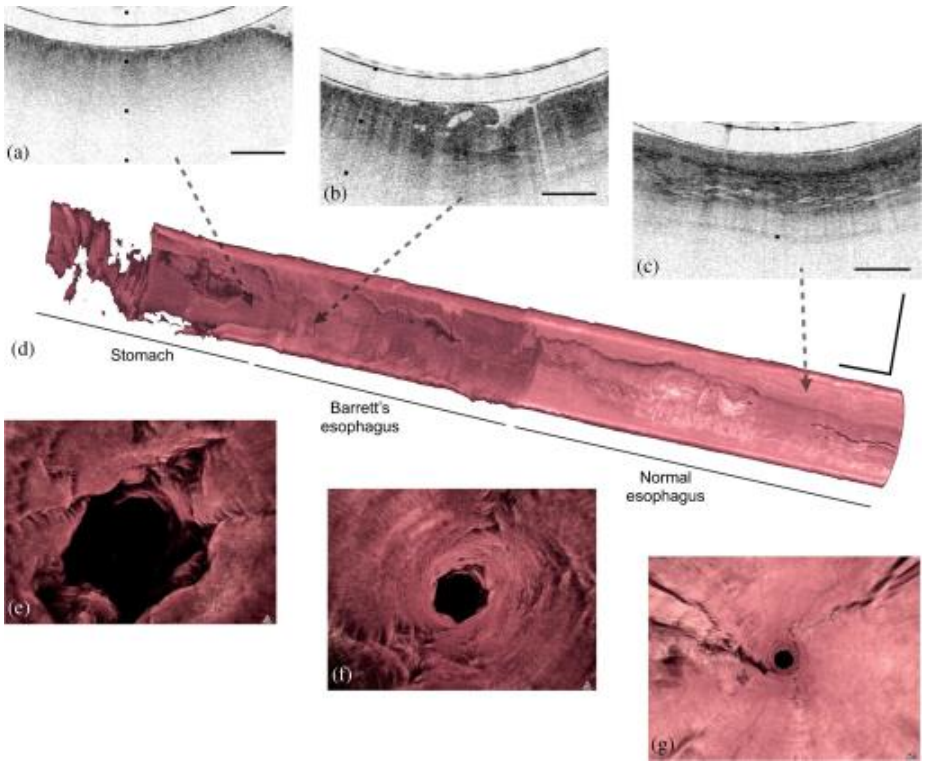

Figure 4. Volumetric OCT imaging of human esophagus *in-vivo* with tethered capsule endomicroscopy. A 3D volume of the endomicroscopy data in panel (d) showing a 4 cm segment of Barrett's esophagus. Tick marks and scale bars, (a–c) 1 mm; scale bars, (d) 1 cm. Figure adapted from[20]. Copyright 2013, Nature Publishing Group.

In cardiology, intravascular OCT (IV-OCT) has become one of the three most important imaging methods, alongside intravascular ultrasound (IVUS) and coronary angiography methods[21]. IV-OCT is a non-contact catheter based method that has 10 times greater resolution in comparison with IVUS[22]. In IV-OCT, a tiny OCT probe located inside a catheter is sent into the desired areas (i.e., coronary arteries, or aorta) through the peripheral artery to scan the artery walls and acquire the morphology *in vivo* at an unprecedented level of detail (Fig.5). In 2012, a group of experts in IV-OCT published a consensus document to standardize the interpretation of IV-OCT images of coronary atherosclerosis into: fibrous and fibrocalcific plaques, fibroatheroma, macrophage accumulations, intimal vasculature and cholesterol crystals, thrombi, plaque rupture and erosion prolapse, stent malapposition, and dissections, covered and uncovered stent struts and restenosis[21]. Today, IV-OCT devices can be found commercially worldwide, and the demand for such systems is growing fast. In 2016, it was reported approximately 100,000 IV-OCT procedures are performed annually, and IV-OCT application is growing at a rate of ~ 20% per year[23]. Application of OCT system in cardiology to monitor coronary atherosclerosis serves as a motivation throughout this thesis, so here, we provide brief description of this type of cardiac disease.

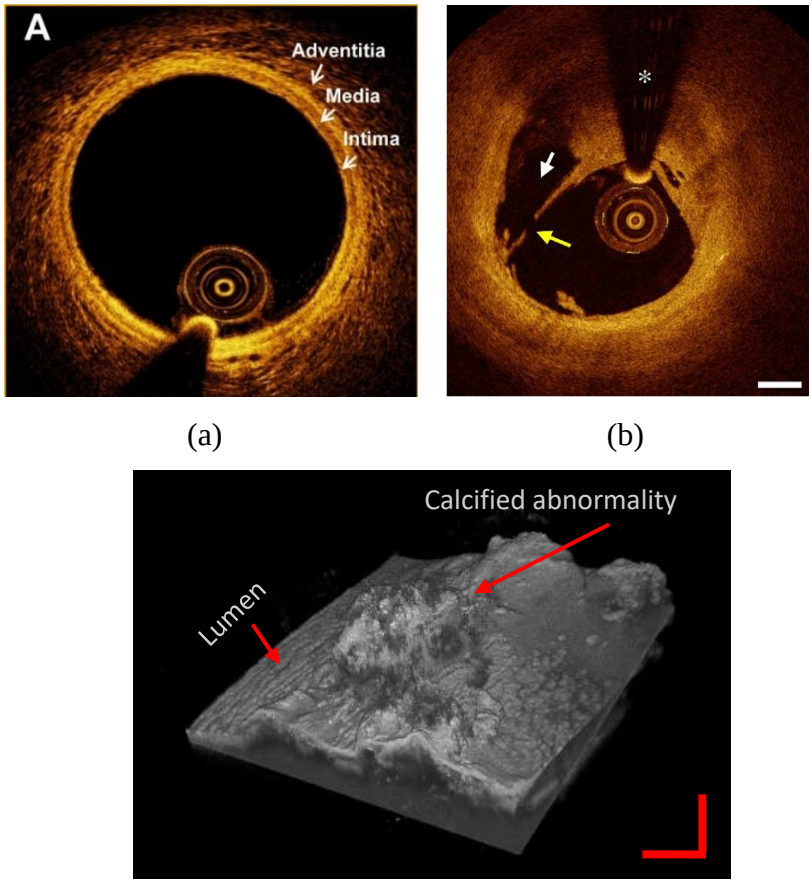

Figure 5. Examples of OCT images from cardiac tissues. (a) A view of normal artery wall and its layers captured by IV-OCT. In this image, the three layers of vessel wall (intima, media, and adventitia) are clearly separable with different scattering properties. Figure adapted from[24]. Copy right 2017, by the American College of Cardiology Foundation, published by Elsevier. (b) An example of plaque rupture captured by IV-OCT. Arrows delineate a broken fibrous cap. In this image, the contents of the ruptured plaque are partially washed out by the flushing medium, leaving behind a cavity, scale bar=500 μm. Figure adapted from[21]. Copyright 2011, Elsevier Publishing Group. (c) A 3D volume of OCT captured from a calcified region in a human aorta sample, *ex vivo*, scale bar=1 mm.

1.1.1.i) Atherosclerosis

The underlying cause of many cardiac diseases is atherosclerosis, a condition developed as a result of continuous accumulation of various materials such as lipid, cholesterol, cellular waste products, calcium, and fibrin in the intimal layers of the arteries. As atherosclerotic plaques build up in the arteries, their walls become thickened and stiff[25, 26]. The exact process of atherosclerosis is still not well understood, but it can happen in all human arteries. It has three different stages of growth that lead to clogged arteries: the fatty streak, the plaque, and the complicated lesion (plaque rupturing) as seen in figure 6[26, 27]. The first visible stage of this disease is the fatty streak that appears as yellow streak consisting of white blood cells, cholesterol, and other dead cellular matter at the site of endothelial damage. In the plaque stage, more debris

including dead foam cells and other substances such as calcium and cholesterol continue to build up at the site of fatty streaks that eventually leads to formation of plaques[27]. The atherosclerotic plaques consist of a large lipid core representing more than 50% of volume of the plaque which is covered by a thin fibrous cap and a heavy infiltrate of inflammatory cells (macrophages and lymphocytes)[28]. A formed plaque may stay stable for a long time. A significant factor that determines the stability of a plaque is the thickness of the fibrous cap. However, the critical thickness of cap as a criterion of stability for plaques in different vessels is not the same. For instance, in a carotid artery, a plaque can be considered as a stable plaque when the thickness of fibrous cap is between 0.7 to 2 mm[29]. When the fibrous cap thickness is decreased, the mechanical stress that is applied to the plaque by the blood pressure will increase. Cap thickness under 130 μm for aortic plaques and 80 μm for carotid plaques indicates a plaque with high risk of rupture[30]. Studies have confirmed the strong correlation between lipid composition of the plaque and the risk of vulnerability[31-33]. A hallmark for high-risk plaques is the thin cap fibroatheroma (TCFA) stage[34, 35]. Pathologically, TCFA in coronary arteries is characterized as a large lipid pool which is overlaid by a thin fibrous cap (thickness<65 μm)[36]. Inflamed TCFA is the most common form of vulnerable plaque and causes 60% to 70% of events of acute coronary thrombosis[35]. Recently, the cholesterol crystal depth inside arterial plaques has been suggested as an index of plaque vulnerability[37].

The last stage of atherosclerosis is plaque rupturing that happens when the grown plaques break open. The rupture of the cap exposes the plaque material to the blood and causes the formation of a thrombus (blood clot). Fatal coronary thrombosis frequently results from the rupture of plaques that have a large lipid core, separated from the lumen by a thin fibrous cap[38, 39]. When the lumen is partially or fully occluded, the patient may develop myocardial infarction (MI; aka “Heart Attack”). As an exceptional case, the unstable angina describes symptoms of a plaque that sufficiently occludes blood flow to cause exercise-induced ischemia, but its cap is still intact[40, 41]. In developed countries, coronary artery disease is one of the most common types of heart disease with a high rate of mortality that is caused by rupture of atherosclerotic plaques[42]. To choose proper interventional techniques in this disease, high accuracy assessment in vulnerability of atherosclerotic plaques is essential[43]. Routine scanning of vessels and treating culprit lesions to get a better understanding of patient’s risk for a subsequent future event in curing procedure were recently suggested[43]. A preferred therapy for such cardiac disease is percutaneous coronary intervention (PCI, formerly known as angioplasty with stent)[44, 45]. PCI refers to a non-surgical and minimally invasive method that utilize a catheter to place a stent to open clogged coronary arteries[45]. During this procedure, scanning of vessel and identification of future events may be possible. However, due to its invasiveness, scanning the coronaries of a broad population could never be done ‘routinely’ by this method.

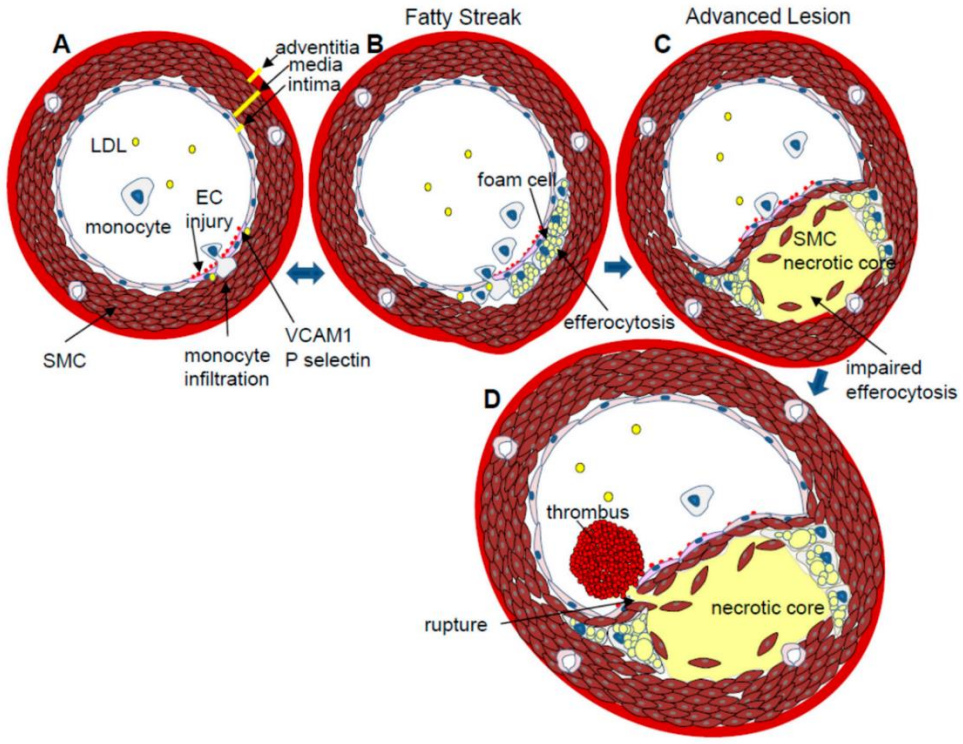

Figure 6. An illustration of the atherosclerotic growing stages including fatty streak, plaque, and rupture; for details of plaque growth stages see text. Figure adapted from[46]. Copyright by the authors.

1.1.2. Principle of OCT

From the mathematical point of view, OCT relies on calculation of cross-correlation of back-reflected light with respect to a reference light. Such mathematical operation is normally carried out in OCT systems in Michelson interferometer configuration. As shown in figure 7(a), in a Michelson interferometer, a light source is split into two arms via a beam splitter. These arms then illuminate two mirrors that are positioned at a distance of d_1 and d_2 from the beam splitter. The back-reflected beams interfere with each other and create an interference pattern on the screen after passing again through the beam splitter. The frequency of dark and bright lines in the interference pattern has a correlation with the difference between d_1 and d_2 lengths[47]. The operation of the Michelson interferometer (and by extension that of OCT) can be mathematically explained in either time-domain or Fourier-domain. In either case, through proper instrumentation and signal processing the depth profile of subsurface reflectors/structures (aka. A-lines) can be found.

Depending on the instrumentation approach of an OCT system, two main types of OCT systems can be developed: Time-domain (TD-OCT) and Fourier-domain (FD-OCT)[48]. In TD-OCT, A-lines are acquired by mechanical movement of the reference mirror of the interferometer. As such, TD-OCT systems are

inherently slow and normally deemed not suitable for interrogation of tissue. FD-OCT systems, on the other hand, is based on Fourier-domain realization of cross-correlation and as such can acquire A-lines without any need for mechanical reference arm scanning. FD-OCT is divided into two major categories based on instrumentation approach for measurement of responses in the Fourier-domain: spectral-domain (SD-OCT) and swept-source (SS-OCT). Although the instrumentation for sensing the light signals in these systems are different, both systems use Fourier-domain mathematical principle of cross-correlation to form images from captured raw signals. Since the system developed and used in this thesis is an SD-OCT system, we will explain the principle of OCT in SD-OCT arrangement.

In SD-OCT systems (Fig.7(b)), the light source is normally a broadband coherent light source. The output light is divided into two arms by a beam splitter and are called reference and sample arms, respectively. In the sample arm, light is focused on the sample surface by an objective lens. In the reference arm, the light illuminates a fixed mirror as the reference. After back-reflection of light from sample/tissue, and the reference mirror, these two beams are combined again in the beam splitter and redirected to a spectrometer for recording of reflectivity interference pattern of the two beams as a function of wavelength. The intensity of the reflectivity pattern in the spectrometer can theoretically be explained as[48]:

$$(k)= S(\kappa)\ (I_R +\sum_{i=0}^{m}[\mathrm{I_{Si}} + 2\sqrt{\mathrm{I_{Si}I_R}}\cos(2\mathrm{k}\Delta\mathrm{L}_i)]). \quad (1.1)$$

Where, $S(\kappa)$ is the spectral power of the light source, I_R is intensity of reference arm, I_{Si} is intensity of i^{th} surface of the sample with m reflective surfaces in depth, k is wave number, and ΔL_i is the optical path length difference (OPL) between the reflected beams from the i^{th} surface and the reference ($\Delta L_i = n_2 L_2 - n_1 L_1$, where n is the refractive index and L is the physical length). As such, the term $2k\Delta L_i$ in Eq. (1.1) represents the phase shift of the light between reference and sample beams.

After illumining tissues with the OCT light, the intensity of back-reflected (I_{si} in Eq. (1.1)) decrease dramatically due to the absorption and the scattering of photons in the tissues. However, in the reference arm, such drop in the intensity of light (I_R in Eq. (1.1)) does not occur, because the light is reflected by the reference mirror. Therefore, the weak signal from the sample is amplified by the much stronger reference signals ($2\sqrt{\mathrm{I_{Si}I_R}}$ in Eq. (1.1)), and we can receive meaningful signal above the noise floor of the spectrometer.

As seen in the equation, intensity of the light recorded by the spectrometer ($I(k)$ in Eq. (1.1)) is a function of wave number which highlights sensing of sample responses in Fourier-domain. To form the OCT image based on the intensity of reflection from individual reflectors, the signals in K-space (wave number/Fourier space) need to be converted to Z-space (optical path length space). Therefore, to obtain the depth profile of

reflections in sample (aka A-line), inverse Fourier transformation is applied to the K-space data, which gives:

$$i(z) = \gamma(z) I_R + \sum_{i=0}^{m} \gamma(z) \otimes [I_{Si} + 2\sqrt{I_{Si} I_R}\,\delta(z \pm 2(z_R - z_{Sn}))]. \quad (1.2)$$

Here δ is delta Dirac function, and γ is the inverse Fourier of the spectral power $S(\kappa)$ appeared in Eq. (1.1). The sample reflectivity profile, $i(z)$ in Eq. (1.2), is obtained by cross correlating the point spread function of the light source with the location of reflector in the sample. Therefore, a light source with a Gaussian spectrum can improve the image quality, provide better contrast, and decrease side lobe effects. Figure 7(b), schematically, demonstrates the OCT signal processing procedure for a sample with three subsurface reflectors. As required by Eq. (1.1), as the depth of reflective surface increases, the modulation frequency of the acquired interference spectrum, $2k\Delta L_i$, increases, resulting in spatial separation of signals along depth after inverse Fourier transformation. It should be noted that since the data/signal measured by spectrometer is real number data, after application of inverse Fourier transformation the depth profile data will be of complex nature with symmetric mirror terms ($\delta(z \pm 2(z_R - z_{Sn}))$ in Eq. (1.2)). Therefore, by calculating amplitude of complex numbers, the location of the surface in depth as well as intensity of reflection is obtained (aka A-line amplitude)[7]. Also, the symmetric mirror terms generate a mirrored image of the sample with respect to the zeroth surface in the tomogram that can be neglected.

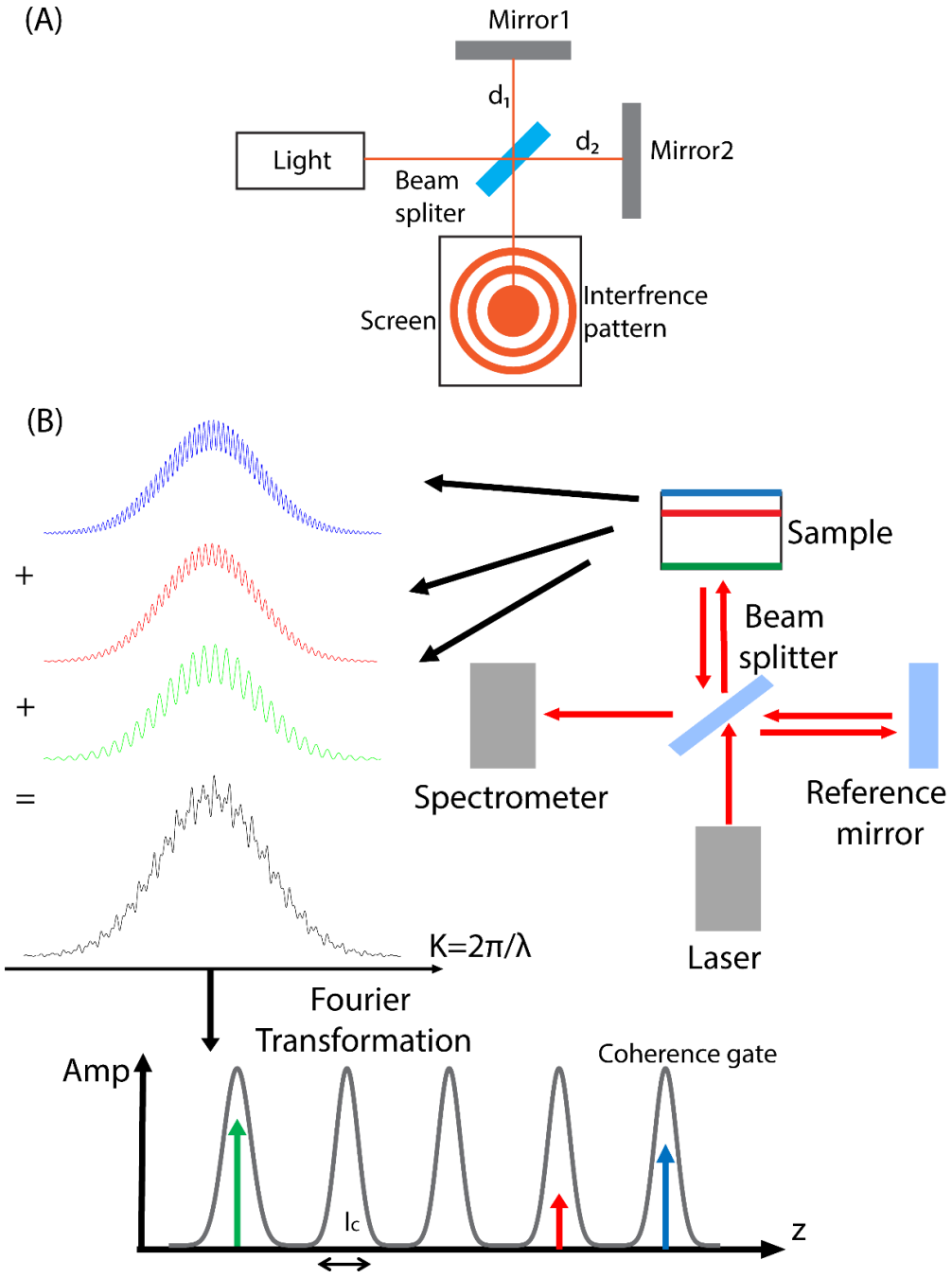

Figure 7. Schematic representation of the principles of interferometry behind OCT. (a) A schematic of Michelson interferometer, the system typically consists of a light source, a beam splitter, 2 mirrors and a screen. The frequency of the interference pattern on the screen is a function of the path length difference of mirrors (d_1-d_2). (b) A schematic of SD-OCT system. The output light from the laser source illuminates the sample and the reference mirror after passing through the beam splitter. The back-reflected light from the sample and the mirror is merged and delivered to the spectrometer. In the spectrometer, the frequency of modulated wave correlates with the depth of layers in the sample. After applying Fourier transformation on received signals, an A-line is obtained. For details, see the mathematical expressions in the main text.

By raster scanning the beam in one direction, a cross sectional image (aka B-Scan or tomogram) is formed. A volumetric 3-D image (C-scan) of the sample can be made by attaching several parallel 2-D tomograms/B-Scans (Fig.8). It should be noted that in OCT context to accommodate the extreme dynamic range of the signal, amplitude images are normally shown in logarithmic dB scale. In OCT, the point spread function of the light source cross-correlates with the reflectivity profile of the sample. Therefore, a light source with Gaussian spectrum can improve the image quality, provide better contrast, and decrease side lobe effects.

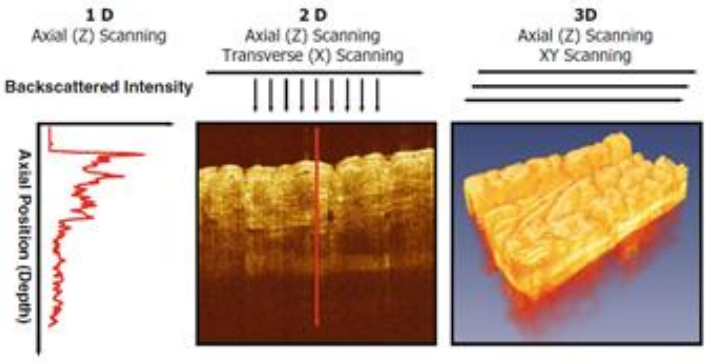

Figure 8. An example of A-line, B-mode, and volume images in OCT. An A-line is a 1D data that represents the location of reflectors along the depth at a specific location on the sample surface. By attaching several A-lines scanned while translating the beam position on the sample surface, a 2D B-mode image is formed. A 3D volume image of the sample is obtained by attaching the parallel B-mode images. Figure adapted from[1]. Copyright 2008, Springer-Verlag Berlin Heidelberg.

One of the important parameters governing OCT image quality is image resolution. In OCT, two types of resolution in an image are defined: axial and lateral resolutions. Light with broad bandwidth and low coherence length is typically used in OCT. By assuming a Gaussian-shaped spectrum, the axial resolution Δz (full width at half maximum, or FWHM) in a low-coherence interferometry system such as OCT is defined as[1]:

$$\Delta z = \frac{2ln2}{\pi} \times \frac{\lambda_0^2}{\Delta\lambda} \ . \qquad (1.3)$$

Where λ_0 is the center wavelength, and $\Delta\lambda$ is the bandwidth (in FWHM criterion) of the light. As seen, in contrast to standard microcopy, in OCT, axial resolution is independent of the beam focusing and spot size. For a Gaussian beam, the axial resolution is also equal to the coherence length l_c. Because of the coherence length, OCT has a coherence gating feature. That is, the detected OCT signal in spectrometer arises only from photons that have been backscattered from a thin layer in the sample selected by the coherence gate of the light source (see Fig.7(b)). Other backscattering photons in tissue whose OPL difference between the

reference arm does not match with the coherence length will not be detected as a meaningful signal in the spectrometer. As this portion of back-reflected light (aka, bulk backscattered detected light) does not provide any spatial information about the tissue layers, it only contributes to the OCT noise signal[1]. Consequently, coherence gating reduces detection of undesired scattered light in the sample, improves image contrast, and enable imaging to greater depths[1]. The lateral resolution Δx for a Gaussian beam is[1]:

$$\Delta x = \frac{2\lambda_0}{\pi} \times \frac{f}{W}. \qquad (1.4).$$

Where f is the focal length, and W is the waist radius of the beam incident on the objective lens. To achieve a fine lateral resolution, a large numerical aperture that focuses the beam to a small spot size can be used.

In OCT, phase images that are formed from phase of OCT signals are more sensitive to changes in OPL than amplitude images. Phase of signals ($2k\Delta L_i$ in Eq. (1.1)) can detect relative displacements on the order of tens of picometers to few nanometers, while the detection limit of changes in OPL via the amplitude of signals is directly linked to the system axial resolution (i.e., on the order of several micrometers). Owing to such enhancement in measurement of relative displacements, OCT phase signals have been explored for introduction of several functional extensions of OCT. For example, Doppler OCT (D-OCT) and OCT-angiography (OCT-A) are two variants of OCT that measure the blood flow velocities in capillaries (especially in the eye) (see Fig.9). In these techniques, the OCT phase is captured over time (aka, M-mode scanning) to obtain the phase shift of OCT signal as a result of back-reflection of light from moving particles inside the sample (Fig.9.(a),(b)). The D-OCT technique was applied on TD-OCT, long before introducing FD-OCT system. For instance, in 1997, the two-dimensional D-OCT for *in vivo* imaging was presented using a short time fast Fourier transformation (STFFT) to measure the fringe signal by TD-OCT system[49]. This method which is called spectrogram methods allows imaging of *in vivo* tissue structure and flow velocity simultaneously. However, a limitation in D-OCT technique with TD-OCT system was the phase stability. Indeed, due to the need for scanning a delay line, the configuration of interferometer in TD-OCT system were a conventional dual-arm Michelson interferometer. The OCT phase in such non-common path configuration was not too stable to receive signals with acceptable signal to noise ratio (SNR). In 2005, a phase microscopy approach with SD-OCT was demonstrated by Izatt et al[50]. In his work, phase change of OCT signals along time (M-mode scanning) of beating heart of a chicken embryo were captured with a common path SD-OCT system. In this study, it was shown that the phase of OCT in a common-path configuration is more stable, leading to greater signal to noise ratio. The development in these systems, since then, has made the D-OCT and OCT-A as two useful techniques for clinical purposes. Recently, hand-

held probes of OCT as a point-of-care for real-time angiography was proposed to make angiography of the eye convenient for everyday clinical usage[51, 52].

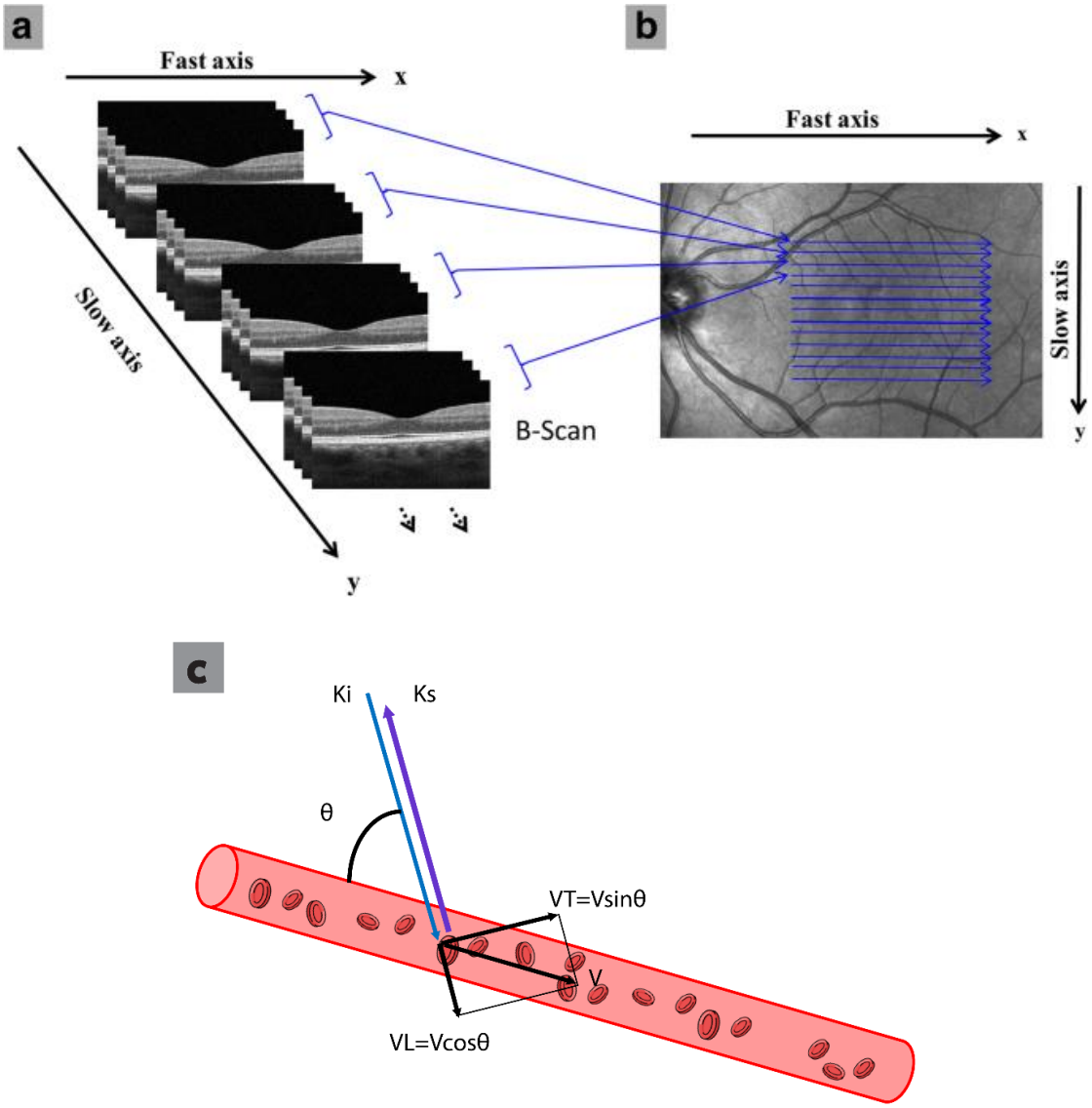

Figure 9. An illustration of OCT-Angio and Doppler-OCT methods. (a) In OCT-A, to form the angiogram of the sample, a few B-scans are taken over time on the "x" fast axis from the sample at each of the "y" slow scan axis points, allowing detection of relative flow signal. (b) Top view of the same general scan pattern on human eye, adapted from [53]. Copyright 2018, Springer Nature. (c) A schematic of blood flow and OCT beam in Doppler-OCT. A vein that blood flows inside it with a velocity V, makes θ angle with the incident OCT beam Ki. The parallel part of the velocity vector with the OCT beam, Vcosθ, affects the back-reflected light Ks, because of the Doppler effect. This effect causes a phase shift in the OCT phase signal that can be related to the velocity of flow.

1.1.3. Shortcomings of OCT

While OCT offers many key advantages over other medical imaging technologies, it forms images based on light scattered from structure of tissue rather than its composition. As a result, OCT is quite sensitive to structural alterations caused by early stages of disease such as atherosclerosis and early dental caries, but it lacks diagnostic specificity (i.e., yield too many false positives). This shortcoming frequently results in poor diagnostic performance at early stages of diseases and restricts applications of OCT. For example, Shokouhi *et al.* in a study compared diagnostic performance of OCT with that of a molecular-contrast imaging method based absorption of light (named thermo-photonic lock-in imaging or TPLI) in detection of early dental caries[54]. The results showed better detection specificity and significantly less false positives in early dental caries with TPLI than OCT due to the more specific nature of light absorption (i.e., TPLI mechanism) over light scattering (i.e., OCT mechanism). As another example, Villiger *et al.* demonstrated that certain stages of atherosclerosis plaques (i.e., intimal thickening and fibro-atheroma) yield similar OCT structural images (see Fig.10), while the chemical compositions of these two stages are different[55].

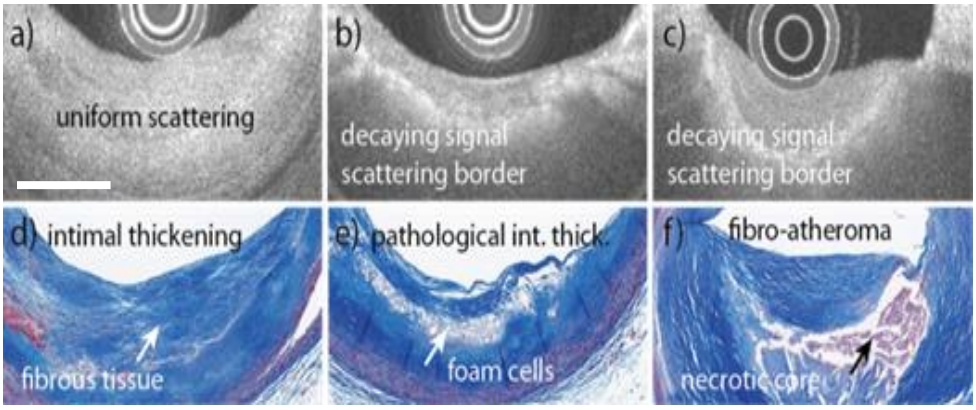

Figure 10. An example of limitation of OCT in detecting molecule of interesting in the sample. The IVOCT images of human cadaveric coronary arteries are plotted in the first row and matching trichrome histology are plotted under each OCT images. (a,d) Fibrous tissue can be readily differentiated from lipid-rich plaques (b,c,e,f), but the structural OCT signal shows very similar features for pathologic intimal thickening (b,e, early disease) and a fibro-atheroma (c,f, advanced disease with high risk of rupture), the outer diameter catheter in this study was 870μm, scale bar=870μm; adapted from [56]. Copyright 2018, by the authors.

1.1.4. Extensions of OCT

To overcome the limitation of OCT in terms of lacking specificity, various functional extensions of OCT and multi-modality OCT-based systems have been introduced. Optical coherence elastography (OCE) is a functional extension of OCT than can measure mechanical elasticity of layers inside the sample and forms a depth-resolved elastogram of tissues visualizing the mechanical stiffness. In this technique, the sample is excited with an external actuator, such as

acoustic radiation force generated by an ultrasound transducer, or air puff (see Fig.11), and the mechanical displacements on the order of a few nanometers in the sample are captured by a phase-sensitive OCT system[57]. Subsequently, this mechanical response to the excitation can be converted to the mechanical elasticity. For instance, Zaitsev *et al.* demonstrated the application of OCE in measurement of the strain dynamics on cornea in the procedure of shape correction with laser[58].

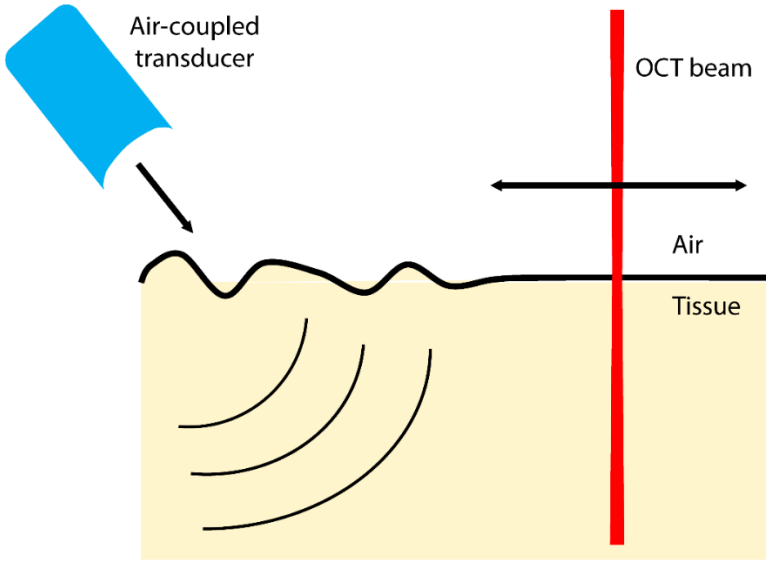

Figure 11. An illustration of OCE with air-coupled trigger. The propagated waves inside the sample as a result of excitation of the sample surface by the air-coupled transducer can be tracked by OCT beam. By analyzing the phase of OCT signals over time, mechanical elastic properties of the sample such as Young's modulus can be measured indirectly.

Indirectly, information about chemical composition may be predicted by the differences in the mechanical elasticity of tissue constituents. As an example, Qi *et al.* showed different mechanical response of necrotic core (NC) and fibrous cap in coronary plaque with OCE (Fig.12)[59]. However, a tissue containing specific chemical composition may generate a different mechanical response to a stimulus at different boundary conditions. For example, in atherosclerosis plaque, a lipid core under different thickness and mechanical stiffness of fibrous cap can generate different responses. Therefore, despite promising results in measurement of tissue mechanical properties with OCE, this method is not entirely specific to chemical composition of tissues.

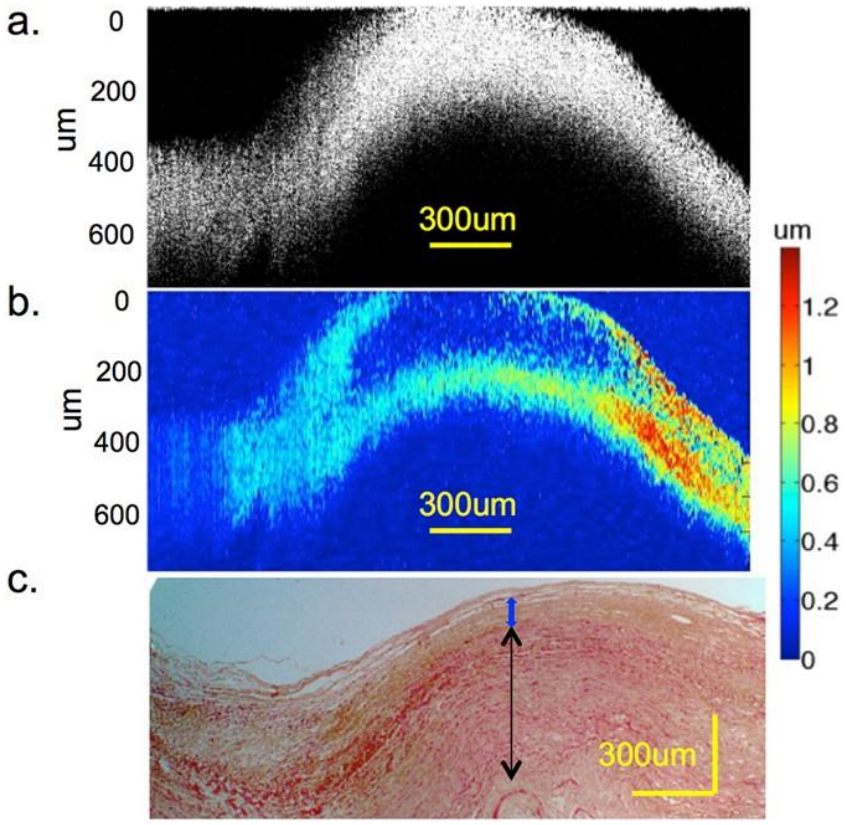

Figure 12. An example of Cadaver tissue imaging with OCE and histology data. (a) Image captured by OCT from human cadaver coronary artery cross-section. (b) Corresponding elastogram obtained with OCE. (c) H&E staining of the region under 4x magnification. The difference in tissue elastic properties than cannot be seen in OCT the image can be observed clearly in the elastogram. Figure adapted from[60]. Copyright 2017, Springer Nature.

Near infrared spectroscopy (NIRS)-OCT is another multimodality system that is sensitive to the chemical composition of tissues[61]. To identify coronary lipids, NIRS is the only method that is approved by Food and Drug Administration (FDA)[62]. In NIRS-OCT structural information are retrieved from scattering of light via OCT and specific molecular and chemical composition related information are retrieved from absorption of light via spectroscopic analysis of reflected light from the sample. The principle of NIRS relies on measuring the amount of scattered and absorbed light by tissues. In this technique, a sample is illuminated by using a laser emitting at NIR band (generally 800 to 2000 nm). The bandwidth of the laser is selected to maximize penetration of the light inside the tissue. The scattered light is received with a detector placed away from the light source (emitter). It is possible to calculate the concentration of chromophores or molecule of interest inside the tissue, by using the modification of the Lambert–Beer law (to consider the scattering phenomenon)[63]. Using these principles, NIRS-IVUS has been used for assessing the vulnerability of plaques[64].

Near-infrared fluorescence (NIRF)-OCT is another multimodality system that utilize the fluorescence response of materials to a NIR radiation to detect the molecule interest in the sample[65]. In this method, the molecule of interest needs to be tagged with some fluorescent agent to produce NIRF signal. For instance, indocyanine green (ICG), a FDA approved agent, has been used as an agent to visualize lipid-laden, inflamed atherosclerotic plaque[66]. In NIRF-OCT, labeling a molecule of interest in samples *in vivo* is a challenging task because the agents usually cannot penetrate deeply into the sample. To overcome this limitation with NIRF, Near-infrared autofluorescence (NIRAF)-OCT method has been proposed that use the natural autofluorescence responses of tissues instead of those of extrinsic labels[67].

While NIRS-OCT, NIRF-OCT, and NIRAF-OCT have shown promise for improving the diagnostic yield, these systems cannot produce depth resolved chemical information from samples as the light-absorption based modality integrated in them are intrinsically diffuse (Fig.13). Consequently, these multimodality systems do not offer sufficient spatial resolution for co-registration of chemical information with the microscopic structural features of OCT in a meaningful way. Moreover, both approaches need extra instrumentation which adds to the complexity and the cost of these systems.

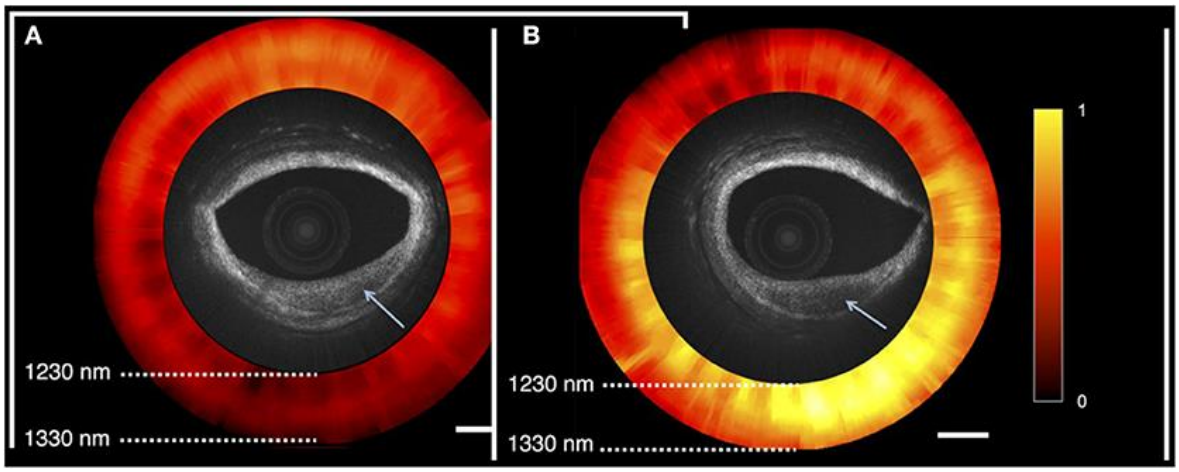

Figure 13. Views of NIRS-OCT scan of human cadaver coronary artery. In this multi-modality system, the structure of the sample can be imaged with OCT. The color bar ring around the image which comes from the NIRS system gives a depth integrated/diffuse sense of chemical information. Both OCT images in these cases show lesions with reduced backscattering (pointed by the arrows). NIRS results as the red and yellow rings represent (a) absorption spectra compatible with fibrotic tissue and (b) lipid-rich tissue. Figure adapted from[62]. Copyright 2020 by the authors.

1.2.Photo-thermal (PT) OCT

Photo-thermal optical coherence tomography (PT-OCT) is a functional extension of OCT with the promise to overcome the nonspecific nature of conventional OCT by forming three-dimensional (3D) images based on both scattering and absorption of light[68]. Compared to other molecular-specific extensions of OCT, PT-OCT is intrinsically able to show depth-resolved maps of targeted molecules of interest (MOI). In PT-OCT, an intensity-modulated photo-thermal (PT) laser with a wavelength at the absorption band of a molecule of interest is added to the conventional OCT system. In such a configuration, absorption of the PT laser by the molecule of interest induces a localized modulated temperature field (aka thermal wave field). This thermal wave field, in return, yields modulated thermo-elastic expansion resulting in modulated variation in the local refractive index. These phenomena ultimately lead to the modulation of the optical path length at the modulation frequency of the PT laser with a modulation amplitude on the order of tens of nanometers[68]. To sense the modulation of OPL with OCT signal, an M-mode OCT dataset is acquired at each lateral imaging location. Since the OCT phase has enough sensitivity to measure such small variations in OPL, PT-OCT has the potential to offer co-registered structural and molecular information through the OCT signals' amplitude and phase, respectively.

To detect a molecule of interest and form depth-resolved maps with molecular specificity, PT-OCT signals can be acquired from either samples labeled with exogenous agents, or label-free using intrinsic light absorption bands of tissue. To date, nanoparticles, as exogenous agents, have been employed in PT-OCT to boost the photo-thermal signal from human[69] and rabbit[70] tissues *ex vivo*, to visualize blood capillaries of mouse ear *in vivo*[71], as well as to detect cancer cells (Fig.14) *in vitro*[72]. Use of both endogenous (melanin) and exogenous (gold nanorods) absorbers have also been reported for imaging mouse retina with PT-OCT *in vivo*[73]. More recently, feasibility of label-free imaging with PT-OCT has also been demonstrated by measuring blood oxygen saturation in vessel phantoms[74] and melanin in zebra fish eye (Fig.15)[75].

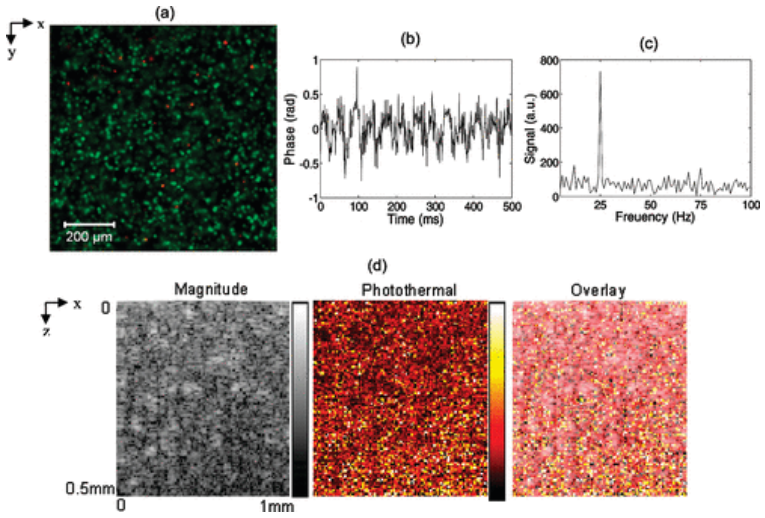

Figure 14. An example application of PT-OCT in detecting labeled cancer cells. (a) An en-face image from the sample containing cancer cell. The green dots are live and red dots are dead cells. (b) Acquired PT-OCT signal in time, (c) and the spectrum of the signal after Fourier transformation. (a) indicates good cell viability and relatively homogeneous cell distribution. (d) The OCT intensity image, photo-thermal image, and overlay of intensity/photo-thermal images. While the OCT result cannot show the location of cancer cells, overlayered PT-OCT information can detect the cancer cells in this sample. Reprinted (adapted) with permission from[72], Copyright 2008, American Chemical Society.

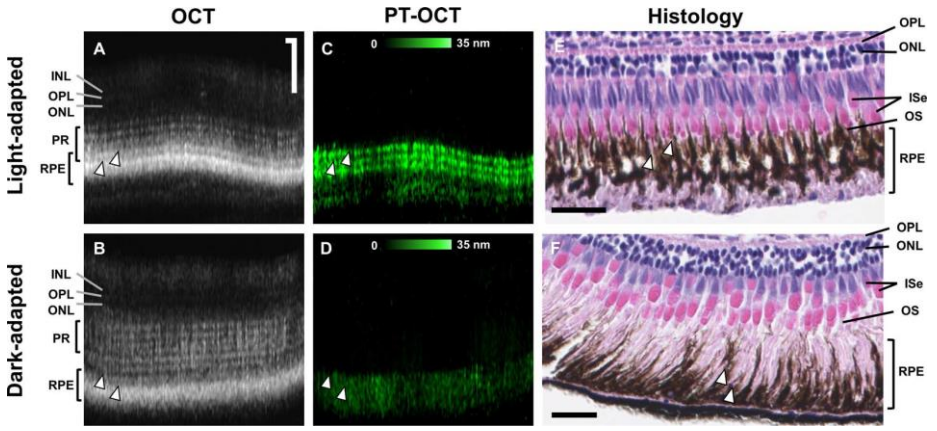

Figure 15. An example of depth resolved detection of melanin in zebrafish eye. In this study, two categories of zebrafish were grown in light and dark environments. In these conditions, the percentage of melanin in the eye will change. (a) , (b) results of OCT images from the layered structure of the eyes , (c) ,(d) PT-OCT images of these two categories show different distribution of melanin. (e), (f) Histology of melanin distribution in zebra fish eye. White arrowheads in OCT and PT-OCT panels indicate various layers where melanin is present; scale bar= 50 μm for OCT and PT-OCT images, 25 μm for histology. Figure adapted from[75]. Copyright 2018, under Creative Commons license (https://creativecommons.org/licenses/by-nc-nd/4.0/)

1.2.1. PT-OCT principle

Figure 16, schematically, illustrates the sequence of physical phenomena that take place leading to PT-OCT signals. In PT-OCT, the sample is simultaneously illuminated with OCT and intensity-modulated PT

lasers. In this configuration, at positions where the modulated PT laser is absorbed, a modulated temperature field (aka thermal-wave field or TW field) is established. This TW field is modulated over time at the modulation frequency of PT laser source and is governed by the bio-conduction differential equation[71]:

$$\frac{\partial T}{\partial t} = \frac{I_{PT}\mu_a}{\rho c} + \alpha\nabla^2 T. \qquad (1.5)$$

Here T is the temperature, t is time, μ_a is the absorption coefficient at PT laser wavelength, I_{PT} is the PT power fluence rate, ρ is the medium density, c is the specific heat of the medium and α is the thermal diffusivity of the medium. The consequence of presence of a TW field at and around an absorber is a change of the local refractive index and physical deformation due to the thermal expansion, and consequently, a change of OPL[76]:

$$\Delta OPL(z) = OPL_{T_0+\Delta T} - OPL_{T_0} = \int_0^z \left(\left[n(T_0) + \frac{dn}{dT}\Delta T\right].[1 + \beta\Delta T] - n(T_0)\right) dZ. \qquad (1.6)$$

Here T_0 is the initial temperature, n represents the refractive index, dn/dT stands for thermo-optic coefficient, and β is the thermal expansion coefficient. The presence of the integral in Eq. (1.6) declares that the absolute phase at a specific depth is the sum of phase changes from sample surface to the interrogated depth. Numerically, the range of ΔOPL is normally between few nanometers to few hundred nanometers. Therefore, such small ΔOPL variations, compared to the ~10μm axial resolution of OCT, cannot shift the location of peaks in the A-line amplitude channel. A-line phase channel, however, offers sufficient sensitivity to reveal the small variation in ΔOPL. Thus, upon absorption of modulated PT excitation, phase of OCT signal will change as a consequence of variation in OPL according to the following equation[50]:

$$\Delta\phi = \frac{4\pi\Delta\mathrm{OPL}}{\lambda_0}. \qquad (1.7)$$

Where λ_0 is the center wavelength of the OCT laser. That is, if the amplitude of the PT laser is modulated in sinusoidal form at a specific frequency, the ensuing temperature field, and consequently OPL, will vary at the same sinusoidal frequency.

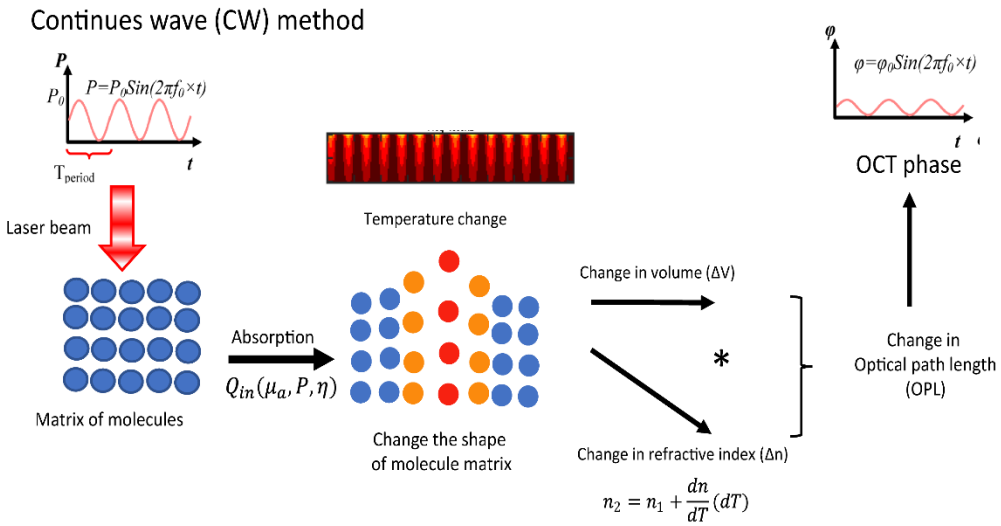

Figure 16. Schematic representation of the physical phenomena taking place in PT-OCT; in this system, the wavelength of PT laser is selected at the absorption band of molecule of interest in the sample. As a result of PT light absorption in the sample by the molecule of interest, a modulated thermal field in the is generated. The produced heat, then, causes a change in the OPL locally near the molecule of interest that can be tracked by OCT phase, for more details about principle of PT-OCT, see text.

Accordingly, by applying FT to the acquired time lapse OCT phase signal (aka M-scan) and evaluating signal amplitude at the modulation frequency of the PT laser, the modulation amplitude of $\Delta\phi$ can be experimentally quantified at each depth (Fig.17). The modulation amplitude of $\Delta\phi$ is proportional to the intensity of the PT laser at the absorber thermo-mechanical properties of medium, and the concentration of the absorbing chromophore.

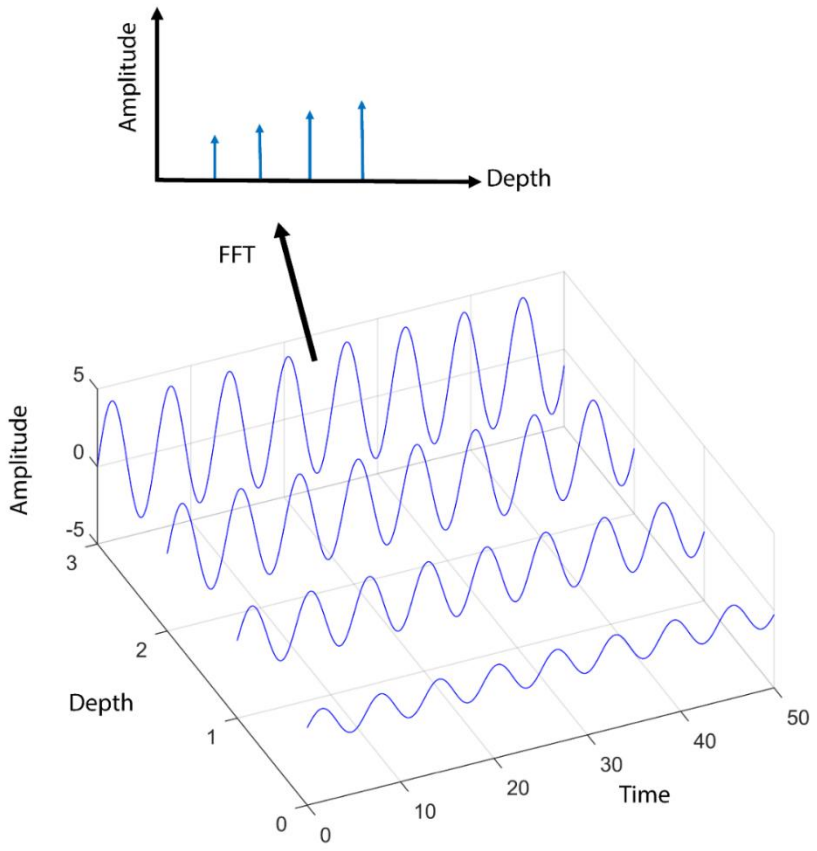

Figure 17. An illustration of variation of the OCT phase signal at different depths of the sample in the time domain. Since OCT phase is cumulative, in deeper levels inside the sample, the amplitude of PT-OCT signal increases. The OCT phase spectrum of all absorbers after applying Fast Fourier transformation (FFT) represents the intensity and the depth of PT light absorption in the sample. The detailed equations are brought in text.

Above text discusses the basic procedure of extracting PT-OCT signals from raw OCT signals. To form a PT-OCT A-line, the amplitude of phase modulations is assigned to each pixel along the depth. To form a B-mode PT-OCT image, obtained A-lines are attached together. Concurrently, co-registered structural images can be produced from the amplitude of OCT datasets. As such, by choosing PT lasers with a wavelength at the absorption peak of MOI (e.g., lipid), co-registered PT-OCT and OCT image pairs can be produced that can be further analyzed to gain depth-resolved insight into chemical composition of tissue.

1.2.2. Shortcomings and gaps

PT-OCT studies to date offer promising results on ability of this functional extension of OCT in depth-resolved visualization of MOI in samples. However, there are several important gaps remaining in the area of PT-OCT that we will point out here. First, as the physics underlying PT-OCT is multifactorial,

consequently, the behavior of PT-OCT signals in complex media such as biological tissues is not well understood. Without a deep knowledge about this multifactorial physics, extracting accurate information from received signals is not feasible. Although some theoretical models have been generated so far to enhance our understanding of PT-OCT signals, the key effects of certain sample and system influence parameters have not been considered in existing models.

Second, there is currently a gap in signal/image processing strategies for decoupling the influences of experimental condition and tissue parameters to enable extraction of quantitative information on tissue chemical composition. That is, significant majority of the approaches suggested to date focus on qualitative assessment of PT-OCT signals with the overarching goal of determining the presence and location of MOIs. Forming predictions based on qualitative assessment of PT-OCT results would be misleading in many cases. For example, a sample containing a high concentration of MOI (i.e., good PT absorber) buried under a thick layer of non-absorbing tissue generates weak PT-OCT signals which is deemed as a non-MOI or low concentration of MOI region in qualitative signal/image processing approaches. Developing strategies for signal processing in light of a comprehensive opto-thermo-mechanical theory is expected to enable more accurate, and perhaps quantitative, PT-OCT imaging of biological tissues.

Third, due to the necessity of extended temporal sampling of responses, PT-OCT inherently suffers from low-imaging speed. This limitation hinders translation of this promising technology into clinics. Attempts made to date for enhancing the imaging speed of PT-OCT suffer from key limitations such as increased complexity and cost of the system, or degradation of SNR of received signals. A functional PT-OCT system for clinical usage must be fast enough to be able to capture images from moving samples (for example motion of cardiac tissues due to the heartbeat).

1.3.Motivations and specific aims

The motivations of this thesis are to generate in-depth knowledge on sample and system parameters affecting PT-OCT signals and to develop strategies for optimal detection and potentially quantification of MOIs. To enable translation of PT-OCT to clinics, development of methodologies for significant enhancement in imaging speed is also pursued. Specifically, the developed knowledge and technology stemming out of this thesis is expected to open the door for more accurate assessment of atherosclerotic plaques based on both tissue structure and chemical composition. Considering the above limitations/gaps and motivations, the objectives of the thesis are defined as follows:

Obj.1: Generating a comprehensive theoretical model for PT-OCT that relates system parameters, the sample geometry, and opto-thermo-mechanical sample properties to PT-OCT signals. Such a comprehensive model enables gaining deep understanding of variables affecting PT-OCT signals and their relation to chemical composition and structure of biological tissues.

Obj.2: Develop experimentation and signal processing strategies for extracting quantitative information about chemical composition of tissues from PT-OCT signals for application in cardiology. Developing such strategies will enable us to analyze multi-factorial PT-OCT signal that leads to detection of the molecule of interest in the tissues with higher specificity, and to quantify tissue properties.

Obj.3: Development of strategies for enhancing the imaging speed in PT-OCT for capturing image from both stationary and moving samples. Generating strategies in PT-OCT to enhance the imaging speed up to at least the kHz effective A-line rate range, that will pave the way for clinical application of PT-OCT. Additionally, with these strategies, we will be able to form PT-OCT images from a noisy and fast acquired signal that reduces the imaging time and volume of saved data.

1.4.Dissertation outline

This dissertation has been organized in 5 chapters in the following way:

Chapter 1 consists of an introduction, a literature review on technology and clinical applications of OCT, advantages and shortcomings of OCT and PT-OCT, the motivation for the dissertation and an overview of the objectives.

Chapter 2 describes two theoretical models for PT-OCT. In the first theory, PT-OCT signal as a function of opto-thermo-mechanical properties of samples is modeled. With this model, the behavior of PT-OCT signal as a result of changing material properties as a function of composition is studied. Next, a comprehensive theory of PT-OCT is generated which models the received PT-OCT signal from a multi-layer sample by considering effect of the opto-thermo-mechanical properties of surrounding media and PT-OCT system parameters. Using this model, a parametric study is done to survey the influence of sample and system parameters on PT-OCT signals. These works were published in the Journal of Biomedical Optics (JBO) and Biomedical Optics Express (BOE), respectively.

Chapter 3 presents methods and strategies for quantifying MOI concentrations in light of the outcomes of the theoretical works of chapter 2. In the first section, a strategy is proposed to increase detection specificity, and to enable distinguishing the PT-OCT responses of MOIs relevant to atherosclerotic plaques from each other (e.g., lipid, water, collagen). To do so, we presented a spectroscopic method in PT-OCT that employs two wavelengths for the PT laser. The response of samples then is decoupled for increasing

specificity of MOI detection. In the next section, another strategy is presented for quantifying MOI concentrations independent of system and sample parameters (e.g., distance to the focal plane of the objective lens, etc.). In this proposed strategy, machine learning models are trained to label PT-OCT images based on the concentration of MOI, in a general imaging condition.

Chapter 4 proposes two strategies for increasing the imaging speed of PT-OCT. The first method works based on response of the sample to a low energy squared PT laser pulse excitation, leading to introduction of a new variant of PT-OCT named transient (TM)-PT-OPCT. We show that proposed variant enables PT-OCT imaging of MOIs at video rate. This work was published in the journal of Optics letters (OL). Next, a method is presented to reconstruct PT-OCT images from noisy, but rapidly captured, datasets. In this strategy, a deep neural network structure is used to denoise signals and to predict the meaningful signal with high similarity to the ground truth. Also, this method will improve the detection limit in PT-OCT signals.

Chapter 5 consist of a conclusion for this dissertation, including a summary of the surveys presented in this dissertation, a discussion of directions and suggestions for future work, and a statement on the scientific contributions and societal impact of this work.

2: Development and Validation of PT-OCT model

2.1.Introduction

As discussed in Chapter 1, PT-OCT has been used in several studies to detect MOI in samples by assessing the received PT-OCT signal qualitatively. Yet, PT-OCT signals contain characteristic trends and attributes (e.g., amplitude, or overall shape) that directly correlate with the physical properties and the spatial distribution of the light-absorbing MOIs in tissue. Quantitative analysis of PT-OCT signals, therefore, offers potential for obtaining depth-resolved maps of tissue composition. Quantitative PT-OCT imaging of real tissue, however, is complicated by the fact that the PT-OCT signal is influenced not only by the concentration of MOIs but also the optical, thermal, and mechanical properties of tissue. Decoupling the effects of MOI light absorption from other influence parameters requires refined understanding of the complex physics underlying the PT-OCT signals. To date, several theoretical models for PT-OCT have been proposed.

In 2008, as the first theoretical model for PT-OCT, the variation of the OPL as a result of a change in the temperature field was modeled[68]. In this work, the solution of heat conduction equation (Eq. (1.5)) as a result of PT laser excitation was used to estimate the OPL in liquid samples. Since the focus of this study was on liquid samples, no mechanical strain/stress equations were generated. The results of the model showed a good consistency with the experimental PT-POCT signals from liquid phantoms inside a channel. This work could present the proof of concept of PT-OCT successfully. However, the missing point in this model was the ability to model multi-layer samples. Additionally, this model assumed samples as a 1-D space that neglects the effect of vicinity area on the PT-OCT signal.

In 2015, a more complex model in 3-D space for the PT-OCT signal in solid phantoms was proposed[77]. In this work, after calculating the illumination distribution and the thermal and the mechanical stress-strain fields, the OPL was calculated in a homogeneous sample. The Monte Carlo method and the Green's function method were employed in this model to estimate the light field and the temperature distribution in the sample, respectively. In this model, no analytical solution for the mechanical field was proposed. The advantage of an analytical solution for a physical system is that the significance and the behavior of each parameter in that system can be understood, clearly. This model served to improve the reconstruction of depth-resolved PT-OCT signal acquired from a single layer sample *in vivo*. The missing point in this study was that no parametric study was done on different inputs to indicate the relation between inputs of the model and the PT-OCT signal as the output.

A more refined model of PT-OCT in quasi-heterogenous multi-layered samples was presented in[78]. This model combined the individual components of the photo-thermal process to investigate the effects of PT laser power on measured PT-OCT signal. In this model, the light field was calculated in the sample with the Monte Carlo method in 3D. Also, to simplify the equations, the thermal field was modeled in 1-D space along the depth of the sample. Validation results proved that there was a great consistency between the model and the experimental PT-OCT signal received from multi-layer samples in some imaging conditions. A limitation of this model was that the mechanical expansion of the sample was modeled in a very specific condition in 1-D space (along the axial direction), neglecting key elastic mechanical properties of a sample such as Poisson ratio or the mechanical stiffness of the surrounding medium. Additionally, heat flux that occurs between the layers of the sample was not considered in this model. Therefore, without considering such important phenomena, this model could not provide enough accuracy to study the PT-OCT signal in general conditions.

More recently, an interesting work on interferometric imaging of thermal expansion for temperature control in retinal laser therapy was published[79]. While the focus of this work was on determination of the optical and thermal parameters of multi-layered tissue via fitting of experimental data to a proposed comprehensive theoretical model, it highlighted the feasibility and the need for similar comprehensive models in the field of PT-OCT.

Our group previously used a 1-D thermal-wave-based model to study the effects of PT laser modulation frequency on PT-OCT images[80]. To model the thermal field, Green's function method was used in frequency domain to solve the heat conduction equation. Through this model, it was shown that the amplitude of the PT-OCT signal is inversely proportional to the square root of the modulation frequency of the PT laser. Our team also investigated how an increase in modulation frequency of the PT laser improves the ability to detect two adjacent point-absorbers (aka. resolution). The key message of this work was that a compromise between the signal amplitude and spatial resolution should be considered to select the optimum modulation frequency. Higher modulation frequency, while reducing SNR, improves the spatial resolution in PT-OCT images.

Combined, existing PT-OCT models developed by our team[80] and others[68, 77, 78] offer key insights for better understanding of PT-OCT signal, yet take limiting assumptions that hinder their use for quantitative PT-OCT imaging of tissue. More rigorous theoretical models are needed to enable:

1) better understanding of the effects of system parameters and tissue opto-thermo-mechanical properties on experimental signals.

2) knowledge-based optimization of experimentation strategies.

3) guidance of reconstruction algorithms for depth-resolved prediction of tissue chemical composition information.

To address these limitations, in this chapter, we will present two models for PT-OCT from two different points of view.

In the first model, we take the first step in understanding the relation between composition and PT-OCT signals by considering the interplay between opto-thermo-physical properties of tissue as a function of its composition. We develop a theoretical model estimating the PT-OCT response in a two-component tissue-like sample. We then present experimental PT-OCT results of mayonnaise (mayo)-ultrasound gel mixtures at various component ratios. Mayo was chosen to mimic the lipid-rich necrotic-core material present in atheromatous coronary atherosclerotic lesions[81, 82]. Mayo, actually, is primarily composed of lipids, which provide an absorption signature that can be targeted with PT-OCT, and its lipid composition is similar to that of the atherosclerotic plaques[81, 82]. Since the composition and lipid content play a critical role in determining the propensity of a plaque to rupture[83], PT-OCT may offer the prospect to leverage the same contrast mechanism as those used by near infrared spectroscopy[84] and photoacoustic imaging[31, 32, 85] (i.e. absorption of lipid) for plaque composition imaging, albeit with much finer resolution.

In the second study, we propose a comprehensive model for prediction of PT-OCT signal in heterogenous multi-layer samples considering the opto-thermo-mechanical properties of all slices in 3-D. The proposed theoretical model has a serial hierarchy with 3 blocks for predicting the OCT and PT laser light fields, determining the induced thermal-wave field upon absorption of PT light by MOIs, and evaluating the subsequent thermo-mechanical expansion field due to the induced temperature change in the sample. For simplification, the model ignores possible coupling between the three blocks. The output of these blocks is then used to calculate the variation in the OPL resulting from the mechanical expansion and the temperature dependence of the refractive index and subsequently the variation of the OCT phase with time (aka, PT-OCT signal). As this model is generated on multi-layer and in 3-D space, it allows us to survey the effects of the thermal and mechanical properties of the layers, such as Poisson ratio and Young's modulus, on PT-OCT signals. Moreover, by considering the induced thermal field as a thermal-wave field, the model can reliably predict the effects of PT laser parameters (e.g., modulation frequency) on the PT-OCT signal. To gauge accuracy of the model, an experimental parametric study is carried out and discussed to realize the significance of the influence of PT laser power, modulation frequency, location of OCT focal plane, and thermal and mechanical boundary conditions on the PT-OCT signal.

2.2. Effects of Lipid Composition on Photo-thermal Optical Coherence Tomography Signals

2.2.1. The theoretical model

As we explained in Chapter 1, lipid is the main chemical of the atherosclerosis plaques. It was reported that the lipid content is different at various growing stages of atherosclerosis plaques[86, 87]. The motivation of this model is to quantify the lipid concentration in samples using the received PT-OCT signal. Figure 18(a) is schematic representation of processes that take place upon absorption of the PT laser in a PT-OCT system (e.g., absorption of 1210 nm laser by lipid-water mixture[31]). Absorption of intensity-modulated PT light results in production of heat, Q_{in}, which subsequently diffuses into the molecular matrix, forming a localized thermal wave field modeled by the bio-heat equation (Eq. (1.5)).

Previously, the generated thermal field in a sample as a results of laser excitation was solved using the bio-heat equation[88]. In this work, the boundary conditions were defined to insulate the boundary of the sample, thermally. The general solution of the bio-heat equation with the eigen function method was not in a closed form solution. However, under some reasonable assumptions, closed form solutions can be obtained for some specific conditions. For small PT spot sizes compared to the absorption depth (in our experiments: PT spot size =30 μm at 10 dB vs $1/\mu_a^{water}$ =1 cm), the amplitude of this temperature modulation, ΔT, at the center of the PT beam is expressed by Eq. (2.1)[88]:

$$\Delta T = \frac{I\mu_a}{\rho c}\left(\frac{W_f^2}{8\alpha}\right)\ln\left(1+\frac{t_L\alpha}{W_f^2/8}\right)\xrightarrow{I=2P/(\pi W_f^2)}\frac{P\mu_a}{4\alpha\pi\rho c}\ln\left(1+\frac{t_L\alpha}{W_f^2/8}\right). \quad (2.1)$$

Here P is the PT-laser power, μ_a is the medium's absorption coefficient at the PT-laser wavelength, α its thermal diffusivity, ρ its mass density, c its specific heat capacity, W_f is the waist of the PT laser beam, and t_L is the laser exposure time, taken as half of the PT laser modulation cycle, assuming a square modulation. The thermal diffusivity ($\alpha = \kappa/\rho c$; κ is the thermal conductivity) appeared in Eq. (2.1) is a material property that represents the rate of transfer of heat in the sample from the hot spot created by the PT light to the surrounding. A key assumption in derivation of Eq. (2.1) is neglecting the scattering of PT light in tissue. For the sake of our estimation in the field of PT-OCT, assumption of an absorption dominated light field is reasonable because here PT light is intentionally selected at a wavelength that is significantly absorbed by the molecule of interest. However, neglecting scattering of PT light can result in slight overestimation of the PT light field in the sample. By expanding the logarithm in Eq. (2.1) as a power series, ΔT can be expressed in form of product of variables:

$$\Delta T = \frac{P\mu_a}{4\alpha\pi\rho c}\left(\frac{t_L\alpha}{W_f^2/8} - \frac{\left(\frac{t_L\alpha}{W_f^2/8}\right)^2}{2} + \frac{\left(\frac{t_L\alpha}{W_f^2/8}\right)^3}{3} - \frac{\left(\frac{t_L\alpha}{W_f^2/8}\right)^4}{4} + \cdots\right) \xrightarrow{power\ series;deg<2} \Delta T \sim \frac{2Pt_L}{\pi W_f^2} \times \frac{\mu_a}{\rho c}. \quad (2.2)$$

The non-linear terms of the power series, however, can be neglected under certain conditions. A case in point is when the PT beam is large (i.e., large W_f), inducing planar thermal waves at the center of the beam. In such cases, the value of higher order non-linear terms become small; therefore, by neglecting the non-linear terms and using the definition of beam intensity ($I = 2P/(\pi W_f^2)$), the familiar expression for temperature change following continuous wave laser excitation can be reached: $\Delta T = I\mu_a t_L/\rho c$. In PT-OCT, while the PT beam size is larger than OCT beam size, it is normally not very large. However, in PT-OCT, the PT laser is modulated at high frequencies which in return make the t_L small. As such, similar to the previous case, the higher order non-linear terms can be neglected to reach a simple expression, Eq. (2.2), for estimating ΔT in PT-OCT. Eq. (2.2) suggests that for a given PT-OCT setting, only parameters c, ρ and μ_a are affected by sample's composition. Considering a linear variation of these parameters in a two-component mixture[89, 90], the value of a given parameter can be modeled as:

$$\zeta = (\zeta_2 - \zeta_1)\Psi + \frac{(\zeta_2+\zeta_1)}{2} = \zeta_{range}\Psi + \zeta_{mean}, \quad -0.5 \le \Psi \le 0.5 \qquad and \qquad \zeta_C = \frac{\zeta_{range}}{\zeta_{mean}}. \quad (2.3)$$

Here ζ is the concentration-dependent material parameter (e.g., ρ), Ψ is the relative concentration with respect to a 1:1 mixture, and ζ_1, ζ_2 are the values of the material parameters of pure individual components, respectively. ζ_C is the contrast of the material property in the two-component mixture which determines the sensitivity of the parameter to variation of concentration. Using Taylor expansion, ΔT can then be expressed in terms of concentration-dependent material parameters as:

$$\Delta T(\Psi) = \frac{2Pt_L}{\pi W_f^2} \times \frac{\mu_{mean}}{\rho_{mean}c_{mean}} \times (1 + [\mu_C - \rho_C - c_C]\Psi + M(\mu_C, \rho_C, c_C)\Psi^2 + \cdots). \quad (2.4)$$

Eq. (2.4) lies at the heart of proposed theory and suggests that the temperature variation resulting from PT-laser illumination depends on non-trivial interactions of multiple physical parameters. Only when PT-OCT imaging is carried out on aqueous samples containing relatively low amounts of exogenous agents or dissolved molecules will ΔT depend linearly on their concentration (e.g., works reported in[74, 75]). That is so because in these scenarios changes in concentration do not lead to considerable change in density and specific heat capacity (i.e., $\rho_C \cong c_C \cong 0$), making the coefficients of non-linear terms in Eq. (2.4) negligible. This linear prediction aligns well with the results reported to date on different concentrations of ICG-water mixtures[91] or those on blood oxygen saturation[74]. Variation of concentration in biological tissue compounds (e.g., lipid), on the other hand, results in considerable change in density and specific heat

capacity, leading to non-linear variation of ΔT with concentration[92]. The degree of this non-linearity is determined by the contrasts of the component's properties, ζ_C.

Once ΔT is induced, the volume and the local refractive index of the molecular matrix change (Fig.18(a)), and the optical path length difference ΔOPL as a function of relative concentration, Ψ, can be found as [80]:

$$\Delta OPL(\Psi) = \int_{L_0}^{L_1} n(T,\Psi)dl = n(T_0+\Delta T)L_1 - n(T_0)L_0 = \left(n(\Psi) + \frac{dn}{dT}(\Psi)\Delta T(\Psi)\right)\left(L_0 + L_0\beta(\Psi)\Delta T(\Psi)\right) -$$

$$n(\Psi)L_0 \rightarrow \quad \Delta OPL(\Psi) = L_0\left[\left(n(\Psi)\beta(\Psi) + \frac{dn}{dT}(\Psi)\right)\Delta T(\Psi) + \left(\frac{dn}{dT}(\Psi)\beta(\Psi)\right)\Delta T(\Psi)^2\right] \qquad (2.5) \qquad \rightarrow$$

$$\Delta OPL \propto \Delta T. \qquad (2.6)$$

Here, T_0 is the initial temperature of the sample, $^{dn}/_{dT}$ is the thermo-optic coefficient, and β is its linear thermal expansion coefficient. Considering the range of values of parameters of Eq. (2.5) in biological systems (see Table 1), the quadratic term of ΔT is negligible compared to the linear term. Therefore, the ΔOPL measured through the phase signal of OCT is directly proportional to variations in temperature, ΔT.

Table 1 Opto-thermo-physical properties of components used in the experiments and the simulations. These properties appear in the proposed solution of the bio-heat equation in Eq. (2.1).

Property (unit)	**Water**	**Mayo**
Absorption coefficient μ_a (m^{-1})	100 [31]	160 [31]
Density ρ (kg/m^3)	1000	910
Specific heat c $(J/Kg\ K)$	4184	2450 [93, 94]
Thermal diffusivity $\alpha (m^2/s)$	0.145×10^{-6}	0.110×10^{-6} [89]
Refractive index n	1.34 [80]	1.49 [95]
Thermo-optic coefficient $\frac{dn}{dT}$	-91×10^{-6} [80]	-531×10^{-6} [95]
Linear thermal expansion coefficient β (k^{-1})	100×10^{-6} [80]	1000×10^{-6} *[96]*

2.2.2. Simulation

To get a better understanding of the predictions of the developed model we simulated the PT-OCT responses of various ratios of mayo-water mixtures. The opto-thermo-physical properties used for pure mayo and water (i.e., ζ_1 and ζ_2) are depicted in Table 1. The simulation results of the normalized ΔOPL as a function of mayo concentration are plotted in figure 18(b). When considering a mixture in which the properties of the solvent are dominant ($\rho_C \cong c_C \cong 0$), the change in the concentration predominantly

induces a change in the absorption coefficient of the PT light. Under this condition, the non-linear terms of Eq. (2.4) become negligible, resulting in a linear relation between ΔT (and consequently ΔOPL; Eq. (2.6)) and mayo concentration as experimentally observed by other groups[74, 91]. However, when the sample is considered as a compound of mayo and water, the material properties are determined by the weight percentage of its components, Eq. (2.3). Since there is a pronounced difference between the opto-thermo-physical properties of mayo and water (Table 1), parameters ρ_c, c_c, μ_c in Eq. (2.4) are all considerable, leading to the non-linear variation of ΔT with mayo concentration seen in figure 19(b). Furthermore, the refractive index, its temperature dependence, and the expansion coefficient in Eq. (2.5) are also concentration-dependent (see Table 1) and contribute to the non-linearity of ΔOPL. Consequently, unlike the linear behaviors reported to date on samples with exogenous agents or dissolved molecules in aqueous media[74, 75], the general variation of ΔOPL with the concentration of one tissue component is non-linear. Another notable point in figure 18(b) is the small ΔOPL predicted for water (i.e., %Mayo=0) despite water's moderate absorption at 1210 nm[31]. The reason behind the small ΔOPL for water is the large heat capacity of water acting against the rise of the temperature as well as the cancellation of contributions of thermal expansion, $n(\Psi)\beta(\Psi)$, and thermo-optic coefficient, $\frac{dn}{dT}(\Psi)$, to OPL-changes. The small ΔOPL of water is specifically important for PT-OCT of biological tissues that generally have high water content because it helps with the detection of PT-OCT signatures of waterless tissue components above the small PT-OCT signal baseline from water. Therefore, in PT-OCT, the large absorption coefficient of a component does not necessarily lead to a strong PT-OCT signal and, in fact, the optimization of PT-OCT experiments needs to take place by considering the interplay between the opto-thermo-physical properties of tissue.

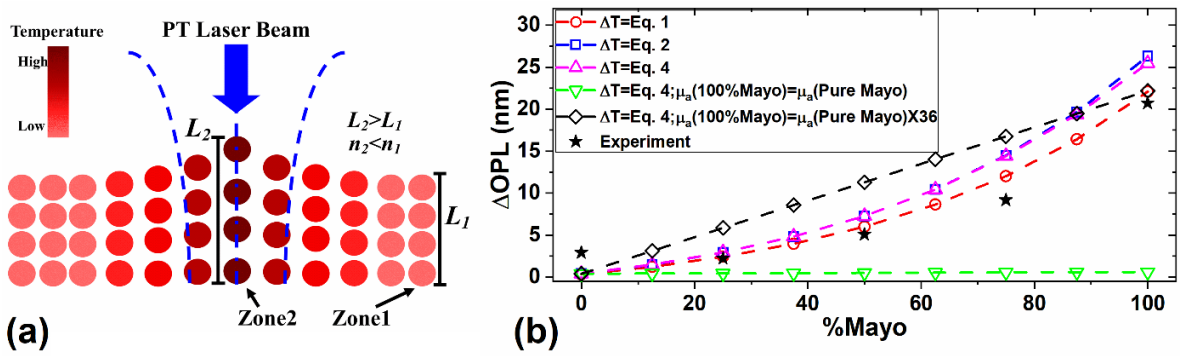

Figure 18. (a) Schematic presentation of sequence of physical processes taking place in PT-OCT upon absorption of PT light. The raised temperature in the sample leads to change in OPL near the MOI. (b) Numerical and experimental results for ΔOPL as a function of concentration of mayonnaise in the sample. The non-linear behavior in the experimental dataset is followed with the presented model.

2.2.3. Experimental Validations

2.2.3.i) experimental setup

(**Note:** *In this section, we explain the PT-OCT setup that we designed and assembled in our lab. In the following sections and chapters, to prevent repetition, we simply refer to this section.*)

To experimentally verify our theoretical predictions, we developed a spectral-domain PT-OCT system, employing broadband light of a superluminescent diode centered at 1310 nm (+/- 75 nm at 10 dB; Exalos, Switzerland), a 2048-pixel line scan camera spectrometer with a maximum acquisition rate of ~147 kHz (Wasatch Photonics; USA), and an intensity-modulated single-mode photo-thermal laser. In our setup we installed 3 PT lasers illuminating at 806 (30 mW- Thorlabs; USA), 1040 (500 mW- Innolume; Germany), and 1210 nm (500 mW- Innolume; Germany). The schematic of our setup is plotted in figure 19.a. The output OCT light is directed to the beam splitter by an optical circulator. The PT laser is also connected to the other input head of the beam splitter. These two lights are merged and split into two beams (i.e., the reference and the sample arms) after passing through the beam splitter. In the sample arm, the output light in the fiber is directed to a reflective collimator (Thorlabs; USA). The collimated beam in the sample arm (see Fig.19(b)) is focused on the sample surface by the objective lens (LSM02, Thorlabs; USA). The 2-DOF Galvo mirror is also used to raster scan the sample surface with the laser beams. In the reference arm, the light illuminates a gold-coated reference mirror after exiting from the collimator. To compensate the dispersion as a result of passing the light from the objective lens in the sample arm, the dispersion compensation block is installed in the reference arm. By changing the polarization of the light in the reference arm with the polarization controller unit (Thorlabs; USA), the polarization of the reference beam is matched with the polarization of the sample beam. The reflected light of these two arms is merged again in the beam splitter and is redirected to the spectrometer by the optical circulator. In the spectrometer, the spectrum of the received signal is digitized and sent to the PC for processing. The two views of the assembled system at the HBO lab, York University are shown in figure 19(c),(d).

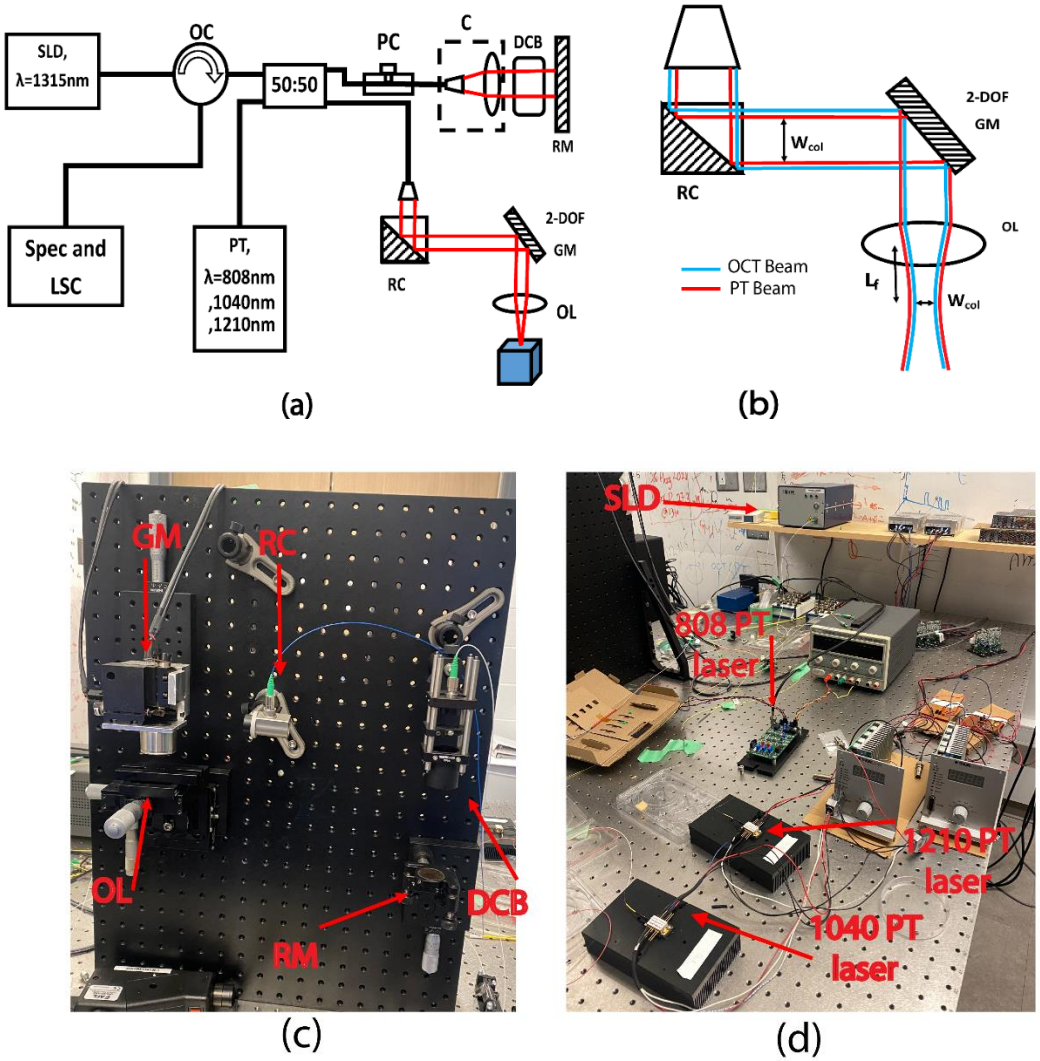

Figure 19. Schematic and assembled views of the designed and developed PT-OCT setup in this thesis. (a) Schematic of the PT-OCT setup including: superluminescent diode (SLD), optical circulator (OC), spectrometer (spec) and 2048-pixel line scan camera (LSC), photo-thermal laser (PT), 50:50 fiber coupler, polarization controller (PC), collimator(C), dispersion compensation block (DCB), reference mirror (RM), reflective collimator (RC), 2 degree of freedom galvo mirrors (GM), and objective lens (OL); (b) Detailed view of the sample arm. (c), (d) Two views of the assembled PT-OCT system.

The flowchart of signal processing for PT-OCT signals is plotted in figure 20. To form the tomogram of the sample, in light of Eq. (1.1) and Eq. (1.2), we need to capture the OCT signal in k-space (wavenumber space, $2 \times \pi/\lambda$), then convert it to the z-space (physical length). To do so, after loading the received signal on the PC, the captured background is subtracted from it. The background subtraction removes the intensity of the reference beam (term I_R in Eq. (1.1)). In the spectrometer, sampling in the wavelength was indeed in a constant interval. Once the wavelength converted to the wavenumber, the sampling interval was no longer constant. Using linear interpolation, the signal is resampled linearly in k-space. This resampling with linear interval allows us to use Fast Fourier Transformation (FFT). By applying inverse FFT (iFFT) on the signal

in k-space, the signal converts to z-space (Eq. (1.2)). The amplitude of complex numbers producing by iFFT forms the OCT amplitude image. The phase of complex numbers for each pixel over time (M-scan) is the basis for forming PT-OCT images. Due to the DC term in the thermal field, there is drift line in the variation of phase over time. To remove the signal drift, a difference in temporal direction is applied on the signal. Removing the signal drift gives us the phase modulating that is generated due to the modulation of PT laser power on the sample. By applying FFT on the phase modulation, and calculating the amplitude of results, the spectrum of the phase is obtained. Eventually, by carrying out lock-in demodulation at the modulation frequency of the PT laser, and using Eq. (2.7)[78], the pixel amplitude in PT-OCT image is calculated using following equation:

$$Amp(Z) = \frac{|p(z,f_0)|\lambda_0}{4\pi^2 f_0 \Delta t}. \quad (2.7)$$

Here $|p|$ is the normalized FFT amplitude of the difference of the phase signal at the PT laser modulation frequency of f_0, λ_0 is the center wavelength of the OCT laser, and Δt is the acquisition time for one A-line.

Considering the absorption band of the MOI, one of the PT lasers is powered on. The axial and lateral resolutions of OCT in air were measured as 10 µm and 11.5 µm, respectively. The OCT and PT beams are concentric and co-scanned, and their FWHM spot sizes are 7 µm and 8.5 µm (30 µm at 10 dB attenuation), respectively. Using a common-path reference, a displacement error of 3 nm at a SNR of 35 dB was measured, which is close to that of a shot-noise-limited system[97]. The methods and results of characterization of the setup are presented in Appendix A.

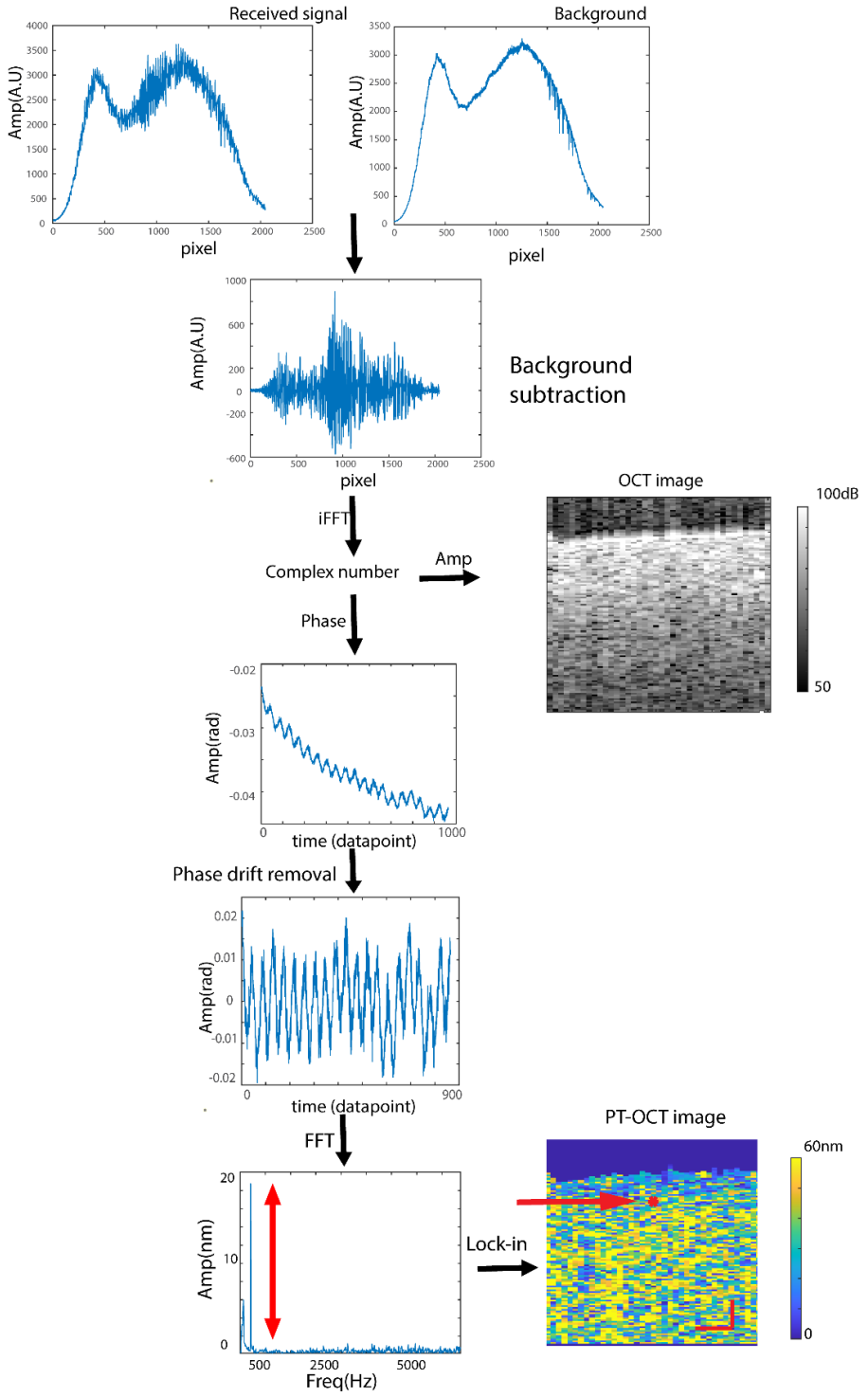

Figure 20. The flowchart of data processing to form OCT and PT-OCT images from the raw data, see text for detailed explanation of signal processing steps, scare bar=60 μm.

2.2.3.ii) The phantoms

To prepare various dilutions of the lipid-water compound, droplets of mayo and ultrasound gel with appropriate weight ratios were dispensed in a petri dish and stirred well to make homogenous samples at five different weight concentrations of mayo (100, 75, 50, 25, 0). The scattering of the 0% mayo sample was adjusted to those of other mayo concentrations using titanium dioxide powder. In addition, to examine the efficacy of the system in detecting lipid in tissue, lipid-rich atherosclerotic plaque was mimicked by injecting 95% mayo compound into fresh normal bovine cardiac muscle. A similar sample was also prepared using 40% mayo compound to examine PT-OCT system's sensitivity to lipid concentration in tissues. The thickness of the cap above the lipid-pool for the 40% and 95% mayo simulated plaques varied between 110 µm to 360 µm and 140 µm to 280 µm, respectively. These simulated cap dimensions are comparable to those encountered in vulnerable coronary plaques[98].

2.2.3.iii) Imaging protocol

In the study, as we chose lipid as MOI, and since lipid has a peak at 1210 nm in absorption band[31], the 1210 nm PT laser with a power on sample 18 mW was connected to the setup. PT-OCT experiments were carried at an A-line rate of 21.6 kHz for OCT spectrometer. Each M-scan consisted of 5000 data points acquired in ~230 ms. The PT signal is sinusoidal and modulated at 500 Hz.

2.2.4. Results and discussion

Figure 21 depicts results obtained from samples at various mayo concentrations. Conventional OCT images of panels a-e cannot discern between different concentration of mayo/lipid. The root cause of this limitation is the fact that conventional OCT forms images based on elastic scattering of light which originates from discontinuities in the materials' refractive index rather than based on the presence of a characteristic molecular marker of the disease. Hence, tissues with very different composition may have very similar OCT structural signatures. A case in point is the identification of the thin cap fibroatheromas (TCFA), characterized by the presence of a necrotic core and extracellular lipid, and their differentiation from less vulnerable pathological intimal thickenings[99]. Both plaque types bear similar structural features when imaged with intravascular OCT, complicating the identification of plaques at increased risk of causing future adverse events. The PT-OCT images of panels f-j, on the other hand, clearly show the strong direct correlation of PT-OCT signal strength with concentration of mayo/lipid. The PT-OCT images of figure 21, qualitatively, suggest a non-linear variation of PT-OCT signal with concentration. The normalized average PT-OCT signals of each mayo concentration is plotted in figure 19(b) together with the simulated results. For the dilution experiments, the average of the pixels in the PT-OCT B-mode images were normalized to that of the 100% mayo sample, as seen in figure 19(b). The non-linear variation of PT-OCT signal with %mayo is evident in this plot, as predicted by the theoretical model. Another key observation is the

significant underestimation of the PT-OCT signal for 100% mayo when only considering the absorption coefficient (μ_a) to be concentration-dependent in the model. In such a single-variable model, a 36-times higher absorption coefficient is needed for mayo to achieve a PT-OCT signal comparable to the experimental value. The reason behind this discrepancy is that in practice both ρ_C and c_C play an intensifying role based on Eq. (2.4) in producing a larger ΔT compared to the case where concentration dependence of ρ_C and c_C are neglected. Also note that while the non-linear trend of variation of normalized ΔOPL with %mayo is reasonably close to the predicted theoretical values in the 25%-100% range, the experimental PT-OCT signal deviates from the predicted theoretical trend at 0% (i.e., water) because the measured PT-OCT signal is dominated, in this case, by the noise floor in the OCT phase channel.

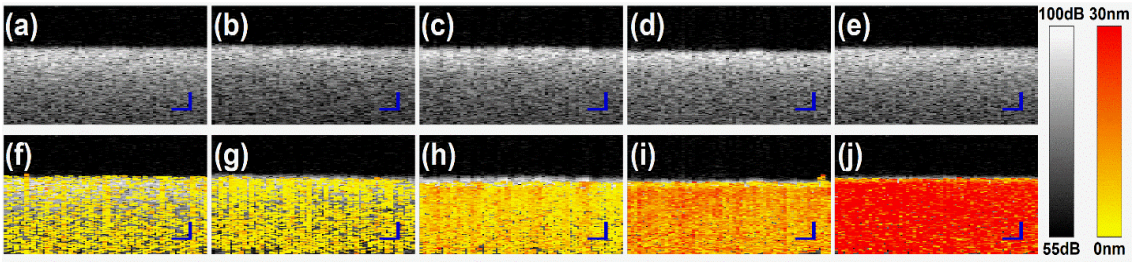

Figure 21. A comparison between OCT and PT-OCT in ability to offer insight into MOI concentration. OCT images of samples with mayonnaise concentration (a) 0% (b)25% (c)50% (d) 75% (e)100%, PT-OCT images of samples with mayonnaise concentration (f) 0% (g)25% (h)50% (i) 75% and (j)100%. While the OCT images are not sensitive to the variation of MOI in the samples, the intensity of pixels in PT-OCT images is a function of concentration of MOI in the sample, scale bars= 50 µm.

Imaging results of the artificial lipid-rich plaques are shown in figure 22. In conventional OCT images, the boundary of the 40% mayo sample can clearly be identified in the OCT image of panel (a) while the boundary of the 95% mayo, panel (b), is diffuse similar to those seen in OCT imaging of the lipid pool in human atherosclerotic plaques[100]. In either case, information about the composition of the tissue cannot be obtained from the conventional OCT images. The PT-OCT image of panel (d) is from the sample with 95% mayo injection (i.e., similar lipid content as atherosclerotic plaques[81, 82]). The lipid-rich pool is clearly identified in this image. The PT-OCT image of panel (c) is from the 40% mayo injection. Here the subsurface diluted lipid pool cannot be reliably recognized as the PT-OCT signals are within the range of noise floor. While the lipid content here is 42% of that of the sample in panel (d), the resulting PT-OCT signal is only about 20% of that of the sample in panel (d). This non-linear variation of PT-OCT signal with concentration is in complete alignment with the theoretical predictions of our model. Results of figure 22 indicate that PT-OCT has potential for offering key insight into the presence of subsurface lipid-rich material in tissue; however, the interpretation of results needs to be carried out with care and by keeping the non-linear interplay between opto-thermo-physical properties and PT-OCT signals in mind.

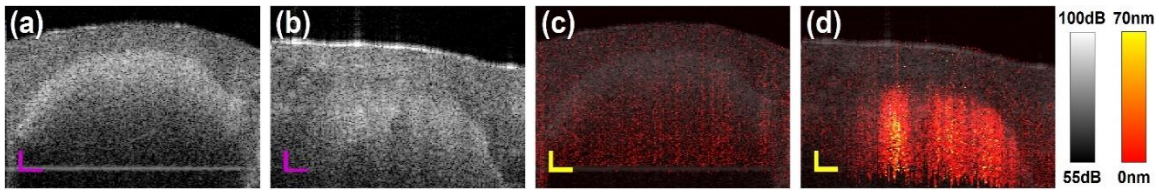

Figure 22. The images of the artificial lipid plaque sample with OCT and PT-OCT. Results of OCT image of the plaque phantom with mayonnaise concentration (a) 40% (b) 95%, PT-OCT image of the plaque phantom with mayonnaise concentration (c) 40% (d) 95%. PT-OCT results has a correlation with percentage of MOI in the sample, scale bar=100 µm.

2.2.5. Summary

In summary, this section provides a theoretical model and a preliminary experimental study demonstrating the feasibility of obtaining quantitative insight into the chemical composition of biological tissues using PT-OCT. The developed model and experimental results suggest that the relation between PT-OCT signals and the concentration of an absorbing component in the tissue is non-linear, and that the degree of this non-linearity is determined by the contrasts of component's opto-thermo-physical properties, ζ_C. Another key conclusion of this work is that in PT-OCT a large absorption coefficient of a component does not necessarily lead to a strong PT-OCT signal. Instead, the strength of the PT-OCT signal is highly dependent on the interplay between the opto-thermo-physical properties of the tissue, all of which are concentration-dependent. Our experimental results suggest the possibility of obtaining insight into the lipid content of tissue-like samples and may offer a pathway towards refined assessment of atherosclerotic plaques in the future. In this potential application, decreasing the noise floor in a catheter-based PT-OCT system for in-vivo imaging leads to improvements in the accuracy of detecting lipid in atherosclerotic plaques. This can be done either by tuning parameters in PT-OCT imaging or designing the hardware so that it is more stable and suppresses phase variation. It should be noted that executing a complicated phase stable system in a such small volume of catheter has technical challenges. In this section, we have shown PT-OCT signals contain information from which MOI concentration can be predicted. The next logical step is to explore what other sample and system parameters influence PT-OCT signals (i.e., the motivation behind development of next theoretical work).

2.3. A 3D Opto-Thermo-Mechanical Model for Predicting Photo-Thermal Optical Coherence Tomography Responses in Multilayer Geometries

2.3.1. Theory

As we told in the beginning of this chapter, a few models for PT-OCT have been presented so far. In these models, the mechanical strain/stress field, as well as the effect of vicinity area related to the beam axis such as heat flux on the PT-OCT signal neglected. The motivation of the work in this section is

generating a new model for PT-OCT that covers this limitation by considering the effect of vicinity area and the mechanical response of the sample on PT-OCT signal. Based on the sequence of physical phenomena explained in Chapter 2, Section 2.2, we propose a model to simulate the PT-OCT signal in samples in 3-D space using cylindrical coordinates. A layer refers to a homogeneous area of the sample with uniform opto-thermo-mechanical properties, such as a glass layer, or Polydimethylsiloxane (PDMS) layer. Then, we mesh each layer into a series of homogeneous slices with their own constant material properties, stacked on top of each other. For simplicity, we refer to these meshes as slices. With this approach, we can model both single and multi-layer samples. Boundary conditions impose continuity of fields at slice interfaces. The flowchart of the proposed model is depicted in figure 23(a). The model is comprised of three computing blocks in series: light field, thermal field, and stress/strain field. Each block is fed by the results of the previous block(s), system parameters, and material properties.

Coupling between the blocks, while physically possible, is considered negligible and ignored. In this model, we assume that the sample is located between two fixed supports (Fig.23(b)). Depending on the specific sample geometry, the top support may be a constrained sample surface, a constrained glass slide on top of the sample surface, or an imaginary plane above sample surface in air. The fixed bottom support is at the bottom of sample, at a depth well beyond achievable imaging depths. Samples can be mono-layer or multi-layer. Then the volume between the fixed supports, in cylindrical coordinates, is sliced, resulting in a stack of disks. Subsequently, the disks (slices) are assigned with opto-thermo-mechanical properties of the corresponding sample layers. This meshing approach ensures that the sample surface falls within the space between the two fixed supports which, in return, allows us to use the same boundary condition when solving for the stress/strain field regardless of number of layers in the sample and boundary condition on the sample surface.

In the first block, based on the optical properties of the sample and system parameters (e.g., PT laser power and modulation frequency), the PT laser light field in the sample is estimated in 3D. The temperature field in the sample is then determined in 3D considering the thermal properties and the light intensity distribution in the sample. The output of this part is the variation of temperature at every point in the sample over time. In the last block, the mechanical stress/strain field in the sample in response to the temperature change and as a function of the material's mechanical properties are obtained. Eventually, the OPL variation and PT-OCT signal are calculated from the mechanical displacements and the temperature changes. The sections below depict the mathematical modeling of the three serial blocks. In this model, our approach to solve equations in the mechanical strain block was elasto-static and ignored dynamic states and interaction between the associated dynamic effects.

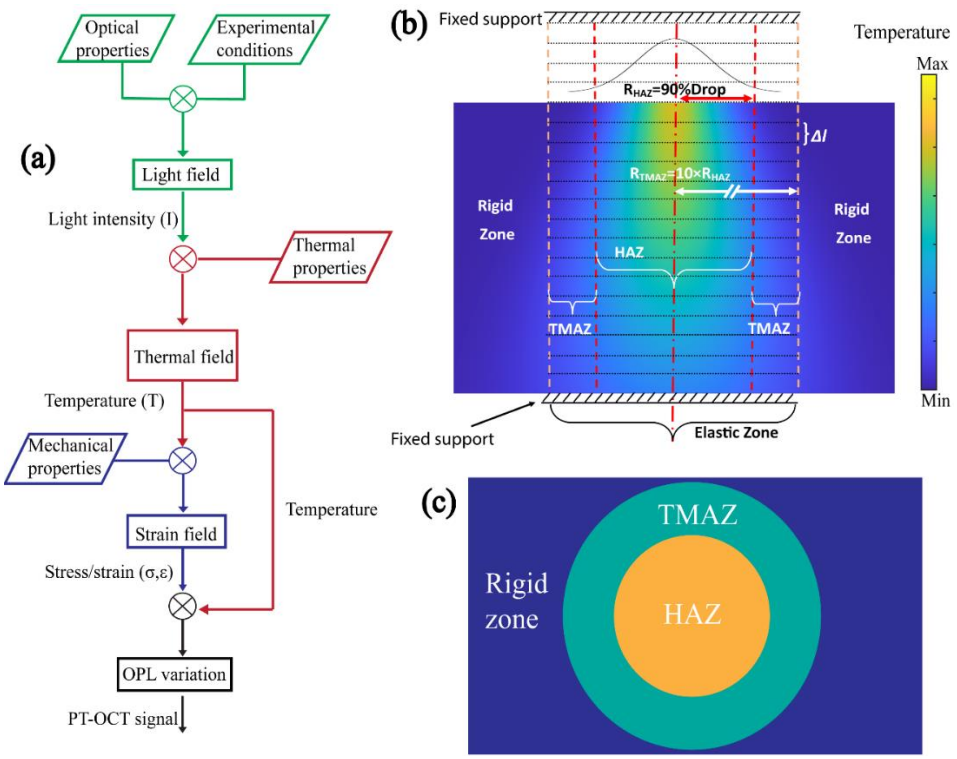

Figure 23. (a) The flowchart of the proposed model. This model mainly consists of three main blocks, including: light, thermal and the strain field. The material properties and experimental conditions and the output of previous blocks are the input for the next block. (b) schematic definition of heat affected zone (HAZ), thermo-mechanically affected zone (TMAZ), and the rigid zone in the sample as a function of thermal field in the sample. In this model the sample is sliced with a pile of disks along the depth; look at the definition of regions in the sample as a function of the generated heat in the sample. (c) a top view of a slice and the location of elastic (HAZ+TMAZ) and rigid zones in it.

2.3.1.i) The light field

Assuming Gaussian beam propagation and absence of scattering, the intensity I of light in the sample can be expressed as[101]:

$$I(\xi,t) = \frac{2P_{inc}(t)e^{-\mu_a z}}{\pi W^2(z)} exp\left[-\frac{2\xi^2}{W^2(z)}\right]. \qquad (2.8)$$

Here, $P_{inc}(t)$ is the incident power of the PT laser on the top surface, μ_a is the absorption coefficient, ξ is the radial to the center of the beam at a specific depth z, t is time, and W is the radius of the waist of the beam at each depth which can be estimated as[101]:

$$W(z) = W_f\sqrt{1+(\frac{z_f}{L_{ray}})^2}. \qquad (2.9)$$

Here, Z_f is the axial distance between a selected depth and the focal plane, L_{ray} is the Rayleigh range, and W_f is the beam waist at the focal plane which is calculated as:

$$W_f = \frac{\lambda_{in}}{\pi} \times \frac{L_f}{W_{col}}. \quad (2.10)$$

Here λ_{in} stands for the wavelength of the incident beam, L_f is the focal length of the objective lens, and W_{col} is the waist of the collimated beam incident on the objective lens. Projecting the beam on a sample with refractive index n, the Rayleigh range L_{ray} can be calculated as:

$$L_{ray} = \frac{n \times \pi}{\lambda_{in}} \times (W_f)^2. \quad (2.11)$$

Combined, this block estimates the intensity of the PT beam in the sample. We should reiterate here that the above derivations are ignoring light scattering and assume that light attenuation within the effective imaging depth of PT-OCT is dominated by absorption of light. The rationale for this simplifying assumption is that in practice the imaging depth of PT-OCT is limited to at most the imaging depth of OCT, which is on the order of few scattering mean free paths. Within this imaging range contributions of scattering to the light field are expected to be significantly less than when approaching the transport mean free path or the diffuse regime. At these imaging depths, there would not be any OCT signal left. Moreover, in PT-OCT, the PT laser wavelength is intentionally selected at a wavelength at which the PT laser is very efficiently absorbed. These considerations motivated us to assume an absorption-dominated light field for our approximation. It should also be noted that the PT-OCT depends on the modulated (AC) portion of the thermal field and not the bulk temperature rise. This point is important because the AC portion of the temperature field is attenuated exponentially in spatial directions. That is, absorption of scattered light that is more than a thermal diffusion length (e.g., 4.3μm at 2.5 k Hz PT laser modulation) away from the OCT beam axis is not expected to contribute significantly to the measured PT-OCT signal. Light scattering can, however, create an offset error in the proposed model. A potential remedy to this limitation of our model is to convolve model predictions with an empirical spread function to account for scattering of light (as shown in Ref[79]).

2.3.1.ii) The thermal field

Absorption of photons' energy by molecules generates heat in the sample. The partial differential equation governing the thermal diffusion field in time-domain is[102]:

$$\nabla^2 T(\mathbf{\Phi}, t) - \frac{1}{\alpha}\frac{\partial}{\partial t} T(\mathbf{\Phi}, t) = -\frac{1}{\kappa} Q(\mathbf{\Phi}, t) = -\frac{\mu_\alpha}{\kappa} I(\mathbf{\Phi}, t). \quad (2.12)$$

Where T is the temperature, $\boldsymbol{\Phi}[\xi,z]$ is vectorial distance to the center of the beam α is thermal diffusivity of the medium, κ is the thermal conductivity of the medium. Since the heat source Q originates from an intensity-modulated PT-laser excitation, it is more convenient to solve the heat equation in the frequency domain[103]. After applying FT on Eq. (2.12) with respect to time, the heat equation is converted from time domain to the frequency domain as[102]:

$$\nabla^2\tilde{\theta}(\mathbf{\Phi},\omega) - \tilde{\sigma}^2(\omega)\tilde{\theta}(\mathbf{\Phi},\omega) = -\frac{1}{\kappa}\tilde{Q}(\mathbf{\Phi},\omega) = -\frac{\mu_\alpha}{\kappa}\tilde{I}(\mathbf{\Phi},\omega). \quad (2.13)$$

Here $\tilde{\theta}$ is the temperature in the temporal frequency domain, $\tilde{Q}$ is the heat source distribution in the frequency domain, $\tilde{I}$ is the intensity in the frequency domain and $\tilde{\sigma}$ is the complex wave number which is defined as[102, 103]:

$$\tilde{\sigma} = \sqrt{\frac{i\omega}{\alpha}} = \frac{1}{\mu}(1+i). \quad (2.14)$$

Here, $\mu = \sqrt{\frac{2\alpha}{\omega}}$ is the thermal diffusion length. Using the Green's function method to solve the heat equation (Eq. (2.12)), the temperature field for a semi-infinite volume in frequency domain can be obtained as[102]:

$$2\tilde{\theta}(\mathbf{\Phi},\omega) = \frac{\alpha}{\kappa}\iiint_{V_0}\tilde{Q}\tilde{G}_0 dV_0 + \alpha \oiint_{S_0}[\tilde{G}_0\nabla_0\tilde{\theta} + \tilde{\theta}\nabla_0\tilde{G}_0]dS_0. \quad (2.15)$$

In the above equation, $\tilde{G}_0$ is the three-dimensional Green's function. In PT-OCT, the penetration depth of the PT light is usually shorter than the thickness of the sample, so a homogeneous sample can be considered as a semi-infinite medium. For a semi-infinite medium and homogenous thermal properties slice, the Green's function is[102, 104]:

$$\tilde{G}_0 = \frac{1}{\pi\alpha}\left(\frac{e^{-\tilde{\sigma}(\omega)|\mathbf{\Phi}-\mathbf{\Phi}_0|}}{|\mathbf{\Phi}-\mathbf{\Phi}_0|} + \frac{e^{-\tilde{\sigma}(\omega)|\mathbf{\Phi}-\mathbf{\Phi}_0'|}}{|\mathbf{\Phi}-\mathbf{\Phi}_0'|}\right). \quad (2.16)$$

Where $\boldsymbol{\Phi_0}(r_0, \theta_0, z_0)$ is the location of the heat point source, and $\mathbf{\Phi}_0'(r_0, \theta_0, -z_0)$ is its mirror-point corresponding to reflection at the top surface. The result of the temperature field in frequency domain can be converted to time domain using inverse Fourier transformation as follows[103]:

$$T(\mathbf{\Phi},t) = \int_{-\infty}^{\infty}\tilde{\theta}(\mathbf{\Phi},\omega)e^{-i\omega t}dt. \quad (2.17)$$

In multi-layer geometries, the heat exchange between layers with different thermal properties (different materials) is considered by taking the thermal effusivity at the boundary of two adjacent layers into account. The thermal effusivity ($e = \sqrt{\kappa\rho c}$) is a thermal material property that measures the ability of a material to exchange heat with its surroundings (i.e., other layers with different materials) as heat flux. However, to calculate the thermal waves inside a layer consisting of a single material, in light of Eq. (2.12), the thermal diffusivity ($\alpha = \kappa/\rho c$) of the layer is normally used. As an example, in modeling of an atherosclerosis plaque sample, the thermal field inside the lipid pool is estimated using the thermal diffusivity of lipid. However, the effect of the heat sink that occurs because of the heat flux between the blood flow on the top of the plaque and the plaque, can be estimated by considering the thermal effusivity mismatch of the plaque and the blood.

The heat flux effect can be applied in the model by superposing the temperature field in absence of any heat flux with the temperature distribution in presence of a heat flux. Assuming perfect thermal contact, the temperature at the contact surface of two layers (e.g. layer1 and layer2) T_m is estimated as[105]:

$$T_m = \frac{e_1 T_1 + e_2 T_2}{e_1 + e_2}. \qquad (2.18)$$

Here *e* stands for thermal effusivity. The generated thermal flux *q* in terms of the distance related to the top surface $|z_r - z_0|$ can then be calculated as:

$$q = \kappa \frac{\Delta T}{\Delta z} = \kappa \frac{T_m - T(\boldsymbol{\Phi},t)}{|z_r - z_0|}. \qquad (2.19)$$

Once the thermal flux at boundaries is calculated via Eq. (2.19), the updated temperature will be calculated with Eq. (2.15)[102]. The accuracy of this superposition method was tested with a precise numerical solution obtained with finite difference method (FDM), in Appendix B. The ultimate output of the subtraction of the thermal field from the heat flux is the 3D temperature field of the multilayer geometry, $T(\boldsymbol{\Phi},t)$.

2.3.1.iii) The mechanical stress/strain field

To estimate the thermo-elastic expansion of the sample as a consequence of the temperature change, the sample is radially divided into three zones (Fig.23(b)). The cylindrical zone concentric with the PT beam where most of temperature rise takes place is named the heat affected zone (HAZ). The zone outside of HAZ that is not significantly affected by the temperature change, but still mechanically contributes to thermo-elastic expansion as an impedance is named thermo-mechanically affected zone (TMAZ). These two elastic zones are surrounded by a rigid zone in which temperature rise and thermo-elastic expansions are considered negligible. Figure 23(c) shows the location of these three zones in a top view of a slice. To find the radii of HAZ and TMAZ, first we find the maximum temperature amplitude inside the sample. A 10 dB radial drop in the temperature amplitude at that depth defines the HAZ radius for all depths (Fig.23(b)). The radius of TMAZ is defined as 10 times that of HAZ (thick-walled cylinder condition). Note that series of simulations were done to justify this selected ratio between HAZ and TMAZ, available in Appendix C. Outside TMAZ is the rigid zone where no material is displaced. Using constitutive thermoelastic equations in the cylindrical coordinate system and assuming an axially-symmetric problem[106, 107], the radial and axial displacements (*u,w)* under assumption of these boundary conditions (B.Cs) are (see Appendix C for more information):

$$\frac{\partial \sigma_r}{\partial r} + \frac{1}{r}(\sigma_r - \sigma_\theta) = 0, \qquad (2.20)$$

$$\text{B. C. 1: } \sigma_r^{HAZ}|_{r=r_{HAZ}} = \sigma_r^{TMAZ}|_{r=r_{HAZ}},$$
$$\text{B. C. 2: } u^{HAZ}|_{r_{HAZ}} = u^{TMAZ}|_{r_{TMAZ}},$$
$$\text{B. C. 3: } u^{TMAZ}|_{r_{TMAZ}} = 0,$$

$$\text{B. C. 4: } [\sigma_z^{HAZ}]_1 = [\sigma_z^{HAZ}]_2 = [\sigma_z^{HAZ}]_3 = \ldots,$$
$$\text{B. C. 5: } [\sigma_z^{TMAZ}]_1 = [\sigma_z^{TMAZ}]_2 = [\sigma_z^{TMAZ}]_3 = \ldots,$$
$$\text{B. C. 6: } \sum_i [\varepsilon_z^{HAZ}]_i = 0, B.C.7 \Rightarrow \sum_i [\varepsilon_z^{TMAZ}]_i = 0.$$

The goal of above system of equation is to estimate the displacement field by meshing the sample along the depth into a stack of disks with the same radius. That is, in above equations nonuniformity in distribution of axial stress (σ_z) due to thermal gradient along the depth is ignored (B.C.4 and B.C.5). This simplifying assumption enables the model to focus on calculation of normal stresses and strains as main contributors to changes to the axial physical length of each slice (i.e., needed for estimation of OPL). In addition, the total strain along the depth is considered to be zero (B.C.6.), assuming that the distance between the top and bottom sample supports is fixed (i.e., to satisfy continuity in axial direction). The steps to solve these equations are explained in more detail in the Appendix C.

2.3.1.iv) PT-OCT signal

PT-OCT works based on measurement of the change in OPL as a function of depth and at the center of HAZ via the time-lapse (M-mode) OCT phase. OPL is defined as the product of the refractive index and the physical length of each HAZ slice, *L*:

$$\Delta OPL = n_2 L_2 - n_1 L_1. \qquad (2.21)$$

The new length of all slices L_2, is calculated from Eq. (2.20). Changing the temperature not only alters the length of HAZ, but also affects its refractive index:

$$n_2 = n_1 + \left(\frac{dn}{dT}\Delta T\right). \qquad (2.22)$$

Where, $\frac{dn}{dT}$ is the opto-thermo coefficient of the sample. Finally, the change in the OCT phase $\Delta\Phi$ can be obtained by:

$$\Delta\phi = \frac{4\pi n \Delta OPL}{\lambda_0}. \qquad (2.23)$$

Here λ_0 is the center wavelength of the OCT laser. The detected signal by PT-OCT system is the cumulative effect of phase variation at each slice.

2.3.2. Experimental methodology

2.3.2.i) The PT-OCT setup

The setup is explained in detail in Section 2.3.i and figure 19. We should add that the 806 nm PT laser was used with a 5 mW power on the sample.

2.3.2.ii) The Phantoms

For evaluating the accuracy of the model, two kinds of phantoms were prepared. The first kind used PDMS (SYLGARD184, DOW, USA) as the matrix material. The two parts of PDMS (base and curing agent) were mixed in a ratio of 1:10 by weight. To enhance light scattering, 25 mg titanium dioxide (TiO_2, Sigma Aldrich, USA) was added to 1 ml of curing agent before combination with the base; the particle-curing agent mixture was then shaken in the ultrasound bath for 10 minutes to make a homogenous liquid. A dye (IR-806, Sigma Aldrich, USA) which is soluble in methanol was selected as the absorber of the PT laser light at 808 nm. Using a UV-VIS spectrometer (Shimadzu, Japan), the absorption coefficient of a solution of the dye with a concentration of 19.58 mg/ml was measured (Table.2). The dissolved dye in methanol then was added to the PDMS mixture and was stirred well. After pouring a mold with the PDMS sample and degasification for 15 minutes, the mixture was put on the hot plate at 70 °C for 10 h to cure. Finally, the cured sample was ejected from the mold. Four phantoms with 0.22, 0.43, 1.3, and 2.2 mg/ml absorber concentrations were made. The second kind of phantoms used plastisol as the matrix material. In an aluminum dish, 10 ml of liquid plastisol was heated up on a hot plate to 110 °C. Then the dye solution and 25 mg of the scattering powder were added to the boiling plastisol and stirred well for 2 minutes to make a homogeneous mixture. Next, this mixture was cast into a cube mold and was cooled in air to solidify. The concentration of the dye in this sample was 5.2 mg/ml. To make a multi-layer phantom, a slice of PDMS absorber layer was sandwiched between two layers of standard glass slides. These layers were bonded together mechanically via clear tape. The thickness of each absorber layers (4 PDMS and 1 plastisol samples) was about 1 cm.

2.3.2.iii) Imaging protocol

To image samples, PT laser intensity was modulated in the form of a sinusoidal waveform from 0 mW to a set maximum power (for example 0 to 2 mW). In all experiments, 1000 points over time (M-scan) at an A-line rate of 21.6 kHz were captured from each point on the sample surface (duration $\simeq$ 46 ms). The PT laser was then turned off for 460 ms before acquiring the M-scan data of the next point on the sample surface, laterally spaced from the previous point by 5 μm.

2.3.2.iv) The Simulation and the input parameters

To examine the performance of the model, using the generated equations, a series of simulations under various conditions were performed. These conditions can be divided into two categories, including: conditions which relate to PT illumination parameters and ones related to material properties. In the first category, the power of the PT laser, the frequency of the PT laser modulation, and the location of the sample with respect to the focal plane were studied on the same sample. The second simulation category consisted of simulation of: a single-layer phantom with various concentrations of absorber, a multi-layer phantom submerged in different liquids, and an absorber layer sandwiched between layers with different mechanical stiffness. These simulations were carried out under identical illumination condition. Simulated and experimental signals were processed in the same way.

The inputs to the simulation were sample properties and system parameters. Those that could reliably be measured (e.g., beam size) were measured and are depicted in Table 2. For parameters that could not be reliably measured, we used an optimization code to find optimum values (e.g., thermal conductivity, thermal expansion coefficient, etc.). Through this code, we tried to minimize the difference between simulated and experimental signal by defining the goal function based on the root mean square error (RMSE). It should be pointed out that in this optimization, a PT-OCT signal data from an individual experiment was selected. This selected signal data as is marked with a green arrow in Fig.24(a). In the optimization procedure, considering the reported values in references for each parameter, a reasonable scanning range was defined for each parameter. At each step of this procedure, the value of only one parameter was changed within the predefined range (other parameters were kept constant) while the RMSE between the experimental signal and the simulated signal was calculated. This process was repeated for all parameters. Eventually, the values that generated smallest RMSE was selected as the optimized values for inputs of the model. Once the missing parameters/properties were found from the single experimental dataset, values were used for all subsequent simulations/comparisons. The optimized values are compared to literature values in Table 3. Here, the scanning range of parameters corresponds to doubling of MSE in each direction with respect to MSE of the optimal values (i.e., the global minimum). Discussion on uncertainty of predictions can be found in Appendix D.

Table 2. Values for experimental inputs and material properties used in the simulation and the experiments. Some parameters in this table were measured directly. The other parameters are reported from other references.

Parameters (Units)	Value
PT Parameter	
Absorption coefficient μ_a (cm^{-1}) of dye with concentration of (19.58mg/ml)	89.04
PT laser power P_{inc}(mW)	0 to 4.5
PT laser wavelength (nm)	808
PT laser amplitude modulation frequency *f* (Hz)	500-1000-1500-2000-2500
PT Laser beam radius after collimator (mm)	2.5
OCT Parameter	
OCT center wavelength (nm)	1315
OCT laser power (mW)	30
Sample Parameter	
Young's modulus of PDMS (kPa)	400 (reported 360-870[108])
Young's modulus of Plastisol (kPa)	70 (reported 40-70[109])
Young's modulus of BK7 Glass (GPa)	90

Table 3 The values of material properties in the simulation for PDMS and plastisol. For each material, the optimized values, the scanning range in the optimization procedure and the reported values for materials are listed.

	PDMS		Plastisol	
Material properties (Units)	Optimized value[scanning range]	Reported value	Optimized value[scanning range]	Reported value
Refractive index	1.4[1.34;1.46]	1.4 [110]	1.45[1.39;1.51]	1.45 [111]
Thermal conductivity (W/mK)	0.11[0.128; 0.098]	0.15 [110]	0.06[0.78; 0.049]	0.06-0.12 [112]
Specific heat (kJ/kg/K)	1.2[0.093;1.85]	1.46 [110]	1.08[0.089;1.80]	1.16-2.65 [112]
Density (Kg/m^3)	968[870;1370]	970[110]	958[830;1340]	962[113]
Thermo-optic coefficient (K^{-1})	$-460x10^{-6}$[(-520; -395)$x10^{-6}$]	$-450x10^{-6}$ [114]	-400 $x10^{-6}$[(-460;-350)$x10^{-6}$]	-340 $x10^{-6}$ [115][a]
Linear thermal expansion coefficient (K^{-1})	$310x10^{-6}$[(286;334)$x10^{-6}$]	$320x10^{-6}$ [116]	$230x10^{-6}$[(180;255)$x10^{-6}$]	$50\text{-}200x10^{-6}$ [117]
Poisson ratio	0.4[0.37;0.43]	0.5 [110]	0.4[0.37;0.43]	0.6 [118]

[a]Value for silicone since this value could not be found in the literature for Plastisol.

2.3.3. Results and discussion

2.3.3.i) Effect of the PT laser light field on the PT-OCT signal

To study the effects of the PT laser parameters, a sample with 2.2 mg/ml of absorbing dye concentration (μ_a=10 cm^{-1}) was defined for the simulation. To verify the simulation results, a series of experiments with matching conditions were performed on a fabricated phantom. First, to study the effect of power of the PT laser, the sample was illuminated by the PT laser at 5 different levels of power (0, 1.07, 2.47, 3.6, and 4.5

mW). In all these cases, the focal plane was aligned with the top surface of the sample, resulting in highest intensity of the PT laser on the top sample surface. Simulated PT-OCT signals and smoothing-filtered experimental signals versus depth at various power levels are plotted in figure 24(a). Both simulated and experimental signals exhibit monotonic increase with depth. This trend is due to the cumulative nature of PT-OCT signal in a homogenous layer with the signal amplitude at each depth encoding the effect of all preceding layers. It can also be seen that PT-OCT signals exhibit a jump in amplitude at the sample surface (i.e., the Y-intercept) followed by an increase in signal values along depth. The rate of increase in signal values is higher at depths closer to surface because in these experiments and simulations the top surfaces of the sample are exposed to higher intensity of PT beam than deeper sample areas which results in larger thermo-elastic expansion of top levels. This behavior is also predicted by Eq. (2.8) and Eq. (2.15), as larger intensity of PT laser yields larger heat source Q and subsequently larger amplitude of thermal-wave fields. Given that the movement of the sample is not restricted on the top surface in this case (i.e., zero axial mechanical stress on each slice of HAZ/TMAZ), these warmer top levels tend to expand upward, so the OPL varies drastically near the top levels which contributes to the initial jumps in the PT-OCT signals at the first few depth levels of the sample (see Fig.24(a)). Gradually, as the light penetrates deeper in the sample, the light intensity decreases due to absorption of PT light by overlayers, and the variation of temperature and OPL in deeper levels reduces. The results of figure 24(a) suggest good alignment of the experimental data with the developed theory. Results also demonstrate ability of developed theory in predicting the initial signal jump in PT-OCT signals which could not be predicted by any of previous theoretical models.

In figure 24(b), the average of PT-OCT signals within a 20 μm window below the sample surface were plotted in terms of PT laser power at various modulation frequencies. As seen at each modulation frequency, increasing the power on the sample increases the amplitude of PT-OCT signal. These experimental observations are consistent with the predicted linear increase of the model. Deviations of experimental values from linearity are likely due to noise. Such deviations are larger at lower modulation frequencies due to the pink nature of noise in PT-OCT systems (i.e., larger error bar at the lower frequencies). Also, in experimental data points, there is deviation from the linearity.

To understand the effect of the absorber concentration on PT-OCT signal, single layer samples with three different concentrations of absorber (0.22, 0.43, and 1.3 mg/ml) with absorption coefficient (μ_a) of 100, 200, and 600 m^{-1} were imaged under PT illumination at various powers (0.6, 1.07, 2.98 mW). In figure 24(c), experimental and simulated PT-OCT signal as a function of absorption coefficient (dye concentration) are plotted. As seen, there is proportional relation between PT-OCT signal and dye concentration. Also, the slopes of these lines are determined by the PT laser power. At higher

concentrations, PT light is absorbed more efficiently, leading to the generation of more heat and eventually larger temperature variations. The greater temperature leads to a greater variation in OPL and subsequently greater PT-OCT signals. Therefore, the effects of the dye concentration and the PT laser power on the PT-OCT signals are identical and cannot be directly distinguished from each other as both parameters influence the thermal energy delivered to the sample. One possible way of decoupling the effects of MOI concentration from PT laser power is to perform spectroscopic PT-OCT at dual PT wavelengths as shown before[74, 119]. Another key point in figure 24(c) is the increase in size of error bars at higher concentrations which is due to the degradation of SNR caused by enhanced attenuation of PT laser at larger dye concentrations.

To study the effect of the focal plane position, its location within the sample was changed on a single layer PDMS sample with 15 mg/ml of absorber at a constant PT laser power level (4.5 mW). The amplitude of experimental and simulated PT-OCT signals from top surface of the sample in terms of distance between top sample surface and the focal plane are plotted in figure 24(d). Negative values of the distance axis in this figure indicate that the sample was closer to the objective lens than the focal plane. As seen in both experimental and simulation results, the maximum signal was obtained when the top surface of the sample was located in focus at the focal plane. As the top surface moves away from the focal plane, the PT-OCT signal of the top surface drops approximately in a symmetric manner. Based on Eq. (2.9), at the focal plane, the beam diameter reaches a minimum, so a focused thermal field is then generated in the sample. This focused thermal field causes greater change in temperature locally at the center of the beam than a defocused beam far from the focal plane. The more change in temperature, the more variation in OPL; thus, the amplitude of the PT-OCT signal is maximum when the top surface is located at the focal plane. Regarding this inverse relation between signal amplitude and the focal plane, the intensity of the beam becomes half after displacing the sample by the Rayleigh range (150 μm for our setup). As seen in figure 24(d), both experimental data and simulated signals confirm this drop in intensity on order of the Rayleigh range. In addition, at off-focus planes, the OCT beam is also defocused which, in return, results in deterioration of OCT phase SNR[50]. Results of figure 24(d) suggest that in interpretation of PT-OCT signal, the location of focal plane relative to the sample must be considered; otherwise, a strong absorber at deeper regions can give the same signal as that of a week absorber in focus. To conclude, the optimum location for the desired depth of the sample that needs to be imaged with PT-OCT is the focal plane. This important point should be considered in design of PT-OCT catheters in the future.

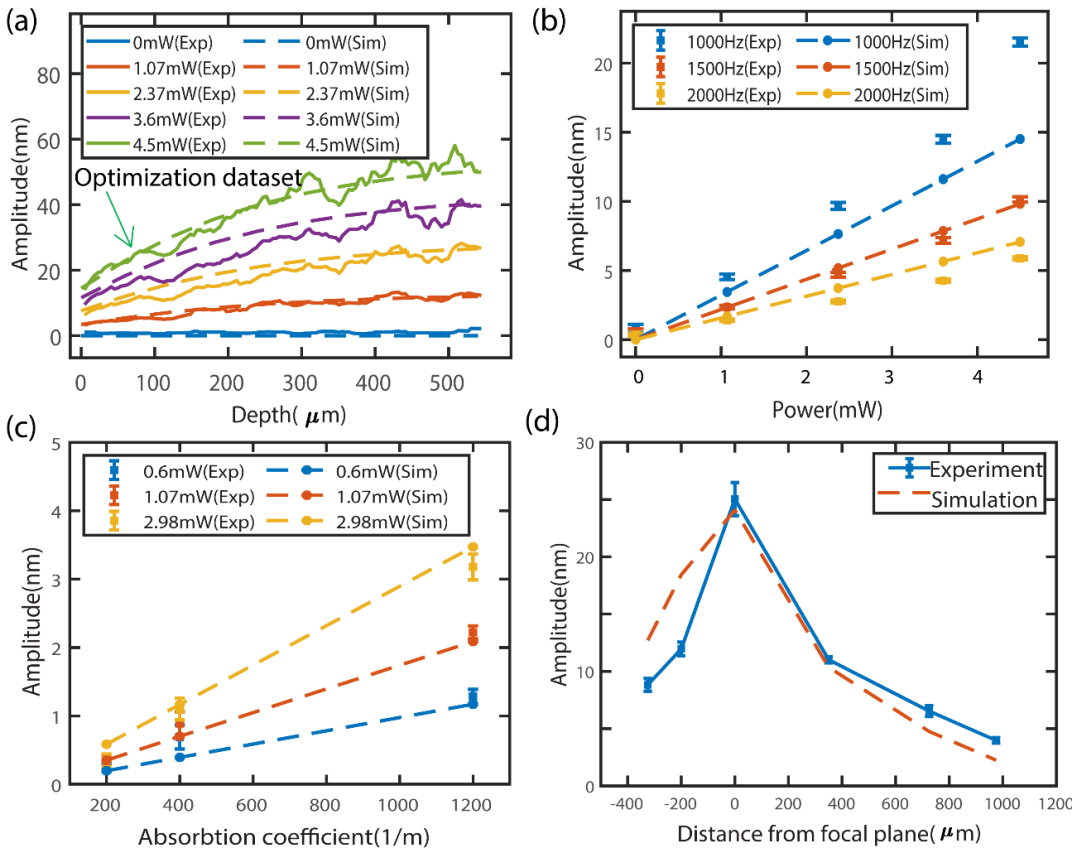

Figure 24. The results of simulated signal after changing the light field in the sample. (a) Simulated and experimental PT-OCT signals in terms of depth at various PT laser power at modulation frequency of 1000Hz; the green arrow indicates the experimental signal that was used for fitting and optimization of input parameters. (b) Simulated and experimental PT-OCT signals versus power in various frequencies. (c) PT-OCT signals as a function of absorption coefficient (dye concentration) at various PT laser power at modulation frequency of 1000Hz. (d) PT-OCT signals in terms of the location of focal plane related to the sample surface at modulation frequency of 500Hz.

2.3.3.ii) Effect of the modulation frequency on PT-OCT signal

To survey the effect of the PT laser modulation frequency, a single layer PDMS phantom with 2.2 mg/ml concentration of absorber was used. This sample was illuminated by the PT laser at modulation frequencies of 1000, 1500, 2000, and 2500 Hz at various power levels (1.07, 2.37, and 3.6 mW). The simulated signals and average of experimental PT-OCT signals acquired in a window of 20 μm just below the sample surface as a function of modulation frequency are plotted in figure 25(a). As seen, there is an inverse relation between the modulation frequency and the PT-OCT signal. In other words, as the modulation frequency increases, the amplitude of the thermal-wave field, and thus the PT-OCT signal, decreases. This relation can be justified by the simulated thermal fields in the sample at various frequencies. Figure 25(b) and figure 25(c) show the results of simulated thermal fields in the sample at the sample surface and along the depth, respectively. These plots show the temperature variation in time domain of a section passing the center of the sample. As seen, as the modulation frequency increases, the amplitude and size of the thermal field

decreases, because the penetration depth of the thermal waves (i.e., thermal diffusion length) is inversely proportional to the square root of the modulation frequency (see Eq. (2.14)). This trend, however, does not necessarily mean that lower modulation frequencies have priority to higher ones because in practice PT-OCT systems suffer from pink noise. In other words, at lower modulation frequencies, the PT-OCT signal is larger, but the noise floor becomes larger as well. Another relevant consideration in choosing the PT laser modulation frequency is its effect on resolving adjacent MOIs. It has been shown in a previous study[80] that at higher modulation frequencies, the resolution of the PT-OCT for distinguishing two adjacent point absorber improves. This improvement in resolution occurs because at higher frequencies, the thermal diffusion length becomes shorter, preventing the interference of the generated thermal fields of the two adjacent point absorbers. Results of figure 25 show that the SNR of PT-OCT systems is a function of the PT laser modulation frequency and a compromise need to be considered in selection of the optimal modulation frequency of a given PT-OCT system. In previous works, the modulation frequencies were selected from few hundred[91] to few kilo hertz[68] without any optimizing and justification. Indeed, for each sample, the optimum range of modulation frequency must be obtained specifically in light of sample properties and experimental conditions. To find this range of frequency, a compromise between SNR and spatial resolution must be considered.

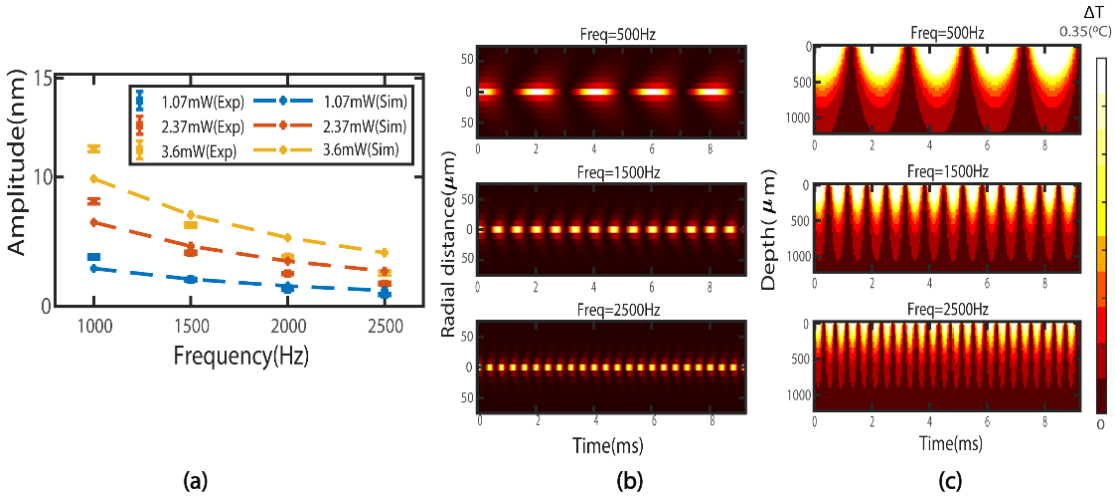

Figure 25. The effect of thermal field in the sample on the PT-OCT signal. (a) Simulated and experimental PT-OCT signals in terms of modulation frequency at various PT powers. (b) Simulated temporal thermal field at the top surface, and (c) along the depth at various frequencies. As the frequency of modulation increases, the thermal diffusion length becomes shorter.

2.3.3.iii) Effect of the surrounding medium on PT-OCT signal

The thermal and mechanical properties of the surrounding medium of an absorber affects PT-OCT signal. To observe the thermal effect of the surrounding on an absorber experimentally, the plastisol sample with higher dye concentration was selected (5.2 mg/ml concentration of absorber). To magnify this effect,

the thermal properties of plastisol such as lower thermal conductivity, allowed us to have greater thermal field amplitude in the sample. To generate two different heat fluxes on the sample surface, the sample was imaged in air or submerged in oil. The simulated and experimental signals are plotted in figure 26(a). Air and oil as the surrounding media have different thermal effusivities, so the generated thermal fields in the sample are not the same at the proximity of these media. In fact, the thermal effusivity is a thermal property of materials that determine how much heat can transfer in boundary of two different media. The thermal effusivity of the edible oil (500-700 $Ws^{0.5}/m^2K$[120]) is much greater than that of air ($\simeq$6 $Ws^{0.5}/m^2K$). Based on the principles of heat transfer and Eq. (2.18), the sample surface temperature in case of submerging in oil is lower compared to the one in air. So, because of larger effusivity of oil, more heat is sunk from the sample, and as a result the amplitude of the generated thermal field decreases. In Eq. (2.15), the last part of the right-hand side stands for the thermal flux on the surface. Because the defined Green's function in Eq. (2.16) as a solution for Eq. (2.15) has an inverse relation with the distance from the top surface where is the location of the heat flux, the temperature drop at the top surfaces is greater than for deeper levels. Considering these results, the surrounding media can penalize the PT-OCT signal. In practice, for example, tissues consist of water and blood that can act as a powerful heat sink and destroy the PT signal, so the thermal effect of the surrounding media of HAZ should be considered in the analysis of PT-OCT signal. Besides this, as an application, the amount of decrease in initial jump can be used to measure the thermal flux at the proximity of HAZ.

To study the effect of mechanical stiffness of the surrounding medium on the PT-OCT signal, the PDMS sample containing 2.2 mg/ml of the absorber dye was sandwiched between two glass slides. The simulation and the experimental PT-OCT signals in terms of depth for the free and the sandwiched samples are shown in figure 26(b). It can be seen that there is no jump (zero Y-intercept) in the signal from the sandwiched sample. However, in the sample with glass top layer, the top layer with greater mechanical stiffness (Young's modulus$\simeq$90Gpa) opposes this expansion, resulting in compression of the layer below and/or radial expansion of the material. In this scenario, the physical length in the axial direction near the junction of these layers does not change that much (unlike in the case of the free sample). Moreover, at the junction of the PDMS and the glass layers, because of heat flux, the amplitude of temperature change will be less. OPL and PT-OCT signals from the sample with glass top layer are much lower than from the free sample, because maximum temperature and the physical displacement that are the two parameters in the definition of OPL are less for the sandwiched sample. In light of these results, the stiffness of the top layer can alter the signal amplitude, and when the MOI is buried under a top layer (e.g., subsurface lipid pools in atherosclerotic plaques), this effect should be considered. Also, the change in the initial jump because of stiffness can be considered as a criterion to determine the stiffness of the top layer. For example, as a potential application, the stiffness of the cap layer in lipid-rich coronary plaques may be evaluated by

analyzing the PT-OCT top surface signal jumps to get an insight into vulnerability of plaque to rupture[121, 122] .

Finally, to show the effect of the Poisson's ratio, simulated signals with/without considering the Poisson effect were plotted in figure 26(c). As seen, the signal amplitude in the sample without considering Poisson's ratio (ν=0) is significantly smaller than that of a sample with non-zero Poisson's ratio (ν=0.4). Indeed, the Poisson's effect describes how molecules of the sample tend to displace in directions perpendicular to the direction of an applying force. After heating, when the HAZ tends to expand in radial direction, because of interaction with TMAZ, a radial pressure is generated on HAZ. Consequently, because of this pressure and Poisson's effect, more material tends to expand in the axial direction. These results show that neglecting Poisson's ratio leads to underestimation in simulation of signal. The fact that we find Poisson coefficients that are consistent with literature values when optimizing the simulation parameters offers further evidence for the validity of the model.

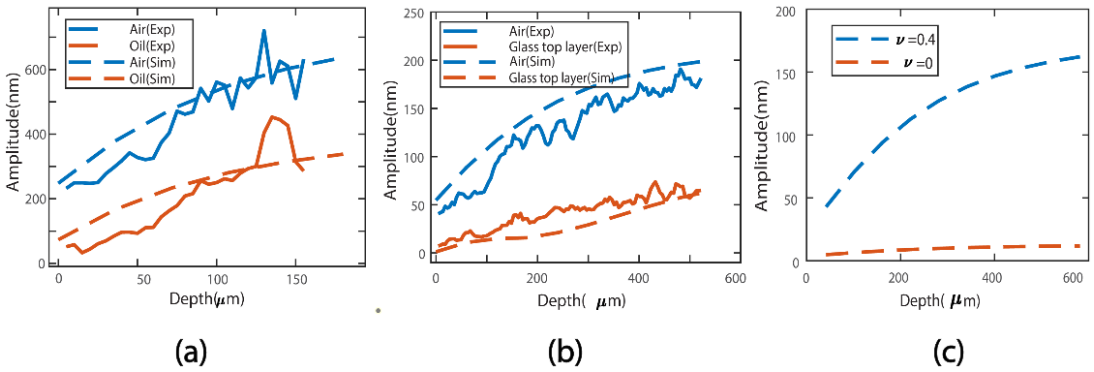

Figure 26. Effect of different boundary conditions on the PT-OCT signals. Simulated and experimental signals of the sample (a) in air and submerged in edible oil, (b) free sample and sandwiched sample with glass top layer. (c) Simulated signals with different values of Poisson ratio. The mechanical and thermal boundary conditions can affect the signal significantly. The effect of boundary conditions, however, was not considered in the previous models.

2.3.4. Summary

In this section, we propose a comprehensive and 3D theoretical model for predicting PT-OCT responses in multilayer geometries. The proposed model considers optical, thermal, and mechanical properties of samples as well as PT-OCT system parameters such as PT laser modulation parameters and location of system focal plane with respect to sample. Simulation and experimental parametric studies presented in this work demonstrate the ability of the developed model to predict the general behavior of PT-OCT signals in multi-layer phantoms with different optical, thermal, and mechanical properties. Our results also highlight how the properties of the material in the vicinity of light absorbing molecules contribute critically to the acquired PT-OCT signals. We should, however, caution the reader that the developed model is an approximation model based on simplifying assumptions such as neglecting scattering

of light in the light field block, or based on a thermal model developed for solid materials rather than tissue. These assumptions together with other random and systematic sources of noise and error resulted in suboptimal alignment of presented simulation and experimental data (e.g., in Figs.24(b) and 25(a)). Nevertheless, we anticipate the proposed model to open the door for better understanding of the effects of system parameters and tissue opto-thermo-mechanical properties on experimental signals, enabling informed optimization of experimentation strategies. The model can potentially also be used as a tool for identifying parameters that are most significant in specific experiments to subsequently guide signal processing and machine learning solutions for depth-resolved prediction of tissue molecular composition information.

3: Experimentation and Signal Analysis Strategies for Enhancing the Performance of PT-OCT

3.1.Introduction

PT-OCT is capable to form images from tissues by taking advantage of fine resolution structural images coming from OCT, and depth-resolved insight into chemical information coming from the absorption of the PT light by MOI. As we discussed before, PT-OCT has the potential to address the detection specificity shortcoming of OCT. For example, in figure 22(a), (b) (the artificial lipid plaques), while different concentration of lipid had the same "look" under OCT, the differences in lipid concentrations were clearly recognized by PT-OCT. In this chapter, we will be introducing experimentation and signal analysis strategies for further enhancement of detection performance of PT-OCT. These strategies serve as a first step for tailoring PT-OCT to the specific needs of interventional cardiology (i.e., one of the two major clinical applications of OCT). Such modalities can better aid interventional cardiologists in assessing the risk of atherosclerosis plaques because studies have shown great correlation between the probability of rupturing of lipid plaques in artery walls with both the chemical composition and structure of the plaque[31, 32, 85]. Current state-of-the-art in PT-OCT, however, cannot satisfy these imaging requirements because: 1- absorption of light at a given wavelength is not necessarily specific to only one MOI (e.g., water and lipid both absorb 1210 nm light), and 2- obtaining refined insight into tissue chemical composition directly from PT-OCT signals is not reliable as many system and sample parameters affect PT-OCT signals (as discussed in the previous chapter). These two major challenges of PT-OCT have held back translation of the technique to clinical studies. In this chapter, we will develop two strategies for addressing the challenges.

The first challenge that will be discussed is about specificity of PT-OCT to tissue type and chemical composition. Conventional PT-OCT is successful in depth-resolved sensing of absorption of PT light. The absorption of the PT light at a given wavelength, however, is not unique to a single MOI. That is, PT light absorption takes place at the location of targeted MOI in the sample as well as other not-targeted tissue constituent (pseudo-MOI). As there is no metric in conventional PT-OCT to distinguish between signals originating from MOI and pseudo-MOIs, conventional PT-OCT images are not entirely specific to certain tissue constituent. To tackle this limitation, we will increase the specificity in detection of MOI by analyzing their PT-OCT responses to more than one PT laser excitation (aka spectroscopic PT-OCT).

Extracting quantitative insight into chemical composition of tissue is another key challenge of PT-OCT. As discussed in Chapter 2 (Fig.24 to Fig.26), PT-OCT signals are, intrinsically, multi-factorial. That is, aside from tissue absorption spectrum, system parameters and sample properties influence the acquired PT-OCT signals. Quantitative interpretation of tissue composition from PT-OCT signals, therefore, requires decoupling of influences not related to chemistry and absorption spectrum. For example, for quantitative imaging of atherosclerotic plaques with PT-OCT, both imaging condition (e.g., the distance from the lipid pool to the focal plane) and sample parameters (e.g., the thickness of the fibrous cap) affect the strength of the acquired PT-OCT signal, in addition to lipid concentration. In the second part of this chapter, we will introduce a machine-learning-based strategy for decoupling the effect of influence parameters to enable obtaining quantitative insight into tissue chemical composition with PT-OCT.

3.2. Spectroscopic PT-OCT for specific detection of MOIs

In conventional PT-OCT, signals originate from absorption of a narrow-band PT light source in the sample. Such absorption events take place not only at MOI sites, but also at other tissue constituent sites that absorb the PT light. Therefore, presence of PT-OCT signal cannot be used to uniquely identify/detect a MOI. For instance, in cardiology, arterial plaque is made up of materials, including: lipid, water, elastin, and collagen[31, 82]. Absorption spectra of these materials in near-IR (NIR) are shown in figure 27. Based on these spectra, at 1210 nm, water, lipid, elastin/collagen all absorb the PT light, therefore one cannot distinguish the MOIs based on their responses to the PT laser.

To increase specificity in detection of MOI, spectroscopic method PT-OCT can be employed. In such systems, to discern MOI from pseudo-MOI, considering spectroscopy principles and absorption spectra of MOI, two (or more) PT wavelengths are used in the setup. The PT-OCT signal is gathered during illumination of the sample by each of these PT lasers. Then, by comparing the dual (or multi) wavelength responses of sample to the characteristic spectral absorption signatures of MOIs, a depth-resolved map of distribution of MOI within the OCT image is formed. For example, based on the absorption spectra in figure 27, PT lasers at 1040 nm and 1210 nm can be used for enhancing the detection performance. Exciting lipid with 1210 nm PT-laser is expected to produce a strong PT-OCT signal while PT-OCT signals at such excitation from water, elastin and collagen are expected to be moderate. PT excitation at 1040 nm, on the other hand, is expected to yield moderate PT-OCT signal for elastin and collagen while producing minimal PT-OCT signal for lipid and water. As such, interrogation of PT-OCT signals at all of these PT laser wavelengths and decoupling the received responses from the samples can provide depth-resolved insight into the chemical composition of tissues with higher specificity.

The idea of spectroscopic PT-OCT was introduced by the group of Prof. Milner for the purpose of measuring the level of saturated oxygen in blood with high accuracy, both in phantoms and *in-vivo*[74, 119,

123]. We are not aware of any other work in the field that has utilized spectroscopic PT-OCT. For cardiology applications, use of PT-OCT has so far been reported only in one conference publication in which single PT laser of utilized for detecting and visualizing lipid in human cardiac tissue *ex-vivo*[124]. As such, the spectroscopic PT-OCT work offered in this section for detection of atherosclerotic plaque constituents is a first of its kind.

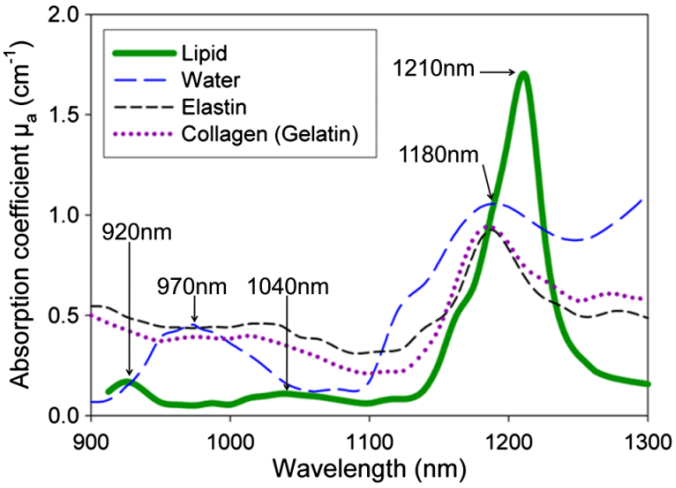

Figure 27. Absorption spectrum of common constituents of cardiac tissue in the NIR range, including: lipid, water, elastin, and collagen. Figure adapted from[31]. Copyright by the authors.

3.2.1. Methodology

3.2.1.i) The setup and imaging protocol

The experimental setup used for spectroscopic PT-OCT was explained in Section 2.2.3.i. Considering the absorption spectra depicted in figure 27, 1040 nm and 1210 nm PT lasers were selected for experiments. The PT laser power on the sample at both 1040 nm and 1210 nm was 30 mW. To image samples, modulation frequency of PT laser was set to 500 Hz. Also, at each M-scan, 1000 data points at an A-line rate of 21.6 kHz were captured.

3.2.1.ii) The samples

To evaluate the efficacy of spectroscopic PT-OCT, three studies were designed. The objective of the first study was to find the characteristic ratio of PT-OCT responses at the two PT wavelengths for different plaque materials including water, lipid, collagen, and elastin. Then, a two-layer water-lipid sample was studied to evaluate system's ability in discerning between these two materials from each other. Finally, a human cardiac tissue sample was studied to see how the previous findings from phantoms compare to those from real tissue.

To carry out these studies, a series of phantoms containing the dominant material of cardiac tissues were made. Mayonnaise (Kraft) was chosen as the rich source for lipid (>80%)[82]. The used soybean oil in mayonnaise that is composed of primary lipid compositions of linoleic acid, oleic acid and Palmitic acid has a similar composition to coronary plaques[81, 125, 126]. Moreover, scattering and simplicity in shaping of mayonnaise are the other features that convinced us of using mayonnaise as main material for our lipid phantoms.

To make water-based tissue like phantoms, agar powder (Sigma Aldrich, USA) was dissolved in water to make a solution with 98% of water weight ratio. As the sample provide enough scattering in OCT images, no other scattering agent was added. Then the solution was heated up and stirred well for 5min until the water was boiling. After that the solution was poured into a petri dish and was put in a refrigerator (4^{o}C) to solidify. Also, to make a two-layer sample, a wedge of the agar-water sample was put on a mayonnaise substrate.

The collagen sample was obtained from chicken cartilage as a rich source of collagen[127]. A fresh chicken leg was cut from the knee joint, and tendons above the cartilage were removed, then the sample was washed with Phosphate-buffered saline (PBS). The tissue was placed on a glass slide at room temperature (24 ^{o}C) to image with the system. The elastin foam sample was made with elastin from bovine neck ligament (Sigma Aldrich, USA). After dissolving elastin in 0.05% acetic acid solution, and freezing it at -20^{o}C for 24hr, the sample was sublimated to make a foam scaffold of elastin.

The next sample was prepared from a piece of fresh human aorta tissue. This tissue was obtained through the National Disease Research Interchange (NDRI; PA, USA) from a woman (88 year) who died of cardiac issues. The fresh sample was shipped to our lab at the York university within 24h after tissue collection. The acquisition of human sample and the preparation steps were done at Hybrid Biomedical Optics (HBO) lab under approved ethics protocols by York university (e2020-234 and e2020-250). After unpacking and washing the aorta sample with PBS serum, a longitudinal cut was made with dissection scissors to make a rectangular flat tissue from a pipe-shape aorta (Fig.28). There were some calcified regions (harder than normal tissue) on the inner side of the aorta(intima). A square region containing one of these calcifications was cut carefully with a surgery knife (see Fig.28). Two points with regular tattoo ink and tattoo needle were carved on this sample to set the orientation for raster scanning by OCT and later guide the histology sectioning (Fig.29). This sample was then put on a glass slide and imaged by PT-OCT system at room temperature. During imaging, 10cc of PBS was poured on the sample every 15 minutes to prevent tissue dehydration.

Figure 28. The procedure of preparing the aorta sample. Cutting the aorta sample in 3 steps with a dissection scissor and a surgery knife.

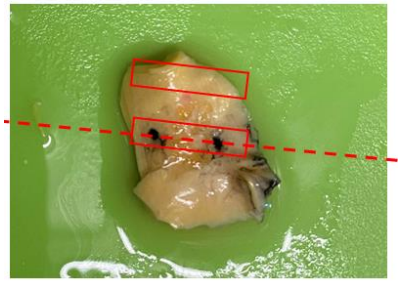

Figure 29. Direction of scanning that is set with two black dots with ink tattoo. The two selected parts (red windows) were used to image with PT-OCT and to perform histology procedure.

3.2.1.iii) Histology

After imaging the two selected parts (red windows in Fig.29) of this sample, it was immediately submerged to the optimal cutting temperature (O.C.T) compound (Fisher, USA) and was kept in a -80 ^{o}C fridge. The same procedure was done on another piece of the aorta sample, but this time, to fix the tissues after imaging, the cut sample was placed into Formalin (Sigma Aldrich, USA). Histology on frozen and fixed samples gives us a better insight into the chemical composition. After few days, histology study were conducted on these two types of samples (the frozen and the fixed in Formalin).

First, the process of histology for Formalin sample will be explained. The sample was placed in histology cassette (Fig.30(a)). The closed lid cassette then was submerged into ethylenediaminetetracetic acid (EDTA) decalcifying solution for 3-5 days with agitation. After decalcification, samples were washed well in running tap water, then the cassette was placed in 70% ETOH (water and ethanol solution). The cassette was loaded into a tissue processor for 16-18 hours. In the processor, tissue samples were subjected to a series of increasing concentrations of ethanol, followed by xylene, and finally molten wax. The next day, the tissues were removed from the tissue processor and placed in the embedding center. Note that in the tissue embedding procedures, the “embedding center” terminology refers to workstations and accessories designed for this purpose. The sample was trisected based on the region of interest marked by tattoo ink,

then cut surfaces were embedded down into a metal mold (Fig.30(b)). After this step, final Paraffin blocks were produced (Fig.30(c)). Eventually, sectioning was done on a microtome at 4 micron thickness.

(a) (b) (c)

Figure 30. (a) Histology cassette for the Formalin fixed tissue, (b) the sliced samples, (c) the paraffin embedded blocks

To slice the frozen sample, a cryostat was used. Cabinet chamber and specimen head of the cryostat is set to about -19 to -20 ◦C. The frozen sample in O.C.T compound was taken out of -80 ◦C case and held in the chamber to of cryostat to reach the temperature of the chamber. The frozen sample block (Fig.31(a)) was cut into 4 sections (Fig.31(b)) and was then mounted on specimen chucks for sectioning at 5-6 µm-thick sections.

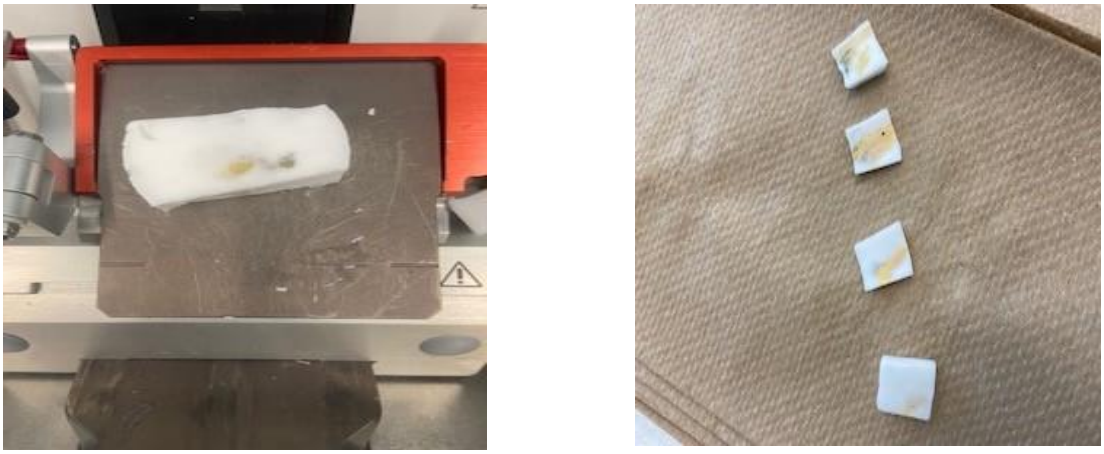

(a) (b)

Figure 31. (a) the frozen block, and (b) slice blocks with cryostat

Subsequently, the prepared slices of both types were stained with Movat pentachrome and haematoxylin and eosin (H&E). Finally, the stained slices were scanned with the high resolution (0.5 µm, 20X) bright field slide scanner (Aperio, LeicaBioSystems, Canada). Sample histology images with Movat and H&E stains can be seen in figure 32 and figure 33, respectively.

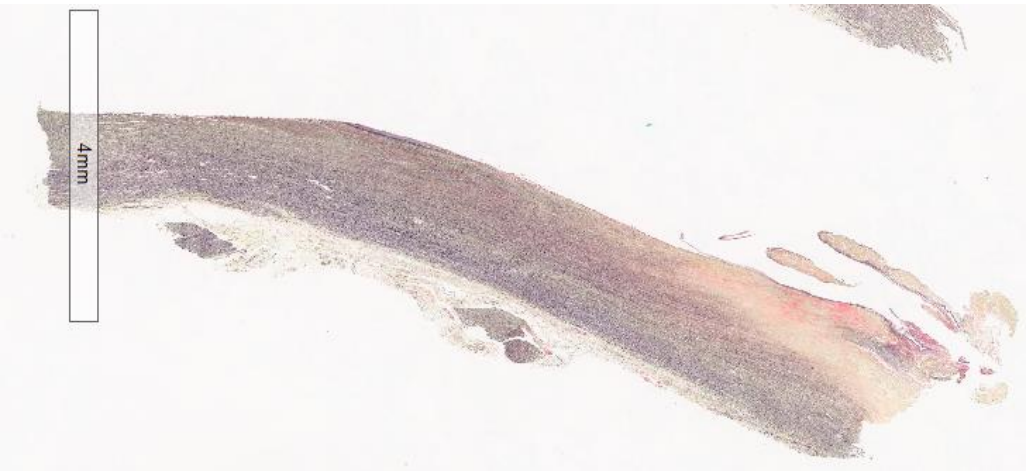

Figure 32. A view of a Movat-stained slice.

Figure 33. A view of a H&E-stained slice.

3.2.2. Results and discussion

The OCT B-mode and PT-OCT B-mode images of the standard phantoms are depicted in figure 34. The PT-OCT B-mode images were captured in 3 conditions: when both PT lasers were off (base line), the 1040 nm PT laser was on, and the 1210 nm PT laser was on. Comparing the dual wavelength PT-OCT responses of phantoms with respect to the baseline allows us to study characteristic absorption signatures of the samples. For example, both water-based agarose (Fig.34(a.1) to (a.4)) and lipid (Fig.34(b.1) to (b.4)) samples absorbed PT laser at 1210 nm but did not absorb 1040 nm. These images that show the map of absorption of light have a strong consistency with the absorption spectra of lipid and water at these two wavelengths, in figure 27. Next, to compare the amplitude of signals acquired from water and lipid, the two-layer sample consisting of a substrate of lipid under a wedge of water-agarose sample was imaged (see Fig.34(c.1) to (c.4)). Although both water and lipid generate strong PT-OCT signal at 1210 nm, the amplitude of lipid signal is much greater than that of water. The reason behind this can be found in their material properties. Indeed, the optical properties of lipid (absorption coefficient) and thermal properties

(specific heat and diffusivity) of lipid results in generation of a stronger thermal field in the sample than that of the water. These key differences were discussed in detail Chapter 2 under Section 2. Similarly, the results of collagen (chicken cartilage) in figure 34(d.1)-(d.4) and elastin foam figure 34(e.1)-(e.4) show a moderate absorption at both wave-lengths which are consistent with expectations from the reference absorption spectra of figure 27.

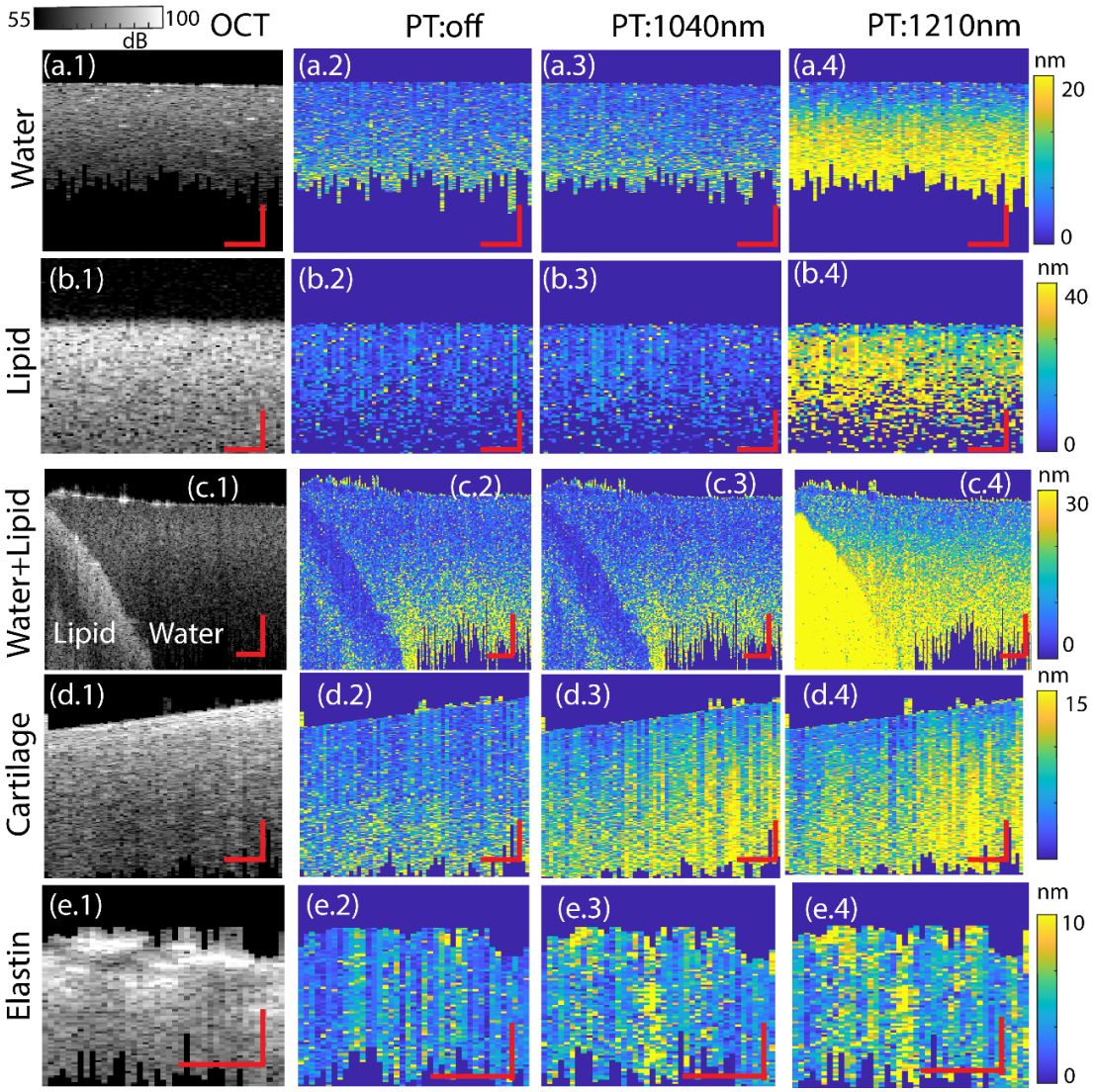

Figure 34. The results of spectroscopy on the controlled phantoms. The OCT and the PT-OCT images from the (a)water, (b) lipid, (c) two-layer sample, (d) cartilage, and (e) elastin samples. By comparing the received signals at 1040 and 1210 nm with the PT:off mode, it is seen that there is great consistency between the absorption spectra of these materials and the received PT-OCT signals, scale bar=80 μm.

To get better understanding of characteristic spectroscopic PT-OCT responses, histograms of PT-OCT images are plotted in figure 35. As seen, in histograms of water (Fig.35(a)) and lipid (Fig.35(b)) the

difference in count of pixels in 1210 nm condition are quite discernible from the off and 1040 nm conditions. These observations suggest that these samples absorb 1210 nm effectively, because the distribution of pixels in histogram shifts to the right. Also, the pixel counts for these samples for both “off” and “1040 nm” cases are almost the same, indicating no notable absorption at 1040 nm. Despite the fact that both water and lipid absorb at 1210 nm, the characteristic differences of lipid and water allows us to discern between the two tissue constituents. Due to the differences in the opto-thermo-mechanical properties, PT-OCT signals from lipid are, intrinsically, greater than water. In addition, because of the higher scattering property of lipid related to the water, the look of lipid under OCT is quite different (Fig.34(c), the two-layer sample).

For the cartilage (Fig.35(c)), and the elastin samples (Fig.35(d)), by comparing the pixel counts for 1040 nm and 1210 nm modes with the off mode, there is moderate absorption at both wavelengths. However, as the shift to the right in these histograms is lower than that of the water and lipid cases, the absorption of PT light is lower in these samples. We should say at the two PT wavelengths used, elastin and collagen absorb similarly, so we can only detect the combined category of elastin/collagen but not individual components. This behavior has consistency with the absorption spectra of these chemicals in figure 27.

Based on these phantom studies, we see that it is possible to discern between lipid, water, collagen/elastin category with this spectroscopic strategy. Lipid and water samples have completely different absorption map from collagen/elastin category (i.e., greater signals at 1210 nm and almost nothing at 1040 nm) with PT-OCT. Additionally, to increase accuracy in discerning water from lipid, looking at the OCT images along with the PT-OCT signal amplitudes will be helpful.

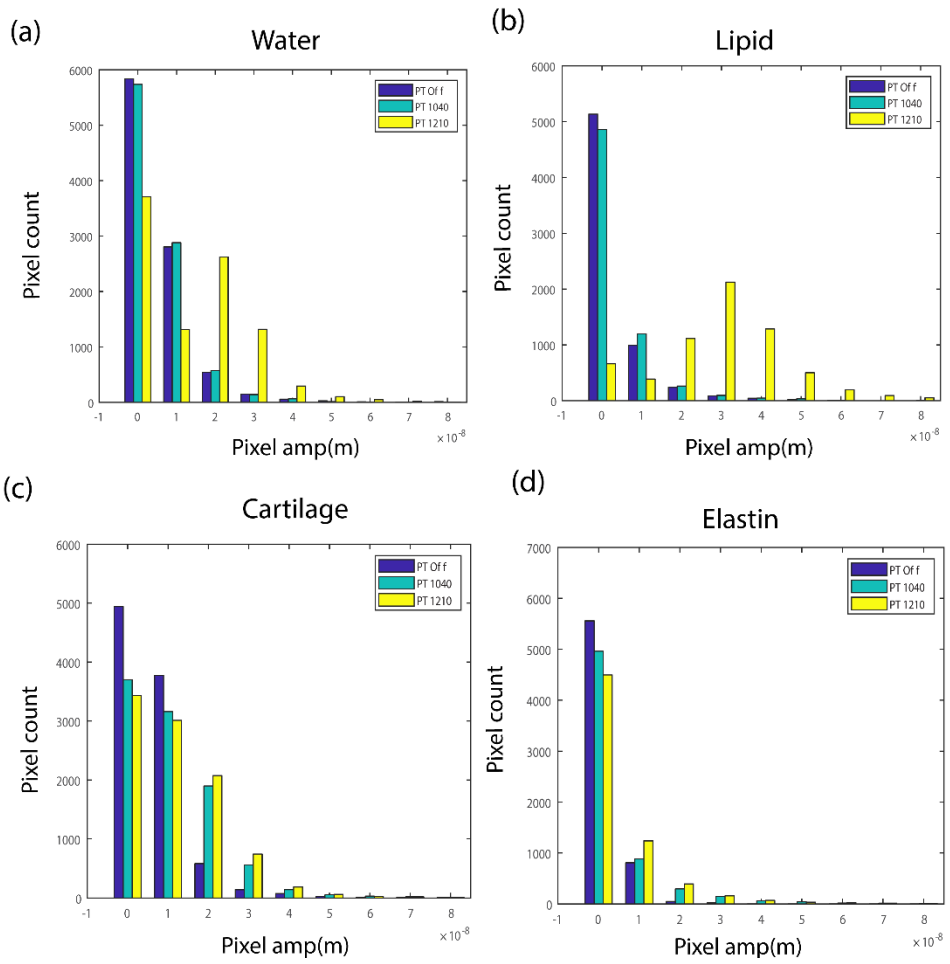

Figure 35. Quantitative analysis of images depicted in previous figure. Histogram of pixel amplitude in PT-OCT images for the (a)water, (b) lipid, (c) cartilage, and (d) elastin samples. Histograms follow characteristic light absorption behaviors of water, lipid, and elastin/collagen.

After performing a feasibility study with the spectroscopic strategy on the standard phantoms, we extended the study to the human tissues. The results of human aorta samples with PT-OCT and histology are depicted in figure 36. While the OCT and histology images show high degree of structural similarity, we cannot claim them to be exactly co-registered. Exact co-registration proved to be very challenging because the structure of the tissue changes during the decalcification processing of histology.

Results suggest that both the histology (Fig.36(a)) and the OCT image (Fig.36(b)) show a multi-layer structure inside the sample. In the OCT image, there is an area in the top left that has a greater scattering than other areas (labeled with A1). The layer under A1 area has a poor scattering as it appears as a dark region in the OCT image (labeled with A2). Beneath these two layers, the other layer which is labeled with A3 has a scattering property between the scatterings of the two upper layers. Although we can distinguish these layers from OCT image, no chemical composition information can be obtained from the OCT image.

By comparing PT-OCT results (Fig.36(d)-(e)) with the base line (Fig.36(c)) small absorption at 1040 nm and stronger absorption at 1210 nm at the left side of images can be seen (A1 in the OCT image). The possible source for the weak signal at 1040 nm can be elastin/collagen in this layer. The histology results (Fig.36(a)) also showed elastin composition in this region (purple and dark color with Movat stain). The elastin composition in tissues is responsible for the extensibility and elastic recoil features of tissues, therefore we speculate this region is a soft tissue that contains a notable percentage of water[128, 129]. Therefore, a large portion of the strong signal at 1210 nm comes from water in this layer. The elastin/collagen also generates PT-OCT signal at 1210 nm, but it will be much smaller than that of water. Because of the poor scattering and deep levels related to the surface, the other regions do not generate a meaningful PT-OCT signal.

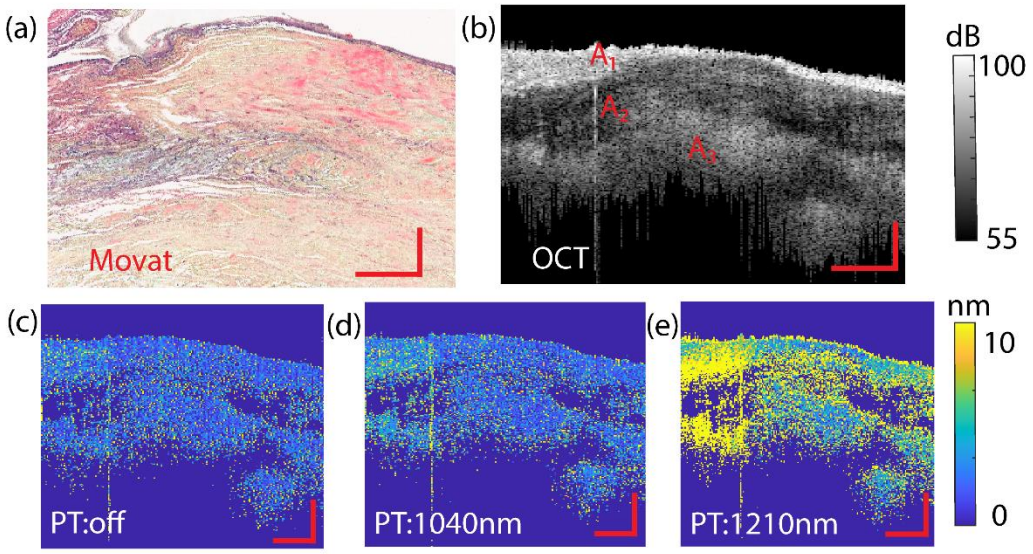

Figure 36. The results of spectroscopic PT-OCT of the human aorta sample; (a) histology, (b) OCT, (c) PT-OCT base line, (d) PT-OCT at 1040 nm, and (e) PT-OCT at 1210 nm images. The OCT result represents that sample has 3 different layers, marked with A1 to A3. By comparing the PT-OCT results and the histology results as the gold standard, it is assumed that signals come from water and collagen/elastin. Further studies with more wavelengths will improve the accuracy of detecting material; see text for more information, scale bar= 200 μm.

The results of another region of the aorta tissues are depicted in figure 37. This area is far from the calcified abnormality, and had a normal tissue look. Similar to the previous case, the histology slice and the corresponding OCT image demonstrate high degree of similarity (i.e., a single layer structure). The histology image (Fig. 37(a)) shows an accumulation of collagen/elastin (yellow and green color for collagen and purple for elastin with Movat stain) in this sample. The obtained PT-OCT responses are consistent with presence of collagen/elastin in the fresh tissue sample; comparison of the acquired signals at 1040 nm and 1210 nm with the baseline (Fig.37(c)) suggest moderate light absorption at 1040 nm (Fig.37(d)) due to light

absorption by collagen and elastin and strong light absorption at 1210 nm (Fig.37I) due to light absorption by the water in this fresh tissue.

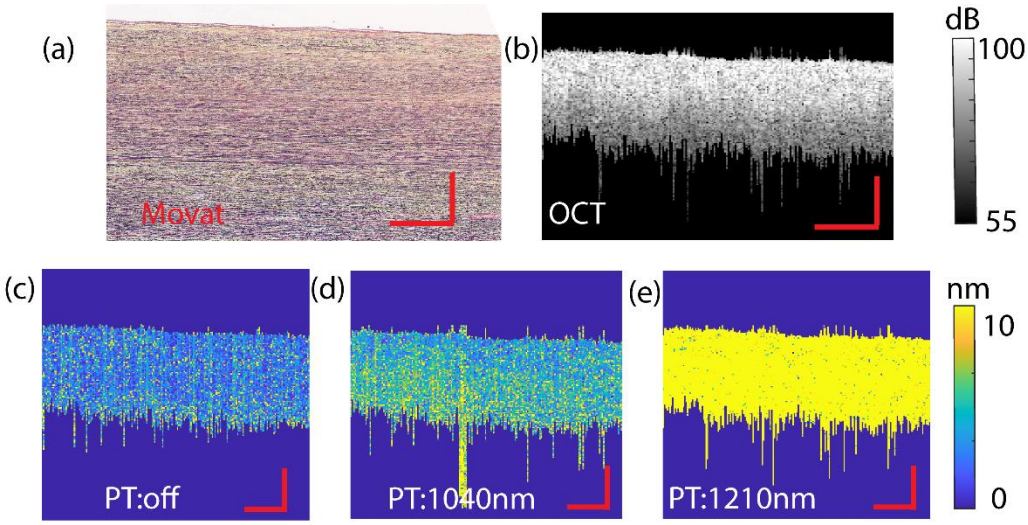

Figure 37. The results of spectroscopic PT-OCT method of a normal human aorta sample (a) histology, (b) OCT, (c) PT-OCT base line, (d) PT-OCT at 1040 nm, and (e) PT-OCT at 1210 nm of human aorta sample. These preliminary and promising results demonstrate the potential of spectroscopic PT-OCT method as a new method for digitized histology; scale bar= 200 μm.

To summarize, in this section, we proposed and discussed a strategy for enhancing the specificity of PT-OCT using principles of spectroscopy on MOIs relevant to atherosclerotic plaques. The promising results are consistent with what we anticipated from the absorption spectra, and lead to specific detection of materials. This study can be considered as a future direction of application of PT-OCT in intravascular imaging. Without the dual wavelength spectroscopic method, presence of some chemical cannot be seen in the sample. For instance, in figure 37, by considering only the 1210 nm results, the detection of collagen and elastin in the tissues is impossible as lipid, collagen/elastin, and water all absorb at this wavelength (see their spectra in figure 27). However, when 1040 nm image is also considered, detection of collagen/elastin is rendered as water and lipid do not absorb at 1040 nm.

To design a spectroscopic setup, a compromise should be considered in light of sample properties, sample geometry, and tissue constituents. In general, to decrease the detection uncertainty, at least two PT lasers are needed in which the target MOI absorbs moderately or strongly but with different ratio. That is, poor absorption of the PT laser by the target MOI may not be very helpful in the spectroscopic approach. For example, the 1040 nm used in our system was not an optimal choice for differentiation of lipid and water from each other because both entities have no/minimal absorption at 1040 nm. Distinction of water from lipid can be performed by adding for example a 970 nm PT laser at which water offers moderate

absorption but lipid does not absorb (Fig.27). Probing at more than two PT wavelengths, generally, is expected to enhance detection performance at the cost of added complexity and cost of the setup and increased processing time of imaging. A possible way to decrease the imaging time is shining all PT lasers simultaneously but with slightly different modulation frequencies so that individual responses can later be demodulated from the acquired data. Eventually, the spectroscopic PT-OCT is a complementary approach to the conventional PT-OCT and is a helpful method in detection of MOI with a higher specificity.

3.3.Quantitative PT-OCT imaging with AI-powered classifiers

In this section, the goal is to label the PT-OCT image pixels based on their concentration of MOI. Theoretical and experimental results discussed in previous sections and chapters show that PT-OCT signals contain characteristic trends and features that are correlated with tissue composition. To date, few efforts have been made to quantify MOI concentrations such as concentration of dissolved oxygen in blood[123] or ICG in water[91] from PT-OCT signals. Although these preliminary results were encouraging, the design of studies were disconnected from clinical scenarios as in these works all the sample and system influence parameters (other than MOI concentration) were kept constant. This type of single-parameter quantification is not normally valid because two or more influence parameters (e.g., surrounding medium, distance to the focal plane, depth of MOI, etc.) are expected to vary from one tissue to another. As we discussed earlier in Chapter 2, the PT-OCT signal depends on various system and sample parameters that make the functionality of the signal highly non-linear to the input parameters; these non-linearities affect each other and often increase the order of non-linearity. Analytic inversion of such multifactorial problems is inherently challenging and noise sensitive. Machine learning (or simply ML) has demonstrated, time and again, that it offers a compelling solution to this type of multifactorial and non-linear problems.

ML models consists of algorithms that can improve themselves through gaining experiences over time[130]. The main models of ML include: support vector machine (SVM), artificial neural network (and also deep net), decision tree, regression analysis, Bayesian networks and genetic algorithms, that can be used for various purposes such as classification, regression, and clustering with supervised, reinforcement, and non-supervised learning methods[130-132].

In the field of OCT, ML models have been used as a powerful tool for analyzing captured images for a variety of applications spanning from pattern recognition and texture[133-135], to labeling and segmentation (classification) of regions of interest in OCT images[136-140]. For instance, a pixel-wise ML method was presented for classifying OCT images obtained from tumor and normal samples of murine ear tissues[141]. As another example, a combined ML model consisting of SVM and principal component analysis (PCA) has proved to be helpful in automated tissue classification in brain metastases from human samples[142]. In multi-modality OCT-based systems, ML has been utilized to classify materials based on

the mechanical properties from OCE datasets; here, using a SVM model on OCT and OCE data, the glomerulonephritis (inflammation and damage to the filtering part of the kidneys) in mouse samples were analyzed[143].

To the best of our knowledge, feasibility of classifying MOI concentrations with ML models have not yet been examined in the field of PT-OCT. As such, in this section, we will discuss the design and the development of a ML model for labeling PT-OCT image pixels based on MOI concentration (e.g., lipid). The developed ML model is trained to decouple the effects of influence parameters not linked to MOI concentration (e.g., MOI depth or distance to focal plane).

3.3.1. The machine learning (ML) model

3.3.1.i) Feature selection

Given the significance of lipid concentration to the vulnerability of atherosclerotic plaques[31], a ML model was designed for labeling/classifying lipid composition of pixels in a PT-OCT dataset. To do so, the influence parameters having significant contributions to the PT-OCT signals were first identified (aka, feature selection step). This step was deemed essential because for example the received signal from a high concentration region of lipid far from the focal plane can very well be comparable with that of a low concentration region close to the focal plane. Therefore, the net needs to form its prediction based on a collection of parameters and not just the intensity of the PT-OCT signal of a given pixel. Based on the outcomes of the theoretical models developed in the previous chapter, the following parameters were deemed to be of significant relevance to the ML model:

1) the distance from the selected pixel to the focal plane (D_{fp}; see Fig.38).

   Figure 24(d) in Chapter 2 shows that regardless of MOI concentration, PT-OCT signal decreases sharply with distance from the focal plane. As such, the distance of a pixel to system focal plane (D_{fp}) was considered as a significant parameter as input of the model.

2) the distance of the selected pixel to the top surface of the sample (D_{top}; see Fig.38).

   It is shown in figure 24(a) that the amplitude of PT-OCT signal versus depth is cumulative. That is, the received signal from a given depth inside the sample is the summation of the signal of all surfaces from the top surface down to that depth. However, the rate of increase in the signal amplitude along depth is not constant. The rate depends on the PT power and the optical properties of the sample. Therefore, the spatial location of each pixel relative to the top surface should be taken into account by the model.

3) the gray level of the selected pixel in the OCT image (Gr_{pix}; see Fig.38).

The gray level of a pixel in OCT image represents the amount of the back-reflected light from that depth inside the sample and can be used as a metric for SNR of received OCT signal from that specific depth. In the characterization of the setup section (Appendix A), the inverse proportionality of phase stability and the square root of SNR of OCT is discussed. Due to such proportionality, the PT-OCT signals originating from pixels with lower gray level (i.e., lower OCT SNR) are noisier (i.e., poor phase stability). The level of noise in the phase of OCT affects the PT-OCT signal and needs to be considered by the model.

4) the average of gray level of the pixels above the selected pixel (Gr_{line}; see Fig.38).

   As we explained at the beginning of this thesis, OCT works based on the back-scattered light from the sample. As such, optical scattering properties of samples can be estimated from the OCT image [144]. Generally, as the scattering properties of medium increases, the light power attenuates more along the depth which, in return, leads to smaller PT-OCT signal from the MOI (Fig.24(b)). Note that the wavelengths of the PT light (1210 nm) and the OCT light (1315±75 nm) in this study were not too far apart, so considering the scattering of OCT light gives the model a relevant estimation (not exactly) about the scattering of the PT light in the sample.

5) the amplitude(s) of pixel's PT-OCT signal (PT_{Amp}).

   The amplitude of pixel in PT-OCT images is directly correlated with the amount of absorption of PT light. This parameter is, perhaps, the most obvious parameter that can be used to label pixels based on their concentration of MOI. However, it was shown in Section 2.2 that the relation between PT-OCT signal and the concentration of MOI is non-linear and the degree of non-linearity depends on sample thermal and physical parameters.

The information provided to the model by above parameters were expected to offer the model an estimation of the medium's light attenuation properties, the roll-off of OCT and PT-OCT signal sensitivity with depth, and the strength of PT light absorption by MOI. Using this information, the model was designed to classify a given pixel into one of the following groups/classes of lipid concentration: low (~[0-30%]), medium (~[30-70%]), and high (~[70-100%]).

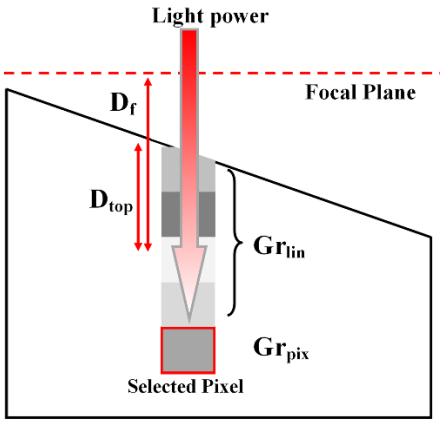

Figure 38. An illustration of spatial parameters of a single pixel in an OCT image that are deemed of significance to proper predictions by the ML model. These parameters provide the ML model with information about strength of pixel's OCT signal, the depth of selected pixel in the sample, the distance of the selected pixel related to the focal plane, and the scattering of the medium above the selected pixels.

3.3.1.ii) Model selection

To generate and train a ML model, supervised learning SVM method was used. SVM is one of the most robust classification methods in multi-factorial problems which works based on the statistical learning frameworks. SVM can efficiently perform classification in high non-linear datasets[145] and has shown interesting results in OCT signal analysis with a high accuracy[138, 146]. Briefly, to explain the principle of SVM classifiers, in a distribution of two-class data (the green and the blue-colored datapoints in Fig.39), several possible lines (e.g., S1, S2, S3 in Fig.39) can be drawn to separate the two classes.

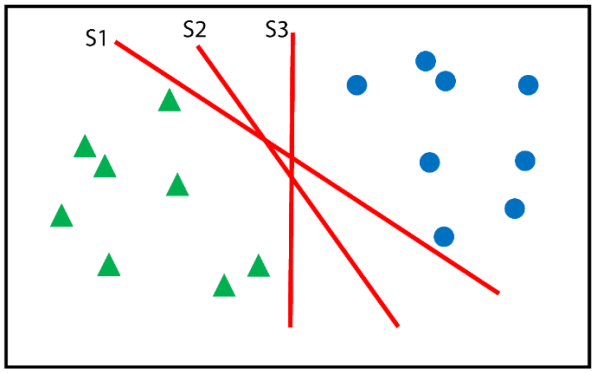

Figure 39. In this distribution of data (green triangles and blue dots), there exists an infinite number of solutions to separate these regions. Which one is the best line?

To find the optimum line, SVM algorithm, first, finds the closest data points to one of the lines. These points that determine the optimum separation line are called support vectors. The distance between the line and the supported vectors is named margin. In SVM algorithm, the goal is to maximize the margin for each

class (the distance between the two dashed lines in Fig.40). According to mathematical optimization, the hyperplane that makes the margins maximum is the optimal hyperplane (classifier plane with general equation in form of w.x+b=0 in Fig.40)[147]. Similar to other ML algorithms, training of SVM can be supervised or unsupervised (when combined with unsupervised feature learning). In our study, as the input data for training the model is labeled with the known concentrations of samples (and by extension corresponding concentration classes), the SVM classifier used is a supervised method.

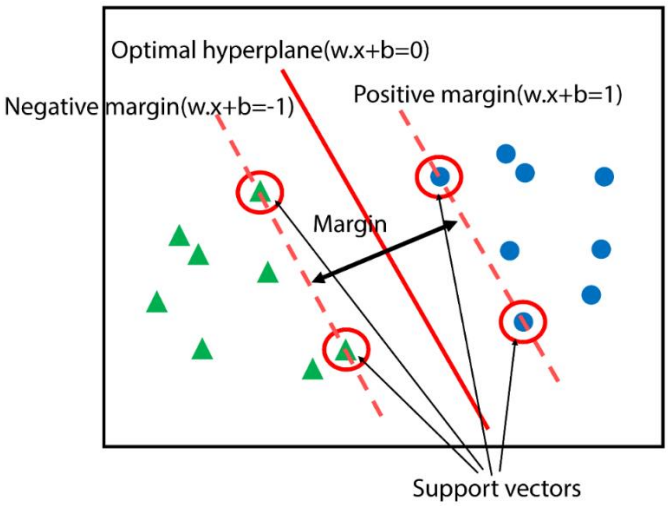

Figure 40. Illustration SVM algorithm on a distribution of data. The unique and optimal hyperplane in a two-dimensional input space based on margin maximization was drawn. In this schematic, *"w"* is the trained weights, *"x"* is the input vectors and *"b"* is a constant that is called bias.

3.3.2. Methodology

3.3.2.i) The setup and imaging protocol

The PT-OCT setup was described before under Section 2.2.3.ii in Chapter 2. Since lipid was selected as the target MOI in this study, the 1210 nm PT laser was used. The PT laser power and modulation frequency were 10 mW on sample surface and 1000 Hz, respectively. At each M-scan, 1000 data points were captured at an A-line rate of 21.6 kHz.

3.3.2.ii) The phantoms

To make different concentrations of lipid, mayonnaise (Kraft) was mixed with a water-based gel in different weight ratios. After weighting by a scale, the two components were stirred well for 10min to make a homogenous sample. To generate a training data set for the net, mixtures with lipid percentage of 20% (the top border of low concentration class), 40%, 60% (the top and the bottom borders of mid concentration class), and 80% (the bottom border of high concentration class) were made. Additional samples with lipid percentages of 10%, 50%, 95% were also prepared as unseen datasets for testing the performance of the

net. For more sophisticated evaluation of the net, double-layer phantoms were also prepared in which agar was used as a top layer over substrates with 50% and 95% lipid percentage. The agar overlayer was made by dissolving agar powder (Sigma Aldrich, USA) in water with a weight ratio of 2%. The mixture was then heated up and stirred well till boiling. Next, the mixture was poured into a petri dish and stored in a refrigerator at 4 ^{o}C for 30 min. After solidification, a wedge shape slice of the agar sample was cut and placed over lipid substrates to simulate 50% and 95% lipid samples with various thicknesses of a non-absorbing overlayer.

3.3.2.iii) Preparation of datasets

As we discussed before, the SVM model has 5 inputs. The inputs to the model are the PT-OCT amplitude of pixel (Amp_{PT}), the grayness level of the pixel in OCT image (GR_{pix}), the grayness level of the A-line above the pixel (GR_{line}), the distance of the pixel to the top surface of sample (D_{top}), and the distance of the pixel to the focal plane (D_{foc}). Note that these selected parameters have a relation with the received PT power on a given pixel. The output of the model was lipid percentage label as either low, mid, or high classes. A schematic of the inputs and output in the designed SVM model is illustrated in figure 41.

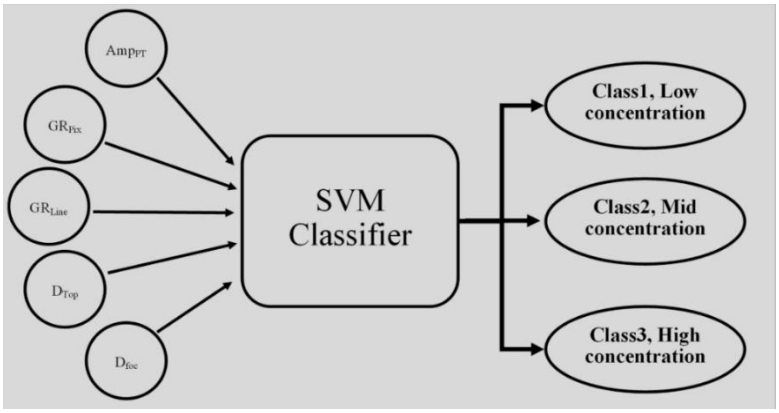

Figure 41. An illustration of the designed classifier model. The five significant inputs are extracted from the raw OCT and PT-OCT images and are sent to the SVM classifier model. The model is trained for labeling pixels in PT-OCT images into three bins, labeled with “low”, “mid” and “high” class.

The values of these parameters for each pixel were extracted from OCT and PT-OCT B-mode images by the written code in MATLAB. First, the level of focal plane in the OCT images were entered manually in the code. Then, the top edges of the sample in OCT image were detected automatically by thresholding method. Noted that there were 55 pixels per each line in average, after this masking. Therefore, the maximum depth of a pixel of the images in training was approximately equal to 190 μm. Finally, the values of all these 5 inputs for each pixel were extracted and listed in the data base. In this data base, the data of

about 27,000 pixels were collected. To train the model, 90% of these datapoints (≃24,000) were selected randomly.

The samples that were used to train the model are plotted in figure 42. Given the non-linear relation between PT-OCT signal amplitude and the concentration of MOI that was explained in Chapter 2, the differences between the high class with other classes is larger, so we anticipate the accuracy of labeling in this class to be higher.

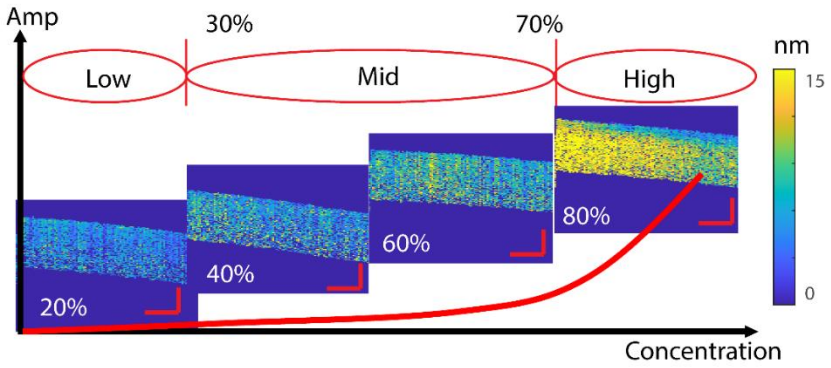

Figure 42. The PT-OCT images of the samples used for training the SVM model. In this plot, the non-linear relation between the amplitude of PT-OCT in terms of the concentration of lipid is illustrated schematically, scale bar=150 μm.

3.3.2.iv) The SVM classifier

Following the procedures discussed in Section 3.1, a SVM classifier model was designed in MATALB. To train the SVM model, 95% of the training dataset for each class was used for training and the remaining 5% was considered as outlier. The outliers were detected by calculating the distance of each datapoint with respect to the average of all datapoints. Then, by sorting the distance of these datapoints, the first 5% with the largest was labeled as the outliers. Such strategy for removing the outliers enables the model to find better support vectors in data, leading to a higher precision in sketching of boundary of classes. Polynomial kernel was used for the SVM model to allow learning of non-linear behaviors that are intrinsic to PT-OCT responses (as discussed in Section 2.2). To analyze generalization on the training dataset and to optimize the trained model, the cross-validation with the k-fold method (here, k=10) was performed on the trained model. The k-fold method is an effective validation method when dealing with relatively small training datasets. In the k-fold method, the training dataset is randomly partitioned into “k” equal sized subsets. One out of these “k” subsets is retained as the validation data for evaluating the model, and the remaining “k-1” subsets are used as training data. For k times, the cross-validation process is repeated, so that each of the k subsets exactly used one time as the validation data. These k training results can then be averaged to produce a single and optimized model. The advantage of this method over random subsampling is that we can make

sure all data points in a dataset are used for both training and validation. This enables us to train a model with a better performance in generalization.

3.3.2.v) The method for evaluation

Eventually, the ability of the model in generalization in classifying was evaluated with the unseen test dataset both qualitatively and quantitatively. The concentrations of lipid in the unseen datasets were 10, 50, and 95%. To visualize the performance of the model in prediction, the labels of ground truth images were assigned on each pixel based on their known lipid concentrations. Also, to analyze the performance of the model, the confusion matrix for each class was calculated. The calculated confusion matrix allowed us to compare the accuracy of classification in each class.

3.3.3. Results and discussion

To evaluate the training accuracy, the trained SVM model was fed with the training dataset. The OCT images and the model predictions for the training samples are plotted in figure 43. Theses samples are wedge-shaped which allows us to verify the performance of the net in classification of samples located at a continuum of distances from the focal plane. Note that to test the failing conditions and the limits of the model, the maximum sample depth considered for analysis in these images are 80 μm deeper than what was used to train the model (190 μm). As seen in figure 43, regarding the approximated range of classes (0-30 for low, 30-70 for mid, and 70-100 for high), most of pixels are labeled correctly. It is worth pointing out that in SVM models, the accuracy of classification normally degrades for data points closer to the class boundary. Therefore, we anticipate having regions with poor accuracy in classification due to closeness of the data points to the boundaries of classes. In the samples with 20, 40 and 60% of mayo, the accuracy of classifying decrease as we go deeper in the sample. A possible reason is that at the deeper locations, the PT-OCT signals becomes noisier, because the SNR and phase stability of the OCT signals deteriorates. At such depths, the amplitude of noise gets added to the amplitude of the PT-OCT signal, therefore, the model classifies these noisy pixels into the high-concentration class. As evidence, the depth of correct predictions in the 20% sample is shallower than the other samples, because the scattering of this sample in OCT images is greater than others. The wrong prediction also happens in the sample with 40 and 60% of mayo, but at the deeper levels. Additionally, in the sample with 40% of mayo, most of failure in classifying occurs in pixels closer to the top surface, because at levels close to the surface, there is no big difference between PT-OCT signal amplitude for the sample with 20% and 40%. At deeper levels, however, the difference between PT-OCT signals becomes larger due to the accumulation of PT-OCT signals, which in turn, enhances the accuracy of the model. Visually, the model has a good accuracy in the prediction of the 80% sample, because the difference in amplitude with other samples is quite large (see Fig.42) that makes the classification easier for the model. Statistically, the performance of the model on the training dataset is

evaluated by the k-fold method. For every fold, the calculated value indicates the loss (mean squared error) for validation-fold observations using the model trained on training-fold observations. The losses obtained by the k-fold cross-validated SVM model are 0.46 for the low class, 0.38 for the mid class, and 0.13 for the high class. Note that class labels in this study were the same as the predefined classes (low<30%, 30%≤mid<70%, and 70%≤high). It should also be pointed out that the original depth for training (190 μm) was used to calculate these loss values.

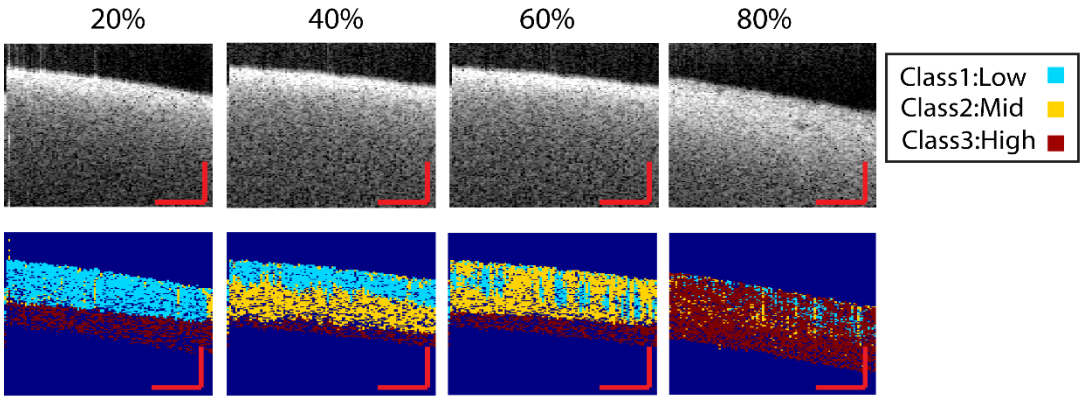

Figure 43. The OCT images and the prediction results of the trained SVM model on the training data with 20,40,60, and 80% lipid. The SVM model has a good performance in the prediction of the high class pixels, due to the non-linear behavior of the PT-OCT signal, for more details, see text. scale bar=180 μm.

To evaluate generalization of the model, the unseen test datasets from samples with 10, 50, 95% of lipid were sent to the model. The OCT and PT-OCT images of theses samples are plotted in figure 44. As seen, the PT-OCT signal changes in the sample as a function of distance from the focal plane, distance from the top surface, concentration of lipid, and the received power on each pixel.

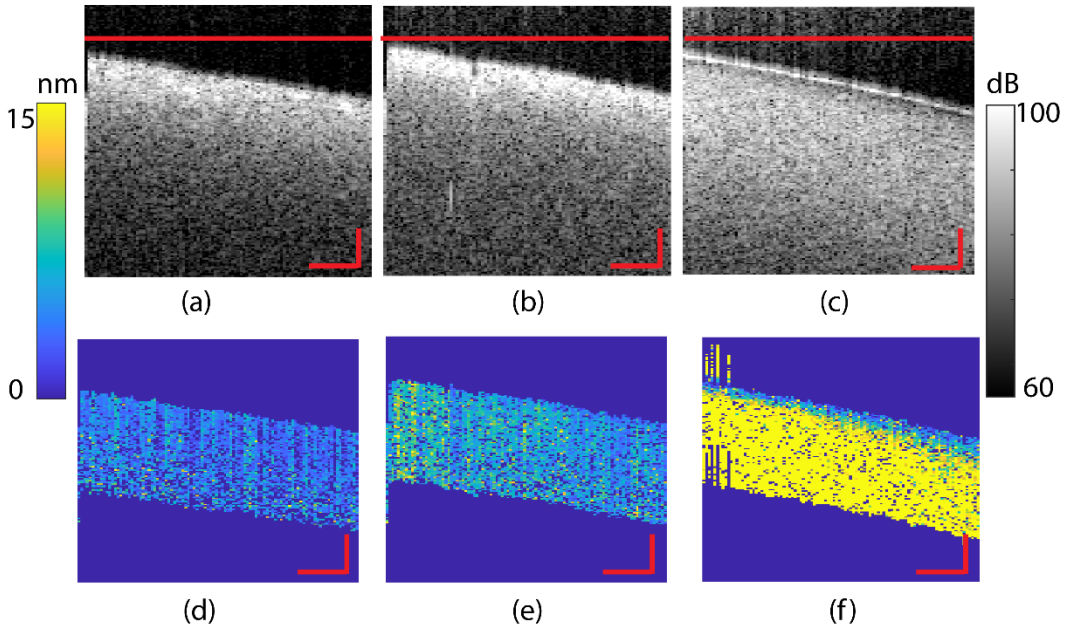

Figure 44. The OCT and PT-OCT images of the single layer data tests with a lipid concentration of (a,d)10, (b,e)50, and (c,f)95%. The red continuous line represents the location of focal plane, scale bar=180 μm.

In figure 45(a) to (c), the ground truth information (i.e., known phantom concentrations) are visualized by three different colors into three classes (low, mid, high concentration). To recall again, the approximated ranges are from 0 to 30% for the low, from 30 to 70% for the mid, and from 70 to 100% for the high classes. The classifying results of the model on the test dataset are depicted in figure 45(d) to 45(f). The color coding used to label the pixels are the same as the ground truth labels. Similarly, to survey the failing cases of the model, these plots are 80 μm deeper than the training depth. The qualitative assessment of the model classification performance can be done by comparing the prediction and the ground truth. This comparison indicates that the model correctly labeled most of the pixels. In general, the quality of classification for these unseen concentrations by the model improves related to prediction by the training cases (Fig.43). The reason is that these unseen concentrations are further away from the boundary of the SVM than the training concentrations. As seen in figure 45(d) to 45(f), at deeper surfaces, the accuracy of classification is lost due to the missing OCT signals and low SNR in such highly scattering media. Misclassifications also take place at pixels close to surface because the PT-OCT signals have not accumulated enough, leading to relatively same PT-OCT signals regardless of lipid percentage.

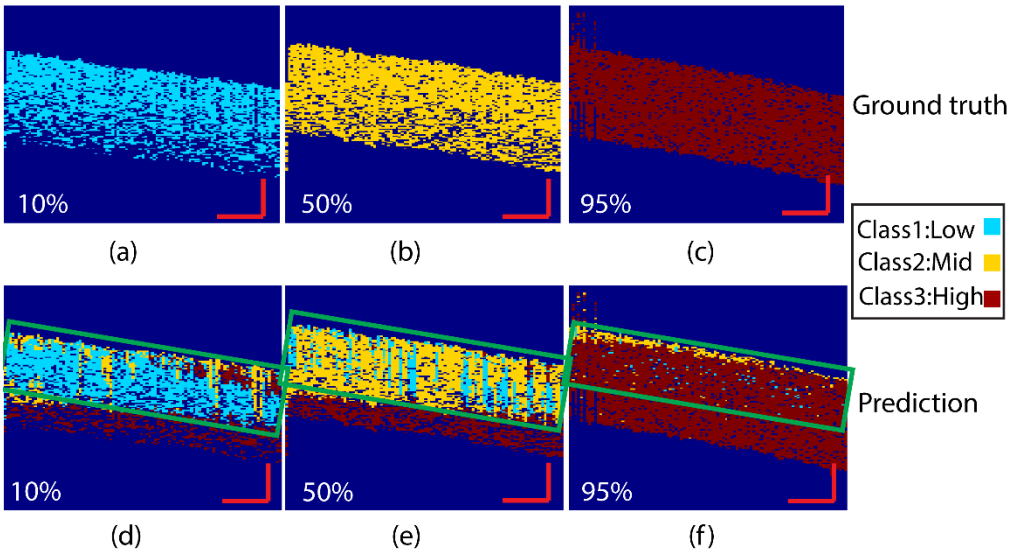

Figure 45. The ground truth of the sample with lipid concentrations of (a) 10%, (b) 50%, and (c) 95%, and the prediction results of the samples with lipid concentrations of (d) 10%, (e) 50%, and (f) 95%. The green windows are showing a region with good accuracy in the prediction. In the deeper surfaces, due to significant attenuation of signals and poor SNR, the accuracy of predictions is diminished. scale bar=180 μm.

To justify using the ML approach, we compared this approach with conventional thresholding method. In the thresholding method, the classification is done based on pixels' amplitude in the PT-OCT images. To define class boundaries based on thresholding, the distributions of pixel intensities for all samples are first plotted (Fig.46(a)). By looking at the histogram plots, the samples in the high class (e.g., 80% and 100%) can be clearly distinguished from other concentrations. Distinguishing the other classes by the histograms, however, is challenging.

To create a fair comparison between the SVM and the thresholding, first, the threshold of the most trivial class (the high class) is selected in a way that results in the same values of accuracy with the SVM. The values of classification accuracy are obtained by the confusion matrix. Note that to define all thresholds, the histogram of the training sample samples (20, 40, 60, and 80%) is used. The pixels values greater than 9nm in the PT-OCT images is recognized as the high class with thresholding. Next to define the thresholds for the other classes, the histogram of pixel amplitude is depicted in the range of 0 to 9nm (see the inset of Fig.46(a)). As seen, the distribution of pixels for the low and mid classes are not detached clearly. Therefore, to give a pixel the same change to classify in both classes, the thresholds are defined as: $0 \leq \text{low} < 4.5$ nm, $4.5 \leq \text{mid} < 9$ nm. The classification results with the thresholding method for the test sample (10, 50, and 95%) are depicted in figure 45(b). Qualitative analysis of results suggests that the performance of classifying for the high class is good. However, in the 50% and 10% samples, the classification is not accurate. As seen, there is no pattern to justify these misclassifications, therefore thresholding method leads

to a random classification. These results indicate that thresholding method in such non-linear data is not an effective method. It is also worth to point out that from mathematical point of view, in a histogram plot, if each histogram has a span of[0 to mean+2×std], they may actually be quite similar.

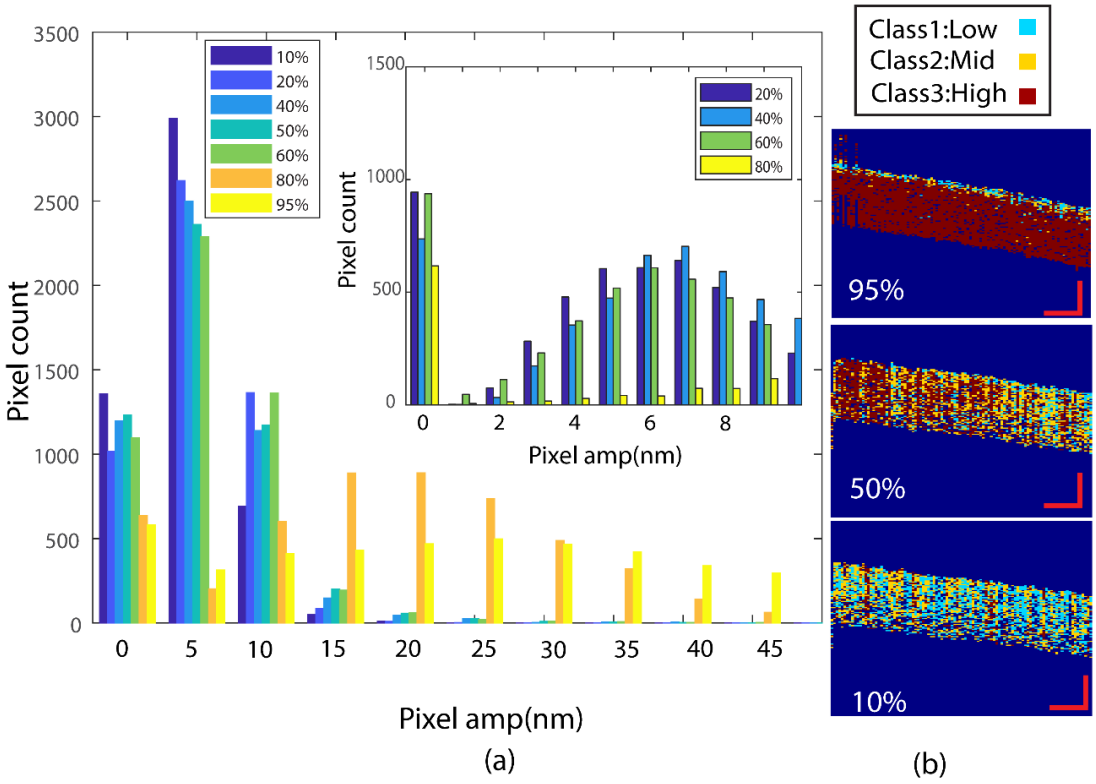

Figure 46. The results of the conventional 1-parameter thresholding method. (a) Histogram of pixel amplitude in PT-OCT images for samples with various concentrations of lipid; inset shows the histogram of the training dataset with finer intervals, (b) the results of classification with the thresholding approach for the samples with 95, 50 and 10% lipid. This classification approach offers poor accuracy, especially at mid and low classes; scale bar=150 μm.

To analyze the performance of these two approaches (SVM and thresholding) quantitatively, the confusion matrix of predictions and ground truth on the test data (the unseen data) are plotted in figure 47. These confusion matrixes for both approaches are obtained from data selected by the green window in figure 45(d) to 45(f). The accuracy in correct classification of the "high" class is approximately equal in both approaches (~91%). However, the accuracy for the "low" and the "mid" classes with the SVM method (64.4%-low class and 68.2%-mid class) are significantly greater than those of the thresholding method (43.8%-low class and 36.6%-mid class). In other words, after using the SVM approach, the accuracy of classifying in the low and the mid classes improved by 47% and 86.3%, respectively. It is worth pointing out that the accuracy of the thresholding for the mid class is only slightly better than that of an arbitrary

classifying. From the statistical point of view, the probability of correctly classifying a pixel into 3 bins is 1/3 or 33.3%.

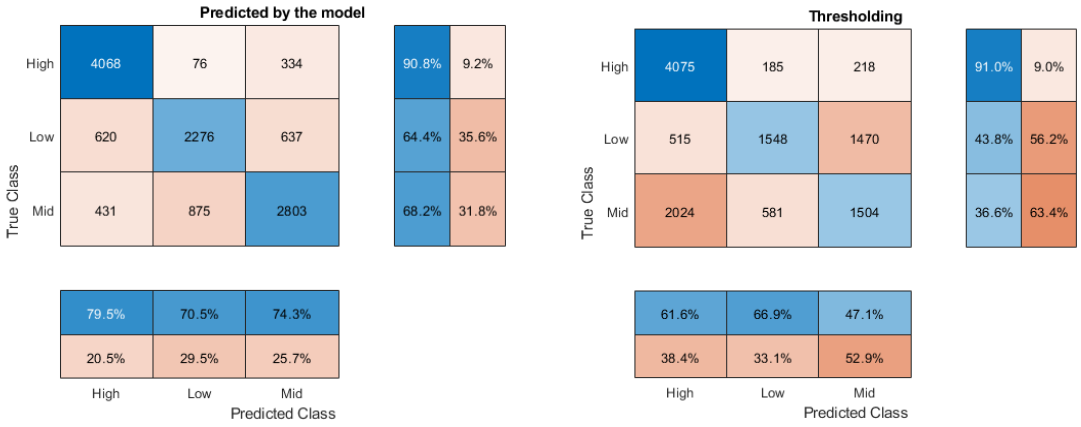

Figure 47. Comparison of the SVM model performance and the conventional thresholding. Confusion matrix results between the true and predicted classes with the SVM model (left) and the thresholding method (right). Although the performance of both method is comparable for the high-class predictions, the performance of the ML method in the other two classes is significantly better.

Next, as a sanity check, the impact of the features as the inputs on the performance of the model is studied. The goal is to learn if all inputs are necessary and if classification could be done with fewer inputs to reduce the complexity of the model to a simple thresholding problem. To do so, another SVM model was designed with only two inputs including: PT-OCT amplitude of pixels and the pixel distance to the focal plane. The reason to select these two parameters among all 5 parameters is that the range of variations in these values are greater than others, that may lead to a better classification. The training datasets and the process of training were the same with the previous SVM model. The results of classification with this 2-input SVM model are plotted in figure 48. As seen, it seems the model classifies most of the pixels into the mid concentration class. The model is almost senseless to the low concentration pixel, as all these pixels are labeled incorrectly (Fig.48(a)). Also, the performance of the model in classifying high concentration pixel (Fig.48(c)) is much inferior to that of the complete model (Fig.45(f)). This sanity check suggests that PT-OCT amplitude of pixels and the pixel distance to the focal plane alone are not sufficient for reliable classification. However, when the net is fed by the 5 inputs that were deemed influential by our theoretical works, the classification performance is improved significantly. In the end, it is worth pointing out that lots of cases can be created by combination of these 5 parameters or by adding other feature to these five features. Some of these combinations may work better; but, evaluating each of them, one by one, is outside the scope of this section.

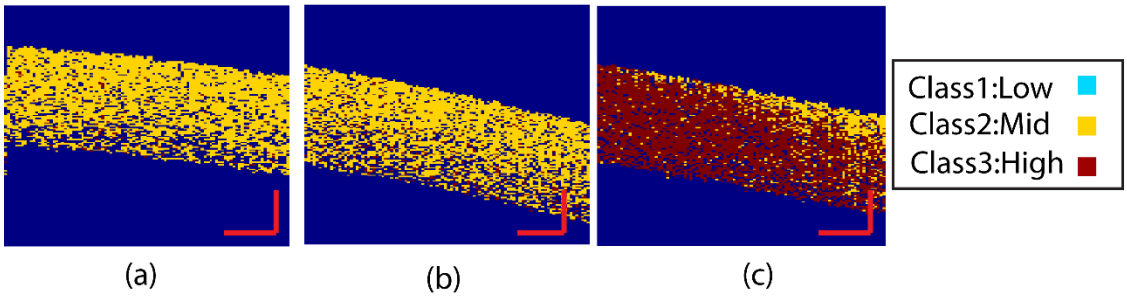

Figure 48. Results of partial ablation study. In this study, a SVM model is trained with only 2 inputs, instead of 5 inputs. The prediction results and labeling with the 2-input model for the single layer sample with a lipid concentration of (a)10, (b)50, and (c)95%. The accuracy of this model is very poor for the low-class predictions, scale bar=180 μm.

Next, to extend this study to multi-layer samples, the two-layer samples consisting of an agar top layer, and a lipid bottom layer with concentrations of 50% and 95% were imaged. The OCT and PT-OCT results are depicted in figure 49. The top layer thickness varies between 30 to 300 μm, that is the same range of fibrous cap thickness of high risk atherosclerotic plaques[29]. Note that in multi-layer samples (Fig.49(c)-49(d)), to focus on the lipid pixels, the PT-OCT signals of the agar top layer is masked, therefore, only the received PT-OCT signals from the lipid bottom layer are plotted.

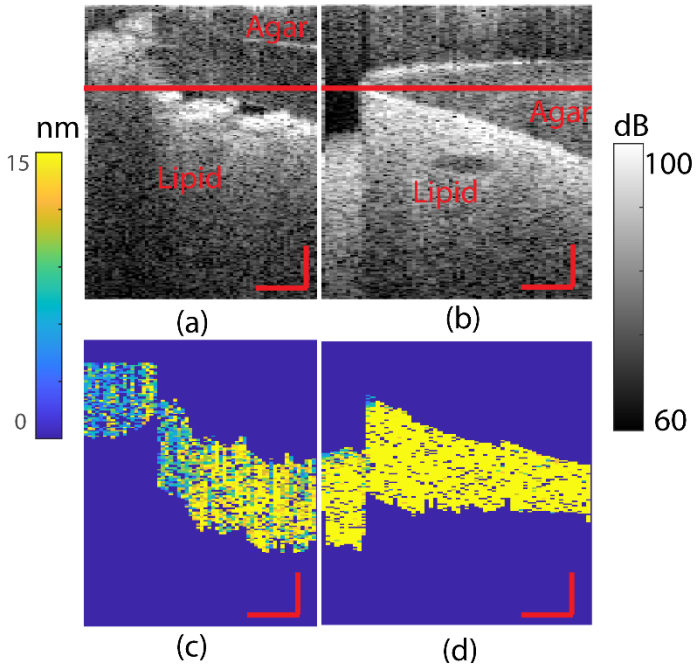

Figure 49. Extension of the SVM model to more complicated samples. The sample consists of two layers, the top layer is made up of agar, and the bottom layer is made up of lipid. The OCT and PT-OCT images of the two-layer samples with a lipid concentration of (a,c)50, (b,d)95%. The red lines in panel (a) and (b) represents the focal plane of OCT system. In the PT-OCT images, panels (c),(d), the top agar layer is masked and removed, scale bar=180 μm.

The results of classification performance for the double layer sample are plotted in figure 50. Visual assessment shows that most of pixels are classified correctly. Although the top layer has an impact on the received PT power to the bottom layer, obtained results suggest that the model is robust to the presence of the top layer by considering the depth of absorber in the sample (D_{top}), and the scattering of the A-line (Gr_{lin}). The double-layer classification result is promising because these samples simulate the structure of atherosclerotic plaques in which lipid pools are located under a fibrous cap overlayer. As discussed before, the received PT-OCT signals from two lipid plaque at different depth and with different thickness of fibrous cap do not necessarily represent their lipid concentration. To estimate and compare the concentration of lipid composition in such plaques, classifiers such as the one developed in this thesis can help in getting refined insight into the lipid percentage of plaque by decoupling the effects of sample and system influence parameters not related to the lipid content.

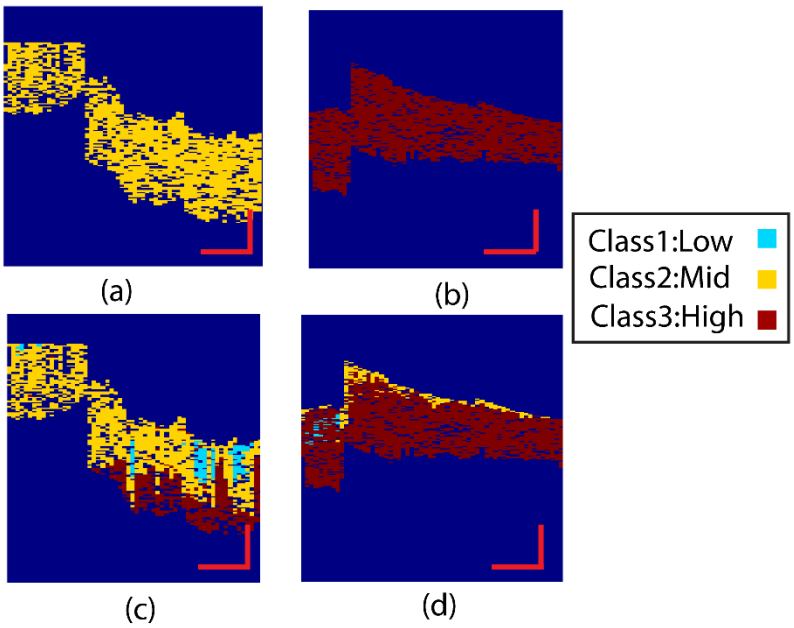

Figure 50. The results of extended study to the complex multi-layer samples. The ground truth and the prediction results with the SVM model on the sample with a lipid concentration of (a,c)50, (b,d)95%. In these images, the top agar layer is masked and removed. The performance of the model in these complex layers is reasonably good. The model can compensate the effect of the top non-absorbing layer; see text for more details; scale bar=180 μm.

To sum up, in this section, by applying a ML classifier on PT-OCT data, we try to address a common issue in PT-OCT that is quantification of MOI as a function of received signals in different conditions. PT-OCT signal depends on sample properties and the imaging condition, therefore quantification of lipid composition via classic signal processing is very challenging. To do so, we select SVM classifying approach, that can label MOIs based on their concentrations in various experimental conditions. To design

the SVM classifier, the significant variables influencing the PT-OCT signals were identified from the theoretical works presented in the previous chapter. In the training procedure, standard phantoms that covered most of imaging conditions were designed and fabricated. The preliminary results on phantoms show acceptable performance (about 70 to 90% accuracy) of the model in classification of pixels based on their lipid concentration. In addition, we get 47% and 86.3% improvement in the precision of classifying for two classes with the SVM over the basic thresholding method. A limitation of such multiclass classification is that the concentration of MOI in a pixel is discreated, therefor the exact value of the concentration of MOI in pixel cannot be found. By increasing the number of bins, the intervals of bins will become finer, but still the concentration values of pixels are not continuous. A suggestion to overcome this limitation would be using a regression model. Indeed, a regression approach is capable to provide us continuous values of MOI concentration for each pixel. However, robustness to noises and outlier datapoints in such regression model will be a challenge[148, 149]. Eventually, these encouraging results in classifying presented in this section can be considered as the first step in quantifying PT-OCT signal with a high accuracy that enable us to gain more information from tissues precisely.

4: Strategies for Increasing PT-OCT Imaging Speed

4.1.Introduction

As shown in previous chapters, PT-OCT has the promise of offering depth-resolved/3D molecular maps of tissue. One major shortcoming of PT-OCT that limits translation of this technique to the clinic, however, is PT-OCT's slow imaging rate. In conventional PT-OCT (continuous wave- CW method), several harmonic cycles of OCT phase variation (M-scan) are captured for each PT-OCT image A-line. Applying Fourier transformation on this long-acquired signal, in return, produces a frequency axis with finer resolution and enhanced SNR, enabling generation of good contrast PT-OCT images. The relatively long acquisition time needed for each M-scan intensely lowers the effective A-line rate of PT-OCT to a few Hz. Such low effective imaging speed is problematic in clinical settings as it makes PT-OCT prone to significant motion artifacts. Translation of PT-OCT to the clinic, therefore, requires technological advances that can enhance the imaging speed to at least to k Hz A-line rate range. In this chapter, we will present two strategies for increasing effective A-line rate in PT-OCT. In the first strategy, we introduce a new variant of PT-OCT which forms images using thermo-elastic response of the sample to a low-energy PT pulse. We demonstrate that this new variant can enhance the effective A-line rate of PT-OCT up to k Hz rate that enables recording of PT-OCT responses at video rate. Spectroscopic PT-OCT imaging with the new variant is also demonstrated. In the second approach, we will present a strategy that employs deep artificial neural networks to reconstruct PT-OCT signals/images with acceptable contrast and SNR from PT-OCT signals that use the conventional PT excitation but are acquired over only very few excitation cycles. This method allows us to increase imaging rate and to save fewer datapoints in the conventional PT-OCT.

4.2.Transient-mode photo-thermal optical coherence tomography (TM-PT-OCT)

The speed of imaging in PT-OCT is significantly lower than for OCT, as point-by-point establishment of the thermal-wave field and its subsequent temporal sampling is time consuming. Photo-thermal optical lock-in optical coherence microscopy (poli-OCM) has been proposed as a potential solution to increase the imaging speed[150]. In poli-OCM, the intensity of OCM reference beam is also modulated, leading to optical lock-in demodulation of the phase signal during signal integration on the detector/spectrometer. This enabled k Hz line rate photo-thermal imaging of MOIs in cells and very thin samples. Tucker-Schwartz *et al.* integrated optical lock-in detection in an OCT system (aka. poli-OCT) and reported on 3D imaging of NIR absorbing contrast agents *in vivo*[151]. While this work demonstrated an order of magnitude increase in the effective imaging line rate, from 10 Hz to 100 Hz[151], the achieved imaging speed remained insufficient for high speed *in vivo* imaging of an appreciable region of interest.

In the present section, we introduce thermal transient-mode photo-thermal optical coherence tomography (TM-PT-OCT) as a new variant of PT-OCT that significantly enhances the imaging speed without introducing any costly or complex modification to the system. While conventional PT-OCT (referred to hereafter as simply CW method) and poli-OCT methods interrogate the steady-state thermal wave fields in response to harmonically modulated PT optical excitations, TM-PT-OCT interrogates the sample's transient thermal response to excitation by a relatively short optical pulse. We demonstrate that using a pulse of ~100 µs leads to 15-fold faster effective PT-OCT line rates compared to poli-OCT at comparable SNR. Such pulses can be readily produced with low-cost and low-power laser diodes of conventional PT-OCT systems as opposed to the nanosecond/femtosecond pulses of costly pulsed lasers used in thermo-elastic optical coherence tomography (TE-OCT)[152].

In PT-OCT, absorption of PT laser light by the MOI results in creation of a local temperature field around the absorber. The induced local temperature field, in return, yields thermo-elastic expansion and alteration of the local refractive index which collectively give rise to the variation in optical path length measured by the OCT phase. As such, in PT-OCT, the temporal pattern of the measured OCT phase is directly correlated with the temporal pattern of the PT laser modulation and the thermal point spread function of the medium (aka. thermal Green's/transfer function). In conventional PT-OCT and poli-OCT, the temporal pattern of PT laser is harmonic (e.g., sinusoidal, or square wave) with all or most of energy contained in the fundamental modulation frequency, as illustrated in figure 51. In such a modulation scheme, the amplitude of the thermal response received from the MOI and the effective speed of imaging are highly dependent on the choice of modulation frequency. On the one hand, high modulation frequencies are desired in order to increase the effective imaging speed; on the other hand, the amplitude of the thermal Green's function is inversely proportional to the square root of the modulation frequency (dashed spectral line in Fig.51), resulting in significant attenuation of the PT-OCT signal at high modulation frequencies [80, 102, 153, 154]. In practice, this fundamental compromise limits the achievable effective imaging line rate of conventional PT-OCT and poli-OCT to ~10 Hz and ~100 Hz, respectively[151].

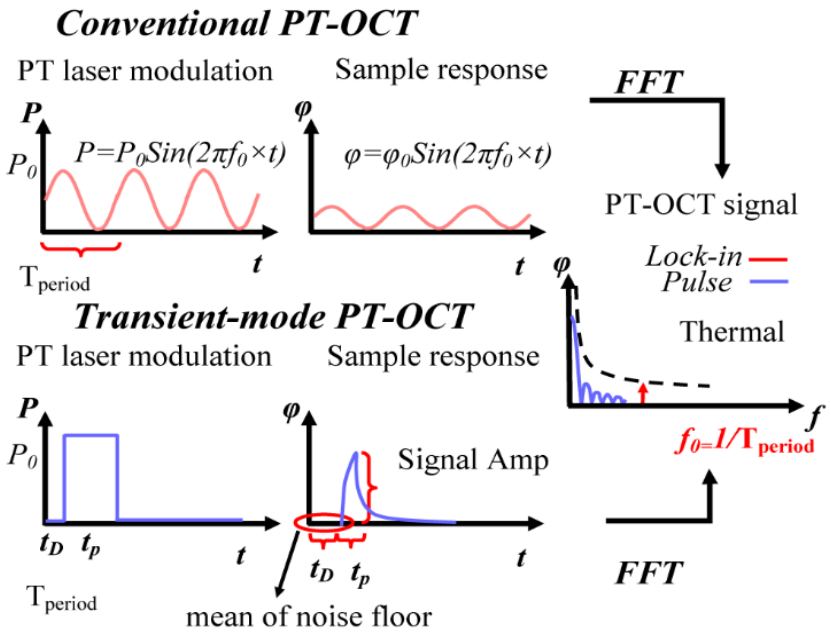

Figure 51. An illustration of excitation and sample response in time and Fourier-domains in conventional PT-OCT (CW) and TM-PT-OCT. In the CW method, the amplitude of PT laser is continuously modulated, leading to a harmonic sample response. In the TM-PT-OCT method, a low-energy squared pulse is used to excite the sample. The Fourier analysis on the received sample responses shows larger energy of the TM-PT-OCT signal compared to that of conventional Pt-OCT.

TM-PT-OCT, on the other hand, excites MOIs with a short pulse of duration t_P, figure 51. Such a short pulse contains energy mostly at low modulation frequencies. Owing to the frequency response of the thermal Green's function, these low frequency thermal waves yield pronounced transient thermal responses in a short duration which can be quantified in time-domain to enable faster acquisition of high SNR PT-OCT signatures. However, proper analysis of TM-PT-OCT responses in time-domain require compensation for instabilities in the OCT phase. For this purpose, the baseline phase is measured during an initial delay time t_D, preceding the pulse. Figure 51 also depicts the schematic of a TM-PT-OCT temporal response; upon loading ($t = t_D$), the OCT phase increases above the baseline, reaching its maximum value at $t = t_D + t_P$. Once the PT laser is turned off, the OCT phase decreases with a slower rate because of the conductive dissipation of heat. Accordingly, the following signal definition is suggested for TM-PT-OCT:

$$\boldsymbol{S_{pulse}(z) = \varphi_{time}(z, t = t_D + t_P) - \frac{1}{t_d}\int_0^{t_d} \varphi_{time}(z,t)dt.} \quad (4.1)$$

Here, $\varphi_{time}(z,t)$ is the time-lapse (aka. temporal) OCT phase signal at depth z, sampled at the OCT A-line rate.

4.2.1. Methodology

To demonstrate the efficacy of TM-PT-OCT, a series of experiments were carried out with a conventional PT-OCT setup; the details of the system can be found in Chapter 2. Briefly, the 808 nm PT laser was used with a maximum power of 5 mW on the sample. The overarching goals of the conducted experiments were to: 1) characterize the acquired transient thermal responses under different pulse conditions; 2) compare the detection sensitivity and SNR between TM-PT-OCT and CW method; 3) investigate if adherence to the proposed TM-PT-OCT method in a conventional PT-OCT setup with a given PT laser source enables high speed imaging of photo-thermal responses. Two phantoms were used in experimentation, containing PDMS as the matrix material, the absorber dye (IR806, Sigma Aldrich, USA; λmax = 806 nm), and titanium dioxide powder as scatterer. The first phantom was made by adding 300 mg of the dye and 200 mg of scatterer powder to 10 ml of PDMS (1: 10 ratio of curing agent and base); then, the mixture was well stirred, degasified, and heat-cured for 4 hours to yield a phantom with dye concentration of 30 mg/ml. In a similar manner, a second phantom was made with dye concentration of 15 mg/ml. The PDMS samples were subsequently placed on a glass slide and imaged with TM-PT-OCT and CW method. All experiments were carried out at the system's maximum A-line rate of 147.8 kHz. Standard OCT signal processing was applied to the recorded datasets to obtain M-mode OCT phase signals. For TM-PT-OCT, Eq. (4.1) was used in time-domain to construct images. For CW method, time-lapse phase datasets were zero padded and transformed to Fourier domain to determine signal intensities at the PT laser modulation frequency. Identical experiments were carried out with the PT laser turned off to emulate the response of a non-absorbing sample, and to study the noise floor. The ratio of signals in ON and OFF modes was defined as SNR and reported as average ± standard deviation of 40 replications.

4.2.2. Results and discussion

Figure 52 compares the photo-thermal responses of TM-PT-OCT and CW method obtained 100 μm below the surface of the 30 mg/ml phantom. While the acquisition time was 6.8 ms, only the first 1 ms is plotted in figure 52. For the TM-PT-OCT experiment, panel (a), a 133 μs pulse consisting of a 33 μs delay time, t_D, and a 100 μs pulse duration, t_P, was used; the PT laser was off during the remainder of the acquisition time of 6.8 ms – 133 μs. Accordingly, CW experiments (panels b-d) were conducted at a PT laser modulation period of 133 μs (i.e., f = 7.5 kHz); the PT laser was on for durations corresponding to 1, 2, and 25 complete modulation cycles and then off for the remainder of the 6.8 ms recording period. In the TM-PT-OCT response of panel (a), the OCT phase is reflecting the extent of measured system noise floor during the initial delay time ($0<t<33$ μs) and the maximum measured OCT phase at $t = t_D + t_P = 133$ μs for both laser ON and OFF cases. Panel (b) depicts the frequency-domain response of CW method carried out at identical laser on-time to that of panel (a). Comparing panels (a) and (b) demonstrates that at a fixed OCT

line rate and fixed maximum PT laser power, the transient thermal response of TM-PT-OCT yields more than 9 dB enhancement in the SNR. This significant enhancement in SNR is due to that fact that pulse excitation results in creation of a collection of low-frequency thermal waves that are minimally damped; thus, leading to sizable changes in OPL and OCT phase. Panel (c) depicts the response in CW method to two modulation cycles of PT laser (266 μs; i.e., twice the duration of panel (a)). While here the PT laser energy exposure is even slightly more than that of TM-PT-OCT experiment ($\frac{5\ mW}{2} \times 266\ \mu s > 5\ mW \times 100\ \mu s$), the SNR remains far inferior (1.44±0.53 < 10.47±1.56). In fact, panel (d) demonstrates that the high SNR of TM-PT-OCT is marginally matched by CW method (9.08±1.91 vs 10.47±1.56) only when the effective line rate is significantly reduced to record 25 times longer steady state PT responses, exposing the sample to ~12.5 times more PT laser energy than TM-PT-OCT.

In these experiments, the sample was excited with only one pulse of excitation for each acquired A-line, and a sufficient settling time was considered to allow the induced heat to dissipate. In cases where multiple pulses are used and averaged for acquisition of an A-line, inter-pulse duration needs to be considered to avoid unwanted effects of sample bulk heating on the received signals. Insufficient inter-pulse duration impedes complete dissipation of the generated heat, leading to gradual increase of bulk temperature which, in return, changes the refractive index of medium non-linearly. It should be pointed out that this effect is not a fundamental barrier for enhancing the imaging speed, because the galvo-mirrors can be set to scan the sample in a random (or zigzag) pattern to avoid issues caused by incomplete dissipation of heat.

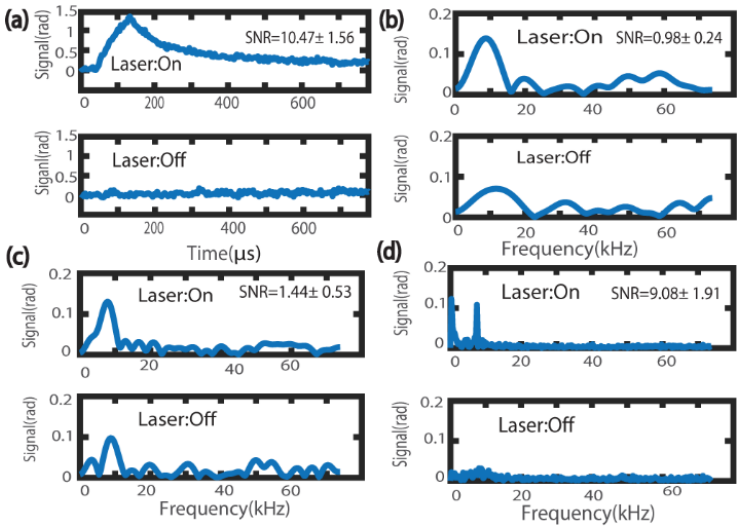

Figure 52. Pixel-wise comparison between SNR of the TM-PT-OC method and the CW method, at the same data acquisition time (a vs b), same exposed energy to sample (a vs c), and same obtained SNR (a vs d). The TM-PT-OCT signal 100μm below sample surface (a) using a 133μs PT pulse. CW (Conventional PT-OCT) signals at cycle period of 133μs (7.5 kHz) and recording durations of (b) 1, (c) 2 and (d) 25 cycles. Results shows that to get the same SNR with the CW method under the same power of illumination, we need to increase acquisition time by 25 times.

Having established the intrinsic SNR advantages of TM-PT-OCT, the next set of experiments was aimed at understanding the effect of pulse and modulated PT laser parameters on detectability of MOI. Figure 53(a) depicts TM-PT-OCT phantoms responses to pulses with a 33 μs delay time, and durations of 100, 200, and 400 μs at various laser power levels. TM-PT-OCT with a 100 μs pulse can reliably discern the 15 mg/ml phantom from the 30 mg/ml one at power levels over 2 mW. The plots also suggest that detection sensitivity (i.e., slope of lines) can be enhanced by increasing the pulse duration. A similar signal level is obtained from pulses delivering the same energy to the sample (e.g., 30 mg/ml phantom: 100 μs and 4 mW vs. 400 μs and 1 mW). That is, in TM-PT-OCT, the maximum permissible PT laser power can be used with a short pulse duration to enable significant increase in the effective A-line rate (100 μs and 5 mW for our case). Figure 53(b) depicts the CW method responses of the 30 mg/ml sample obtained at cycle period of 133 μs (i.e., 7.5 kHz). When one cycle of excitation is used to match the A-line rate to that of TM-PT-OCT, increasing the laser power (even to 5 mW) won't result in differentiation of absorber from the baseline noise. However, reliable detection of absorber is possible with CW method through averaging of more excitation cycles (Fig.53(b)), albeit at the cost of dramatic decrease in effective A-line rate. Results depicted in figures 53(a) and 53(b) suggest that on average TM-PT-OCT offers more than 3-fold improvement in SNR compared to the CW experiments carried out at identical effective A-line rate.

Given the significance of averaging in CW method, next set of experiments was aimed at investigating if at a given effective A-line rate, increasing the number of cycles (i.e., increasing the modulation frequency) can yield any improvement in performance of CW method. These experiments were carried out at 500 μs effective A-line period to enable studying the effect of a larger range of number of cycles (1-16 cycles corresponding to modulation frequencies of 2-32 kHz). To match the delivered energy, PT laser power of the TM-PT-OCT pulse (470 μs pulse duration+30 μs delay) and CW waveform were set to 2.5 mW and 5 mW, respectively. Results plotted in figure 53(c) demonstrate that in CW method as the number of cycle increases, the contrast between ON and OFF modes deteriorates. The reason for this observation is the characteristic behavior of thermal Green's function (Fig.51) which results in significant attenuation of thermal responses with increase in modulation frequency. The superior contrast offered by TM-PT-OCT between ON and OFF modes is clearly recognized in figure 53(c).

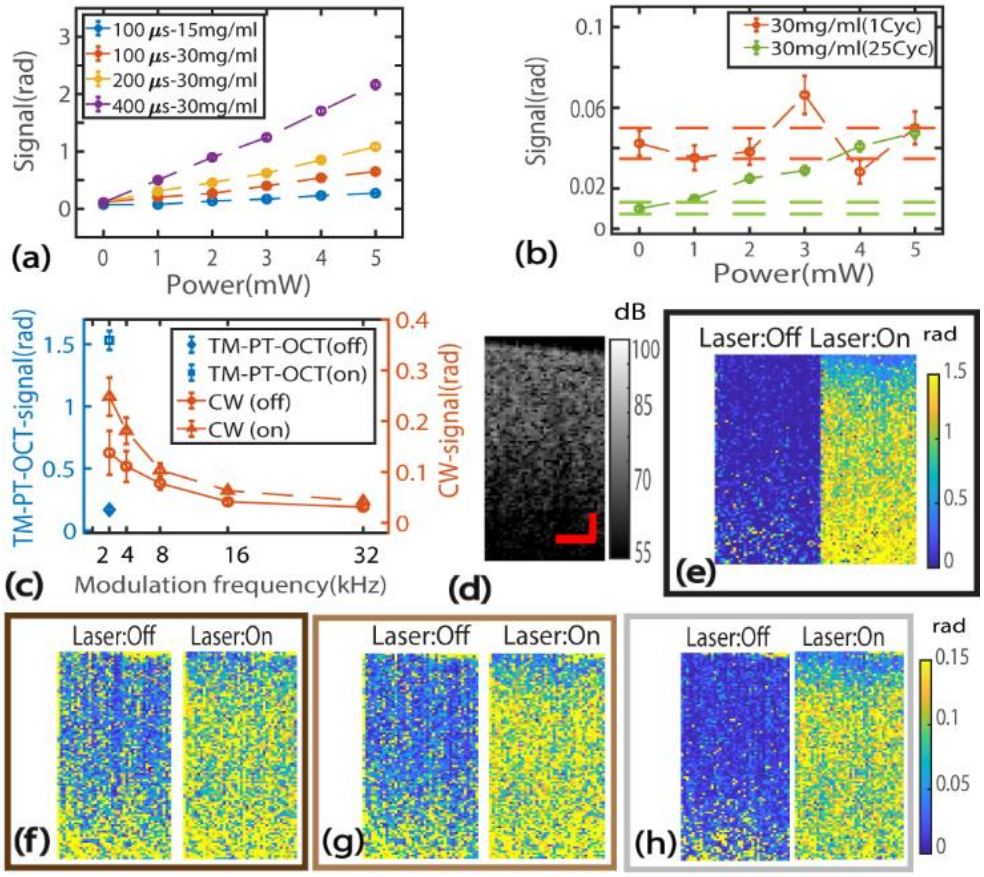

Figure 53. Results of image-wise comparison between the TM-PT-OCT method and the CW method. (a) TM-PT-OCT and (b) CW (conventional PT-OCT) signals obtained at various laser powers and excitation durations. (c) CW signals at various modulation frequencies at a recording duration matched to TM-PT-OCT (pulse method). (d)OCT and (e) TM-PT-OCT B-mode images of 30 mg/ml phantom with a 133μs pulse. CW images at cycle period of 133μs (7.5 kHz) and recording durations of (f) 1, (g) 2 and (h) 25 cycles. Results demonstrate the ability of TM-PT-OCT method in providing good contrast and SNR in much shorter time, scale bars= 50 μm.

Having characterized the effect of modulation parameters in the two methods, the next experiment aimed to compare the quality of B-mode images produced with the 30 mg/ml phantom. TM-PT-OCT and CW experiments were carried out with same condition as those used in experiments of figure 52. Panels (d) and (e) in figure 53 show OCT B-mode and TM-PT-OCT images, respectively. Comparison of figure 53(e) with figures 53(f)-53(h) demonstrate the enhanced ability of TM-PT-OCT to create sharp contrast between PT laser excitation and no excitation cases (or absorbing vs non-absorbing samples) compared to the CW at a similar effective line rate (panels e vs f), similar PT laser exposure (panels e vs g), or even when the steady state PT responses were recorded 25 times longer (panels e vs h). To evaluate B-mode images in figure 53(e) to 53(h), the histograms of these images are plotted in figure 54. Comparison of histograms of the signals confirms the ability of TM-PT-OCT in better differentiation of PT responses from noise floor/non-absorber (Fig.54). As seen, in figure 54(a) that is related to the TM-PT-OCT results, the

distribution of pixels in the PT off and on modes are distinguishable. However, in figure 54(b) and figure 54(c) that are related to conventional method with the same duration and same energy, the distributions of pixels in PT laser state are not discernible. Histogram in figure 54(d) that comes from the conventional method with 25 times longer acquisition time than the pulse method, shows the pixel distributions in the PT laser modes is separable.

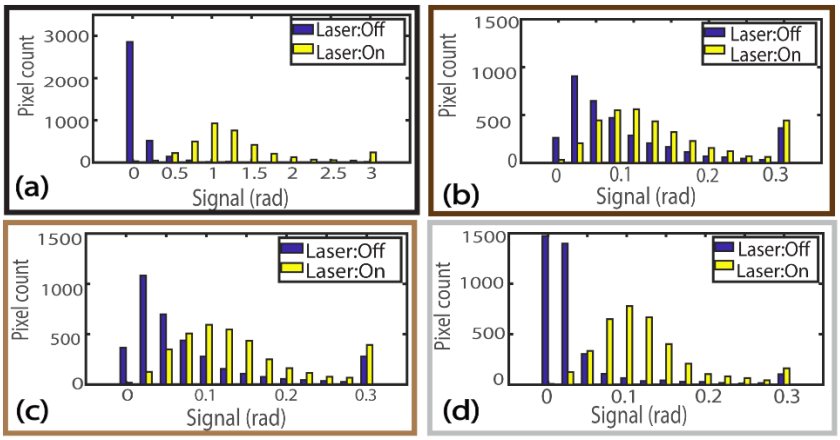

Figure 54. Histogram of PT-OCT B-mode images in Figure.53. with (a) TM-PT-OCT with a 133µs pulse, and CW (conventional PT-OCT) at cycle period of 133µs (7.5 kHz) and recording durations of (b) 1, (c) 2 and (d) 25 cycles The distribution of pixel intensities in this histogram can be separated clearly with the results from the TM-PT-OCT method and the CW method with 25 cycles. It shows that with the CW method, the acquisition time needs to be increased 25 times longer related to the period of the TM-PT-OCT method to get enough contrast in images.

The final study was focused on high-speed imaging of MOIs. Here the 30 mg/ml phantom was submerged in a mixture of ultrasound gel (>95 % water) and titanium dioxide powder, placed on an automatic translation stage, and imaged across a 400 µm-wide window while translating through the system field of view at a speed of 100 µm/s. At each spatial location, OCT signals were recorded for 666 µs. The PT laser was on during the first 333 µs and off during the second half to allow for dissipation of induced heat. During the 333 µs laser on-time, the TM-PT-OCT experiment involved a 33 µs delay time t_D and a 300 µs pulse duration t_P. Accordingly, CW experiments involved sinusoidal modulation of the PT laser with modulation period of 333 µs (i.e., f = 3 kHz). This experiment protocol allowed us to image the photo-thermal responses of the moving sample at an effective PT-OCT line rate of ~1.5 kHz. Figure 55 depicts representative snapshots of high-speed imaging of photo-thermal responses of a moving sample with TM-PT-OCT and CW method. The OCT B-mode image of panel (a) confirms the comparable scattering and attenuation properties of absorbing and non-absorbing regions. Absorbing region is the 30 mg/ml phantom, while non-absorbing region is made of scatterer powder (TiO) in the water-based gel medium without any absorbing chromophore. In the CW snapshot of panel (b), these regions cannot be differentiated because the signal from the absorbing region at this high line rate is dominated by noise; however, when TM-PT-

OCT is incorporated at identical line rate, significant improvement in signal SNR can be realized, leading to reliable differentiation of absorbing from non-absorbing areas. It should be noted we could record a video from the a moving sample with TM-PT-OCT method, that can be found in the supplementary files of our published paper[155]. To the best of our knowledge, visualization recorded with TM-PT-OCT is the first demonstration of high-speed imaging of photo-thermal responses of an appreciable window size with PT-OCT. A few frames of this video are depicted in figure 56. Frames from the recorded video depict high-speed imaging videos of the moving sample with CW method and TM-PT-OCT at 1.5 kHz effective line rate; while frame of CW method fails to distinguish the absorber, frames grabbed with TM-PT-OCT clearly demonstrate the ability of performing reliable high-speed imaging of photo-thermal responses.

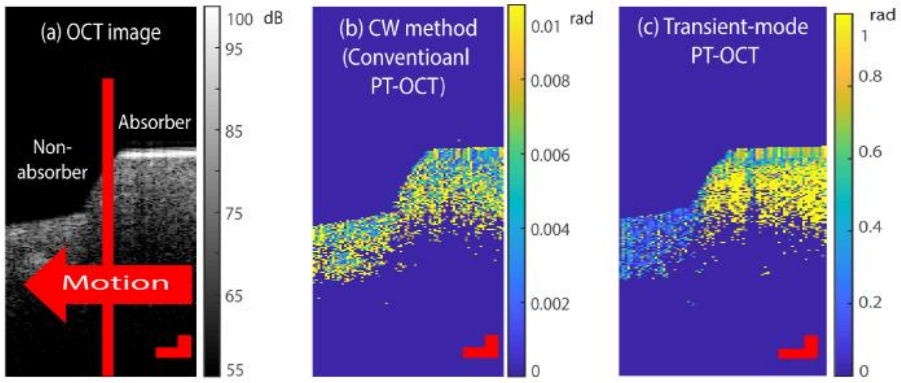

Figure 55. The results of capturing a video from a moving sample contains an absorbing region and a non-absorbing region. (a) OCT B-mode image of a moving phantom. Corresponding PT-OCT images using (b) CW and (c) pulse methods. With the OCT and conventional PT-OCT methods the two regions are not discernable, however, with TM-PT-OCT we can distinguish the two regions clearly, scale bars= 50 μm.

In summary, this section proposes a new variant of photo-thermal optical coherence tomography (PT-OCT), named transient-mode PT-OCT (TM-PT-OCT), which forms images based on the transient thermal response of absorbers to pulsed laser excitation from conventional laser diodes. Due to the relatively short duration of the excitation pulses, the effective PT-OCT imaging line rate can be drastically improved to the kHz range, which is over one and two orders of magnitude faster than the current state-of-the-art in photo-thermal optical lock-in OCT and CW method, respectively. Our comparative results at fixed acquisition duration (or fixed exposure to PT laser) demonstrate superiority of TM-PT-OCT over conventional PT-OCT in terms of SNR and produced contrast between absorbing and non-absorbing samples. This section also demonstrates the possibility of resolving the PT responses of a moving sample at video rate. The significantly improved imaging speed of TM-PT-OCT can open the door for downstream integration of TM-PT-OCT in clinical systems for *in-vivo* imaging.

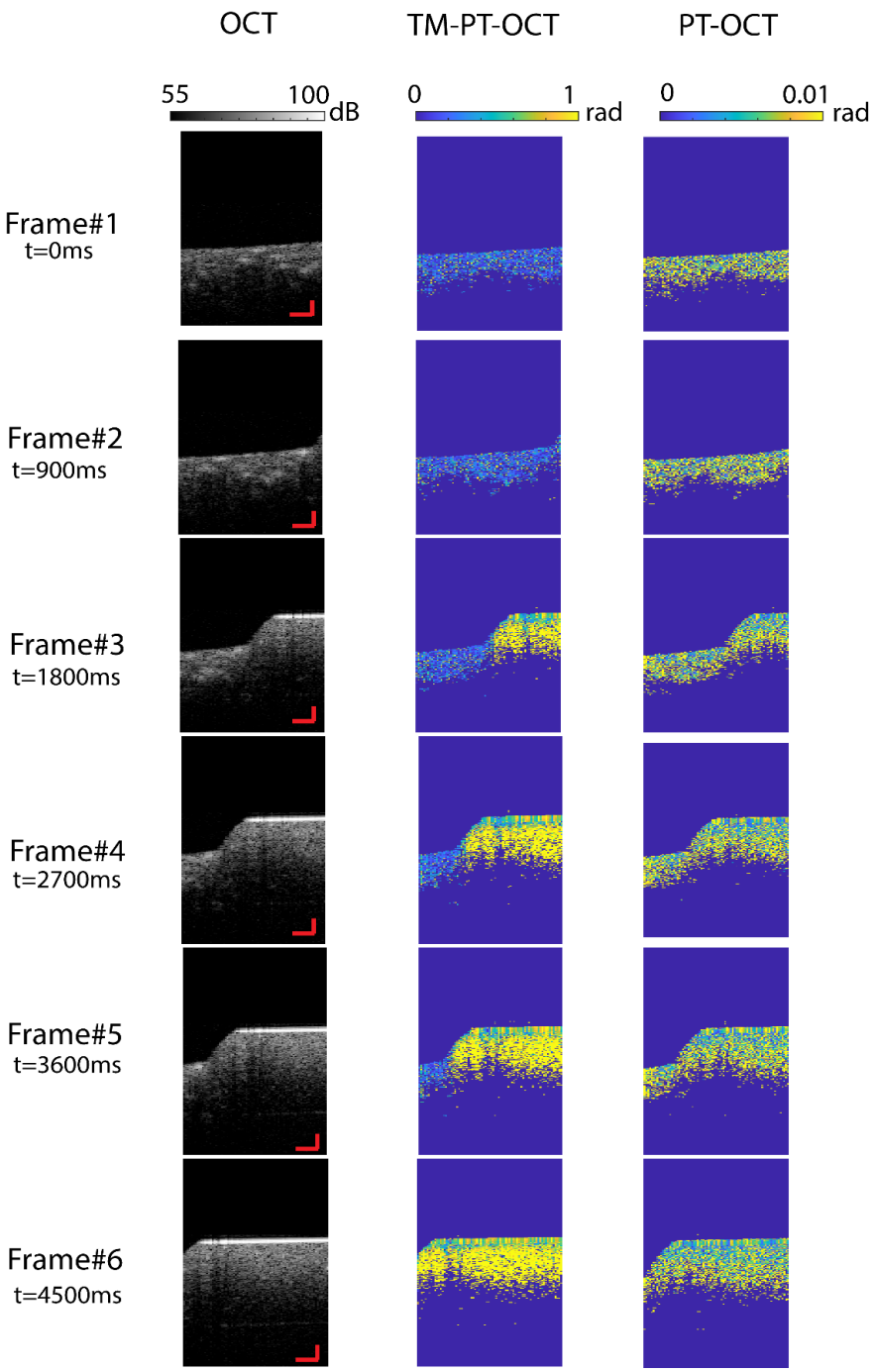

Figure 56. Frames of recorded video from the moving sample with OCT (left), TM-PT-OCT (middle) and the conventional PT-OCT (right) methods. These frames of the recorded video clearly demonstrate that while OCT and PT-OCT method cannot provide enough contrast, the two different regions in the sample can be detected by TM-PT-OCT method scale bars= 100 μm.

4.3. Spectroscopic TM-PT-OCT

The enhancement of speed offered by TM-PT-OCT also enables utilization of multiple PT lasers to perform spectroscopic PT-OCT. For example, 1210 nm and 1040 nm excitations can be used for detection of lipid and collagen, respectively, as the key constituents of atherosclerotic plaques (Fig.27). The experimental system used in this study is a dual-wavelength spectral-domain PT-OCT system including 1040 nm and 1210 nm PT lasers. To show the ability of the system to perform video rate PT-OCT, OCT A-line rate was increased to 147 kHz. Laser pulses had t_D and t_P of 300 μs and 700 μs, respectively.

Lipid and collagen samples were used to demonstrate feasibility. Mayonnaise (Kraft) was used as the main source of lipid (>80%)[82] and samples with desired lipid concentration were produced by mixing mayo with water-based ultrasound gel (water>95%). The collagen sample was obtained from chicken cartilage[127]. A fresh chicken leg was cut from the knee joint, and tendons above the cartilage were removed, then the sample was washed with PBS serum. The tissue was placed on a glass slide at room temperature to image with the system. For spectroscopy approach, the absorption spectrum of samples in NIR range (900-1700 nm) was measured with a handheld spectrometer (Texas instrument, USA).

4.3.1.i) Results and discussion

The preliminary results of spectroscopic transient-mode PT-OCT for detection and differentiation of collagen and lipid are shown in figure 57. Comparison of lipid 1040 nm TM-PT-OCT image (Fig.57(c)) with the baseline image (i.e., PT laser off; Fig.57(b)), confirms absence of PT-OCT signals from lipid at 1040 nm (as expected from spectra in Fig.27). At 1210 nm (Fig.57(d)), on the other hand, strong TM-PT-OCT signals are registered from lipid. In the case of collagen, moderate TM-PT-OCT signals are observed for both 1040 nm and 1210 nm compared to the base-line image (Figs.57(g)-57(h) vs Fig.57(f)). Results of figure 57 demonstrate the ability of TM-PT-OCT in registering the characteristic absorption spectral responses of lipid and collagen at video rate. Also, the spectra obtained from the handheld spectrometer from lipid and collagen sample (Fig.57(k),57(l)) confirm the similarity of the characteristic responses measured by the developed system from the samples. Eventually, to give a better sense the difference in the signal's strength of lipid and collagen, results with the PT laser at 1210 nm (Figs.57(i), 57(j)) is plotted with broader color bar. As seen in figure 57(i),57(j) the signal from lipid is much stronger than collagen, because of greater absorption coefficient of lipid at 1210 nm, and higher thermal resistance properties.

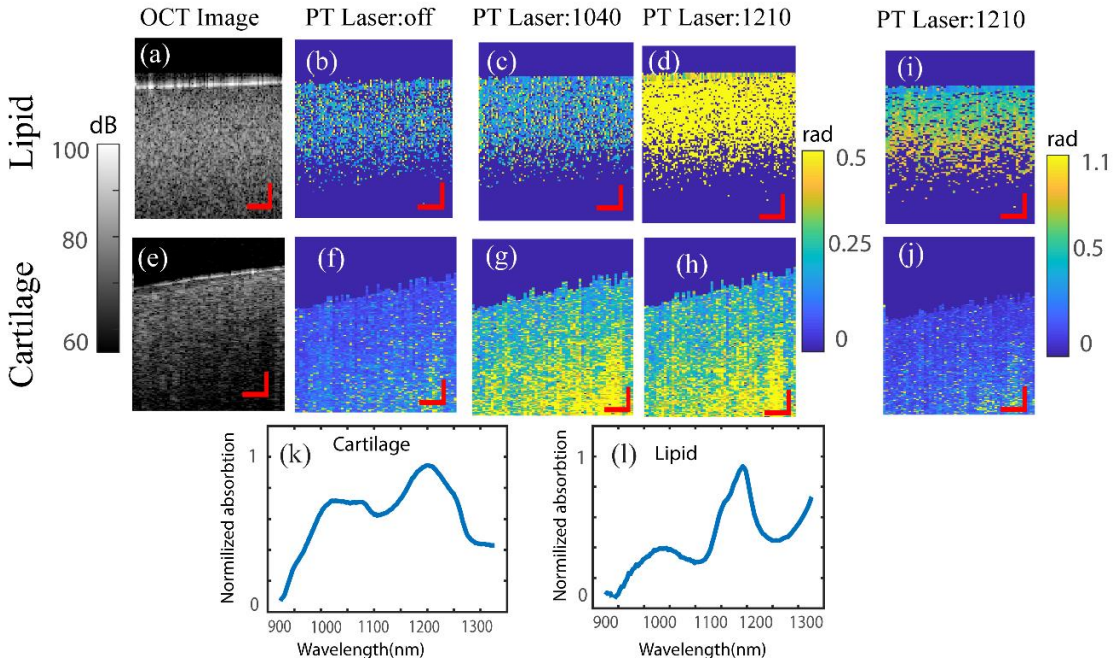

Figure 57. Results of spectroscopic TM-PT-OCT on different materials using two PT wavelengths. (a) OCT image and (b-d) PT-OCT images of lipid, and (e) OCT image and (f-h) PT-OCT images of collagen samples. Measured absorption spectra of (k) lipid (l) collagen. To show significant difference in absorption of 1210nm light by lipid and collagen, panels (d) and (h) are shown in panels(i) and (j) using a colormap with a larger upper limit. The acquired signals with the spectroscopic TM-PT-OCT show great consistency with the measured spectra of the samples; scale bars=50 μm.

To capture videos, two different concentrations of mayo (100% and 10%) separated by a thin glass wall were imaged while translating the sample through the 300 μm-wide field of view at a speed of 100 μm/s (Fig.58(a)). Conventional PT-OCT was performed at 1 kHz, corresponding to the period of TM-PT-OCT (i.e., 300 μs+700 μs). Representative frames of video-rate TM-PT-OCT are depicted in figure 58. The OCT image of figure 58(b) suggest that OCT alone cannot differentiate between the high and the low concentrations of lipid. Conventional PT-OCT at video rate (Figs.58(c)-58(d)) is also incapable of differentiating between lipid concentrations as PT-OCT signal levels are insignificant at such high imaging speed. However, when the moving sample is imaged with TM-PT-OCT at identical speed (Figs.58(e)-58(f)), pronounced PT-OCT signals can be measured which enables reliable differentiation of lipid concentrations. As seen in figure 58(e), in the case that the sample is illuminated by the PT laser at 1210 nm, the PT-OCT signals from the sample are received. The stronger PT-OCT signal comes from the part of region with higher concertation of the lipid. However, when this sample is excited by the PT laser at 1040 nm (Fig.58(f)), no notable PT-OCT signal is generated. The acquired signals with this spectroscopic method with TM-PT-OCT corresponds with the absorption spectrum of lipid. Additionally, it is shown that the amplitude of received signal with TM-PT-OCT has a relation with the concentration of MOI in the

sample that can be used for quantifying as well. Comparison of the upper limits of color maps in figures 58(c) and 58(e) is also indicative of the enhanced SNR of PT-OCT signals in the transient-mode.

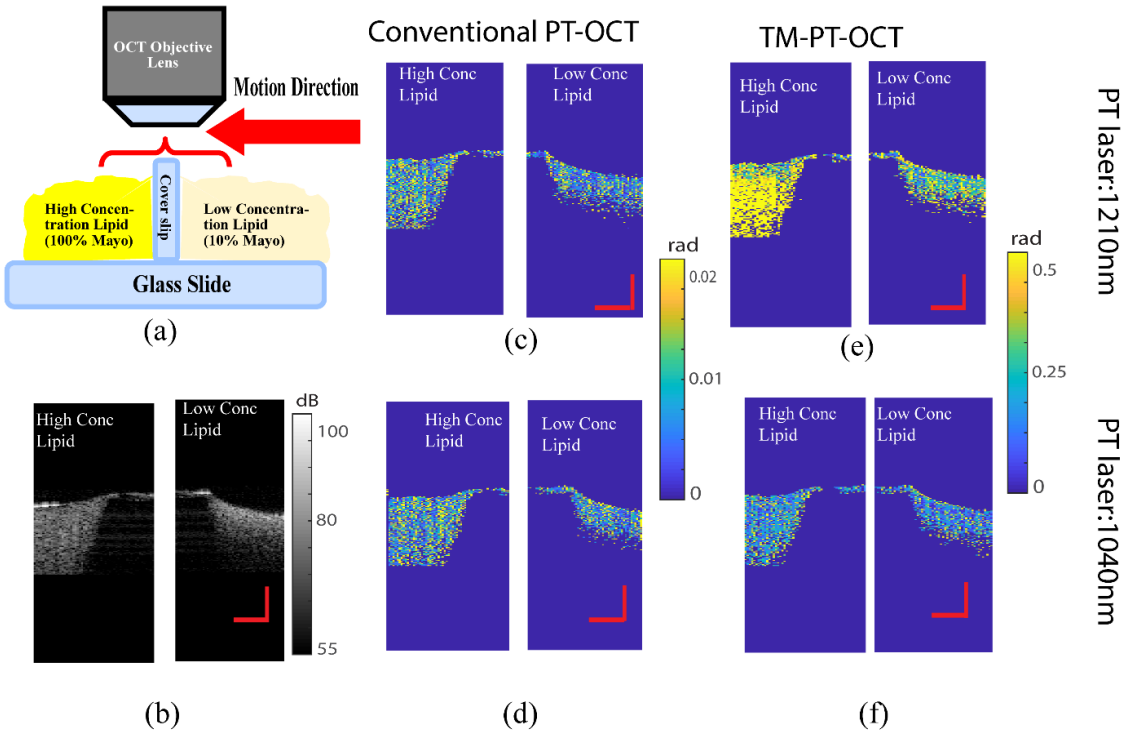

Figure 58. The results of recording videos from the moving sample with the spectroscopic TM-PT-OCT method. (a) Illustration of the experiment with a moving sample containing high (left) and low (right) lipid concentration regions. Representative (b) OCT image; (c-d) transient-mode PT-OCT images; and (e-f) conventional PT-OCT images. While OCT and conventional PT-OCT cannot distinguish the two chemically distinct regions of the sample, the results of TM-PT-OCT method can separate them. scale bars=100 μm.

In summary, in this section we demonstrate the performance spectroscopic TM-PT-OCT. The spectroscopic method helps us to increase specificity in detection of MOI in tissues. As an application of this system, lipid, the main material in coronary plaques, is detected in a captured video. Developed innovation is expected to pave the way to translation of PT-OCT systems to clinics. Specifically, this technology can open the door for live structural imaging co-registered with chemical information of coronary arteries *in vivo*, that is highly desirable in risk assessment of vulnerability of plaque. As a suggestion, AI-powered routines can be employed for analysis of spectral TM-PT-OCT images for automated detection, segmentation and characterization of lipid and collagen.

4.4.Improvement in SNR and imaging rate of PT-OCT using deep neural networks

As discussed before, the slow effective A-line rate of conventional PT-OCT holds back translation of this technology to the clinic. In conventional PT-OCT, lock-in demodulation is normally used to suppress the background noise and to improve the detection limit. That is, the intensity of PT excitation is modulated at a specific frequency, enabling demodulation of photothermal responses via quadrature/lock-in demodulation of OCT phase at the known frequency. To enhance detectability, the photothermal responses from each point are acquired for many cycles to suppress noise via averaging. The necessity of acquiring lengthy M-mode datasets fundamentally limits the imaging rate of conventional PT-OCT. To address this limitation, few solutions have been suggested so far (as discussed in Section 4.2). These solutions all require modifications to instrumentation and/or modulation scheme of PT laser. Another strategy to increase effective imaging rate is to use artificial intelligence (AI) models. In this approach, the information required for forming PT-OCT images are predicted from rapidly captured and low SNR signals via trained AI models (aka. denoising models). For example, in the field of atomic force microscopy (AFM), encouraging results were presented by Borodinov *et al.* on improvement of the detection limit of AFM images using deep learning models[156]. In the field of OCT, by employing various AI models, structural OCT images were reconstructed form noisy and unclear images[136, 157, 158]. In recent years, promising results have been presented using deep learning models in the field of OCT as well. Hao *et al.* demonstrated reconstruction of OCT images of retina from low bit-depth signals with deep learning models[159]. Additionally, several deep models have been suggested to analyze and to segment the retina layers[160]. Deep learning is also employed in functional extensions of OCT for various purposes. In OCE, Neidhardt *et al.* applied a deep model on images to quantify the mechanical elasticity of samples[161]. Kim *et al.* reported an improvement in the imaging rate in OCT-A using deep models[162].

In this section, we employ deep net models to reconstruct PT-OCT images from noisy but fast-captured conventional PT-OCT datasets. Using this net, we can improve the SNR of the system, without any hardware modification to the conventional PT-OCT system. Another added value of this approach is significant reduction in the volume of acquired data which is highly desirable for clinical devices. The performance of the trained net is verified with standard phantoms, biological tissues containing lipid, and calcified human aorta samples. To the best of our knowledge, this is the first report of utilizing deep learning in the field of PT-OCT.

4.5.Deep learning strategy for PT-OCT image reconstruction

In conventional PT-OCT, to improve the SNR and decrease the noise floor, the lock-in method is used[68]. To recall the lock-in quickly, in the scanning plane (Fig.59(a)), OCT images are captured over time (Fig.59(b)) which is called M-scanning. By calculating the OCT phase as a function of time for each

pixel, the amplitude of phase modulations due to absorption of the modulated PT laser is obtained (Fig.59(c)).

In lock-in method, according the Parseval's theorem, to increase the SNR, longer signals need to be captured. In a long-captured signal, SNR improves because of averaging of more cycles of signal. The illustrations of figure (59) show that the FFT spectrum of signal that is acquired for a longer time "L_2" leads to higher SNR (Fig.59(d)) than that of a shorter time "L_1" signal (Fig.59(e)). Correspondingly, the formed PT-OCT image from the longer signal (Fig.59(f)) shows more details and provides better contrast in comparison to that obtained from the shorter signal (Fig.59(g)).

In this study, the idea is using a deep net model to convert a fast-captured image with poor SNR (Fig.59(g)) to a slow-captured image with high SNR (Fig.59(f)). The assumption is that the net can learn additional features of the PT-OCT signal such as the transient signal (discussed in Section 4.2) that are ignored in the conventional lock-in method. To test this idea, we design a deep net with a pixel-wise approach. This net uses time sequence datapoints for each pixel (e.g., L_1 in Fig.59(c)) as the input to predict the pixel value of a reference image (e.g., Fig.59(f)) as the ground truth that is formed from long-captured signals (e.g., L_2 in Fig.59(c)). The trained neural network can potentially improve the SNR and contrast of a fast-captured image in PT-OCT using the *a priori* information it captures during the training process. Another promising aspect of this deep net is that it can enable formation of PT-OCT images with fewer data points that leads to lighter computation and smaller volume of storage for saving and loading data.

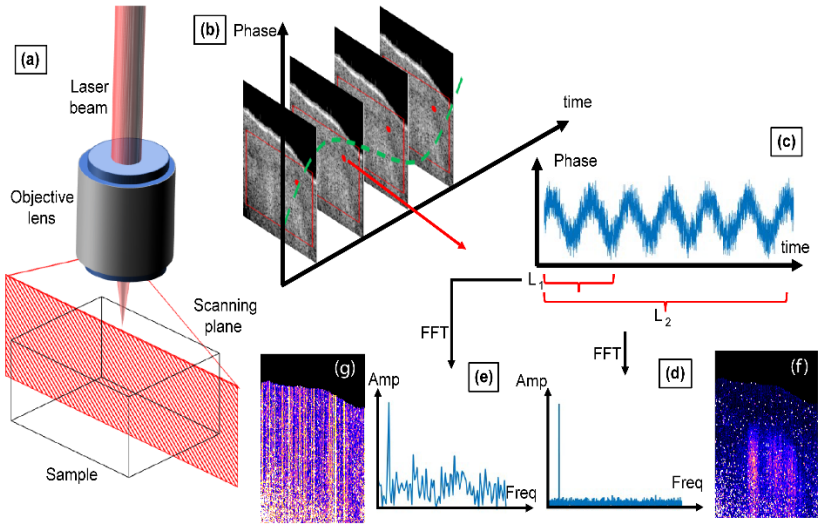

Figure 59. A schematic of PT-OCT beam and the scanning plane in the sample, (b) capturing the scanning plane data over time, the harmonic modulation of the red points as a results of amplitude modulation of PT laser beam is selected, and (c) is plotted in terms of time. Applying FFT on two different lengths of signals results is (d) a spectrum with low detection limit, (e) and a spectrum with high detection limit. Doing lock-in on the spectra forms (f) PT-OCT image with good contrast, and (g) PT-OCT image with poor contrast.

4.5.1. Methodology

4.5.1.i) Samples

The standard controlled phantom in this study was the PDMS-based sample that was explained in Section 4.2.1. To do further studies on biological tissues, we prepared 3 different samples, including: lipid-rich tissue, artificial lipid plaque (bovine cardiac tissue with subsurface lipid[82]), and human aorta sample. To prepare the lipid tissue, a fresh slice of fresh bacon (Kirkland) was cut into a 2×2 cm^2 piece with a surgical blade. This specimen was selected from a region rich in lipid (white parts). To make artificial lipid plaques, a piece of fresh bovine cardiac muscle was cut into a 5×5 cm^2 sample with a surgical blade. Then the cut piece was washed with PBS solution. Afterward, mayonnaise (Kraft) as a rich source of lipid (>80%) was injected to this sample with an insulin needle at a depth about 70 to 500 μm beneath the surface to make the similar cap thickness of an artery plaque[29, 82]. The third kind of biological sample was obtained from a human aorta tissue. A part of donated fresh aorta of an 88-years-old female who died because of cardiac disease was prepared with standard dissection procedure. The selected region contains lots of calcified abnormalities. The study on the human sample was done at HBO lab under approved ethics protocols by York university (e2020-234 and e2020-250). All biological specimens were put on a standard glass slide and imaged immediately after preparation at room temperature.

4.5.1.ii) Imaging protocol and datasets

To image the PDMS sample and the tissues samples, the PT lasers at 806 nm and 1210 nm were used, respectively. The power of the laser modulated on the sample in a sinusoidal shape from zero to a maximum power. The frequencies of amplitude modulation were set at 500 and 4000 Hz. These experiments were performed with an OCT A-line rate of 21.6 kHz. In M-scanning mode, each A-line was captured for 1000 points (1000/21600≃46 ms). Each sample was imaged at various distances related to the focal plane and different PT power levels. Also, to test generalization in the net, various areas of the samples were captured by PT-OCT.

To create datasets for the net, OCT phase signal over time for each pixel was calculated. Then, 88 datapoints were chopped from the 1000-datapoint signal to make input vectors of the net. Note that 88 points was almost equal to 2 modulation cycles of PT-OCT signal with a modulation frequency of 500 Hz at a sampling rate of 21.6 kHz. The obtained pixel amplitude after performing lock-in on 1000-datapoints signals was used as the ground truth for the net. To evaluate the improvement in denoising by the net, the lock-in processing was done on the chopped signals a well.

4.5.1.iii) The deep net

The deep neural network was designed for reconstructing a PT-OCT images from fast-captured signals. The structure of the net is illustrated in figure 60(a). This net consisted of 4 layers (2 hidden layers) in a fully connected (FC) configuration. In our implementation, the input of the net was the time sequences of OCT phase signals for each pixel. The input layer of the net was a vector with a length of 88 points. The first hidden layer was a dense layer with 10 nodes. It was followed by the second dense layer with 5 nodes. The output of the network was the one parameter that gives us the corrected pixel value in a PT-OCT image. The activation function for layer 1 and 2 was selected as the rectified linear response (ReLU), and for the last layer, was selected as the linear function.

4.5.1.iv) Training of the net

Note that in this study, we focus on the proof-of-principle study and a detailed study on the optimization of the architecture can be considered in future works. In brief, to optimize the net architecture and to combat overfitting, we used cross-validation k-fold method (here, k=10) with MSE loss function. The dataset for training the net was created by choosing randomly 80,000 signal traces out of 96,000 signal traces. For training process, 10 percentage of this selected dataset (8,000 signal traces) was used for validation. To test content-aware feature of a trained net, such libraries for training and validation were created from each sample, including the PDMS, the lipid tissue, the artificial lipid plaque, and the human aorta sample. Training of the net was done after 120 epochs with adaptive moment estimation (ADAM) optimizer. The code was written in Spyder environment powered by python using the Keras library. The training process was performed on a GPU (GeForce GTX 1060, NVIDIA) and takes few minutes to complete. After completing the training process, to test the net performance, the trained net was fed with unseen datasets that were captured from parts of samples other than the part used for the training.

4.5.2. Results and discussion

4.5.2.i) The net performance on the phantom

To demonstrate the performance of the trained net, the results of two pixels are plotted in figure 60(b), 60(c). These plots are showing the amplitudes of the ground truth (GT), chopped signal, and the predicted values by the net as a bar plot as well as the OCT phase raw signal captured for 4ms (2cycles). The GT and chopped amplitudes come from the results of lock-in on the references signal (1000 points) and the chopped signal (88 points). As seen, while the net had no explicit information about the relationship between input and output, it could extract the amplitude of the modulation frequency component. However, there are cases of poor prediction (Fig.60(b)) and good prediction (Fig.60(c)) by the net.

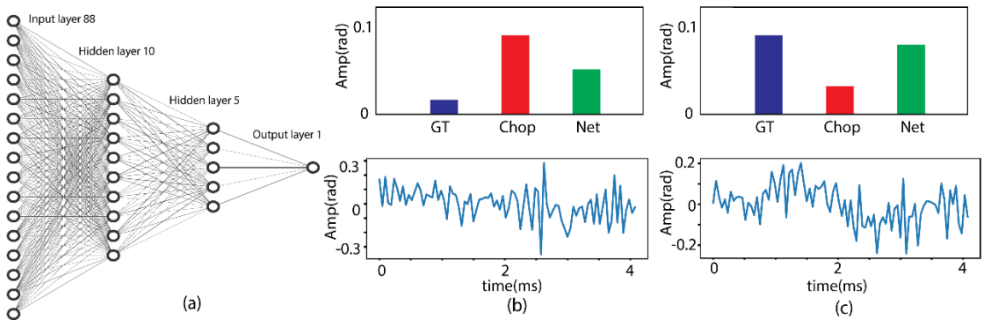

Figure 60. (a) The structure of the net; this net consists of 4 fully connected layers (b) an example of poor and (c) good prediction of amplitude of a pixel, by comparing the Net with Chop and GT. These predictions are obtained by the net from the chopped signal traces over time for 4ms.

To show the performance of the net in reconstruction (denoising) of PT-OCT B-mode images, the results of an unseen dataset captured from the PDMS phantom is plotted in figure 61. This sample is imaged at various PT power levels of 0, 1, 2.25, and 3.5 mW (marked with P_0 to P_3 in figure 61(b), respectively). Qualitative assessment of results suggests that the reconstructed image (i.e., net output; Fig.61(d)) is more similar to the ground truth (Fig.61(a)) than the PT-OCT image obtained from the chopped signal (Fig.61(c)). For instance, although the warp texture (marked with the green cross in Fig.61(b) to 61(d)) is hidden in the chopped image in figure 61(c), it can be seen clearly in the reconstructed image by the net. Moreover, the noise floor (P_0 regions) in reconstructed image is significantly lower than that obtained from the chopped image. This low noise floor improves the contrast in the net images, particularly between the P_0 and P_1 regions. Examples of a good prediction (Fig.61(e)) and a poor prediction (Fig.61(f)) of the pixel amplitudes by the net in comparison with the ground truth (GT) and the chopped signal, as well as the signal traces in time are shown.

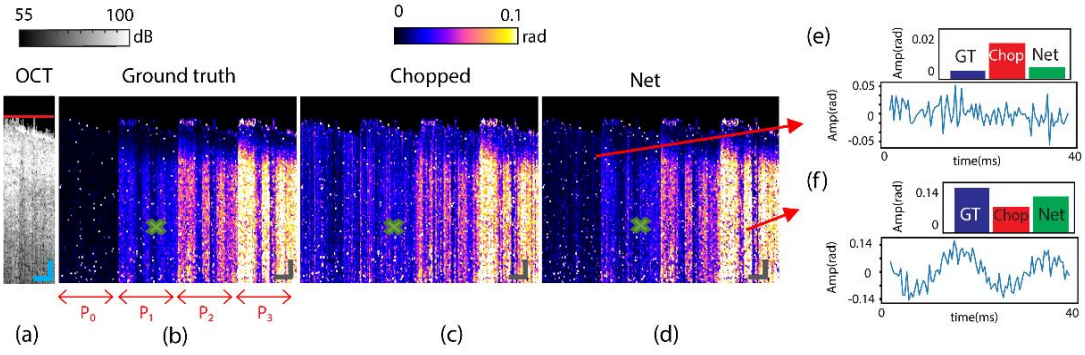

Figure 61. The results of PDMS sample in on-focus condition: (a) OCT image; PT-OCT images of (b) the ground truth, (c) chopped, and (d) net reconstruction. (e) and (f) are examples of pixel predictions by the net form raw data signal, the sample is illuminated with 4 different PT laser powers, determined with P_0 to P_3. The missing features in the chopped (marked with the green cross) is retrieved by the net after reconstruction of the image; scale bar=100 μm.

To verify the performance of the net in “out of focus” condition, the PDMS sample was imaged approximately 200 μm out of the focus. The OCT and PT-OCT results are depicted in figure 62. The red lines in figure 61(a) and 62(a) represents the focal plane in OCT images. Similar to the in-focus condition, a greater similarity can be seen between reconstructed image by the net (Fig.62(d)) and the ground truth (Fig.62(a)), particularly in P_0 and P_1 regions. Also, the examples of poor and good predictions in pixel amplitude by the net and the signal traces are plotted in figure 62(e) and figure 62(f), respectively.

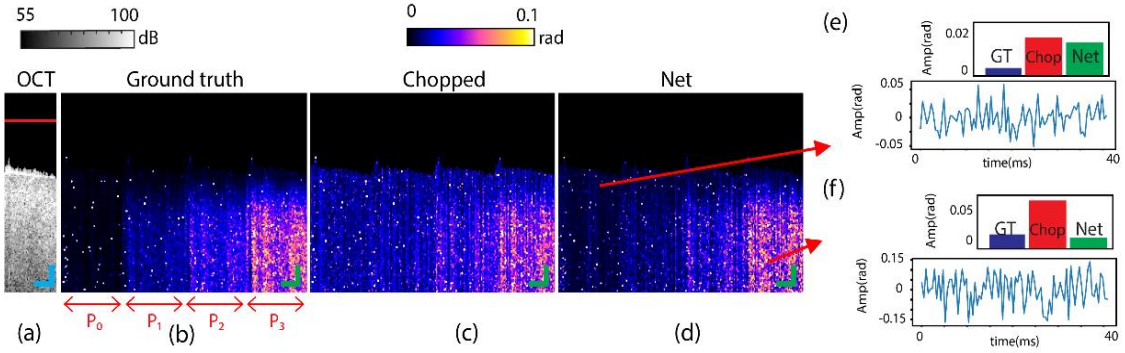

Figure 62. The PDMS sample in off-focus condition: (a) OCT image, (b)the ground truth, (c) chopped, and (d) reconstructed images by the net. (e), (f) Examples of pixel prediction by the net form raw data signal; scale bar=100 μm.

Next, to investigate the effect of modulation frequency on the performance of the net, an additional experiment was carried out at a higher modulation frequency of 4000 Hz. The OCT and PT-OCT results are depicted in figure 63. As seen, the PT-OCT signal amplitudes in the ground truth (Fig.63(b)) drop dramatically compared to the those obtained at 500 Hz (Fig.61(b)) due to characteristic frequency response of the thermal Green’s function and pink noise of system (discussed in Section 2.2 and Section 4.2). Due to such dramatic SNR drop, the net shows poor performance in extracting the small signals from the time sequences and in reconstructing the PT-OCT image (Fig.63(d)). The results of this study can be used to address a major dilemma in PT-OCT that is the compromise between the SNR and imaging rate. That is, at lower modulation frequencies, owing to the thermal Green’s function response, the amplitude of PT-OCT signal is larger; however, lock-in at lower frequencies are noisier because of the pink noise of the system which necessitates acquisition of long sequences. Above results suggests that the trained deep net allows us to form acceptable PT-OCT images from only few cycles of lower modulation frequencies responses.

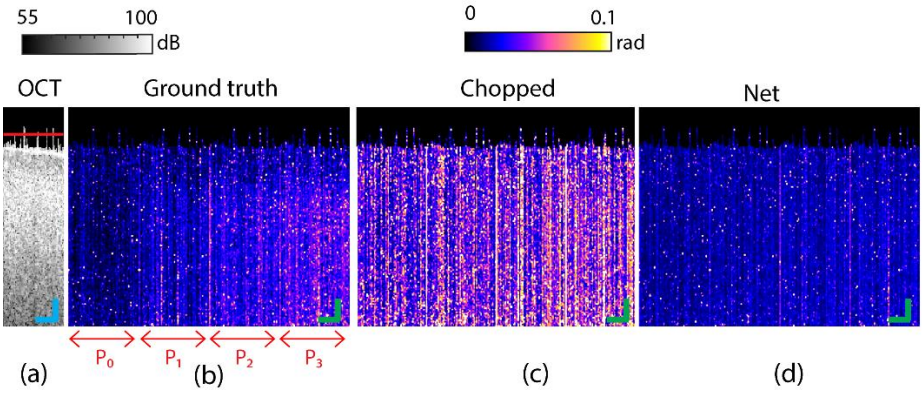

Figure 63. The PDMS sample results at PT modulation frequency of 4000Hz: (a) OCT image, (b)the ground truth, (c) chopped, and (d) reconstructed images by the net, the net has poor performance in such high modulation frequency due to deterioration of SNR. See text for more detail; scale bar=100 μm.

To quantify the reconstructing results obtained from the in-focus and the off-focus studies at 500 Hz, we use the Michelson contrast, MSE, and structural similarity (SSIM) metrics. Values in Table 4 show the net improves the contrast between regions in images, specifically between P_0 (noise floor) region and other regions. Note that P_0 region, here, can be assumed as a non-absorber PT light part in the sample as well. So, the improved contrast between an absorber and a non-absorber region in images will enable us to determine the borders of absorber regions with higher accuracy.

Table 4 The calculated Michelson contrast between different regions in the images. This value is calculated for the ground truth image (GT), chopped image (Chop) and the reconstructed image by the net (Net) in on-focus and off-focus imaging conditions. Improvement in the provided contrast can be seen from the values obtained from the Net rows.

		Contrast				
Conditions		P_0-P_1	P_0-P_2	P_0-P_3	P_1-P_2	P_2-P_3
	GT	61.8	77.4	86.7	29.9	28.2
	Chop	6.9	23.5	47.4	16.9	26.8
On focus	Net	35.4	57.7	75.6	28.0	31.7
	GT	42.9	62.8	77.8	27.1	29.4
	Chop	0.4	15.9	32.17	16.3	17.1
Off focus	Net	12.2	39.4	61.3	28.2	29.3

Table 5 lists the MSE and SSIM values between the GT, the net, and the chopped images. As seen, MSE between GT and the net images is much smaller (in order of 10 times) than that of GT and chopped. Also, the SSIM values between the GT and net, in average, approximately 10% is greater than SSIM between GT and chopped. It is worth to be pointed out that the difference in similarity in the "GT-Chop" and "GT-Net" cases will become less as the power of the PT laser increases on the sample. The possible reason is that by increasing the PT power, the SNR of the PT-OCT signals increases, therefore, the influence of noise on the

signal will be negligible. In general, the data of these metrics indicated the ability of the net to reconstruct PT-OCT images with a good similarity with the ground truth.

Table 5 The calculated values for MSE and structural similarity for different regions in the PT-OCT image. These values were obtained by comparing the ground truth and the chopped images and the ground truth and the reconstructed images. Results show the ability of the net to denoise and reconstruct the noisy images.

		MSE					SSIM				
Conditions		P_0	P_1	P_2	P_3	Overall	P_0	P_1	P_2	P_3	Overall
On focus	GT-Chop	0.0025	0.0105	0.0139	0.0231	0.0167	51.2	82.2	82.9	84.6	77.0
	GT-Net	0.0014	0.0024	0.0014	0.0016	0.0017	83.4	88.5	91.3	92.3	89.2
Off focus	GT-Chop	0.0132	0.0091	0.0111	0.0113	0.0107	63.0	83.3	84.3	85.1	80.4
	GT-Net	0.0018	0.0019	0.0005	0.0011	0.0013	88.1	91.3	92.5	89.8	90.8

4.5.2.ii) The net performance of tissues

To evaluate the performance of the trained net on unseen datasets, biological tissue samples were used. Note that the net was trained with data only captured from the PDMS samples. Figure 64 displays the performance of the net on the tissue samples. The top surface of all sample is placed in-focus. Also, the chopped images are all obtained from the first 2 modulation cycles of the ground truth PT-OCT signal. The bacon tissue (Fig.64(a1) to 64(a4)) is imaged at 3 different PT power levels that are marked by P_0 to P_2 (0,1.6, and 3.2 mW). As seen, the amplitude of pixels in the "PT-off" region that determine the noise floor, in the reconstructed image by the net (Fig.64(a4)) is much lower than that of the chopped image (Fig.64(a3)). Also, the absorber areas (red rectangles) in the ground truth and the reconstructed images have sharper contrast with the noise floor, leading to easier detection of the absorber region.

Next, the two captured shots from the artificial lipid plaques are plotted in figure 64(b1) to 64(b4) and figure 64(c1) to 64(c4). By comparing the reconstructed images (Fig.64(b4) and 64(c4)) with the ground truth images (Fig.64(b2) and 64(c2)), it can be seen that the net provides us sufficient contrast to detect and measure the borders of the lipid region and the thickness of the cap (red arrows). As an example, in cardiology, such improvements in contrast may enable better determination of the size and the depth of lipid core and thickness of the fibrous cap in arterial plaque that is crucial in the risk assessment of plaques[29, 163, 164]. Also, the texture details of the reconstructed images are more similar to the ground truths. For instance, the selected red window in the chopped image (Fig.64(c3)) shows a region with relatively large PT-OCT signals. However, in the reconstructed image and the ground truth, this region seems like a mild absorber.

The results from the human aorta tissue are shown in figure 64(d1) to 64(d4). It can be seen from the OCT image (Fig.64(d1)) that this sample is made up of three regions, the shiny top layer, the middle dark layer, and the gray layer beneath all layers (marked with 1, 2, and 3). In the ground truth image (Fig.64(d2)), by considering the color bar, the signals in the regions 1 and 3 are weak. However, in the chopped image, the pixels in these regions mostly are colored blue and purple, showing larger amplitude of pixels. These high intensity pixels in these layers are corrected in the reconstructed image by the net.

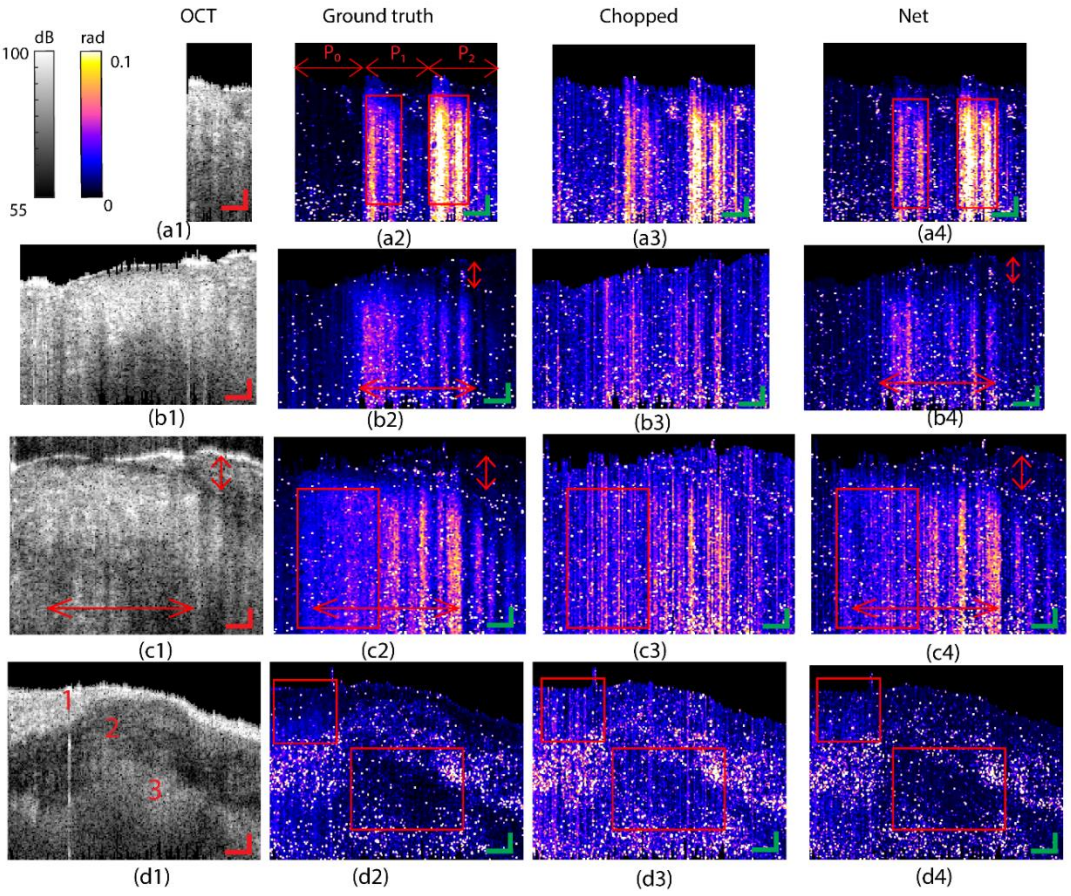

Figure 64. The results of study on tissue samples. OCT, PT-OCT ground truth, chopped, and reconstructed by the net results of (a1) to (a4) the bacon sample, (b1) to (b4) the artificial artery plaque sample, (c1) to (c4) another location of the artificial artery plaque sample, and (d1) to (d4) human aorta sample. Using the deep net, the missing important features, such as the depth and the width of the lipid region are retrieved; scale bar=150 μm.

4.5.2.iii) Analysis of the net

We conducted some surveys to evaluate the performance of the net in sensitivity to the transient response of the signal, different samples, and different length of input vectors. First, we explain the conducted study on the transient response of the signal. In PT-OCT, temperature inside the sample raises due to the absorption of the PT laser. In mathematical point of view, this temperature variation has a transient and a

steady state component. In an ideal condition (with no noise), the steady state response of a sample to an external single-frequency harmonic modulation is a harmonic response with the same frequency. This response, in the frequency domain, has a single component at the modulation frequency. However, the transient response in the frequency domain, due to the Green's thermal function has several components. As the lock-in method is supposed to be done on the steady-state response, the first few cycles of PT-OCT signals that the transient response appears in them needs to be neglected[103, 165].

To survey the effect of the transient response of the PT-OCT signal on the performance of the net, the ground truth signals were chopped with a length of 18 cycles into 9 groups. Each group was made up of 2 cycles that the number of the group shows the order of each pair. For example, group 2 contained of the 3rd and the 4th cycle of modulation. After that, we trained 9 nets with these 9 training datasets. In the same way, 9 groups of an unseen test dataset were created. Then, these 9 trained nets were applied on these 9 unseen test datasets. Note that the ground truth in all runs was unique and was selected from the first 18 cycles of training datasets. The MSE values between the net results and the ground truth are plotted in figure 65(a). As seen, the pattern of these MSE values is similar to a minimum diagonal pattern, meaning that each trained net has a better performance around its order in time sequence. For example, a net that is trained with the 3rd and the 4th modulation cycle, has a better performance in prediction on unseen signals taken from the 3rd and 4th cycles. The result suggests that the net is sensitive to the transient thermal response and can extract the necessary information from a signal with transient response. However, in conventional lock-in method, such sensitivity to the transient response is not seen. Apparently, the effect of the transient response on the overall shape of the signal in initial groups are greater, because the transient response disappears within few cycles.

Next, to survey the generalization in this strategy, 3 nets with the same structure were trained with the 3 different datasets collected from the PDMS, the artificial lipid plaque, and the bacon samples. Also, another net was trained with a data pool containing all of datasets from these 3 samples. Then, these 4 trained nets were applied on unseen test datasets from the PDMS, the artificial lipid plaque and the bacon. The MSE values between the ground truth and the net are plotted in figure 65(b). As seen, the deviation of MSE values from each other is not too large, however, a trained net with a specific sample has a slightly better performance with the test datasets from that specific sample. Moreover, the MSE values obtained from the net which was trained with the data pool (the dataset containing datapoints from all samples) is not extremely smaller than others. It shows that training the net with the suggested strategy is not dependent on the sample. In other words, it is possible to train a net with data from a sample (for example PDMS), then use this trained net to do prediction on data from other samples (for example lipid). This independency

of training to the sample can be considered as the generalization in training data sets, which is beyond the content awareness.

The other study is finding the optimized signal lengths in terms of the MSE of prediction and imaging rate. In this study, we trained nets with different number of modulation cycles (from 1 to 4). At an A-line rate of 21.6 kHz and modulation frequency of 500 Hz for the PT laser, each cycle consists of 44 datapoints (44/21600≃2 ms). To combat against overfitting in this study, we decided to increase the net configuration to a net with 3 dense hidden layers consisting of 40, 20, 5 neurons, that connect the input vector to a single neuron as the output. The ground truth for all runs were the same as well and it was taken from the first 20 modulation cycles of the ground truth signal. The MSE between the net prediction and GT, and the chopped signals and GT are plotted in figure 65(c). By looking at the results of net, as the modulation cycle becomes larger, both MSE in chopped-GT and the net-GT values reduces. As seen, when the net is trained with 2 cycles, the MSE between GT and the net decreases more than 50% related to the training with 1 or 1.5 cycles. However, it seems after 2 cycles, the MSE values reaches to an asymptote, meaning that there will be no significant improvement in the net performance. Therefore, 2 cycles for training a net are an optimum point in this plot, in terms of imaging time and MSE values. Besides this, the chopped-GT values drop with the faster rate than that of net-GT. It touches the lower limit of the MSE values of 2 cycles, at a length of 7.2 cycles. Thus, the 2-cycle trained net can improve the imaging rate up to 3.6 times.

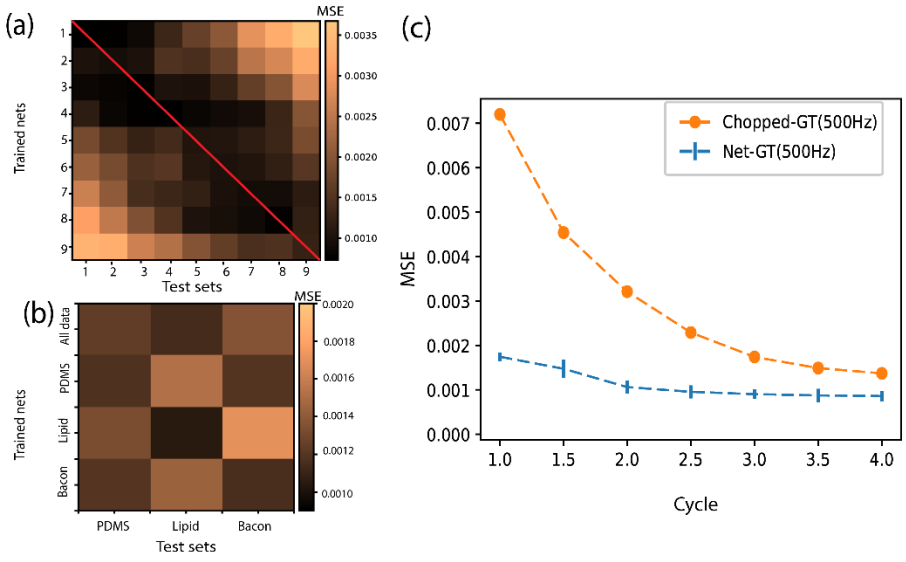

Figure 65. The results of the study on the performance of the net in terms of learning signal features, generalization, and improved speed. (a) MSE values of 9 trained nets with different datasets from the PDMS sample applied on the 9 group of data tests from that sample, (b) the MSE values of trained nets with various samples applied on test datasets from those samples, (c) the MSE in terms of modulation cycle between the ground truth and the net, and the ground truth and the chopped images.

4.5.3. Conclusion

We present a strategy to improve imaging rate and SNR of PT-OCT using a deep net model. To process the signals in PT-OCT, lock-in method is usually used. In this method, to form a high-quality B-mode image with sharp contrast, several modulation cycles of PT-OCT signal need to be captured. This process, however, limits the effective imaging rate of PT-OCT. We address this issue by training a deep net that can improve the contrast and SNR of fast-captured images. Results on both standard phantoms and tissues proved that the reconstructed image by the net indicate good similarities with the ground truth. Also, the important texture inside the sample (such as the cap thickness in the artificial plaques) can be seen clearly after reconstruction of images. Additionally, the study of behavior of the net in training with different conditions indicated generalization of a trained net to other samples. The analysis on the performance of net showed that the net can accelerate the imaging speed up to 3.6 times as well. Additionally, by using this net, fewer datapoints needs to be captured, to be saved/loaded, and to be processed, that leads to faster computation, and smaller volume of saved data.

5: Conclusion

5.1.Summary and conclusion

PT-OCT is a functional extension of OCT with the promise to provide micron resolution structural images of tissue co-registered molecular contrast maps. As such, PT-OCT has great potential to overcome the non-specific limitation of OCT which is of great value to the clinical practice. To date, applications of this useful imaging technique has been demonstrated in several studies to assess presence of MOI in sample, qualitatively. Analyzing PT-OCT signal quantitatively has a potential to give insight into the properties of sample. Although PT-OCT signal in limited cases and conditions such as liquid samples was analyzed, a comprehensive analysis in different sample and experimental conditions has not been done so yet[74, 91]. Another key limitation of PT-OCT is its intrinsic slow imaging rate. To capture an image in conventional PT-OCT, several data points need to be read over each A-line that automatically increases the imaging time, as well as the volume of saved data. The low imaging rate limits the system to imaging stationary samples, that is not useful for *in vivo* imaging. Processing large volumes of saved PT-OCT data is also not desired in the clinics as it necessitates use of complex, bulky, and expensive computers.

The overarching goal of this dissertation was to develop new knowledge and experimentation strategies to enable gaining refined insight into chemical composition of biological tissues with PT-OCT. As such, three aims were defined for this dissertation:

1- Studies focused on development of knowledge on the effects of sample and system influence parameters on PT-OCT signals.

2- Studies focused on development of experimentation and signal processing strategies for extracting information about chemical composition of tissues from PT-OCT signals.

3- Studies focused on development of new instrumentation and signal processing approaches for enhancing the imaging speed of PT-OCT

Under the first Aim, two theories were developed and discussed in Chapter 2. In the first theory, the relation between PT-OCT signal amplitude and sample properties was modeled in general sample state including liquid and tissues-like samples. To generate this model, all significant opto-thermo-mechanical properties of samples were considered. Using this model, the behavior of PT-OCT signal by changing a sample property such as the absorption coefficient or the thermal conductivity was predicted. As an achievement, the concentration of lipid compositions in artificial phantoms mimicking the lipid plaques was analyzed as a function of received PT-OCT signal. Besides this, a second comprehensive theory for PT-OCT was generated for estimating PT-OCT signals of multi-layer samples in 3D. In this theory, by

considering physical phenomena in PT-OCT, the light, the thermal, and the mechanical fields were modeled. This comprehensive model enabled understanding of the effects of parameters such as the mechanical stiffness, the heat flux, and the Poisson ratio on signals which could not be understood from previous models. A parametric study was also performed to find the significant sample and system parameters affecting PT-OCT signals. The validation results for both theories indicated a strong correlation between experimental signals and model simulation results, suggesting that these validated models can be used as simulator when designing and optimizing PT-OCT systems and experiments.

Chapter 3 was focused on addressing Aim2. Two strategies were presented in this chapter for obtaining refined insight into tissue chemical composition. In the first strategy, we introduced a spectroscopic approach to PT-OCT imaging to increase specificity of detecting and differentiating between MOIs (e.g., lipid and collagen/elastin). In brief, two PT laser wavelength were installed in the setup to excite the sample at two different wavelengths. After decoupling the responses of the sample to these two wavelengths, MOI was detected with higher specificity. To test the feasibility of applying PT-OCT in cardiology, studies on this chapter were carried out on phantoms containing the abundant chemical constituents of human cardiac tissues as well as excised human cardiac tissues. The promising results of this study suggest ability of spectroscopic PT-OCT in specific detection of MOIs in samples. This work demonstrated the ability of the system in the depth-resolved detection of lipid as the most common chemical in the arterial plaques with a high specificity. In the next section of Chapter 3, quantification of received signal form lipid was done using a machine-learning powered model. The theories generated in Chapter 2 showed that quantification of PT-OCT signal is a multi-factorial and non-linear problem. Therefore, quantification of PT-OCT signal in a general condition was not fruitful with classic signal processing approaches. In light of the outcomes of the parametric study of Chapter 2, we employed a SVM classifier model to classify and to label pixels in PT-OCT images based on their lipid concentrations. The results showed that our trained SVM model, qualitatively, had a good performance in classifying pixels from single and multi-layer samples. Further analysis on the results proved that the SVM model improved the precision of classification by approximately 47% and 86% for two classes. Strategies presented in this chapter will help us to gain more reliable molecular information from tissues, that is essential in early diagnosis of various diseases. For instance, in cardiology, estimating the concentration of lipid pool or measuring thickness of fibrous cap are significant factors in risk assessment of an arterial plaque[85].

In Chapter 4, we focused on addressing Aim 3 by generating strategies for enhancing the imaging speed of PT-OCT. In the first approach, a new variant of PT-OCT, named transient-mode (TM) PT-OCT, was introduced. In this method, the thermo-elastic response of the sample to a low-power squared PT pulse was used to form PT-OCT images at imaging speeds orders of magnitude higher than that of conventional PT-

OCT. Such significant enhancement in imaging speed became possible because the transient response of the sample occurs with significantly higher amplitude and much shorter time than the steady-state response used in conventional PT-OCT. Previously, the fastest reported PT-OCT acquisition rates were on the order of 10-100 Hz[150, 151]. With TM-PT-OCT, we showed that PT-OCT imaging rate can be increased to 3 kHz (1-2 order of magnitude improvement). Also, as an important achievement, for the first time, we demonstrated possibility of capturing a PT-OCT video of a moving sample with TM-PT-OCT. This video showed the structure of a moving sample co-registered with depth-resolved molecular information. As a complementary study, spectroscopic TM-PT-OCT was also demonstrated which enabled video-rate imaging of tissue structure and insight into chemical composition with high specificity. In the last part of this chapter, we introduced a deep learning strategy for enhancing imaging speed of PT-OCT. In this approach, a de-noising deep net was designed and trained which could take fast-acquired and noisy datasets as input and produce PT-OCT images with SNR and contrast normally obtained from dataset with long acquisition times. The deep net showed promise in not only enhancing the imaging speed, but also reducing the volume/size of data needed for PT-OCT imaging. The two strategies offered in Chapter 4 did not require any major modification or addition of any costly equipment to the conventional PT-OCT systems.

We anticipate the knowledge and strategies developed in this thesis opens the door for translation of PT-OCT technology into the clinics. PT-OCT promise for generating depth-resolved structural images co-registered with molecular map is specifically attractive for detection of early stages of diseases when structural abnormalities are minimal.

5.1.1. Novelty/ innovation presented in the dissertation

The overarching goal of this dissertation was to develop knowledge and strategies that enable downstream translation of PT-OCT to the clinics as an imaging tool for gaining depth-resolved and refined insight into tissue chemical composition. To do so, we, initially, developed theoretical models to shed light on the multifactorial physics behind generation of PT-OCT signals.

In Chapter 2, the first presented model predicted the PT-OCT signal behavior as a function of material properties. With this model, for the first time, we showed (theoretically and experimentally) that this relation is non-linear, and that the degree of non-linearity is a function of material properties; all previous works assumed solvent-dominated media leading to linear PT responses with MOI concentration [74, 91]. The significance of these findings is that it opened the door for correlating MOI concentration with PT-OCT signals. In the second presented model in Chapter 2, a 3D model was presented to simulate PT-OCT signals in multi-layer samples. In this model, by involving the mechanical stress-strain field and thermal boundary conditions in the sample, the accuracy of the signal simulation was increased. This model was also verified in various conditions. The missing points in the previous models were neglecting the

mechanical field and the heat flux between sample layers [68, 77, 78], both of which significantly affect recorded PT-OCT signals. We also demonstrated that without considering sample mechanical properties, such as the Poisson's ratio, the simulation leads to large underestimations. The comprehensive 3D model offered in Chapter 2 opened the door for in-depth understanding of the sample and system parameters that influence PT-OCT signals.

The knowledge we obtained from the modelling endeavors of Chapter 2 were subsequently used for developing experimentation and machine learning strategies for specific detection of molecules of interest and their classification based on concentration. Given the significance of atherosclerosis in cardiology, our developed strategies were mostly geared toward specific detection and quantification of atherosclerotic plaque constituents (e.g., lipid). In Chapter 3, we utilized a spectroscopic approach for label-free specific detection of MOIs. In this work, by unmixing the acquired absorption map of the sample as a result of excitation with two PT wavelengths, for the first time, depth-resolved maps of MOI was obtained. Lipid, as a key constituent of plaques, was detected and visualized in 3D with high specificity with the spectroscopic method. The only previous work on PT-OCT of lipid was a conference paper utilizing only 1210nm PT laser for lipid sensitive (but not lipid specific) imaging [124]. It is, however, also worth pointing out that dual-wavelength PT-OCT setups were previously used for quantifying blood oxygen saturation on phantoms [74, 123]. In the ML study presented in Chapter 3, we employed a ML model to quantify the concentration of MOI in the sample in general conditions. Due to multifactorial physics behind the PT-OCT signal (as learned from Chapter 2 works), the concentration of MOI cannot be directly quantified from received signals. The results of this study showed an acceptable performance of the trained net in quantifying the percentage of MOI in the sample in different conditions. Previous works in this area attempted quantifying MOI concentrations under certain experimental conditions with solvent-dominated samples using classic statistical method [74, 91]. Works presented in Chapter 3, show that such simplistic quantification approaches result in significant quantification errors due to overlooking of the effects of sample and system influence parameters on acquired PT-OCT signals. The developed ML model, on the other hand, has the ability to decouple the effects of sample and system parameters in order to offer more accurate quantification of MOI concentration in biological tissues.

Limited imaging speed has long been a key inhibitor for translation of PT-OCT to the clinics. In the last chapter of the thesis, instrumentation and AI-enabled advancements are proposed for significantly enhancing the imaging speed of PT-OCT. In Chapter 4, two methods (TM-PT-OCT and the deep net) method were presented to improve the imaging speed of the system. Using TM-PT-OCT method, the A-line rate of the system of increased by over two orders of magnitude, enabling co-registered structural and molecular-specific imaging of moving samples at video-rate. In TM-PT-OCT, the sample is excited with a

low-energy squared pulse that add no cost or complexity to the setup. In the previous efforts, complex and costly instrumentation had to be added to PT-OCT setups to only marginally increase the imaging speed [150, 151]. Given the significant enhancement of imaging speed with TM-PT-OCT, we also demonstrated possibility of performing spectroscopic PT-OCT imaging at video-rate which is of significant relevance to downstream clinical applications of PT-OCT. In the next study of Chapter 4, PT-OCT images was reconstructed with AI platforms to improve both imaging time and SNR. Here we showed that deep neural nets can be trained to enhance PT-OCT image contrast by denoising PT-OCT signals. This survey, to the best of our knowledge, is first report on reconstruction of PT-OCT images with deep learning.

5.2.Future direction

5.2.1. Improvement in the PT-OCT theory

In Chapter 2, a comprehensive theory for PT-OCT in 3D space was generated. In this theory, for simplification, optical scattering property of the sample was not considered. That is, it was assumed that light attenuation was dominated by absorption of light. Use of this assumption reduced complexity and volume of calculations in the model. However, to simulate a sample more accurately, scattering regime of PT light in the sample may also be considered. We should be aware that as there is no analytical solution for scattering of light, this will add further calculation steps to the model. Besides this, in developing equations of the thermal field in the sample, we used Green's function theory in the frequency domain. Using this approach leads to calculation of the steady-state response of the thermal field. However, as this analytical solution is not unique, for each geometry a modified solution needs to be generated by carrying out additional mathematical steps such as calculating integral on complex functions. Alternatively, to calculate thermal field in the sample more accurately, heat transfer resistance modeling of the sample can be solved with finite difference method (FDM). Although this time-dependent numerical solution is valid in every geometry, it takes longer time in simulation.

5.2.2. AI in PT-OCT

In Chapters 3 and 4, two applications of AI in PT-OCT were discussed. These studies demonstrated encouraging results for gaining refined insight into tissue chemical composition and for enhancing PT-OCT imaging speed. AI models, in general, enable multifactorial analysis of acquired signals and frequently their use leads to improvement detection/classification performance without adding complexity to the hardware or increased cost. As AI is a fast-growing topic in the world, countless efficient methods powered by AI have been presented. For our purposes, we used some of them (e.g., SVM and deep net), however, there is an opportunity to apply or combine other methods in these problems for getting better performance. In Chapter 3, a more comprehensive ablation study on the input of the SVM model can be done to analyze the impact of each input parameter. In this suggested study, by selecting different inputs from all these 5 inputs

and comparing the predicted results, the significance of each input can be better understood. Also involving the texture features of the OCT images in the model would be helpful as a new channel of information. As another suggestion, the possibility of developing SVM models with more classes (or finer resolution of concertation) can be studied. For example, we can add semi-high and semi-mid classes between the three classes that we defined before (low, mid, and high). As another suggestion is use of different kernels such as the radial basis function (RBF) kernels for potential enhancement of model performance. Using regression ML models to obtain continuous concentration of MOI in each pixel would be another possible approach to these issues. Imaging more complex phantoms should also be done to evaluate performance of generalization in the model.

In Chapter 4, one can test other type of layers such as convolutional layers in the structure of a deep net to denoise the signals. Convolutional layers that consist of a set of filters (or kernels), have a potential to extract more features for denoising signals. However, it should be considered that training a convolutional net needs more datasets and also takes longer time. To improve the accuracy, we can also analyze a whole A-line or a tile in images over time instead of temporal signal of a single pixel. This approach can potentially analyze spatial and temporal phase information simultaneously that may lead to better reconstructions. Using generative adversarial networks (GANs) would be a helpful approach in denoising and reconstructing the PT-OCT images more effectively. GAN models contain generator and discriminator components which can learn to generate new data with the same statistics as the training set, in unsupervised, semi-supervised and fully supervised learning methods. Promising results in denoising speckles in OCT images with GANs has been reported [166]. Also, there is opportunity to extent the study in Chapter 4 into the TM-PT-OCT method to improve the SNR and contrast in the captured images and recorded videos. Besides this, as a suggestion in the field of PT-OCT, AI can be employed in other fashions; for example, to segmentize PT-OCT images, or to quantify signals by regression models. Accurate and reliable segmentation of images from multi-layer tissues such as aorta wall or retina are among the important issues in clinical surveys that may be addressed by AI models.

5.2.3. Enhancing Speed of PT-OCT Imaging

In Chapter 4, TM-PT-OCT was introduced as a new variant of PT-OCT that can improve imaging rate significantly. However, the setup was not optimized for such method. Therefore, there is still room for increasing the imaging rate. As an important factor, the scanning path of glavo mirrors must be optimized. In this presented work, as we moved galvo mirrors in straight line, by scanning a point after a point, to dissipate the heat, we had to have a delay after acquisition of each A-line. This made the effective A-line rate at last 3 times slower. As a suggestion, if the motion path of galvo is modified in a zigzag path, the delay between A-lines can be significantly lowered. Another suggestion in TM-PT-OCT is reducing the PT

laser spot size to increase PT laser intensity and, consequently, generating much stronger thermal fields. This approach can help with acquiring signals with higher SNR. In this reduction of the spot size, a correction in signal processing must be considered, because when the PT laser spot is smaller than OCT spot, a uniform thermal field will not be formed while scanning an A-line. Analyzing such condition needs further studies in light of heat transfer principles. Although increasing the intensity of the PT laser would be helpful in SNR of the signal, the maximum permissible exposure of biological samples must be considered. Combination of TM-PT-OCT with developed deep net can also be a logical next step for further enhancement of imaging speed.

5.2.4. Clinical translation of PT-OCT

In Chapter 3, we presented results of studies focused on application of PT-OCT in cardiology. In these studies, samples were composed of abundant chemical constituents of human cardiac tissues. The results showed the ability of PT-OCT in detection and quantification of these chemicals. Also, a feasibility test was carried out *ex-vivo* on excised human aorta samples. The promising results that obtained by comparing PT-OCT images and histology indicated a consistency between them. To translate this technique to clinics, however, more studies on human tissues must be performed; unfortunately, due to COVID-19 pandemic and the lockdowns, I did not get the chance to carry out such studies. In Chapters 3 and 4, we introduced a spectroscopic PT-OCT approach aimed at distinguishing different types of chemicals. As a suggestion, we can illuminate the sample simultaneously with all PT lasers but set the modulation frequencies of PT lasers at slightly different values so that their individual responses can later be retrieved. This approach will cut the imaging time in half. However, to apply this method, the effects of the two modulating thermal fields on each other must be studied. The other important milestone that has not been addressed so far, is design and development of PT-OCT catheters. Such catheters are ultimately needed for assessment of performance of PT-OCT in clinical settings for *in-vivo* imaging of cardiac tissue. Hopefully, the theoretical works and developed strategies presented in this dissertation can open the door for development of such catheters.

5.3. Societal impact

5.3.1. Contribution to biophotonics

In the field of bio-photonics, this dissertation has led to several contributions including the first captured video from moving samples with PT-OCT. The video displayed structural information of samples co-registered with depth-resolved chemical composition information that may open the door for future *in vivo* studies. Also, in the presented theory in Section 2 of Chapter 2, we generated a relatively comprehensive theory of PT-OCT with good accuracy that involves mechanical properties of samples such as the Poisson's ratio and Young's modulus. These parameters that influence the received PT-OCT signals were not included in previous models. Besides this, with the other model presented in the first part of Chapter 2, we

could justify the general behavior of PT-OCT signal as a function of material properties in any type of sample (i.e., liquid or tissue). The previous works only considered a linear variation of PT-OCT signal as a function of concentration of MOI in liquid samples. Moreover, we presented a spectroscopic PT-OCT approach to enable differentiation of MOIs from each other, enhancing the specificity of PT-OCT imaging. Additionally, for the first time, in light of generated knowledge from these theories, we employed AI models to quantify and label PT-OCT images based on MOI concentrations. Introduction of TM-PT-OCT and applications of deep nets for signal de-noising are among other key thesis contributions that enable significant enhancement of PT-OCT imaging speed. The journal and conference papers as outcomes of this thesis were listed in Appendix E.

5.3.2. Contribution to clinical imaging and cardiology research

In the works presented in this dissertation, we conducted a feasibility study with PT-OCT to image samples consisting of the key constituents of human cardiac tissues that serves as a first step for tailoring PT-OCT to the specific needs of interventional cardiology. Lipid as the main chemical in atherosclerosis plaques was detected with a high specificity and is quantified based on concentration. Also, collagen/elastin as the other constituents in cardiac tissues were detected by PT-OCT that would be helpful in estimating the plaque risk by determining the thickness of fibrous cap.

At the end, it is worth to point out that heart attack (acute cardiac syndromes) and sudden cardiac death, remain one of the leading causes of death in the developed world[167]. As an example, in Canada, heart disease and stroke account for 20% of all deaths (>46,000 in 2011) and are the leading cause of hospitalization[168]. The underlying cause of many of such diseases is atherosclerosis. In this dissertation, we suggested concepts and potential solutions that can be critical to screening and risk assessment of atherosclerotic plaques. Eventually, studies of this dissertation can serve as a small, yet important, step in translating PT-OCT imaging to the clinics for addressing pressing and high impact clinical needs such as identification of rupture-prone atherosclerotic plaques.

References

1. W. Drexler and J. G. Fujimoto, *Optical coherence tomography: technology and applications* (Springer Science & Business Media, 2008).
2. A. Fercher, "Ophthalmic interferometry," in *Optics in Medicine, Biology and Environmental Research First International Conference on Optics Within Life Sciences (OWLS I), Garmisch-Partenkirchen, Germany*, 1990), 12-16.
3. S. Chiba and N. Tanno, "Backscattering optical heterodyne tomography," in *prepared for the 14th Laser Sensing Symposium*, 1991),
4. D. Huang, E. A. Swanson, C. P. Lin, J. S. Schuman, W. G. Stinson, W. Chang, M. R. Hee, T. Flotte, K. Gregory, and C. A. Puliafito, "Optical coherence tomography," science **254**, 1178-1181 (1991).
5. J. G. Fujimoto, "Biomedical Imaging and Optical Biopsy using Optical Coherence Tomography," The Journal of the Japan Society for Respiratory Endoscopy **23**, 188 (2001).
6. M. E. Brezinski, G. J. Tearney, B. E. Bouma, J. A. Izatt, M. R. Hee, E. A. Swanson, J. F. Southern, and J. G. Fujimoto, "Optical coherence tomography for optical biopsy: properties and demonstration of vascular pathology," Circulation **93**, 1206-1213 (1996).
7. J. G. Fujimoto and W. Drexler, "Introduction to OCT," Optical Coherence Tomography: Technology and Applications, 3-64 (2015).
8. J. Fujimoto and D. Huang, "Foreword: 25 years of optical coherence tomography," Investigative ophthalmology & visual science **57**, OCTi-OCTii (2016).
9. S. Marschall, B. Sander, M. Mogensen, T. M. Jørgensen, and P. E. Andersen, "Optical coherence tomography—current technology and applications in clinical and biomedical research," Analytical and bioanalytical chemistry **400**, 2699-2720 (2011).
10. M. Kim, S. Y. Choi, and Y.-H. Park, "Analysis of choroidal and central foveal thicknesses in acute anterior uveitis by enhanced-depth imaging optical coherence tomography," BMC ophthalmology **17**, 1-7 (2017).
11. C. X. Qian, D. Charran, C. R. Strong, T. J. Steffens, T. Jayasundera, and J. R. Heckenlively, "Optical coherence tomography examination of the retinal pigment epithelium in best vitelliform macular dystrophy," Ophthalmology **124**, 456-463 (2017).
12. A. I. Dastiridou, E. Bousquet, L. Kuehlewein, T. Tepelus, D. Monnet, S. Salah, A. Brezin, and S. R. Sadda, "Choroidal imaging with swept-source optical coherence tomography in patients with birdshot chorioretinopathy: choroidal reflectivity and thickness," Ophthalmology **124**, 1186-1195 (2017).
13. V. Gupta, A. Gupta, and M. R. Dogra, *Atlas optical coherence tomography of macular diseases and glaucoma* (JP Medical Ltd, 2010).
14. M. Restori, "Imaging the vitreous: optical coherence tomography and ultrasound imaging," Eye **22**, 1251-1256 (2008).
15. E. C. Sattler, R. Kästle, and J. Welzel, "Optical coherence tomography in dermatology," Journal of biomedical optics **18**, 061224 (2013).
16. V. Demidov, X. Zhao, O. Demidova, H. Y. Pang, C. Flueraru, F.-F. Liu, and I. A. Vitkin, "Preclinical quantitative in-vivo assessment of skin tissue vascularity in radiation-induced fibrosis with optical coherence tomography," Journal of Biomedical Optics **23**, 106003 (2018).
17. J. Olsen, J. Holmes, and G. B. Jemec, "Advances in optical coherence tomography in dermatology—a review," Journal of biomedical optics **23**, 040901 (2018).

18. M. C. Pierce, J. Strasswimmer, B. H. Park, B. Cense, and J. F. De Boer, "Advances in optical coherence tomography imaging for dermatology," Journal of investigative dermatology **123**, 458-463 (2004).
19. J. Wang, Y. Xu, and S. A. Boppart, "Review of optical coherence tomography in oncology," Journal of biomedical optics **22**, 121711 (2017).
20. M. J. Gora, J. S. Sauk, R. W. Carruth, K. A. Gallagher, M. J. Suter, N. S. Nishioka, L. E. Kava, M. Rosenberg, B. E. Bouma, and G. J. Tearney, "Tethered capsule endomicroscopy enables less invasive imaging of gastrointestinal tract microstructure," Nature medicine **19**, 238-240 (2013).
21. G. J. Tearney, E. Regar, T. Akasaka, T. Adriaenssens, P. Barlis, H. G. Bezerra, B. Bouma, N. Bruining, J.-m. Cho, and S. Chowdhary, "Consensus standards for acquisition, measurement, and reporting of intravascular optical coherence tomography studies: a report from the International Working Group for Intravascular Optical Coherence Tomography Standardization and Validation," Journal of the American College of Cardiology **59**, 1058-1072 (2012).
22. V. Nagaraja, A. Kalra, and R. Puri, "When to use intravascular ultrasound or optical coherence tomography during percutaneous coronary intervention?," Cardiovascular Diagnosis and Therapy **10**, 1429 (2020).
23. E. A. Swanson, "Beyond better clinical care: OCT's economic impact," Laser Focus World **52**, 35-38 (2016).
24. Z. A. Ali, K. Karimi Galougahi, A. Maehara, R. A. Shlofmitz, O. Ben-Yehuda, G. S. Mintz, and G. W. Stone, "Intracoronary optical coherence tomography 2018: current status and future directions," JACC: Cardiovascular Interventions **10**, 2473-2487 (2017).
25. Q. T. Bui, M. Prempeh, and R. L. Wilensky, "Atherosclerotic plaque development," The international journal of biochemistry & cell biology **41**, 2109-2113 (2009).
26. F. L. Celletti, J. M. Waugh, P. G. Amabile, A. Brendolan, P. R. Hilfiker, and M. D. Dake, "Vascular endothelial growth factor enhances atherosclerotic plaque progression," Nature medicine **7**, 425-429 (2001).
27. M. E. Rosenfeld, "An overview of the evolution of the atherosclerotic plaque: from fatty streak to plaque rupture and thrombosis," Zeitschrift für Kardiologie **89**, VII2-VII6 (2000).
28. M. Sirol, "Atherosclerosis Plaque Imaging and Characterization Using Magnetic Resonance Imaging," US Cardiology 2 (2005): 129-132.
29. Z.-Y. Li, S. P. Howarth, T. Tang, and J. H. Gillard, "How critical is fibrous cap thickness to carotid plaque stability? A flow–plaque interaction model," Stroke **37**, 1195-1199 (2006).
30. J. Fog Bentzon and E. Falk, "Atherosclerosis, Vulnerable Plaques, and Acute Coronary Syndromes,," in *Genomic and Personalized Medicine (Second Edition),*, G. S. Ginsburg and H. Willard, eds. (Academic Press, 2013), pp. 530-539.
31. T. J. Allen, P. C. Beard, A. Hall, A. P. Dhillon, and J. S. Owen, "Spectroscopic photoacoustic imaging of lipid-rich plaques in the human aorta in the 740 to 1400 nm wavelength range," Journal of biomedical optics **17**, 061209 (2012).
32. K. Jansen, M. Wu, A. F. van der Steen, and G. van Soest, "Photoacoustic imaging of human coronary atherosclerosis in two spectral bands," Photoacoustics **2**, 12-20 (2014).
33. S. Sethuraman, J. H. Amirian, S. H. Litovsky, R. W. Smalling, and S. Y. Emelianov, "Spectroscopic intravascular photoacoustic imaging to differentiate atherosclerotic plaques," Optics express **16**, 3362-3367 (2008).
34. R. Virmani, A. P. Burke, A. Farb, and F. D. Kolodgie, "Pathology of the vulnerable plaque," Journal of the American College of Cardiology **47**, C13-C18 (2006).
35. R. Virmani, F. D. Kolodgie, A. P. Burke, A. Farb, and S. M. Schwartz, "Lessons from sudden coronary death: a comprehensive morphological classification scheme for atherosclerotic lesions," Arteriosclerosis, thrombosis, and vascular biology **20**, 1262-1275 (2000).

36. A. P. Burke, A. Farb, G. T. Malcom, Y.-h. Liang, J. Smialek, and R. Virmani, "Coronary risk factors and plaque morphology in men with coronary disease who died suddenly," New England Journal of Medicine **336**, 1276-1282 (1997).
37. M. Koide, A. Matsuo, S. Shimoo, K. Takamatsu, A. Kyodo, Y. Tsuji, K. Mera, Y. Tsubakimoto, K. Isodono, and T. Sakatani, "Cholesterol crystal depth in coronary atherosclerotic plaques: A novel index of plaque vulnerability using optical frequency domain imaging," PLoS One **12**, e0180303 (2017).
38. R. Virmani, A. P. Burke, A. Farb, and F. D. Kolodgie, "Pathology of the unstable plaque," Progress in cardiovascular diseases **44**, 349-356 (2002).
39. P. Libby, "Mechanisms of acute coronary syndromes and their implications for therapy," N Engl J Med **368**, 2004-2013 (2013).
40. E. Braunwald, "Unstable angina: an etiologic approach to management," Circulation **98**, 2219-2222 (1998).
41. E. Braunwald, "Unstable angina: a classification," in *Unstable angina* (Springer, 1990), pp. 103-111.
42. Y. Li, J. Jing, E. Heidari, J. Zhu, Y. Qu, and Z. Chen, "Intravascular optical coherence tomography for characterization of atherosclerosis with a 1.7 micron swept-source laser," Scientific reports **7**, 1-6 (2017).
43. R. Waksman and R. Torguson, "The vulnerable plaque detected: time to consider treatment," The Lancet **397**, 943-945 (2021).
44. P. W. Serruys, M.-C. Morice, A. P. Kappetein, A. Colombo, D. R. Holmes, M. J. Mack, E. Ståhle, T. E. Feldman, M. Van Den Brand, and E. J. Bass, "Percutaneous coronary intervention versus coronary-artery bypass grafting for severe coronary artery disease," New England journal of medicine **360**, 961-972 (2009).
45. E. D. Grech, "Percutaneous coronary intervention. II: The procedure," Bmj **326**, 1137-1140 (2003).
46. A. Huang, S. Patel, C. S. McAlpine, and G. H. Werstuck, "The role of endoplasmic reticulum stress-glycogen synthase kinase-3 signaling in atherogenesis," International Journal of Molecular Sciences **19**, 1607 (2018).
47. E. Hecht, *Optics* (Pearson Education India, 2012).
48. M. E. Brezinski, *Optical coherence tomography: principles and applications* (Elsevier, 2006).
49. Z. Chen, T. E. Milner, D. Dave, and J. S. Nelson, "Optical Doppler tomographic imaging of fluid flow velocity in highly scattering media," Optics letters **22**, 64-66 (1997).
50. M. A. Choma, A. K. Ellerbee, C. Yang, T. L. Creazzo, and J. A. Izatt, "Spectral-domain phase microscopy," Optics letters **30**, 1162-1164 (2005).
51. A. Moiseev, S. Ksenofontov, M. Sirotkina, E. Kiseleva, M. Gorozhantseva, N. Shakhova, L. Matveev, V. Zaitsev, A. Matveyev, and E. Zagaynova, "Optical coherence tomography-based angiography device with real-time angiography B-scans visualization and hand-held probe for everyday clinical use," Journal of biophotonics **11**, e201700292 (2018).
52. J. Yang, L. Liu, J. P. Campbell, D. Huang, and G. Liu, "Handheld optical coherence tomography angiography," Biomedical optics express **8**, 2287-2300 (2017).
53. L. Wang, O. Murphy, N. G. Caldito, P. A. Calabresi, and S. Saidha, "Emerging applications of optical coherence tomography angiography (OCTA) in neurological research," Eye and Vision **5**, 1-11 (2018).
54. E. B. Shokouhi, M. Razani, A. Gupta, and N. Tabatabaei, "Comparative study on the detection of early dental caries using thermo-photonic lock-in imaging and optical coherence tomography," Biomedical optics express **9**, 3983-3997 (2018).
55. H. Stary, "Composition and classification of human atherosclerotic lesions," Virchows Archiv A **421**, 277-290 (1992).

56. M. Villiger, K. Otsuka, A. Karanasos, P. Doradla, J. Ren, N. Lippok, M. Shishkov, J. Daemen, R. Diletti, and R.-J. van Geuns, "Coronary plaque microstructure and composition modify optical polarization: a new endogenous contrast mechanism for optical frequency domain imaging," JACC: Cardiovascular Imaging **11**, 1666-1676 (2018).
57. G. Lan, M. Singh, K. V. Larin, and M. D. Twa, "Common-path phase-sensitive optical coherence tomography provides enhanced phase stability and detection sensitivity for dynamic elastography," Biomedical optics express **8**, 5253-5266 (2017).
58. V. Y. Zaitsev, A. L. Matveyev, L. A. Matveev, G. V. Gelikonov, A. I. Omelchenko, O. I. Baum, S. E. Avetisov, A. V. Bolshunov, V. I. Siplivy, and D. V. Shabanov, "Optical coherence elastography for strain dynamics measurements in laser correction of cornea shape," Journal of biophotonics **10**, 1450-1463 (2017).
59. W. Qi, R. Li, T. Ma, J. Li, K. Kirk Shung, Q. Zhou, and Z. Chen, "Resonant acoustic radiation force optical coherence elastography," Applied physics letters **103**, 103704 (2013).
60. Y. Qu, T. Ma, Y. He, M. Yu, J. Zhu, Y. Miao, C. Dai, P. Patel, K. K. Shung, and Q. Zhou, "Miniature probe for mapping mechanical properties of vascular lesions using acoustic radiation force optical coherence elastography," Scientific reports **7**, 1-8 (2017).
61. A. M. Fard, P. Vacas-Jacques, E. Hamidi, H. Wang, R. W. Carruth, J. A. Gardecki, and G. J. Tearney, "Optical coherence tomography–near infrared spectroscopy system and catheter for intravascular imaging," Optics express **21**, 30849-30858 (2013).
62. J. Muller and R. Madder, "OCT-NIRS imaging for detection of coronary plaque structure and vulnerability," Frontiers in Cardiovascular Medicine **7**, 90 (2020).
63. F. Rasulo, B. Matta, and N. Varanini, "Cerebral blood flow monitoring," Neuromonitoring Techniques, 31-56 (2018).
64. D. Erlinge, A. Maehara, O. Ben-Yehuda, H. E. Bøtker, M. Maeng, L. Kjøller-Hansen, T. Engstrøm, M. Matsumura, A. Crowley, and O. Dressler, "Identification of vulnerable plaques and patients by intracoronary near-infrared spectroscopy and ultrasound (PROSPECT II): a prospective natural history study," The Lancet **397**, 985-995 (2021).
65. G. J. Ughi, J. Verjans, A. M. Fard, H. Wang, E. Osborn, T. Hara, A. Mauskapf, F. A. Jaffer, and G. J. Tearney, "Dual modality intravascular optical coherence tomography (OCT) and near-infrared fluorescence (NIRF) imaging: a fully automated algorithm for the distance-calibration of NIRF signal intensity for quantitative molecular imaging," The international journal of cardiovascular imaging **31**, 259-268 (2015).
66. C. Vinegoni, I. Botnaru, E. Aikawa, M. A. Calfon, Y. Iwamoto, E. J. Folco, V. Ntziachristos, R. Weissleder, P. Libby, and F. A. Jaffer, "Indocyanine green enables near-infrared fluorescence imaging of lipid-rich, inflamed atherosclerotic plaques," Science translational medicine **3**, 84ra45-84ra45 (2011).
67. G. J. Ughi, H. Wang, E. Gerbaud, J. A. Gardecki, A. M. Fard, E. Hamidi, P. Vacas-Jacques, M. Rosenberg, F. A. Jaffer, and G. J. Tearney, "Clinical characterization of coronary atherosclerosis with dual-modality OCT and near-infrared autofluorescence imaging," JACC: Cardiovascular imaging **9**, 1304-1314 (2016).
68. D. C. Adler, S.-W. Huang, R. Huber, and J. G. Fujimoto, "Photothermal detection of gold nanoparticles using phase-sensitive optical coherence tomography," Optics express **16**, 4376-4393 (2008).
69. C. Zhou, T.-H. Tsai, D. C. Adler, H.-C. Lee, D. W. Cohen, A. Mondelblatt, Y. Wang, J. L. Connolly, and J. G. Fujimoto, "Photothermal optical coherence tomography in ex vivo human breast tissues using gold nanoshells," Optics letters **35**, 700-702 (2010).

70. A. S. Paranjape, R. Kuranov, S. Baranov, L. L. Ma, J. W. Villard, T. Wang, K. V. Sokolov, M. D. Feldman, K. P. Johnston, and T. E. Milner, "Depth resolved photothermal OCT detection of macrophages in tissue using nanorose," Biomedical Optics Express **1**, 2-16 (2010).
71. J. Tucker-Schwartz, T. Meyer, C. Patil, C. Duvall, and M. Skala, "In vivo photothermal optical coherence tomography of gold nanorod contrast agents," Biomedical optics express **3**, 2881-2895 (2012).
72. M. C. Skala, M. J. Crow, A. Wax, and J. A. Izatt, "Photothermal optical coherence tomography of epidermal growth factor receptor in live cells using immunotargeted gold nanospheres," Nano letters **8**, 3461-3467 (2008).
73. M. Lapierre-Landry, A. Y. Gordon, J. S. Penn, and M. C. Skala, "In vivo photothermal optical coherence tomography of endogenous and exogenous contrast agents in the eye," Scientific reports **7**, 1-9 (2017).
74. R. V. Kuranov, J. Qiu, A. B. McElroy, A. Estrada, A. Salvaggio, J. Kiel, A. K. Dunn, T. Q. Duong, and T. E. Milner, "Depth-resolved blood oxygen saturation measurement by dual-wavelength photothermal (DWP) optical coherence tomography," Biomedical optics express **2**, 491-504 (2011).
75. M. Lapierre-Landry, A. L. Huckenpahler, B. A. Link, R. F. Collery, J. Carroll, and M. C. Skala, "Imaging melanin distribution in the zebrafish retina using photothermal optical coherence tomography," Translational vision science & technology **7**, 4-4 (2018).
76. G. Guan, R. Reif, R. K. Wang, and Z. Huang, "Depth profiling of photothermal compound concentrations using phase sensitive optical coherence tomography," Journal of biomedical optics **16**, 126003 (2011).
77. S. Makita and Y. Yasuno, "In vivo photothermal optical coherence tomography for non-invasive imaging of endogenous absorption agents," Biomedical optics express **6**, 1707-1725 (2015).
78. M. Lapierre-Landry, J. M. Tucker-Schwartz, and M. C. Skala, "Depth-resolved analytical model and correction algorithm for photothermal optical coherence tomography," Biomedical Optics Express **7**, 2607-2622 (2016).
79. D. Veysset, T. Ling, Y. Zhuo, V. P. Pandiyan, R. Sabesan, and D. Palanker, "Interferometric imaging of thermal expansion for temperature control in retinal laser therapy," Biomedical Optics Express **13**, 728-743 (2022).
80. A. Gupta, M. Villiger, and N. Tabatabaei, "Optimal selection of laser modulation parameters in photothermal optical coherence tomography," in *Optical Elastography and Tissue Biomechanics IV*, (International Society for Optics and Photonics, 2017), 1006718.
81. T. De Bruin, C. B. Brouwer, M. van Linde-Sibenius Trip, H. Jansen, and D. W. Erkelens, "Different postprandial metabolism of olive oil and soybean oil: a possible mechanism of the high-density lipoprotein conserving effect of olive oil," The American journal of clinical nutrition **58**, 477-483 (1993).
82. C. P. Fleming, J. Eckert, E. F. Halpern, J. A. Gardecki, and G. J. Tearney, "Depth resolved detection of lipid using spectroscopic optical coherence tomography," Biomedical optics express **4**, 1269-1284 (2013).
83. R. D. Madder, J. L. Smith, S. R. Dixon, and J. A. Goldstein, "Composition of Target Lesions by Near-Infrared Spectroscopy in Patients With Acute Coronary Syndrome Versus Stable Angina," Circulation: Cardiovascular Interventions **5**, 55-61 (2012).
84. R. D. Madder, J. A. Goldstein, S. P. Madden, R. Puri, K. Wolski, M. Hendricks, S. T. Sum, A. Kini, S. Sharma, D. Rizik, E. S. Brilakis, K. A. Shunk, J. Petersen, G. Weisz, R. Virmani, S. J. Nicholls, A. Maehara, G. S. Mintz, G. W. Stone, and J. E. Muller, "Detection by Near-Infrared Spectroscopy of Large Lipid Core Plaques at Culprit Sites in Patients With Acute ST-Segment Elevation Myocardial Infarction," JACC: Cardiovascular Interventions **6**, 838-846 (2013).

85. S. S. Choi, B. Lashkari, A. Mandelis, J. J. Weyers, A. Boyes, S. F. Foster, N. Alves-Kotzev, and B. Courtney, "Interference-free detection of lipid-laden atherosclerotic plaques by 3D co-registration of frequency-domain differential photoacoustic and ultrasound radar imaging," Scientific reports **9**, 1-11 (2019).
86. C. Felton, D. Crook, M. Davies, and M. Oliver, "Relation of plaque lipid composition and morphology to the stability of human aortic plaques," Arteriosclerosis, thrombosis, and vascular biology **17**, 1337-1345 (1997).
87. A. Ravandi, S. Babaei, R. Leung, J. C. Monge, G. Hoppe, H. Hoff, H. Kamido, and A. Kuksis, "Phospholipids and oxophospholipids in atherosclerotic plaques at different stages of plaque development," Lipids **39**, 97-109 (2004).
88. M. J. van Gemert, G. W. Lucassen, and A. Welch, "Time constants in thermal laser medicine: II. Distributions of time constants and thermal relaxation of tissue," Physics in Medicine & Biology **41**, 1381 (1996).
89. G. Szafner, D. Bicanic, and O. Dóka, "Effect of fat content on the thermal effusivity of foods: an inverse photopyroelectric study," International Journal of Food Properties **14**, 666-674 (2011).
90. A. Hagermann, J. Zarnecki, M. Towner, P. Rosenberg, R. Lorenz, M. Leese, B. Hathi, and A. Ball, "Physical properties as indicators of liquid compositions: Derivation of the composition for Titan's surface liquids from the Huygens SSP measurements," Monthly Notices of the Royal Astronomical Society **359**, 637-642 (2005).
91. M. Lapierre-Landry, T. B. Connor, J. Carroll, Y. K. Tao, and M. C. Skala, "Photothermal optical coherence tomography of indocyanine green in ex vivo eyes," Optics letters **43**, 2470-2473 (2018).
92. J. Valvano and B. Chitsabesan, "Thermal conductivity and diffusivity of arterial wall and atherosclerotic plaque," Lasers Life Sci **1**(1987).
93. X. Zhu, "Prediction of specific heat capacity of food lipids and foods," (Doctoral dissertation, The Ohio State University, 2015).
94. E. Contreras-Gallegos, F. A. Domínguez-Pacheco, C. Hernández-Aguilar, J. A. Salazar-Montoya, E. G. Ramos-Ramírez, and A. Cruz-Orea, "Specific heat of vegetable oils as a function of temperature obtained by adiabatic scanning calorimetry," Journal of Thermal Analysis and Calorimetry **128**, 523-531 (2017).
95. H. Lim, "Temperature dependent refractive index of lipid tissue by optical coherence tomography imaging," (Doctoral dissertation, University of Texas, 2011).
96. A. Raudino, F. Zuccarello, C. La Rosa, and G. Buemi, "Thermal expansion and compressibility coefficients of phospholipid vesicles: experimental determination and theoretical modeling," Journal of Physical Chemistry **94**, 4217-4223 (1990).
97. E. W. Chang, J. B. Kobler, and S. H. Yun, "Subnanometer optical coherence tomographic vibrography," Optics letters **37**, 3678-3680 (2012).
98. J. Narula, M. Nakano, R. Virmani, F. D. Kolodgie, R. Petersen, R. Newcomb, S. Malik, V. Fuster, and A. V. Finn, "Histopathologic characteristics of atherosclerotic coronary disease and implications of the findings for the invasive and noninvasive detection of vulnerable plaques," J Am Coll Cardiol **61**, 1041-1051 (2013).
99. J. E. Phipps, T. Hoyt, D. Vela, T. Wang, J. E. Michalek, L. M. Buja, I.-K. Jang, T. E. Milner, and M. D. Feldman, "Diagnosis of Thin-Capped Fibroatheromas in Intravascular Optical Coherence Tomography Images: Effects of Light Scattering," Circ Cardiovasc Interv **9**, 10.1161/CIRCINTERVENTIONS.1115.003163 e003163 (2016).
100. H. Yabushita, B. E. Bouma, S. L. Houser, H. T. Aretz, I.-K. Jang, K. H. Schlendorf, C. R. Kauffman, M. Shishkov, D.-H. Kang, and E. F. Halpern, "Characterization of human atherosclerosis by optical coherence tomography," Circulation **106**, 1640-1645 (2002).
101. B. E. Saleh and M. C. Teich, *Fundamentals of photonics* (john Wiley & sons, 2019).

102. A. Mandelis, "Green's functions in thermal-wave physics: Cartesian coordinate representations," Journal of applied physics **78**, 647-655 (1995).
103. N. Tabatabaei, "Development of Frequency and Phase Modulated Thermal-wave Methodologies for Materials Non-destructive Evaluation and Thermophotonic Imaging of Turbid Media," (University of Toronto, 2012).
104. A. Mandelis and J. F. Power, "Frequency-modulated impulse response photothermal detection through optical reflectance. 1: Theory," Applied optics **27**, 3397-3407 (1988).
105. H. D. Baehr and K. Stephan, *Wärme-und stoffübertragung* (Springer, 1994), Vol. 7.
106. M. Ruhi, A. Angoshtari, and R. Naghdabadi, "Thermoelastic analysis of thick-walled finite-length cylinders of functionally graded materials," Journal of Thermal Stresses **28**, 391-408 (2005).
107. P.Kelly, "Solid Mechanics Lecture Notes Part II, The University of Auckland," 53-82 (2013).
108. D. Armani, C. Liu, and N. Aluru, "Re-configurable fluid circuits by PDMS elastomer micromachining," in *Technical Digest. IEEE International MEMS 99 Conference. Twelfth IEEE International Conference on Micro Electro Mechanical Systems (Cat. No. 99CH36291)*, (IEEE, 1999), 222-227.
109. G. Cortela, N. Benech, W. Pereira, and C. Negreira, "Characterization of Acoustical Properties of a Phantom for Soft Tissues (PVCP and Graphite Powder) in the Range 20-45̊C," Physics Procedia **70**, 179-182 (2015).
110. J. E. Mark, *Polymer data handbook* (Oxford university press New York, 2009), Vol. 2.
111. M. Wróbel, A. Sękowska, M. Marchwiński, S. Galla, and A. Cenian, "Use of optical skin phantoms for calibration of dermatological lasers," in *Reflection, Scattering, and Diffraction from Surfaces V*, (International Society for Optics and Photonics, 2016), 996113.
112. L. Maggi, G. Cortela, M. A. von Kruger, C. Negreira, and W. C. de Albuquerque Pereira, "Ultrasonic Attenuation and Speed in phantoms made of PVCP and Evaluation of acoustic and thermal properties of ultrasonic phantoms made of polyvinyl chloride-plastisol (PVCP)," in *IWBBIO*, 2013), 233-241.
113. A. Tomas, M. Rasteiro, L. Gando-Ferreira, and S. Figueiredo, "Rheology of poly (vinyl chloride) plastisol: Effect of a particular nonionic cosurfactant," Journal of applied polymer science **115**, 599-607 (2010).
114. C. Markos, K. Vlachos, and G. Kakarantzas, "Guiding and thermal properties of a hybrid polymer-infused photonic crystal fiber," Optical Materials Express **2**, 929-941 (2012).
115. A. Norris, J. DeGroot, F. Nishida, U. Pernisz, N. Kushibiki, and T. Ogawa, "Silicone materials for optical applications," Midland, MI: Dow Corning Corporation (2003).
116. B. E. Schubert and D. Floreano, "Variable stiffness material based on rigid low-melting-point-alloy microstructures embedded in soft poly (dimethylsiloxane)(PDMS)," Rsc Advances **3**, 24671-24679 (2013).
117. "Techical Data Sheet for PVC plastisol, https://omnexus.specialchem.com/selection-guide/polyvinyl-chloride-pvc-plastic."
118. Y. He, S. Qin, B. A. Dyer, H. Zhang, L. Zhao, T. Chen, F. Zheng, Y. Sun, L. Shi, and Y. Rong, "Characterizing mechanical and medical imaging properties of polyvinyl chloride-based tissue-mimicking materials," Journal of applied clinical medical physics **20**, 176-183 (2019).
119. B. Yin, R. V. Kuranov, A. B. McElroy, S. S. Kazmi, A. K. Dunn, T. Q. Duong, and T. E. Milner, "Dual-wavelength photothermal optical coherence tomography for imaging microvasculature blood oxygen saturation," Journal of biomedical optics **18**, 056005 (2013).
120. J. B. Lopez, T. M. Alvarado, G. G. Coyt, A. M. Diosdado, and J. D. Reyes, "Thermal characterization of vegetable oils by means of photoacoustic techniques," Revista Mexicana de Física **59**, 168-172 (2013).

121. S. S. S. Choi, B. Lashkari, A. Mandelis, J. Son, N. Alves-Kotzev, S. F. Foster, M. Harduar, and B. Courtney, "Frequency-domain differential photoacoustic radar: theory and validation for ultrasensitive atherosclerotic plaque imaging," Journal of biomedical optics **24**, 066003 (2019).
122. K. Jansen, A. F. Van Der Steen, H. M. van Beusekom, J. W. Oosterhuis, and G. van Soest, "Intravascular photoacoustic imaging of human coronary atherosclerosis," Optics letters **36**, 597-599 (2011).
123. R. V. Kuranov, S. Kazmi, A. B. McElroy, J. W. Kiel, A. K. Dunn, T. E. Milner, and T. Q. Duong, "In vivo depth-resolved oxygen saturation by dual-wavelength photothermal (DWP) OCT," Optics express **19**, 23831-23844 (2011).
124. N. Katta, A. Cabe, T. Hoyt, A. B. McElroy, M. Feldman, and T. Milner, "Detection of lipid in coronary arteries using photothermal optical coherence tomography," Journal of the American College of Cardiology **73**, 1421-1421 (2019).
125. U. G. Indahl, N. S. Sahni, B. Kirkhus, and T. Næs, "Multivariate strategies for classification based on NIR-spectra—with application to mayonnaise," Chemometrics and Intelligent Laboratory Systems **49**, 19-31 (1999).
126. E. Stachowska, B. Dołęgowska, D. Chlubek, T. Wesołowska, K. Ciechanowski, P. Gutowski, H. Szumiłowicz, and R. Turowski, "Dietary trans fatty acids and composition of human atheromatous plaques," European journal of nutrition **43**, 313-318 (2004).
127. J.-H. Han, X. Liu, J. U. Kang, and C. G. Song, "High-resolution subsurface articular cartilage imaging based on Fourier-domain common-path optical coherence tomography," Chinese Optics Letters **8**, 167-169 (2010).
128. K. Wang, X. Meng, and Z. Guo, "Elastin Structure, Synthesis, Regulatory Mechanism and Relationship With Cardiovascular Diseases," Frontiers in Cell and Developmental Biology **9**(2021).
129. S. E. Reichheld, L. D. Muiznieks, R. Lu, S. Sharpe, and F. W. Keeley, "Sequence variants of human tropoelastin affecting assembly, structural characteristics and functional properties of polymeric elastin in health and disease," Matrix Biology **84**, 68-80 (2019).
130. C. M. Bishop and N. M. Nasrabadi, *Pattern recognition and machine learning* (Springer, 2006), Vol. 4.
131. F. Pereira, T. Mitchell, and M. Botvinick, "Machine learning classifiers and fMRI: a tutorial overview," Neuroimage **45**, S199-S209 (2009).
132. S. M. Weiss and C. A. Kulikowski, *Computer systems that learn: classification and prediction methods from statistics, neural nets, machine learning, and expert systems* (Morgan Kaufmann Publishers Inc., 1991).
133. A. Butola, A. Ahmad, V. Dubey, V. Srivastava, D. Qaiser, A. Srivastava, P. Senthilkumaran, and D. S. Mehta, "Volumetric analysis of breast cancer tissues using machine learning and swept-source optical coherence tomography," Applied optics **58**, A135-A141 (2019).
134. N. Anantrasirichai, A. Achim, J. E. Morgan, I. Erchova, and L. Nicholson, "SVM-based texture classification in optical coherence tomography," in *2013 IEEE 10th International Symposium on Biomedical Imaging*, (IEEE, 2013), 1332-1335.
135. M. Kulmaganbetov, R. J. Bevan, N. Anantrasirichai, A. Achim, I. Erchova, N. White, J. Albon, and J. E. Morgan, "Textural Feature Analysis of Optical Coherence Tomography Phantoms," Electronics **11**, 669 (2022).
136. L. Fang, S. Li, D. Cunefare, and S. Farsiu, "Segmentation based sparse reconstruction of optical coherence tomography images," IEEE transactions on medical imaging **36**, 407-421 (2016).
137. Z. Burgansky-Eliash, G. Wollstein, T. Chu, J. D. Ramsey, C. Glymour, R. J. Noecker, H. Ishikawa, and J. S. Schuman, "Optical coherence tomography machine learning classifiers for glaucoma detection: a preliminary study," Investigative ophthalmology & visual science **46**, 4147-4152 (2005).

138. M. Alam, D. Thapa, J. I. Lim, D. Cao, and X. Yao, "Computer-aided classification of sickle cell retinopathy using quantitative features in optical coherence tomography angiography," Biomedical optics express **8**, 4206-4216 (2017).
139. D. Le, T. Son, and X. Yao, "Machine learning in optical coherence tomography angiography," Experimental Biology and Medicine **246**, 2170-2183 (2021).
140. J. De Fauw, J. R. Ledsam, B. Romera-Paredes, S. Nikolov, N. Tomasev, S. Blackwell, H. Askham, X. Glorot, B. O'Donoghue, and D. Visentin, "Clinically applicable deep learning for diagnosis and referral in retinal disease," Nature medicine **24**, 1342-1350 (2018).
141. A. Moiseev, L. Snopova, S. Kuznetsov, N. Buyanova, V. Elagin, M. Sirotkina, E. Kiseleva, L. Matveev, V. Zaitsev, and F. Feldchtein, "Pixel classification method in optical coherence tomography for tumor segmentation and its complementary usage with OCT microangiography," Journal of biophotonics **11**, e201700072 (2018).
142. J. Möller, A. Bartsch, M. Lenz, I. Tischoff, R. Krug, H. Welp, M. R. Hofmann, K. Schmieder, and D. Miller, "Applying machine learning to optical coherence tomography images for automated tissue classification in brain metastases," International Journal of Computer Assisted Radiology and Surgery **16**, 1517-1526 (2021).
143. C. H. Liu, Y. Du, M. Singh, C. Wu, Z. Han, J. Li, A. Chang, C. Mohan, and K. V. Larin, "Classifying murine glomerulonephritis using optical coherence tomography and optical coherence elastography," Journal of biophotonics **9**, 781-791 (2016).
144. D. Levitz, L. Thrane, M. H. Frosz, P. E. Andersen, C. B. Andersen, J. Valanciunaite, J. Swartling, S. Andersson-Engels, and P. R. Hansen, "Determination of optical scattering properties of highly-scattering media in optical coherence tomography images," Optics express **12**, 249-259 (2004).
145. J. Cervantes, F. Garcia-Lamont, L. Rodríguez-Mazahua, and A. Lopez, "A comprehensive survey on support vector machine classification: Applications, challenges and trends," Neurocomputing **408**, 189-215 (2020).
146. J.-H. Wu, T. Nishida, R. N. Weinreb, and J.-W. Lin, "Performances of machine learning in detecting glaucoma using fundus and retinal optical coherence tomography images: A meta-analysis," American Journal of Ophthalmology (2021).
147. S. Z. Li, *Encyclopedia of Biometrics: I-Z* (Springer Science & Business Media, 2009), Vol. 2.
148. P. Meer, D. Mintz, A. Rosenfeld, and D. Y. Kim, "Robust regression methods for computer vision: A review," International journal of computer vision **6**, 59-70 (1991).
149. M. Sabzekar and S. M. H. Hasheminejad, "Robust regression using support vector regressions," Chaos, Solitons & Fractals **144**, 110738 (2021).
150. C. Pache, N. L. Bocchio, A. Bouwens, M. Villiger, C. Berclaz, J. Goulley, M. I. Gibson, C. Santschi, and T. Lasser, "Fast three-dimensional imaging of gold nanoparticles in living cells with photothermal optical lock-in Optical Coherence Microscopy," Optics express **20**, 21385-21399 (2012).
151. J. M. Tucker-Schwartz, M. Lapierre-Landry, C. A. Patil, and M. C. Skala, "Photothermal optical lock-in optical coherence tomography for in vivo imaging," Biomedical optics express **6**, 2268-2282 (2015).
152. T. Wang, T. Pfeiffer, M. Wu, W. Wieser, G. Amenta, W. Draxinger, A. F. van der Steen, R. Huber, and G. Van Soest, "Thermo-elastic optical coherence tomography," Optics letters **42**, 3466-3469 (2017).
153. A. Gaiduk, P. V. Ruijgrok, M. Yorulmaz, and M. Orrit, "Detection limits in photothermal microscopy," Chemical Science **1**, 343-350 (2010).
154. A. Gaiduk, M. Yorulmaz, P. Ruijgrok, and M. Orrit, "Room-temperature detection of a single molecule's absorption by photothermal contrast," Science **330**, 353-356 (2010).

155. M. H. Salimi, M. Villiger, and N. Tabatabaei, "Transient-mode photothermal optical coherence tomography," Optics Letters **46**, 5703-5706 (2021).
156. N. Borodinov, S. Neumayer, S. V. Kalinin, O. S. Ovchinnikova, R. K. Vasudevan, and S. Jesse, "Deep neural networks for understanding noisy data applied to physical property extraction in scanning probe microscopy," npj Computational Materials **5**, 1-8 (2019).
157. L. Fang, S. Li, R. P. McNabb, Q. Nie, A. N. Kuo, C. A. Toth, J. A. Izatt, and S. Farsiu, "Fast acquisition and reconstruction of optical coherence tomography images via sparse representation," IEEE transactions on medical imaging **32**, 2034-2049 (2013).
158. A. Abbasi, A. Monadjemi, L. Fang, and H. Rabbani, "Optical coherence tomography retinal image reconstruction via nonlocal weighted sparse representation," Journal of biomedical optics **23**, 036011 (2018).
159. Q. Hao, K. Zhou, J. Yang, Y. Hu, Z. Chai, Y. Ma, G. Liu, Y. Zhao, S. Gao, and J. Liu, "High signal-to-noise ratio reconstruction of low bit-depth optical coherence tomography using deep learning," Journal of Biomedical Optics **25**, 123702 (2020).
160. M. Pekala, N. Joshi, T. A. Liu, N. M. Bressler, D. C. DeBuc, and P. Burlina, "Deep learning based retinal OCT segmentation," Computers in biology and medicine **114**, 103445 (2019).
161. M. Neidhardt, M. Bengs, S. Latus, M. Schlüter, T. Saathoff, and A. Schlaefer, "4D deep learning for real-time volumetric optical coherence elastography," International journal of computer assisted radiology and surgery **16**, 23-27 (2021).
162. G. Kim, J. Kim, W. J. Choi, C. Kim, and S. Lee, "Integrated deep learning framework for accelerated optical coherence tomography angiography," Scientific Reports **12**, 1-12 (2022).
163. M. J. Davies, P. D. Richardson, N. Woolf, D. R. Katz, and J. Mann, "Risk of thrombosis in human atherosclerotic plaques: role of extracellular lipid, macrophage, and smooth muscle cell content," Heart **69**, 377-381 (1993).
164. D. S. Rao, J. G. Goldin, and M. C. Fishbein, "Determinants of plaque instability in atherosclerotic vascular disease," Cardiovascular Pathology **14**, 285-293 (2005).
165. O. Breitenstein and M. Langenkamp, "Lock-in thermography," in *Basics and Use for Functional Diagnostics of Electronics Components* (Springer, 2003).
166. Z. Chen, Z. Zeng, H. Shen, X. Zheng, P. Dai, and P. Ouyang, "DN-GAN: Denoising generative adversarial networks for speckle noise reduction in optical coherence tomography images," Biomedical Signal Processing and Control **55**, 101632 (2020).
167. P. A. Heidenreich, J. G. Trogdon, O. A. Khavjou, J. Butler, K. Dracup, M. D. Ezekowitz, E. A. Finkelstein, Y. Hong, S. C. Johnston, and A. Khera, "Forecasting the future of cardiovascular disease in the United States: a policy statement from the American Heart Association," Circulation **123**, 933-944 (2011).
168. S. Canada, "Available from: www.statcan.gc.ca/pub/82-625-x/2015001/article/14296-eng.htm," The ten leading causes of death, 2012.
169. M. H. Salimi, M. Villiger, and N. Tabatabaei, "Three-dimensional opto-thermo-mechanical model for predicting photo-thermal optical coherence tomography responses in multilayer geometries," Biomedical Optics Express **13**, 3416-3433 (2022).
170. M. Salimi, M. Villiger, and N. Tabatabaei, "Effects of lipid composition on photothermal optical coherence tomography signals," Journal of biomedical optics **25**, 120501 (2020).
171. N. Samadi, D. Thapa, M. Salimi, A. Parkhimchyk, and N. Tabatabaei, "Low-cost active thermography using cellphone infrared cameras: from early detection of dental caries to quantification of THC in oral fluid," Scientific reports **10**, 1-13 (2020).
172. D. Thapa, R. Welch, R. P. Dabas, M. Salimi, P. Tavakolian, K. Sivagurunathan, K. Ngai, B. Huang, Y. Finer, and S. Abrams, "Comparison of long-wave and mid-wave infrared imaging modalities for

photothermal coherence tomography of human teeth," IEEE Transactions on Biomedical Engineering (2022).
173. M. H. Salimi, M. Villiger, and N. Tabatabaei, "Detection of lipid at video rate with spectroscopic transient-mode photo-thermal optical coherence tomography (TM-PT-OCT)," in *Optical Coherence Tomography and Coherence Domain Optical Methods in Biomedicine XXVI*, (SPIE, 2022), 54-59.
174. M. Salimi, M. Villiger, and N. Tabatabaei, "Development of an opto-thermo-mechanical theoretical model for photothermal optical coherence tomography imaging of multilayered samples," in *European Conferences on Biomedical Optics 2021 (ECBO)*, OSA Technical Digest (Optical Society of America, 2021), ETu3D.4.
175. M. Salimi, M. Villiger, and N. Tabatabaei, "New model for understanding the relationship between tissue composition and photothermal optical coherence tomography signals," in *Label-free Biomedical Imaging and Sensing (LBIS) 2021*, (International Society for Optics and Photonics, 2021), 116550Q.

Appendices

Appendix A: System characterization

To characterize the performance of the assembled system, a series of experiments were done, before carrying out PT-OCT studies. These benchmark measurement, consisted of measurement of lateral and axial resolutions, physical dimension of a pixel, SNR, sensitivity roll-off, and phase stability.

I. Axial and lateral and pixel in depth

The theoretical expression to calculate the axial resolution in OCT for a beam with a Gaussian distribution of power is[7]:

$$\Delta z = \frac{2ln2}{\pi}\left(\frac{\lambda^2}{\Delta\lambda \times n}\right). \quad \text{(S.1)}$$

Where ΔZ is the FWHM the autocorrelation function, λ is the center wavelength, and Δλ is bandwidth of the laser. By putting the related values of the laser source in Eq. (S.1), theoretical axial resolution in air can be calculated as:

$$\Delta z = \frac{2ln2}{\pi}\left(\frac{1315^2}{115}\right) \simeq 6.6\mu m. \quad \text{(S.2)}$$

Also, in microscopy, the lateral resolution for a beam with Gaussian power profile is calculated by the following formula[7]:

$$\Delta x = \frac{4\lambda}{\pi}\left(\frac{\mathrm{f}}{a}\right). \quad \text{(S.3)}$$

Here "f" is the focal length of the lens and "a" is the spot size of the laser beam at the back aperture of the object. Using Eq. (S.3), the theoretical lateral resolution is calculated as:

$$\Delta x = \frac{4\times 1.315}{\pi}\left(\frac{18}{3}\right) = 10\mu m. \quad \text{(S.4)}$$

Lateral resolution was measured experimentally following the knife-edge method. In this method, variation of pixel intensity near a reflective line in dark background is measured (line spread function), then by applying a spatial derivative on the intensity in terms of distance, lateral point spread function is generated. FWHM of this point spread function represents the lateral resolution of the system. In this experiment, a microscopy calibration slide (Bioimager, Canada) with reflective scales was used. The 1 mm distance in the captured *en-face* image (Fig.66(a)) is 185 pixels. An area near a reflective line was selected to measure line spread function. The intensity of the line spread function in terms of pixel is shown in figure

66(b). After applying spatial derivative of the line spread function, the point spread function was calculated (Fig.66(c)). The FWHM of this function is 2.1 pixels that can be converted to distance as the follow:

$$\frac{1(mm)}{185(pixel)} = \frac{x}{2.1(pixel)} \rightarrow x = 11.35(\mu m). \quad \text{(S.5)}$$

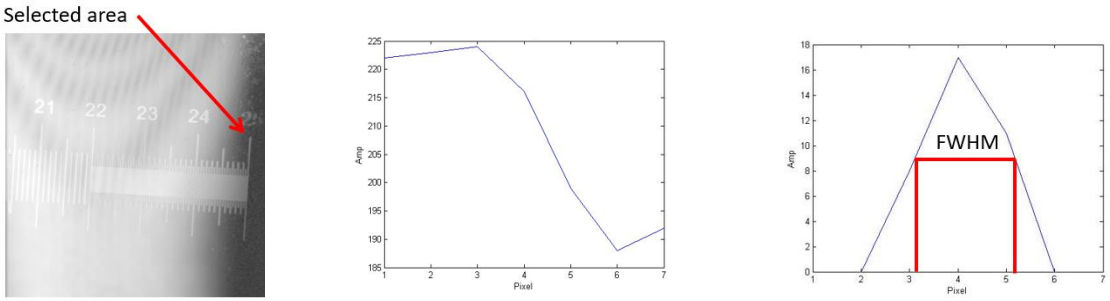

(a) (b) (c)

Figure 66. The experimental results to measure the lateral resolution with the edge response method. (a)En-face image of a microscopy calibration slide in which the selected area is pointed by the arrow, (b) the edge response, and (c)line spread function. See text for mathematical expression and the calculation steps.

The other way to measure the lateral resolution is using standard phantoms made for characterization of OCT systems such as the Arden phantom (Arden Photonics, U.K.). In this phantom there is a special pattern which consists of some parallel shiny lines. The distance of the first two lines is 1 µm, then distance of each line (n_L) by the next line (n_L+1) increases with increment of 1 µm. As depicted in figure 67(a), each 11 lines makes a group (m). By using following formula, lateral resolution can be calculated:

$$\Delta x = 11(m-1)+n_L. \quad \text{(S.6)}$$

Here, n_L is the number of the line in the m^{th} group that can be seen separately. In the captured *en-face* image (Fig.67(b)) the two first lines (which is n_L=1) in the second group (which is m=2) can be distinguished as separate lines, so using Eq. (s.7):

$$\Delta x = 11(2-1)+1=12\ \mu m. \quad \text{(S.7)}$$

Which is consistent with lateral resolution calculated from the knife-edge method.

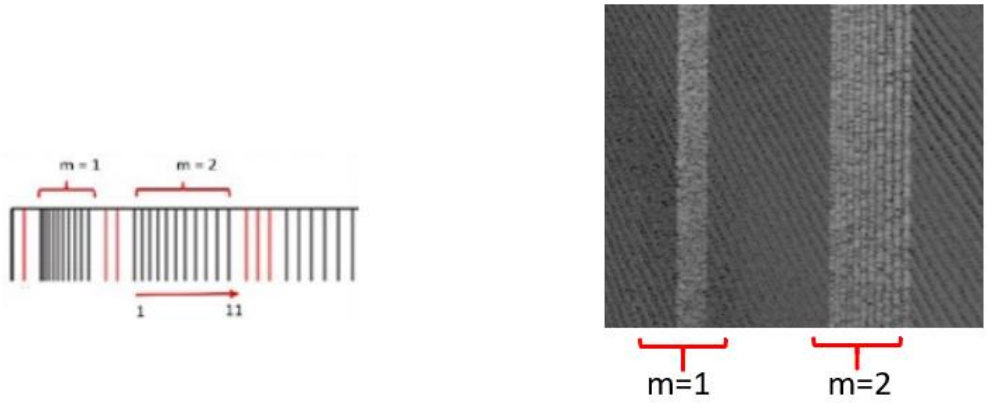

(a) (b)

Figure 67. Measuring the lateral resolution of the OCT system using Arden phantom. (a) Schematic and (b) en-face images of the Arden phantom. By looking at the captured en-face image, the line pair that is completely separable in these spatial patterns determines the lateral resolution. The mathematical formula to calculate the resolution is brought in text.

To measure the physical dimension of a pixel in depth in biological tissues, a droplet of coffee creamer which was diluted 10 times with water was placed in a well, and two B-mode images (Fig.68) were captured where the axial position of the well was physically changed 500 microns using a manual translation stage. Dimension of 1 pixel in depth can be calculated by making this ratio:

$$\frac{(280-185)\,(pixel)}{500(microns)} = \frac{1(pixel)}{x(micron)} \rightarrow x = 5.2\mu m. \qquad \text{(S.8)}$$

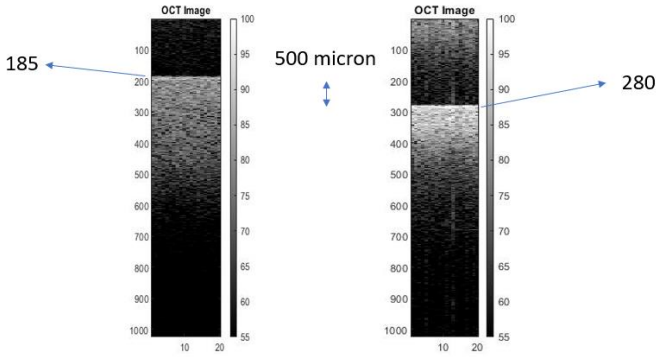

Figure 68. Experimental determination of physical dimension of a pixel. The B-mode images of a droplet of coffee creamer in two different levels. To measure the physical dimension of a pixel, the displacement in the top surface of the sample is calculated in these images. See text for finding the result.

In practice, axial resolution can be measured by calculating FWHM of an A-line. The captured A-line from a mirror as the sample is shown in figure 69. FWHM of this spike signal is 1.9 pixels in depth which can be converted to a physical distance as follow:

$$\frac{1\ (pixel)}{5.2(microns)} = \frac{1.9(pixel)}{x} \rightarrow x = 9.88(\mu m). \quad \text{(S.9)}$$

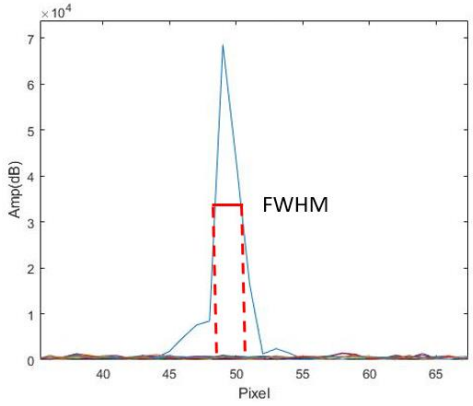

Figure 69. Experimental determination of the axial resolution of the OCT system. An acquired A-line as results of scanning a golden coated mirror in the sample arm. The FWHM of this spike-shape signal can be used to calculate the axial resolution.

II. SNR and Fall-off

To measure variation of the SNR of the system with depth, a golden coated mirror was installed as the sample in the focal plane of the lens, and the angle of mirror was adjusted by using a power meter to maximize the reflected power. To prevent saturation in the spectrometer, an neural density (ND) filter with OD number 3 was placed in the light path in the sample arm between the collimator and the objective lens. Then, using a manual translation stage, location of the reference arm mirror was changed with a constant pitch, and 1000 A-lines over time were captured at each mirror position. Using following formulas, SNR in dB scale was calculated at each mirror position.

$$T_{filt} = 10^{-OD} \times 100. \quad \text{(S.10)}$$

$$SNR_{max} = \left(\frac{I_{samp}}{\sigma_{noise}}\right)^2 - \left(R_{samp}T_{filt}^2\right) \overset{dB}{\Rightarrow} SNR_{max}(dB) = 20\log\left(\frac{I_{samp}}{\sigma_{noise}}\right) - 10\log\left(R_{samp}T_{filt}^2\right). \quad \text{(S.11)}$$

here OD represents OD number of ND filter, T_{filt} is the percentage of light transmittance, I_{samp} is intensity of the signal, σ_{noise} is the standard deviation of the averaged noise, and R_{samp} is the reflectivity of the reference mirror. At each location of the mirror, 1000 A-lines were captured, and averaged signal was plotted (Fig.70(a)). Increase in the length of the reference arm causes to the signal roll-off (amplitude of A-

lines decreases), because the larger ΔL results to the narrower fringes (see Eq. (1.1)), which is called fringe wash-out. To capture this fringe pattern, the camera pixels have a finite width and average the signal, which reduces the fringe visibility. The maximum SNR (Fig.70(b)) is 105 dB in air and fall-off is 23 dB in 4 mm which are comparable to performances typically reported for FD-OCT systems.

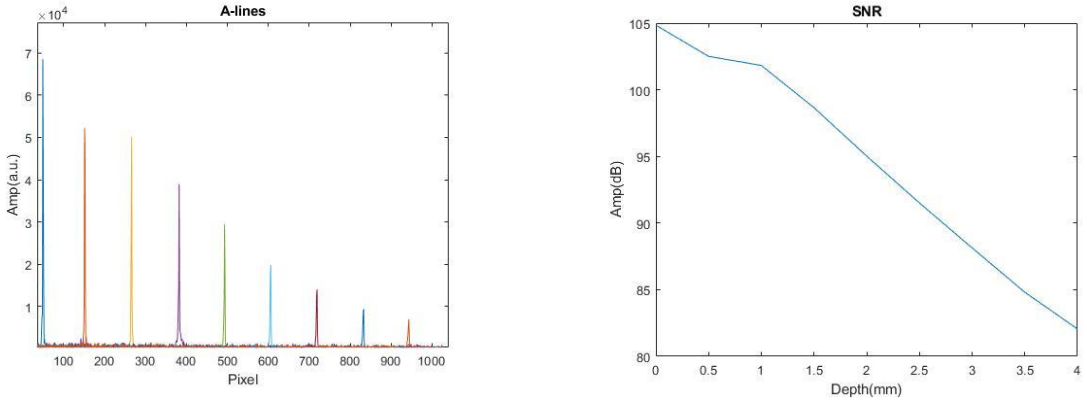

(a) (b)

Figure 70. Experimental measurement of the sensitivity roll-off the developed OCT system. In these experiments, a golden coated mirror was put in the sample arm, and the reference mirror was scanned at different distances. (a) A-line of various reference arm length and (b) calculated SNR in terms of depth. See text for the thretical expression to calcuate the SNR fall-off.

III. Phase stability

Phase stability in PT-OCT systems is a key parameter as it determines the noise floor of the system. To measure the phase stability of the system, a regular glass slide was used as the sample. At a given point, 1000 A-lines were captured over time, then the phase difference between the top and the bottom surface of the glass slide was calculated. The absolute phase of top (1st peak) and bottom surface (2nd peak) are shown in figure 71(a). To measure the phase stability in various SNRs, experiment was repeated at various angles of glass slide. The absolute phase (difference between top and bottom surface phase) at each angle over time is plotted in figure 71(b). These plots show small variations over time which speak to the stability of phase in our system. To quantify this stability, the following theoretical relationship can be used:

$$\Delta Phase = \frac{1}{4 \times SNR^2}. \tag{S.12}$$

Here, *ΔPhase* is the phase stability which is equal to the standard deviation of absolute phase. The standard deviation of absolute phase in terms of relative SNR (geometric mean of top and bottom surface SNR) is plotted in figure 72(a). Noted the SNR values in this plot were calculated using the definition of SNR from the first part of Eq. (S.11) (non-dB scale) The line in this figure, represent theoretical line which

was drawn using Eq.S. (12). The minimum experimental value for standard deviation of phase is about 2 milli radian, which is equal to distance by the following ratio:

$$\frac{2\pi}{\lambda/n} = \frac{phase}{2\times distance} \Rightarrow \frac{2\pi}{1315nm/1.33} = \frac{0.002}{2\times 0.55nm} \quad . \tag{S.13}$$

As such, the phase stability of the system in a glass medium is about 150 Pico meters, which demonstrated a low noise floor for our PT-OCT system. Another important aspect of noise floor is its degree of randomness. By applying FT on the absolute phase (Fig.72(b)), it can be observed that spectrum of noise does not contain any notable peaks, confirming the whiteness of noise and absence of any systematic source of noise in the system.

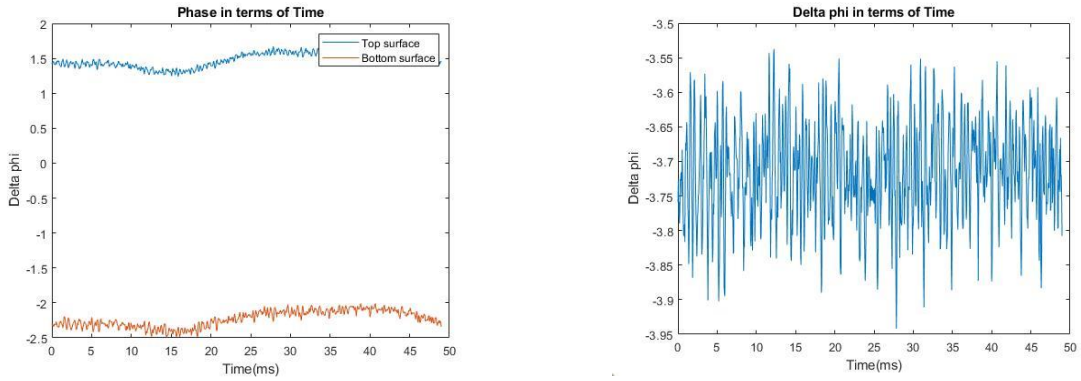

(a) (b)

Figure 71 The results of phase measurement over time. (a)Phase of the top and bottom surface of the glass slide; (b) absolute phase in terms of time, each line related to a slope of the glass slide.

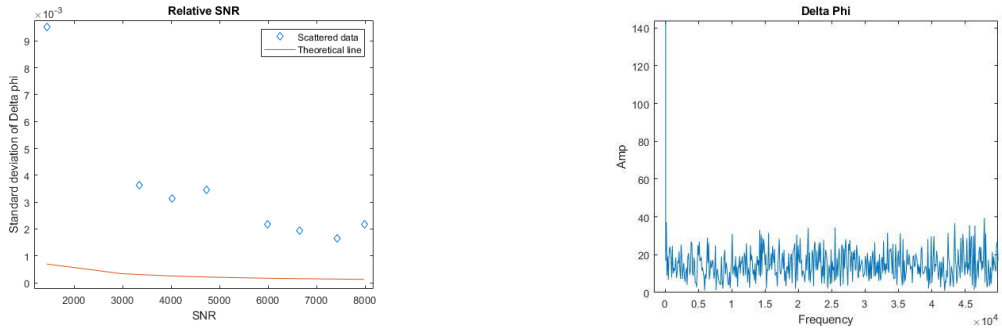

(a) (b)

Figure 72. The results of phase stability of the OCT system. (a) Standard deviation of absolute phase in terms of SNR; (b) Spectrum of absolute phase. The best obtraned value for phase stablity is about 2 millirad. Also the specrum of the phases repsresnts that thers is no systematic noise in the system.

Appendix B: The superposition of heat flux in the thermal field model

In PT-OCT, images originate from the alternating portion of the thermal field (aka. Thermal wave field) rather than the absolute one. That is, the goal of the presented model is to estimate the modulated part of the response (i.e., particular solution of the differential equation). We use the principle of superposition by first calculating the thermal wave field using Eqs. (2.15) and (2.16) in absence of flux at the top boundary and then adding the effect of boundary flux to the solution via the relative effusivity law (Eq. (2.18)). We believe that this approach provides acceptable approximation of the modulated portion of the temperature field, especially because the top surface is normally the hottest part, so this surface contributes to the most part of the flux.

As for validation, figure 73(a) (see below) compares the thermal wave field estimate of proposed model with that found from a finite difference method (FDM) simulation of the heat conduction equation in the time domain. The comparisons are made both in presence and in absence of heat flux at the top surface. As a sanity check, figure 73(a) shows that model and FDM offer almost identical results in absence of flux. In presence of flux, the model offers reasonably good approximation especially in terms of trends but with some overestimation (especially closer to the boundary).

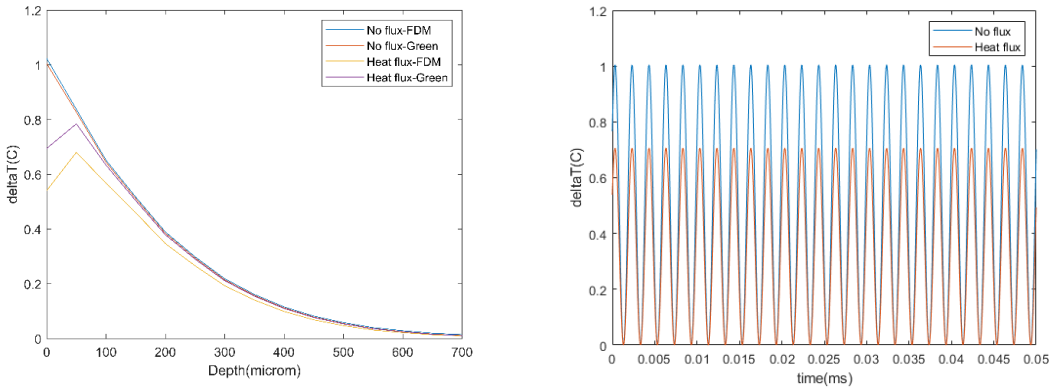

(a) (b)

Figure 73 The results of simulation to validate the suggested approach to calculate the heat flux on the sample surface. In this study, the FDM method was used as the ground truth of the study. The results of the proposed method in Chapter 2 were plotted in presence and absence of the heat flux. (a) Temperature change as a function of the depth, (b)the estimation of temperature change over time with our model. As there is no DC portion in the proposed method, there is no drift in the calculated temperature variation over time.

Figure 73.b depicts temporal variation temperature change (deltaT) on sample surface offered by our estimate model. Note that the Green's function solution does not offer the absolute temperature. Conversely, the FDM solution offers the absolute temperature (Fig.74(a)) from which the bulk heating

needs to be removed (Fig.74(b)) before lock-in demodulation in frequency domain is carried out (Fig.74(c)) to obtain the PT-OCT signal.

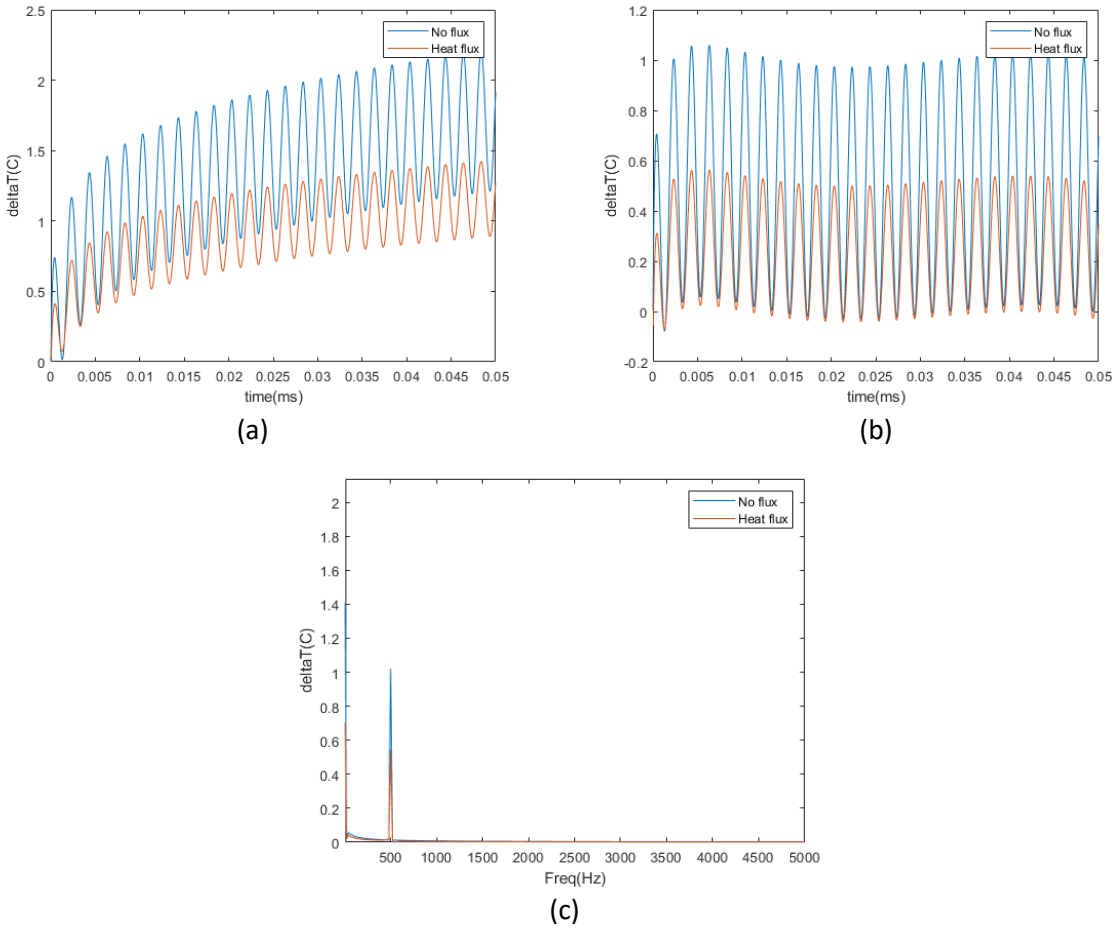

Figure 74. The results of simulation with the FDM method with considering a heat flux and without a hear flux on the sample (a) The temperature change over time with FDM, (b) the modulation of temperature change over time after drift line subtraction from FDM solution, (c) and the FFT results.

In addition to the above discussions and validation, we believe that the alignment of experimental results with overall model estimation (involving all blocks) offered in the manuscript further speaks to reasonable accuracy of our estimate model. To perform a preliminary validation, we expanded the beam size to generate a 1-D heat transfer regime in the sample in our model. Then, using a FDM solution in 1-D space we validated the results.

Appendix C: Mechanical stress/strain field

The equations for mechanical strain-strain field are generated in cylindrical coordination. Given an axis symmetric geometry, stain is mathematically defined in the cylindrical coordination as:

$$\begin{aligned} \varepsilon_r &= \frac{\partial u}{\partial r}, \\ \varepsilon_\theta &= \frac{u}{r}, \\ \varepsilon_z &= \frac{\partial w}{\partial z}. \end{aligned} \tag{S.14}$$

where u and w are the displacement field in radial and axial directions, respectively. Also, the constitutive thermoelastic equations in the cylindrical coordinate system are:

$$\begin{aligned} \sigma_r &= \frac{\nu E}{(1+\nu)(1-2\nu)} e + \frac{E}{1+\nu}\varepsilon_r - \frac{E\alpha\Delta T}{1-2\nu}, \\ \sigma_\theta &= \frac{\nu E}{(1+\nu)(1-2\nu)} e + \frac{E}{1+\nu}\varepsilon_\theta - \frac{E\alpha\Delta T}{1-2\nu}, \\ \sigma_z &= \frac{\nu E}{(1+\nu)(1-2\nu)} e + \frac{E}{1+\nu}\varepsilon_z - \frac{E\alpha\Delta T}{1-2\nu}. \end{aligned} \tag{S.15}$$

here e is:

$$e = \varepsilon_r + \varepsilon_\theta + \varepsilon_z \ . \tag{S.16}$$

Each slice of the sample along the depth is considered as a plane. The two-dimensional equilibrium equations for each plane in polar coordinates is:

$$\begin{aligned} \frac{\partial \sigma_r}{\partial r} + \frac{1}{r}\frac{\partial \tau_{r\theta}}{\partial \theta} + \frac{1}{r}(\sigma_r - \sigma_\theta) = 0, \\ \frac{\partial \tau_{r\theta}}{\partial r} + \frac{1}{r}\frac{\partial \sigma_\theta}{\partial \theta} + \frac{2\tau_{r\theta}}{r} = 0. \end{aligned} \tag{S.17}$$

In our case, as the problem can be considered as a planar axis-symmetric case, both geometry and loads distribution are expected to be symmetric. As such, the functionality of parameters with respect to azimuthal direction (θ) can be neglected. Given these, the equations of equilibrium in planar axis-symmetric condition reduce to:

$$\frac{\partial \sigma_r}{\partial r} + \frac{1}{r}(\sigma_r - \sigma_\theta) = 0 \ . \tag{S.18}$$

The general solution for this differential equation is:

$$u = \frac{1+\nu}{E}\left[-A\frac{1}{r} + 2(1-2\nu)Cr\right] . \tag{S.19}$$

By assuming a non-zero and constant value for axial strain along each slice $\bar{\varepsilon_z}$, we can expand this axis-symmetric planar solution to out of plane solution. This situation is called generalized plane strain. By putting the displacement in the definition of stress and strain, the generalized axisymmetric solution will be:

$$\varepsilon_r = \frac{1+\nu}{E}\left[A\frac{1}{r^2} + 2(1-2\nu)C\right] \quad , \tag{S.20}$$

$$\varepsilon_\theta = \frac{1+\nu}{E}\left[-A\frac{1}{r^2} + 2(1-2\nu)C\right] \quad , \tag{S.21}$$

$$\varepsilon_z = \bar{\varepsilon}_z \quad , \qquad (9)$$

$$\sigma_r = \frac{1+\nu}{E}\left[A\frac{1}{r^2} + 2C + \frac{\nu E}{(1+\nu)(1-2\nu)}\bar{\varepsilon}_z\right] - \frac{E\alpha\Delta T}{1-2\nu} \quad , (S.21)$$

$$\sigma_\theta = \frac{1+\nu}{E}\left[-A\frac{1}{r^2} + 2C + \frac{\nu E}{(1+\nu)(1-2\nu)}\bar{\varepsilon}_z\right] - \frac{E\alpha\Delta T}{1-2\nu} \ , \quad (S.22)$$

$$\sigma_z = 4\nu C + \frac{(1-\nu)E}{(1+\nu)(1-2\nu)}\bar{\varepsilon}_z - \frac{E\alpha\Delta T}{1-2\nu} \quad . \qquad (S.23)$$

In above equations, there are three unknowns: A, C, and ε_z. To obtain them, we need to define boundary conditions in each slice as:

1-At the boundary of HAZ and inner sided of TMAZ, radial stresses are equal. That is, as the boundary of HAZ and inner side of TMAZ have the same area and the forces are action-reaction, at these points radial stresses are equal.

2- At the boundary of HAZ and TMAZ, displacements are equal. As the sample was considered as a continuous medium, the displacement at the boundary of HAZ and inner side of TMAZ must be equal.

3- At the outer edge of TMAZ, displacement is zero. At the outer edge of TMAZ (far enough from the center of PT laser beam), no displacement is expected because the material is not affected by temperature change.

In other words, the mathematical expressions of above boundary conditions are:

$$\text{B. C. 1: } \sigma_r^{HAZ}|_{r=r_{HAZ}} = \sigma_r^{TMAZ}|_{r=r_{HAZ}},$$
$$\text{B. C. 2: } u^{HAZ}|_{r_{HAZ}} = u^{TMAZ}|_{r_{TMAZ}},$$
$$\text{B. C. 3: } u^{TMAZ}|_{r_{TMAZ}} = 0.$$

Moreover, for all slices:

4- The stresses in HAZ slices in axial direction must be equal. As HAZ is consisted of a pile of disk with the same area, therefore any load in axial direction generates the same axial stresses in all disks.

5- The stresses in TMAZ slices in axial direction must be equal. As TMAZ is consisted of a pile of disk with the same area, therefore any load in axial direction generates the same axial stresses in all disks.

6-The total strain in HAZ along the depth is zero. As a slice expands along the depth, the other disk must be squeezed to satisfy continuity.

7-The total strain in TMAZ along the depth is zero. As a slice expands along the depth, the other disk must be squeezed to satisfy continuity.

Therefore, the mathematical expressions are:

$$B.C.4: [\sigma_z^{HAZ}]_1 = [\sigma_z^{HAZ}]_2 = [\sigma_z^{HAZ}]_3 = \ldots,$$
$$B.C.5: [\sigma_z^{TMAZ}]_1 = [\sigma_z^{TMAZ}]_2 = [\sigma_z^{TMAZ}]_3 = \ldots,$$
$$B.C.6: \sum_i [\varepsilon_z^{HAZ}]_i = 0, B.C.7 \Rightarrow \sum_i [\varepsilon_z^{TMAZ}]_i = 0.$$

It should be noted that in HAZ, because the inner radius is zero, coefficient A is zero. So, in each slice, containing a HAZ and TMAZ, there are 5 unknowns, namely: C^{HAZ}, ε^{HAZ}, A^{TMAZ}, C^{TMAZ}, and ε^{TMAZ}. Therefore, in general, if we have n slices, there are 5×n unknowns. On the other hand, boundary conditions 1 to 3 give us 3×n equations; additional 2×(n-1) equations are offered by boundary condition 4 and 5. Finally, additional 2 equations can be generated via boundary condition 6 and 7. As such, it can be seen the number of unknowns and equations are equal, so by putting all equations in matrix system, and using inverse matrix approach, the unknowns will be obtained.

The definitions of HAZ and TMAZ in the model enable us to estimate the mechanical field in a simpler mathematical form by converting a continuous field to a discontinuous field. Figure 75 shows that when the ratio of r_{TMAZ}/r_{HAZ} go over 1.8 there is no change in the modeled signal. In our estimation model, we considered a safety factor and set r_{TMAZ}/r_{HAZ} =10 which will also lead to the more familiar case of thick-walled cylinders condition in the mechanical block.

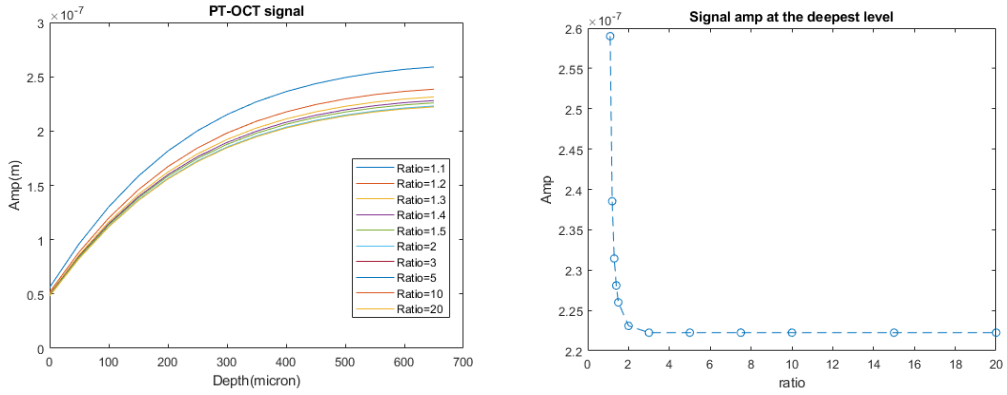

Figure 75. The results of survey on the effect of the ratio between HAZ and TMAZ in the model. A PT-OCT signal as function of depth is plotted at different ratio of TMAZ/HAZ (left). The difference between simulation values of the PT-OCT signals at the deepest depth of the sample (right).

Appendix D: Optimization of parameters in the model

The optimized parameters of Table 3 were found via minimization of MSE between predicted model signals and one set of experimental signals. Both experimental and predicted signals were PT-OCT amplitude vs depth. To find the optimum values all parameters were optimized simultaneously within ranges of likely values (obtained from the literature; see Table 3) and the parameters yielding the global MSE minimum were selected as optimized parameter values. To provide a sense of uncertainty about optimized values we have produce several plots in figure 76. In these plots all other parameters are kept as the optimized values reported in manuscript Table 3 while the one parameter is scanned and the MSE calculated. The minimum in all these plots corresponds to the optimized values that we reported in the Table 3. It can also be seen that deviation from the minima results in sharp increase in MSE which speaks to the reasonable confidence in obtained optimized values.

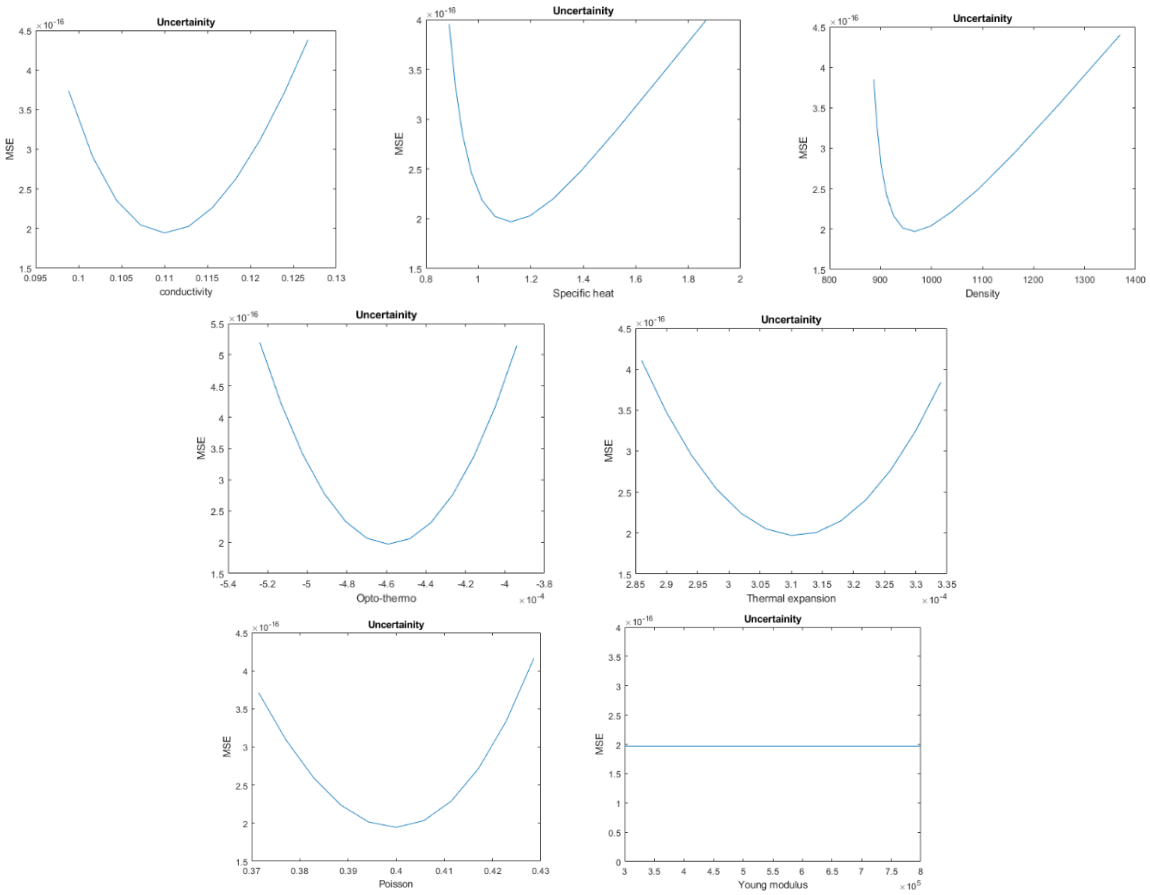

Figure 76. The results of the study of optimization of the inputs parameters in the model. In this survey, seven material property parameters were selected to optimize. One experimental signal was also selected for fitting process. In each panel, the MSE of simulation and experimental signals for each parameter at the scanning range are plotted. The rate of change for each parameters shows the significant of that specific parameter on the model.

Appendix E: List of publications

The peer-review journals:

1- Three-dimensional opto-thermo-mechanical model for predicting photo-thermal optical coherence tomography responses in multilayer geometries[169]

2- Transient-mode photothermal optical coherence tomography[155]

3- Effects of lipid composition on photothermal optical coherence tomography signals[170]

4- Low-cost active thermography using cellphone infrared cameras: from early detection of dental caries to quantification of THC in oral fluid[171]

5- Comparison of long-wave and mid-wave infrared imaging modalities for photothermal coherence tomography of human teeth[172]

Conference paper:

1- Detection of lipid at video rate with spectroscopic transient-mode photo-thermal optical coherence tomography (TM-PT-OCT)[173]

2- Development of an opto-thermo-mechanical theoretical model for photothermal optical coherence tomography imaging of multilayered samples[174]

3- New model for understanding the relationship between tissue composition and photothermal optical coherence tomography signals[175]